Non-thermal plasmas in flames and other inhomogeneous environments

by

Carmen Guerra García

Ing., Universidad Politécnica de Madrid (2007)
S.M., Massachusetts Institute of Technology (2011)

Submitted to the Department of Aeronautics and Astronautics
in partial fulfillment of the requirements for the degree of

Doctor of Philosophy

at the

MASSACHUSETTS INSTITUTE OF TECHNOLOGY

February 2015

Author .....
Department of Aeronautics and Astronautics
October 24, 2014

Certified by .....
Manuel Martinez-Sanchez
Professor Emeritus of Aeronautics and Astronautics
Thesis Supervisor

Certified by .....
Ahmed F. Ghoniem
Ronald C. Crane Professor of Mechanical Engineering
Committee Member

Certified by .....
Paulo Lozano
Associate Professor of Aeronautics and Astronautics
Committee Member

Certified by .....
Youssef M. Marzouk
Class of 1942 Associate Professor of Aeronautics and Astronautics
Committee Member

Accepted by .....
Paulo Lozano
Associate Professor of Aeronautics and Astronautics
Chair, Graduate Program Committee

Non-thermal plasmas in flames and other inhomogeneous environments

by

Carmen Guerra García

Submitted to the Department of Aeronautics and Astronautics
on October 24, 2014, in partial fulfillment of the
requirements for the degree of
Doctor of Philosophy

Abstract

Non-thermal plasmas in non-uniform gases appear in several technological applications (plasma assisted combustion and aerodynamics, and plasma jets), as well as in natural phenomena (sprites). Whereas in the case of plasma jets and sprites this problem has captured significant attention, the implications of an inhomogeneous background gas in the other fields need to be further explored. In particular, non-thermal plasmas used to assist or stabilize flames are subject to gradients in temperature, composition and pre-ionization, which impact the electrical breakdown characteristics and the energy coupling to the flame and its flow field.

In this dissertation, the impact of such inhomogeneities in the breakdown modes of repetitive pulsed nanosecond discharges, one of the main strategies used for plasma creation in the field of plasma assisted combustion, is explored. First, a simplified non-reacting platform is proposed that consists on a sandwich-like structure of gases with different ionization properties, due to differences in composition or temperature. In this configuration, selective breakdown of a region of favorable ionization was experimentally observed, even when this region was not in contact with the electrodes. A numerical model was used to explain the dynamics of streamers at the interface of two distinct gases, within the layered gas configuration. Many similarities with traditional dielectric barrier discharges are revealed, where the role of the solid dielectric is played by the more insulating gas.

The experiments were then extended to a counterflow nonpremixed flame environment for which selective excitation of the flame was also observed. Such a strategy ensures that the plasma-created radicals and short-lived species participate in the combustion reactions, but it is achieved at the expense of a limited energy deposition.

Finally, a discussion of experimental observations using AC voltage in the kHz range on the counterflow nonpremixed flame, highlights the role of the finite size of the pre-ionization zone on the conversion of the electrical energy into kinetic energy of the flow (ionic winds).

Thesis Supervisor: Manuel Martinez-Sanchez
Title: Professor Emeritus of Aeronautics and Astronautics

Acknowledgements

I would first like to thank my advisor, mentor and friend, Professor Manuel Martinez-Sanchez who has shared with me these five years of graduate school, the good and the less good moments. I thank him for the great discussions we have had during the years, for always trusting in my ability and knowledge and for inspiring in all of his students his ever present excitement for physics and science. His guidance and encouragement have been invaluable.

I would also like to thank Professor Richard Miles, who welcomed me to his group in Princeton University for a few months. I will always be grateful for his generosity and mentorship, and for giving me the opportunity to work in such a vibrant and excellent group. I would also like to thank him for taking the time to read my thesis and provide much appreciated feedback.

My time at the Miles Applied Physics Group was full of learning from every member of the group. I would like to specially mention Chris Limbach for taking much of his time to explain to me and help me with the Laser Rayleigh scattering equipment, Nick Tkach for offering a lot of advice in the lab, Dr. Arthur Dogariu for sharing his work space with me and his help in many aspects, and Tat Loon Chng and Sean McGuire for accommodating my equipment needs. Of course, I would specially like to acknowledge Dr. Andrey Starikovskiy for his invaluable help and teaching with the high voltage equipment and ns-time resolved imaging during my time in Princeton. His expertise and willingness to help me with my research have been an extraordinary experience in my graduate training. I also want to thank both him and Professor Richard Miles for participating in my Thesis Defense Committee.

I would like to thank the members of my Thesis Committee: Professor Ahmed Ghoniem, Professor Youssef Marzouk and Professor Paulo Lozano, for all the helpful suggestions along the way. Professor Ahmed Ghoniem's combustion class introduced me to this topic, and his insight has been of great help. Professor Paulo Lozano has always offered his help in the laboratory and his excitement in research has always been an inspiration to me. Professor Youssef Marzouk has always shown enthusiastic support during our meetings.

Much of the work described here would not have been possible without the generous assistance of other groups. The Schlieren system was graciously lent to us by the Gas Turbine Laboratory at MIT. I would like to thank Jimmy Letendre for accommodating all of my equipment needs when I needed optical elements that I had to borrow from the GTL. I would also like to thank Professor Paulo Lozano for lending us his video camera to record the flame dynamics experiments. Needless to say, the Laser Rayleigh scattering measurements, and ns-resolved photography would not have been possible without the collaboration with the Princeton University Applied Physics Group.

There have been many other researchers and engineers whose interest and friendship during the years have greatly enriched my graduate learning. I would like to thank Dr. Choon Sooi Tan, for his interest in our research during the years, for serving as an external evaluator during my Thesis Proposal Defense and for the opportunity to participate with him and Professor Manuel Martinez-Sanchez supervising undergraduate research projects. I want to acknowledge the valuable input generously given by Dr. Mruthunjaya Uddi when I was designing and building my counterflow burner. I have also been fortunate to collaborate with the then visiting students (now both doctoral candidates) Sebastien Mannai and Juan Ruiz-Ruiz. Todd Billings and Dave Robertson have been very helpful when I needed to

build the parts for my experimental setups and with my electronics questions respectively. Devon Sklair enthusiastically helped in the machine shop. Tom Coles has always offered his help in the many computer-related issues during the years. Many useful suggestions have also come from scientists around the world who I have had the pleasure to meet during conferences. Thank you to all those scientists and Professors who offered advice. I want to specially mention Dr. Francisco Gordillo-Vazquez and Dr. Alejandro Luque from IAA-CSIC, Granada, Spain, with whom I have had very interesting conversations.

There are many other people who have contributed to my development at MIT. I am thankful to the many opportunities that I have been given and the trust in me of the AeroAstro Department during my TA and lecturer experiences. I would also like to thank the people that make the student's lives so much easier, and in particular Beth Marois and Marilyn Good for always helping us with the friendliest attitude.

I want to thank the other fellow students in the Space Propulsion Laboratory at MIT, the older and the younger. Special thanks goes to my friend, office mate and colleague Carla Perez-Martinez. I also want to acknowledge the support and friendship of the Aerospace Computational and Design Laboratory crowd, specially Joel, Ferran, Xevi, Abby and Hemant. I also want to mention my friend Christie, whose friendship during all of our years in Cambridge has been a constant factor and has given balance to the MIT environment. Thanks to all the other friends who have helped make my stay in Cambridge so much more enjoyable!

I would not have been able to come to MIT if it had not been for the generous support of the Fulbright Program. Participating in the International Fulbright Science and Technology Award Program has been one of the greatest highlights of my time in the US. I am thankful, not only for their economic support, but also for the many enriching opportunities that the program has given me, and the opportunity to meet many incredible people.

During my time at MIT I have also been very fortunate to be a recipient of the Caja Madrid Foundation fellowship, an Amelia Earhart Fellow (which enabled me to attend several International Conferences) and receive a Vos Fellowship from the AeroAstro department.

I would like to thank my Professors at ETSIA, the Aeronautical Engineering School of the Polytechnic University of Madrid, who made it possible for me to come to MIT, specially Professor Isabel Perez-Grande for her encouragement and support.

Last, but not least, I want to thank my family.

My parents, Carmen and Juan, who are my role model to look up to. Their love for the family, work and simply being good people has been the light and inspiration that has always kept me going. My siblings, Pilar and Juan, have always been my greatest friends. Also, the rest of my family and friends in Spain, who I have had less time for in the last years (I am yet to meet my godson Martin and my niece Ronda!) but have never stopped being there for me despite the distance.

The person who deserves the most thanks, and without whom I could not imagine this whole experience, is my life partner, David Moro. Your love and friendship have been essential throughout the years. Thank you.

Contents

List of Figures **13**

List of Tables **19**

1 Introduction **21**

1.1 Motivation 21

1.2 Literature review 22

1.3 Streamers and Dielectric Barrier Discharges 24

1.3.1 Breakdown under pulsed voltage 24

1.3.2 Repetitive Pulsed Nanosecond Discharges (RPND) 26

1.3.3 The Dielectric Barrier Discharge (DBD) 28

1.3.4 Streamer breakdown in inhomogeneous media 29

1.4 Kinetics of plasma assisted ignition and combustion 32

1.4.1 Homogeneous combustion as a benchmark for kinetic studies 32

1.4.2 Kinetic impact of plasmas on flames 37

1.5 Dynamics of electrically assisted flames 42

1.6 Scope and outline of this thesis 44

2 Experimental methods **47**

2.1 Introduction 47

2.2 Three plane parallel jets 48

2.2.1 Design criteria 48

2.2.2 Experimental setup 49

2.3 Opposed jets facility . . . 50
2.3.1 Design criteria . . . 51
2.3.2 Experimental setup . . . 53
2.4 Electrical system . . . 54
2.4.1 Discharge cells . . . 54
2.4.2 Repetitive pulsed nanosecond discharge generation . . . 55
2.4.3 AC voltage . . . 56
2.5 Diagnostics . . . 57
2.6 Diagnostics: characterization of the medium . . . 57
2.6.1 Schlieren flow visualization . . . 58
2.6.2 Temperature measurements . . . 61
2.7 Diagnostics: electrical discharge . . . 61
2.7.1 Current and voltage waveforms . . . 61
2.7.2 Ns-resolved photography . . . 63
2.7.3 Optical emission spectroscopy . . . 64
2.8 Diagnostics: plasma-flame interaction . . . 65
2.8.1 Laser Rayleigh scattering . . . 66
2.8.2 Monitoring flame dynamics . . . 68

3 Repetitive pulsed nanosecond discharges in non-reacting gradients 69
3.1 Introduction . . . 69
3.2 Non-reacting model: Gas-confined Barrier Discharge . . . 70
3.2.1 Simplified model . . . 70
3.2.2 Analytical evaluation . . . 71
3.2.3 Test cases . . . 74
3.3 Experiments in N_2-He layers . . . 76
3.3.1 Selective breakdown of the helium layer: observations . . . 76
3.3.2 Electrical measurements of the RPND strategy . . . 78
3.3.3 Exploratory optical emission spectroscopy measurements . . . 79
3.3.4 Experiments using AC voltage . . . 80

3.3.5 Environment measurements 84
3.3.6 Discussion 85
3.4 Experiments in a temperature gradient 88
3.5 Summary of findings and implications 90

4 Model of the discharge development in a non-uniform environment 93
4.1 Introduction 93
4.2 Fluid model of the electric discharge 93
4.2.1 The drift-diffusion approximation 94
4.2.2 Layered gas environment 96
4.2.3 Geometry of the problem 97
4.2.4 Boundary conditions 98
4.2.5 Numerical solution of the equations 100
4.3 Numerical results of the GBD model 100
4.3.1 Parameters for the numerical experiment 101
4.3.2 Discharge evolution during application of the voltage pulse 103
4.3.3 Afterglow shortly after the voltage pulse is turned off 106
4.3.4 Results removing the solid dielectrics 106
4.4 Discussion and link to the experimental observations 108

5 Repetitive pulsed nanosecond discharges in counterflow nonpremixed flames 111
5.1 Introduction 111
5.2 The laminar counterflow nonpremixed flame platform 112
5.2.1 Motivation 112
5.2.2 Experimental platform and 1D approximation 113
5.2.3 A note on finite length effects and edge-flames 114
5.3 Flame as an environment for plasma development 115
5.3.1 Dependencies with strain rate and dilution 116
5.3.2 Chemi-ionization 121
5.3.3 Spatial structure of plasma-species creation 129
5.4 Experiments of RPND in counterflow nonpremixed flames 131

5.4.1 Plasma coupling to the flame: ns-resolved photography 132
5.4.2 Coupling to the fuel stream 136
5.4.3 Loss of confinement and transition into a ns-spark 137
5.4.4 Energy deposition versus confinement 139
5.4.5 Frequency effect 142
5.4.6 Flame modification for the RPND flame-confined strategy 143
5.5 Summary of findings and implications 146

6 Sub-breakdown kHz AC fields in counterflow nonpremixed flames 149
6.1 Introduction 149
6.2 Experiments of flame dynamics under AC fields 150
6.2.1 Frequency effect 151
6.2.2 Voltage amplitude effect 154
6.3 Electrical measurements of the flame 155
6.3.1 Impedance of the setup 155
6.3.2 Capacitance of the electrode system 160
6.4 Model of the flame displacement at high frequencies 161
6.4.1 Classical 1D theory of the counterflow nonpremixed flame 163
6.4.2 Incorporating the effect of a sub-breakdown AC electric field 164
6.4.3 Time-dependent body force 165
6.4.4 Flow field modification 166
6.4.5 Flame displacement 175
6.4.6 Other effects 177
6.5 Electrical model of the flame 182
6.5.1 Charge in contact with the electrodes 182
6.5.2 Floating charge 183
6.6 Parameter fit of the model to the experiment 185
6.6.1 Fully symmetric model 185
6.6.2 Contribution of the asymmetry in the ion mobility 187
6.7 Summary of findings and implications 190

7 Conclusion **193**

7.1 Contributions of this thesis 193

7.2 Recommendations for future work 195

A Quantitative Schlieren calibration **201**

B Temperature determination from Rayleigh scattering imaging **205**

B.1 Radial temperature profile 205

B.2 2D temperature map 208

C Details of the discharge numerical model **209**

C.1 Numerical method 209

C.1.1 Discretization in time 210

C.1.2 Discretization in space 211

C.2 Numerical verification (1D) 216

C.2.1 Time-step selection 216

C.2.2 Mesh size convergence 217

C.2.3 Impact of the background density level 217

C.3 Physical validation (2D) 218

C.3.1 Homogeneous and patterned glow (Townsend breakdown) 218

C.3.2 Volume streamer development (streamer breakdown) 221

D 2D numerical results of the GBD **223**

E Supporting evidence of RPND coupling to a flame **225**

Bibliography **227**

List of Figures

1-1 Diagram of plasma-combustion interaction. 23

1-2 Breakdown modes in air. 25

1-3 General approach to solve the 0D plasma-assisted ignition problem. 34

1-4 Energy coupling for an electrically assisted flame. 43

2-1 Three plane parallel jets schematic. 48

2-2 Parallel jets experimental setup. 50

2-3 Opposed jets schematic. 50

2-4 Photographs of flames with and without fuel dilution. 52

2-5 Opposed jets experimental setup. 54

2-6 Electrodes and discharge cells for the two setups. 55

2-7 Schlieren visualization of a helium jet discharging into ambient, effect of Re. 58

2-8 Schlieren setup. 60

2-9 Imaging setup: photography and spectroscopy. 65

2-10 Laser Rayleigh scattering setup. 67

2-11 Obtaining flame dynamics from video recording. 68

3-1 General structure of the GBD. 70

3-2 Breakdown as a function of voltage and pressure times *hot* layer thickness. . 75

3-3 Helium confined plasma in a N_2-He-N_2 structure. 77

3-4 Helium confined plasma for different N_2/He combinations. 77

3-5 Effect of removing the glass slide for different N_2/He combinations. 78

3-6 Helium injected into stagnant air: nanosecond spark. 78

3-7 Representative measurements of voltage and current using RPND. 79
3-8 Time-integrated spectra of the helium-confined discharge. 80
3-9 N_2/He layers with AC voltage. 81
3-10 Current and voltage plots with AC power and no discharge. 82
3-11 Current and voltage plots with AC power and visible discharge. 83
3-12 Helium mole fraction, from Schlieren imaging, for N_2-N_2-He sandwich. 84
3-13 Helium mole fraction, from Schlieren imaging, for N_2-He-N_2 sandwich. 85
3-14 Electron impact processes in He-N_2 mixture. 87
3-15 Effect of increasing the applied voltage for RPND in temperature gradient. . 89
3-16 Thermocouple measurement superimposed to photo of the plasma emission. . 90

4-1 2D geometry of the discharge cell. 98
4-2 Variable composition profile across the gas gap: nitrogen-helium-nitrogen. . . 101
4-3 Electron mobilities and diffusion coefficients in helium, nitrogen and air. . . . 102
4-4 Snapshot of streamer stagnating at the mixing layer (50ns after pulse onset). 104
4-5 Calculated current, net space charge and surface charge. 105
4-6 Cartoon of the operation of the *effective* DBD. 105
4-7 Snapshot of the charge densities and electric potential during the afterglow. . 106
4-8 Comparison of numerical evaluation with and without solid dielectrics. . . . 108

5-1 The flamelet concept for turbulent nonpremixed flames. 113
5-2 Measured temperature profile, across flame, compared to 1D calculation. . . 114
5-3 Flame geometry and temperature ratio as a function of dilution and strain. . 117
5-4 Effect of diluting CH_4 on its EEDF. 119
5-5 Fit of Townsend formula to data from BOLSIG+ (N_2:CO_2:H_2O=80:6.7:13.3). 120
5-6 Townsend ionization coefficients for flame mixtures. 121
5-7 Meek's criterion modified to include a Gaussian seed of plasma (amplitude effect). 127
5-8 Meek's criterion modified to include a Gaussian seed of plasma (width effect). 128
5-9 Energy loss fractions to different electron impact reactions for stoichiometric methane/oxygen. 130

5-10 Time evolution of the plasma emission coupled to the flame. 133
5-11 Time evolution of the plasma emission and spatial profiles across the flame. . 134
5-12 Time evolution of the plasma emission and spatial profiles (pulse comparison). 135
5-13 Selective RPND excitation of the fuel stream by choice of dilutants. 136
5-14 Spatially resolved emission from CH^* at 431.4nm (coupling to fuel stream). . 137
5-15 Nanosecond-spark across flame using pin-to-mesh electrodes. 138
5-16 Spatially resolved emission from C_2^* at 516nm (ns-spark). 139
5-17 Energy estimates for plasma confined to flame. 140
5-18 Current and voltage waveforms for ns-spark. 141
5-19 Time-integrated spectrum for RPND application to an argon diluted flame. . 142
5-20 Effect of the pulse repetition frequency on the time-averaged argon excitation. 143
5-21 Radial temperature profiles along the flame without and with RPND. 146

6-1 Flame dynamics for AC voltage of 2kV peak and 4Hz. 151
6-2 Time response of the flame for 2kV peak voltage. 152
6-3 Amplitude of the oscillation and mean flame displacement with AC voltage. . 153
6-4 Response of the flame to a voltage ramp. 153
6-5 Displacement of the flame towards the oxidizer side when using kHz AC voltage. 154
6-6 Directionality of the flame displacement. 155
6-7 Schematic of the circuit for the measurement of the setup's impedance. . . . 156
6-8 Frequency response without and with the flame lit, for 1kV peak voltage. . . 157
6-9 Complex electrical impedance of the experimental setup with the flame lit and unlit. 158
6-10 Transfer function and resistance values without and with flame, low frequency measurement. 159
6-11 Experimental measurement of the capacitance of the electrode system. . . . 160
6-12 Structure of the flame displacement model. 165
6-13 Spherical coordinates associated to the disk of charge / loop of current. . . . 169
6-14 Instantaneous streamlines for β=0.2 and χ=1. 171
6-15 Fluid particles' trajectories and time-averaged streamlines. 172

6-16 Strain rate reduction and flame displacement as a function of the electric field divided by the frequency. 176
6-17 Stagnation plane displacement for an asymmetric oscillation of the charge. . 179
6-18 Impact of a finite disk-release rate and disk removal. 181
6-19 Equivalent electrical circuit when the charge is redistributed in all the inter-electrode space. 182
6-20 Equivalent electrical circuit for a *floating* charge. 183
6-21 Model fit to experimental data of Figure 6-5. Fully symmetric model. 186
6-22 Model fit to experimental data of Figure 6-5. Asymmetric model. 187
6-23 Comparison of strain rate modification when using the symmetric and asymmetric models. 188
6-24 Contributions to flame displacement. Effect of relative values of β in the fuel and oxidizer sides 189

A-1 Calibration object for quantitative Schlieren calibration. 201
A-2 Calibration procedure using a simple positive lens. 202
A-3 Schlieren visualization of the three parallel jets experiment. 204

B-1 Region imaged with the laser Rayleigh scattering strategy. 206
B-2 Linearity of the Rayleigh signal with the incident laser intensity. 207

C-1 Flow chart of the numerical solution scheme. 210
C-2 Nodes for the numerical evaluation of the fluxes. 212
C-3 Time-step effect on the electron density. 216
C-4 Mesh-size effect on the electron density. 217
C-5 Effect of the background density level. 218
C-6 Flux of charge to walls for uniform glow. 219
C-7 Evolution of the electron density and the surface charge during a current pulse (uniform glow). 219
C-8 Flux of charge to walls for patterned glow. 220

C-9 Evolution of the electron density and the surface charge during a current pulse (patterned glow). 220
C-10 Evolution of the space charge and the axial electric field of a cathode-directed streamer. 221

D-1 Snapshot of lateral streamer propagating along mixing layer. 224
D-2 Comparison of 1D and 2D conduction currents. 224
D-3 Snapshot of charge and electric potential during the afterglow phase. 224

E-1 Direct photographs of RPND coupling to flame (case 1, no fuel dilution). . . 226
E-2 Direct photographs of RPND coupling to flame (case 2, diluted fuel). 226

List of Tables

1.1 Repetitive pulsed nanosecond discharges: electrical parameters. 28

1.2 Breakdown modes in a DBD. 28

2.1 Platforms for the study of non-thermal plasmas in inhomogeneous environments. 47

2.2 Measurement techniques used and parameters diagnosed. 57

5.1 Flame parameters for the temperature profile of Figure 5-2. 114

5.2 Townsend ionization coefficients for major species in flame. 118

5.3 Flame parameters used in the ns-resolved photography experiments. 132

5.4 Measured FWHM of plasma emission. 135

5.5 Flame parameters for selective RPND excitation of the fuel stream. 136

5.6 Flame parameters for ns-spark experiments. 138

5.7 Energy estimates for confined plasma strategy, upon RPND application. . . . 141

5.8 Flame parameters used to obtain the emission spectrum of Figure 5-19. . . 142

5.9 Flame parameters for the laser Rayleigh scattering measurements. 145

6.1 Flame parameters used in the AC experiments. 150

6.2 Magnetics-fluids problem analogy used to solve for the induced flow field. . . 168

E.1 Estimated flame parameters, and RPND conditions, for the images shown. . 225

Chapter 1

Introduction

1.1 Motivation

Pushing challenges in combustion and propulsion demands searching for novel technologies. Stringent regulations on air pollution require the development of low NO_x combustors that to-date generally suffer from combustion instabilities. The development of supersonic combustion systems faces the challenge of short residence times that hinder the process of mixing to the molecular level. Active control of combustion instabilities requires fast, reliable and precise responses with sufficient authority to impact the combustion process...

It has been proposed that non-equilibrium chemistry triggered by non-thermal plasmas can address these problems through a *selective* energy input into the combustion process in the form of dissociation, electronic excitation and production of atoms and radicals [189]. In particular, it has been proved that non-thermal plasmas can extend lean flammability limits, reduce ignition delay times or improve flame stability.

Although the fundamental idea of using an artificial injection of *active centers* to assist a combustion process has been around for a long time [11,225], advances in non-thermal plasma understanding and pulsed power technology have provided a new boost to this effort and have created an established community of Plasma Assisted Combustion in the last decade. Several fundamental questions still remain unaddressed as well as some aspects related to the extension of laboratory experiments to more realistic scenarios.

In general, the greatest efforts in the field have been focused on measuring the enhance-

ment in global combustion parameters when using non-equilibrium plasmas and, at the fundamental level, on defining the energy paths that impact the combustion processes. More specifically, there is an extensive literature centered on defining the kinetic contributions by isolating the effects of the different species produced by the plasma, as well as its heating effects. As an observation, the different enhancement mechanisms are very dependent on the combustion mode that is being considered, the type of gas discharge used and, more importantly, where the plasma is being produced.

In addition it can be said that, the position and timing of the discharge in a complex flame environment is important not only as it influences the combustion process, but also as it affects the development and the characteristics of the plasma itself.

This dissertation aims to investigate two related areas whose coupled effects on the dynamics of the plasma and the combustion remain unexplored. These are the space and time inhomogeneity in the plasma development (streamer breakdown, nanosecond arcs, transition to diffuse glow...) and the inhomogeneity in the combustion gas background environment (flame fronts, hot spots...). More precisely, the main goal of this dissertation is to explore how the inherently inhomogeneous environment of a flame affects the way the electrical energy is coupled when using both short duration high voltage pulses and AC fields.

Specifically, the plasma formation in a fast modulated discharge will be determined by the combustion environment in which it develops, due to the presence of strong temperature non-uniformities (that will directly impact the reduced electric field, leading to local enhancements) and the different composition regions (e.g. neutral gas composition, presence of excited species and ionized species through chemi-ionization at the reaction zone...).

In addition, other electrical aspects of flames that are impacted by the intrinsic inhomogeneities, such as the finite size of a flame or the existence of localized pre-ionization regions, will be discussed.

1.2 Literature review

The work presented requires a fundamental understanding of the development and dynamics of non-thermal plasmas in their different regimes along with an appreciation of how these

plasmas can affect a combustion process and, in particular, the dependencies of the impact on both the plasma and combustion parameters. The literature review is thus organized as follows.

First, the two main ways of producing a non-thermal plasma with an electric discharge will be presented, namely, through the use of pulsed voltage (Sections 1.3.1 and 1.3.2) or the insertion of dielectric barriers (Section 1.3.3). Following this, the dynamics of non-thermal plasmas in inhomogeneous media needs to be reviewed (Section 1.3.4). Although the literature on the plasma dynamics under an inhomogeneous combustion environment is scarce (this dissertation aims at taking a first step towards filling this gap), other communities have looked at this problem and their major findings are here reviewed as many of their conclusions are directly applicable to the problem at hand.

The second part of the literature review deals with the field of Plasma Assisted Combustion and Plasma Assisted Ignition (PAC/PAI) and focuses on the impact of the plasma on the combustion process mainly exploring the different energy paths that have been proposed (Section 1.4). The presentation highlights the importance of the structure and positioning of the plasma within the flow field, depending on which energy paths are being activated. Finally, the dynamic effects that can be triggered by sub-breakdown electric fields are briefly presented (Section 1.5).

With these two blocks in mind, the missing link in the loop of plasma-combustion interaction shown in Figure 1-1 will be addressed, namely the impact the combustion process itself has on the breakdown characteristics and the plasma properties.

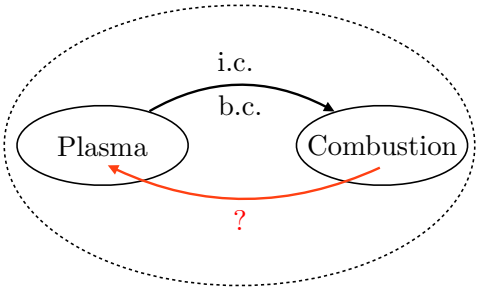

Figure 1-1: Diagram of plasma-combustion interaction.

1.3 Streamers and Dielectric Barrier Discharges

Non-thermal plasmas are characterized by a non-equilibrium situation (mainly a non-thermal deviation from equilibrium, in which the electrons are much more energetic than the heavy species, but can also have non-Maxwellian electron energy distributions and chemical non-equilibrium). This non-equilibrium situation allows for a *guided* energy input to the gas from primarily heating to dissociation, electronic excitation and production of atoms and radicals [189]. Numerous non-equilibrium plasma sources have been proposed and used to assist combustion processes for a wide range of conditions. A good review of the discharges used in PAC/PAI is given by S. M. Starikovskaia [189], and includes gas discharges produced by electric, RF and MW fields (glow, streamer discharges, nanosecond sparks, fast ionization waves, coronas...). In this dissertation, non-thermal plasmas created by electric discharges will be considered which, not only require high electric fields, but also limitation of the current in order to avoid thermalization and transition to an arc. This can be done either using pulsed voltage or inserting dielectric barriers in the discharge gap.

1.3.1 Breakdown under pulsed voltage

Under static conditions, electrical breakdown of a gas refers to a discharge that is self-sustained through secondary emission from the cathode. By introducing the Townsend ionization coefficient, α, or electron production per unit length, it can be shown that a self-sustained current requires that [59]:

$$\alpha d = \ln\left(\frac{1}{\gamma} + 1\right), \tag{1.1}$$

where γ is the secondary emission coefficient, characterizing the probability of a secondary electron being emitted by the cathode upon ion impact, and d is the inter-electrode distance. Combining equation 1.1 with the semi-empirical expression for α derived by Townsend (equation 3.1) leads to the well-known Paschen curves that relate the static breakdown voltage, V_{Paschen}, to the pd parameter (where p is the pressure).

Under pulsed voltage the gap can endure an over-voltage that is higher than the static

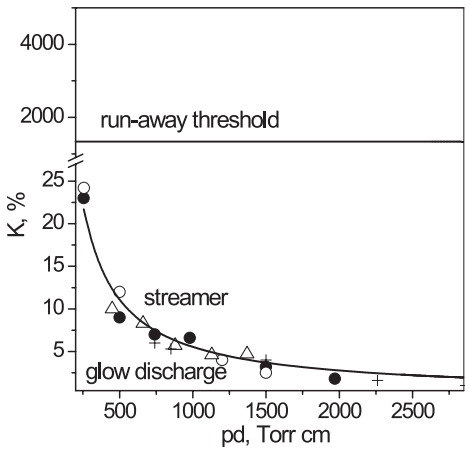

Figure 1-2: Breakdown modes in air as a function of the over-voltage, K, and the pressure times the gap length, pd. Figure taken from [94, 190]. The *glow discharge* is a Townsend discharge and the region above the *run-away threshold* indicates breakdown as FIW's.

breakdown condition, where the over-voltage K is defined as the ratio of the applied voltage, V, minus the static breakdown voltage, V_{Paschen}, to the static breakdown voltage, or $K{=}(V - V_{\text{Paschen}})/V_{\text{Paschen}}$. Depending on the parameters K and pd, three different breakdown modes can occur: Townsend, streamer, and Fast Ionization Waves (FIW) [190]. Figure 1-2, taken from [94, 190], shows the different breakdown modes in air as a function of K (expressed as a percentage instead of a fraction) and pd.

For low values of K and the pressure times gap length parameter, pd, the discharge will develop through the Townsend breakdown mechanism in which emission from the cathode ensures that the phenomenon is self-sustained and the electron avalanche formed does not distort the applied electric field significantly. In Figure 1-2, this region is referred to as *glow discharge*, another way of naming the Townsend discharge, and its appearance is generally uniform.

As the over-voltage increases, so does the electron multiplication in the discharge gap and the electric field distortion by the space charge. Above a certain threshold, the field induced by the space charge becomes at some point stronger than the applied electric field, and the streamer breakdown mechanism can be initiated. The condition is that the number of electrons created per initial electron is above a certain value N_{crit}:

$$e^{\alpha d} > N_{\text{crit}}, \tag{1.2}$$

from which the curve in Figure 1-2 that separates the Townsend and streamer breakdown regions is obtained [94]. For the streamer mode, electric breakdown refers to the creation of a sharp ionization front that propagates into a non-ionized gas, leaving a non-equilibrium plasma behind.

Streamers are transient electrical discharges that propagate as thin filament-like weakly conducting structures with very steep ionization fronts. The general appearance is that of a thin ionization region, the streamer head, with a very strong self-induced electric field that, if fed with seed electrons provides the driving mechanism of growth. Behind the streamer head an ionized channel is formed, the streamer body, which is quasi-neutral [166].

Note that even though conditions such as the ones given by equations 1.1 and 1.2 assume one dimensional breakdown under a uniform applied field, the real situation for the streamer breakdown is two dimensional, with cylindrical symmetry, where constriction is associated with the filamentation.

If the over-voltage is even higher, a fraction of the electrons can be continuously accelerated if they gain more momentum from the electric field between collisions than they loose upon collisions (the so-called run-away electrons). The presence of these *run-away* electrons promotes a uniform pre-ionization front in the volume and breakdown leads to fast ionization waves (FIW) that travel at a speed of 10^9-$10^{10} cm/s$ and leave a uniform plasma behind [190, 213]. In Figure 1-2, transition into the FIW breakdown mode is indicated by the horizontal line that marks the electron run-away threshold for a stationary uniform field.

This dissertation will focus on electrical discharges produced using pulsed voltage of tens of nanoseconds duration under conditions of moderate over-voltage (Repetitive Pulsed Nanosecond Discharges or RPND). The FIW regime has been mainly proposed for uniform ignition applications and is out of the scope of this work, in which precisely the inhomogeneities of the plasma-flame interaction problem are the subject of discussion.

1.3.2 Repetitive Pulsed Nanosecond Discharges (RPND)

The use of high voltage pulses of very short duration, for chemical excitation of a large volume, was first analyzed by the group in the Moscow Institute of Physics and Technology [190, 191]. E.g. in the experiments reported in [190], a high voltage pulse of 10-15kV

amplitude, 25ns duration and 3-5ns rise time was applied to a long discharge gap (30cm length) filled with low pressure (0.5-100Torr) air or nitrogen. In these studies, the high over-voltage led to spatially homogeneous discharges in the FIW regime.

Later, the groups at Stanford University [98, 142] and École Centrale Paris [143–146] proposed the application of a similar pulsed strategy but in this case using significantly lower over-voltages (generally in the streamer breakdown regime) and increasing the pulse repetition frequency, so that a sustained discharge could be obtained from an intrinsically transient phenomenon. This technique is known as the Repetitive Pulsed Nanosecond Discharge (RPND), and has been characterized for single discharges (generally in *homogeneous* gas and *inhomogeneous* electric fields) [135, 148], as well as their repetitive nature [196].

The RPND strategy can be summarized as follows[1]:

- Use of *high voltage* to obtain streamer breakdown conditions and tune the reduced electric field to trigger electron impact reactions of interest: ionization, dissociation, excitation...

- Use of *short duration pulses* to maintain the non-equilibrium situation. If the voltage is applied during a time comparable to the time it takes for the discharge to bridge the gap, the current flowing through the newly created ionized channel will be limited, thus impeding the transition into an arc.

- Repeating the pulses at a certain *pulse repetition frequency* that allows to maintain the desired gas excitation and chemical activity at all times.

Typical parameters used for the RPND are summarized in Table 1.1 (applicable for air at atmospheric pressure, temperatures up to 2000K and discharge gaps ∼1-10mm), a detailed estimation of these three variables can be found in [142, 143].

[1]RPND's in air at atmospheric pressure, and when using needle-like electrodes, present three different regimes [144]. For increasing applied voltage (all other parameters fixed), these are: the *C-Regime* (or corona-like), which consists of a localized discharge that appears close to the anode, has limited energy deposition and negligible gas heating. The *D-Regime* (or diffuse-like), which consists of a fairly uniform plasma with energy ∼10-100μJ, moderate emission and ionization ($n_e \sim 10^{13} cm^{-3}$), and low gas heating <200K. And finally, the *F-Regime* (or filamentary-like) that creates the highest chemical activity and ionization ($n_e \sim 10^{15} cm^{-3}$), has the highest energy deposition >100μJ and is accompanied by a high temperature increase ∼ 2000-4000K.

Table 1.1: Repetitive pulsed nanosecond discharges: electrical parameters.

$V\ [kV]$	$\Delta t\ [ns]$	$f\ [kHz]$
∼10	∼10	∼10-100

1.3.3 The Dielectric Barrier Discharge (DBD)

The strategy of limiting the current through dielectric barrier insertion is called the Dielectric Barrier Discharge or DBD [58]. The DBD was first introduced in 1857 by Siemens in Germany as a non-equilibrium plasma chemical reactor for ozone generation and, since then, has attracted a lot of attention for different applications.

Special mention of the DBD in this literature review is important, not only for its wide use to generate non-thermal plasmas, but also for the similitudes it presents with the discharges in inhomogeneous gases presented in Chapters 3 through 5.

DBDs can present either streamer breakdown, with numerous microdischarges appearing randomly in space and time [34]; or Townsend breakdown, with either a diffuse homogeneous appearance (including the Atmospheric Pressure Glow Discharge, APGD) or through self-organized patterns, both periodic in time [55, 62, 90, 132], see Table 1.2.

Table 1.2: Breakdown modes in a DBD. Parameters taken from [58].

	Microdischarges	Glow (APGD)	Patterned glow
Breakdown	Streamer	Townsend	Townsend
Spatially	Random	Homogeneous	Self-organized
Time	Random	Periodic	Periodic
$n_e\ [cm^{-3}]$	$10^{14} - 10^{15}$	$10^{9} - 10^{11}$	$10^{9} - 10^{11}$
$T_e\ [eV]$	$1 - 10$	$0.2 - 5$	$0.2 - 5$
Duration	$< 100ns$	μs	μs
Characteristic dimension	$< 200\mu m$	∼Gap	∼Gap

For the streamer mode, the space charge is large enough to be self-propagating; whereas, for the glow mode, the accumulated positive space charge is large enough to trap the electrons creating a plasma whose expansion is limited by dielectric charging. Transition between DBD modes depends not only on the over-voltage in the gap, but also on the role of volumetric versus surface charges, seed electrons and metastables present in the gap, memory

effects due to remnants of previous discharges, dielectric material, the dominant ionization mechanism (direct versus step-wise) and the shape of the voltage waveform. When compared to streamer breakdown, Townsend breakdown presents the competing advantages of uniformity and controllability at the cost of a lower degree of non-equilibrium of the discharge and amount of chemical activity produced, and for different applications only one or the other may be of interest.

DBDs in air and noble gases (Xe,Ne,He) are well documented, but fewer non-applied studies are available in pure fuel and combustion gases that have different ionization coefficients and electron affinities [218].

1.3.4 Streamer breakdown in inhomogeneous media

The streamer breakdown mechanism has been thoroughly studied for homogeneous gases and inhomogeneous electric fields (e.g. pointed electrodes) [41, 71, 149].

This dissertation deals with the structure of pulsed plasmas in extremely inhomogeneous media such as the mixing layer between two different gases or a flame. In the area of non-uniform gases, most of the work is due to research on *Atmospheric Pressure Plasma Jets*; recently, to the description of streamer and sprite development in the upper atmosphere or *Transient Luminous Events* above the thunderclouds; and finally to the literature on streamer development in *two-phase media*. These problems will be briefly reviewed due to the insight they provide for the problem at hand: their modeling methods will be borrowed and they will advance what observations should be expected.

Atmospheric Pressure Plasma Jets (APPJ)

APPJ were first introduced by [177] as a plasma source producing high concentrations of reactive species to etch and deposit thin films. The APPJ consists on a dielectric tube with two electrodes and a gas, generally helium, flowing through it and discharging into ambient air. The plasma produced inside the tube is ejected at very high velocities corresponding to streamer velocities of the order of 10^7cm/s. This produces a plasma source that can be deposited remotely (a *plasma bullet*), which makes it a very attractive technology for

applications such as thin film deposition or plasma medicine [99]. Most of the work to date has been experimental and modeling is more recent [17, 23–25, 125, 126, 128, 130] but has provided a lot of insight into the details of the plasma propagation under such conditions. Important findings regarding the propagation of plasma bullets along a helium-air mixing layer include[2]:

- The structure of a streamer is affected by gradients (both in composition and density) orthogonal to the propagation of the streamer [127].
- Plasma bullets are equivalent to cathode-directed streamers guided by the helium jet [17], the mixing layer being essential for the guiding mechanism [25].
- Plasma bullets have a ring-shape structure with the peak of ionization propagating along the mixing layer [125], although different flow fields [129] and the electrical interaction between two opposed bullets [46] may change these results.
- Streamer branching is prevented due to the presence of air [125].
- The structure of the streamer is well explained by direct ionization and the disparity in the electron impact ionization coefficients in helium and air alone, although quantitative results are impacted by Penning ionization and photoionization [23–25, 126]. For certain purposes, this enables the use of a very simple model to describe streamer propagation under such conditions [17].

Weak density gradients: Transient Luminous Events (TLE) and bubbles

The development of streamer plasmas under a gradient in density along the direction of propagation of the streamer, has been studied in the context of sprites, or weakly ionized discharges in the upper atmosphere [110]. For these weak gradients (the density increases by a factor of 6 in 13km in an exponential manner [109]), the overall structure of the streamer is similar to the propagation in homogeneous air.

In this same context of sprites, [140] proposed a laboratory experiment of a hot jet discharging into ambient air (with a temperature ratio of 2.6), to study the behavior of

[2]These observations are consistent with the experimental results presented in Section 3.3.

streamers in gradient-density conditions. Photography of differences in streamer branching and measurements of streamer diameter were reported. In this case, the results are difficult to interpret because the gradient in density also coincides with a gradient in electric field (as they are using a pin electrode) that increases in the same direction so it is not clear what the gradient in E/n is. It is also interesting to remark that streamer bending and *aiming* to specific regions has been observed under other conditions; Ref. [184] proposed a mechanism in which a leader sprays streamers and when these connect to objects the leader follows either the direction of the highest streamer density or the most conductive streamer channel.

[8] also considered the impact of weak density differences, limited to ∼7-8%, in the propagation of a streamer. In this case, the medium was homogeneous but had *bubbles* (regions of higher or lower density with a sharp boundary), on-axis and off-axis of the streamer. These *bubbles* were used to explain streamer branching, i.e. splitting of a single streamer into two or more. Their results indicated that, in order for a bubble to impact the propagation of the streamer, its radius had to be at least comparable to that of the streamer. If that is the case, for bubbles of density below ambient they predicted a focusing of the streamer into the bubble, whereas, if the density was above ambient, their streamers were split and deflected. For the purposes of this dissertation, it is interesting to note how small density differences (below 10%) already impact the dynamics of streamers significantly, if the dimensions of the inhomogeneity are greater than the streamer radius.

Of greater interest is the continuation of this work in [9] in which the propagation of a streamer in a field of low density bubbles is studied (ratios of 0.065-0.33). They found that the enhanced reduced electric field, E/n, in the bubbles initiates avalanches and potentially starts streamers that may combine with the main streamer or streamers of other bubbles appearing as streamer branching. The effect of high density bubbles was not included in the study.

Streamer development in two-phase media

Finally, as an extremely inhomogeneous environment, non-thermal plasmas have also been studied in two-phase media (both discharges in the gas phase with liquid electrodes and

discharges in bubbles in liquids [27]). Actually, streamers in liquids typically propagate in gaseous bubbles or in vapor phase channels produced by the heating of the discharge; other parameters such as the dielectric constant of the liquid also affect the path the streamer takes [10].

1.4 Kinetics of plasma assisted ignition and combustion

A review of the field of (non-thermal) Plasma Assisted Ignition and Combustion is always difficult to perform since several classifications of the literature can be made: depending on the plasma source used (DBD, RPND, FIW..), the combustion mode (supersonic combustion, homogeneous ignition, premixed flame, nonpremixed flame..), the main role of the plasma in the process (produce radicals, heat, excited species, mixing through pressure waves..), the impact of the plasma on combustion (reduce ignition delay time, extend the lean flammability limit, extend the blow out limit..), whether it is a fundamental study (propose a kinetic mechanism for the interaction, isolate a specific species..) or if it is focused on a particular application. In this Section, the literature will be classified in terms of the combustion mode, first reviewing some of the most relevant works related to homogeneous (non-thermal) ignition of a mixture, and then, highlighting how these same energy paths are triggered selectively for inhomogenous combustion (e.g. a flame) depending on the positioning of the plasma within the flow field.

1.4.1 Homogeneous combustion as a benchmark for kinetic studies

A wealth of papers are devoted to studying the kinetics of ignition using shock tube experiments in the presence of a uniform non-thermal plasma using high voltage nanosecond discharges in the form of Fast Ionization Waves. The main advantages in such a configuration are that both the plasma and combustion environment are uniform and, due to the different timescales of the phenomena involved, the plasma and the combustion kinetics are separated in time, so that the plasma can be used as an initial condition for the ignition problem. These studies generally include an experimental evaluation, with measurements of global combustion properties such as the Ignition Delay Time (IDT), coupled to a zero-dimensional

numerical evaluation of the kinetics involved [3, 6, 20, 95, 96].

Experimental evidence of the benefits on ignition when using nanosecond discharges in the form of FIW has been reported for many fuels: from hydrogen [20] and methane [20, 95] to more complex alkanes up to hexane [6, 96]; mostly in the form of reductions in the IDT. Results with hydrogen and methane, when using a FIW created by a voltage pulse of ∼100kV and duration 30-40ns in a highly diluted (80% argon) stoichiometric mixture, showed significant shifts in the ignition threshold and reductions of the IDT (e.g. for the hydrogen case, a factor of 2.2 for an electrical energy deposition of 30mJ/cm^3, a few percent of the main energy release by combustion) [20]; for a similar discharge and a methane-oxygen mixture diluted in 90% Ar, at 0.5bar and 1400K, the reduction was from 15ms (autoignition) to 27μs (plasma-assisted) [96]; for the more complex alkanes in similar conditions an order of magnitude reduction in IDT was observed [3, 96]. These results were obtained at some fraction of atmospheric pressure and at high temperature; [6] extends this range to ambient temperature (and low pressure, 1-10Torr) and demonstrates for all hydrocarbons tested that complete oxidation is achieved.

Additionally, significant effort has been put into determining the exact role of the plasma in the ignition problem by comparing experimental results to numerical simulation.

The model used to this end is generally described by some variation to the approach pictured in Figure 1-3. The plasma is solved for as an initial step by estimating the active species (radicals, excited species, atoms..) produced by the electric discharge. This is done by predicting the electron energy distribution function, EEDF, by solving the Boltzmann equation [72, 122] which in turn can be used either to obtain the fraction of energy from the discharge that goes to each electron collisional process and from there obtain the species densities produced (either from an energy balance [20] or using the G-value [156]) or to obtain the rates of reaction and solve the plasma kinetics in time [3, 95, 96]. In general, the estimate of the main species produced by the plasma is then used as an initial condition for the simulation of the kinetics of ignition. The coupling using this approach is simple for those species that normally would occur in traditional combustion kinetics, e.g. dissociated species or radicals, but more complex if it is desired to include the kinetics of excited species, as these are normally neglected in the most popular combustion mechanisms and generally

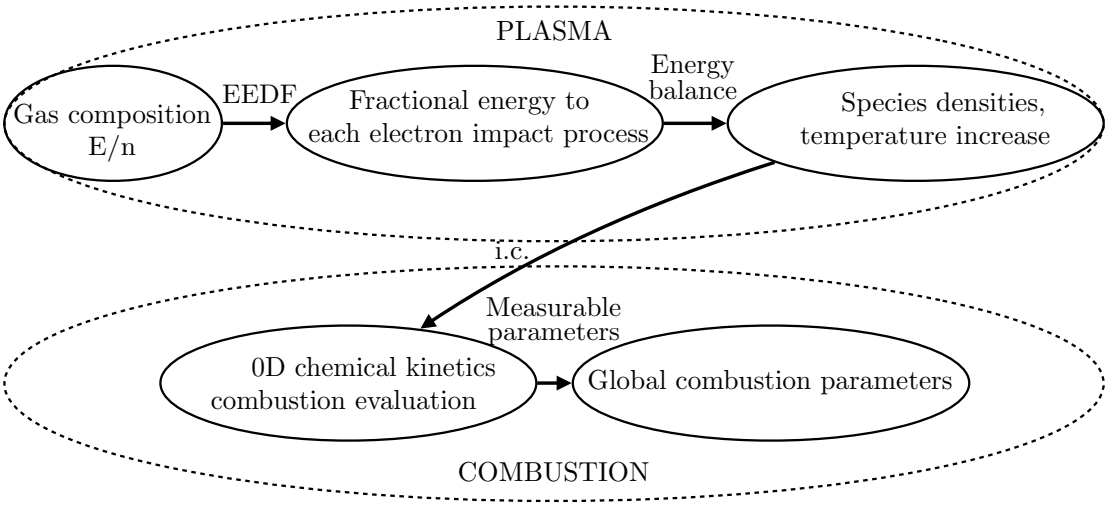

Figure 1-3: General approach to solve the 0D plasma-assisted ignition problem.

not well-known [20].

From all these studies, it is clear that, at low energy input, the non-equilibrium contribution is more efficient than simply increasing the temperature of the mixture at the same energy level [3, 20]. However, different non-thermal paths are possible: from dissociated species, atoms and radicals, to excited species, fast gas heating and, in some occasions, a combination of effects. To help clarify the relative importance of the different energy paths, dedicated studies isolating different effects have been performed in different mixtures and using different gas discharges.

The role of **dissociated species, atoms or radicals** was explored by [3, 20, 95, 96] who proposed that the most important path is electron impact dissociation and excitation of molecules to produce O, H, OH or hydrocarbon radicals that in turn shorten the time of chain formation.

[212] performed TALIF[3] measurements of the atomic oxygen concentration in a DBD driven by a single pulsed nanosecond discharge (20kV amplitude, 25ns duration, 0.76mJ deposition) with different mixtures at ambient temperature and 60Torr, highlighting the dependency of the plasma-produced species on the composition of the gas. Their major finding is the dependency of both peak production and decay rate of O atoms on the gas mixtures: whereas for air and stoichiometric methane/air they obtained a similar peak production of

[3]TALIF=Two-photon absorption laser-induced fluorescence.

O, when using an ethylene-air mixture with $\phi = 0.5$ the peak is reduced by a factor of four; the decay rate in the presence of fuel is faster. Additionally, comparison to a kinetic model revealed the main source of O production: electron impact dissociation of O_2 during the pulse application, and collisions of electronically excited N_2 molecules with O_2 in the afterglow phase.

Apart from the gas composition, [162] discusses the role of the mixture temperature: thus for example, close to the ignition limit, an artificial injection of H and O atoms provides an important reduction in IDT, but at low temperature, the only impact on ignition is a thermal one through the temperature increase by the recombination of the injected atoms (conclusions for a H_2/O_2 mixture).

The importance of **singlet delta oxygen** (the first electronically excited low energy state of molecular oxygen, $O_2(a^1\Delta_g)$), and of other long-lived molecular oxygen states such as $O_2(b^1\Sigma_g^+)$ (which is quenched due to collisions with neutral species into the $a^1\Delta_g$ state), was explored by [162]. In pure oxygen $O_2(a^1\Delta_g)$ is favored for $E/n \sim 10Td$.

The energy of excitation of $O_2(a^1\Delta_g)$, 0.98eV, can significantly reduce the activation barrier of a chemical reaction, increasing the process rate constant. For example, the rate constant of the chain branching reaction, $H+O_2 \rightarrow OH + O$, responsible for chain propagation in hydrogen-oxygen combustion, is nine orders of magnitude larger when $O_2(a^1\Delta_g)$ substitutes ground state molecular oxygen [74]. In addition, its long lifetime makes it interesting in that $O_2(a^1\Delta_g)$ can be used far way from its place of production.

[162] discusses that the role of $O_2(a^1\Delta_g)$ may become important in the low temperature region where the radicals are not so effective: although at high temperature $O_2(a^1\Delta_g)$ can participate in chain initiation (by reaction with H_2) and chain branching (reaction with H) it is also quenched by hydrogen; whereas at lower temperatures this quenching is inactive. Note that high concentrations of $O_2(a^1\Delta_g)$ are produced when using low-to-medium pressure electric discharges and that, at pressures above a few torr, the impact of $O_2(a^1\Delta_g)$ is less effective since the singlet molecular oxygen is quenched rapidly through three body processes [74].

In addition, singlet atomic oxygen $O(^1D)$ (excited atomic oxygen with all electrons paired), more reactive than its triplet $O(^3P)$ ground state, is also generally produced, e.g.

through the electron impact dissociation reaction, $e^- + O_2 \rightarrow O(^3P) + O(^1D) + e^-$, lowering the activation barrier of certain reactions. E.g., the rate constant of the chain branching reaction, $O + H_2 \rightarrow O + OH$, is seven orders of magnitude larger when $O(^1D)$ substitutes ground state atomic oxygen [201].

For completion, the role of **fast heating** has also been investigated for different reduced electric fields and the mechanisms that lead to it have been evaluated using kinetic models. For electric fields $\sim 100Td$, the main source ($\sim$10-15% of the total deposited energy) has been explained as self-quenching reactions of excited nitrogen $N_2(A^3\Sigma_u^+)$; for $E/n \sim 1000Td$, around 50% of the energy was transferred in much less than $1\mu s$ into heat due to different quenching and recombination reactions [4].

For a more detailed discussion of plasma sources used, the role of different energy paths and enhancements of combustion processes using non-thermal plasmas a few topical reviews and book chapters can be consulted [174, 189, 192, 194, 195, 217]. Specifically, the recent paper by A. Starikovskiy and N. Aleksandrov [195] gives an excellent review of the current understanding of the most efficient plasma energy paths that impact the combustion process.

All in all, the role of a non-thermal impact on combustion is well established and the benefits, at least at the conditions of the experiments performed, are clear. When moving away from uniform conditions, the impact of the plasma will not only depend on the E/n parameter and the composition of the mixture, but also, under flame conditions, there will be an impact of the combustion mode, the positioning of the discharge and the gradients involved. Finally, the current trend is to extend the experiments to more realistic conditions, specifically to higher pressures, and the Rapid Compression Machine, RCM, is becoming a popular platform for ignition studies: [168] used a surface dielectric barrier discharge (SDBD) for ignition of a propane-air mixture with $\phi = 0.4$, at temperatures 600-800K and pressures up to 40 bar and observed more than two-orders reduction in the IDT at the expense of a discharge energy of 20-50mJ.

To conclude it must be noted that, recently, the inhomogeneous nature of the discharge, and plasma dynamics, under many regimes of interest is capturing some attention [97], although not necessarily the coupling with a non-uniform environment. In particular, the work in [160] presents numerical simulation of a nanosecond-pulse discharge in air (in a

DBD configuration), solving the conservation equations for charged and neutral species, mass-averaged conservation equations for the bulk gas flow, and Poisson's equation for self-consistent determination of the electric potential. Their calculations highlight the paths of energy transfer in the discharge, as well as their *spatial* structure, emphasizing the chemical kinetics of energy storage and thermalization. For their conditions, the input electrical energy transforms to chemical energy (excitation, ionization, dissociation...) in the nanosecond time scale, and then decays over the microsecond time scale (through quenching of the excited states and electron-ion recombination), appearing as gas heating and weak shock waves. For the purposes of this paper [160], rapid thermalization is desired since the application under study is flow control through shock wave generation by RPND. For the case of plasma assisted combustion, it is desired that the excited and dissociated species participate in the combustion reactions (chain initiation and branching) before the chemical energy stored appears as heat.

Additionally, a paper on full streamer modeling for ignition studies through a self-consistent analysis by L. L. Raja and his team was published at the time this dissertation was written [26].

1.4.2 Kinetic impact of plasmas on flames

Plasmas can assist flames in numerous ways:

1. Plasmas can participate in the inflammation process: obtaining reductions in the IDT and speeding up the process of combustion [150]. A faster inflammation process is of interest to facilitate supersonic ignition [43]. The minimum ignition energy (for a fast enough ignition source [150]) is a measure of the efficiency of ignition and will also depend on the ignition source [207, 208].

2. They can be used to control and mitigate thermo-acoustic instabilities [121] by exploiting the pulsating nature of the discharge, enabling combustion of leaner mixtures.

3. Non-thermal plasmas have been shown to extend lean flammability limits, blow-out limits, to increase flame speeds, to achieve more complete combustion and in general to modify the global flame parameters.

The possibilities for impacting a flame with a plasma are much more varied than for a uniform ignition problem. Not only the same kinetic paths available for uniform ignition are present (radicals, excited species, thermal effects...) but also the mechanisms that can impact the transport properties, e.g. via ionic wind effects even when using DC and AC fields [227,228], pressure wave generation for mixing enhancement [230], or the versatility in being able to decide where the plasma energy is going to be introduced (in the fuel stream possibly pre-cracking it, in a premixed stream providing a pre-oxidation, an injection in the flame front directly participating in the flame reactions...). The same way as for ignition studies plasma and combustion are separated in time, many studies of plasma impact on a flame separate the plasma and the flame in *space* and the plasma becomes a boundary condition for flame behavior, in some cases to try to isolate the effect of a particular species [138,139]; additionally, *in-situ* deposition of the plasma on the flame has also been considered.

The effect of a DBD plasma produced in the **fuel stream** prior to mixing with air and burning has been studied by [170,171,186], who observed extensions in the blow out limit, increased flame speeds and more complete combustion in flames: e.g. [186] published some images demonstrating the change in flame speed and tentatively explained it as *cracking* of the propane into smaller fragments and possibly other radical and H_2 formation; [170] presented mass spectrometry results showing an enhanced combustion for the plasma *activated* propane.

The effect of a non-thermal plasma applied to excite the **oxidizer stream** has been extensively researched as excited O_2, ozone and O atoms are important enhancement paths for combustion. The different effects have been systematically studied [136,138,139].

The role of the excited oxygen is to accelerate the formation of O, H and OH due to a reduction in the activation barrier, intensifying the chain reactions. [139] experimentally isolated the effect of $O_2(a^1\Delta_g)$ by catalytically removing other species produced by the MW discharge (O and O_3 were removed by addition of NO), by selecting the distance of plasma production from the flame front such that only this species survived and by using low pressure (<10kPa) to avoid collisional quenching of the $O_2(a^1\Delta_g)$. Under the conditions studied for ethylene/oxygen laminar lifted flames diluted in argon, the impact of 5500ppm of $O_2(a^1\Delta_g)$ was to increase the flame speed by 2-3%.

Chemical kinetic models have also been used to assess the impact of singlet oxygen molecules. [187] incorporated reactions of singlet oxygen molecules, $O_2(a^1\Delta_g)$ and $O_2(b^1\Sigma_g^+)$, in the mechanism of H_2/O_2/He mixtures and estimated a significant increase of flame propagation velocity for fuel lean mixtures, enabling an extension of the lean limit. [19] also performs numerical simulations using different packages of CHEMKIN [42] and a kinetic mechanism that includes the presence of singlet oxygen molecules in the initial mixture of H_2/O_2 (in accordance to realistic concentrations from experiments, $< 5\%$ excited oxygen) and predicts reductions in IDT and minimum temperature for inflammation, increases of the laminar flame speed and increased extinction strain rates.

The isolated effect of ozone is given in [138], in this case, $O_2(a^1\Delta_g)$ is quenched by using higher pressures (101kPa). The effect is more pronounced $\sim 8\%$ for a range of conditions for 1260ppm of O_3, although direct comparison to [139] is impeded due to the different pressure used as well as the fuel (propane) and dilutant (nitrogen). The impact of ozone addition is that it acts as a cold (temperatures below 400K) transport means of O by attachment to O_2 which firstly overcomes the short lifetime of O atoms and second lowers the energy barrier to produce O atoms.

The direct effect of atomic oxygen production was evaluated by [202] on a counterflow burner with the plasma produced in the oxidizer stream. As the quenching rate of atomic oxygen is strongly dependent on the temperature, they concluded that, in order for the O atoms to reach the reaction zone, the oxidizer temperature needs to be above a certain threshold and so a combination of thermal and non-thermal effects is required for the strategy to work.

Finally, the catalytic effect of other stable species such as NO_x when the plasma is produced in the air stream (for a counterflow burner), has also been discussed [137] (in their experiments the NO produced by the discharge amounted to $\sim$5000ppm) as well as the dual role of thermal effects (temperature increase that enables to sustain species concentrations) and non-thermal effects (to produce NO_x and radicals) as the active species need to be transported to the flame front. This NO production should be considered when assessing the benefits of using non-thermal plasmas [84, 85] as one of the main applications envisioned for these strategies is to extend the lean flammability limits in order to decrease the temperature

of the process and so reduce peak NO emissions.

Many experiments center on the application of the plasma on a **premixed stream**, in this case, the main effect of the plasma is to pre-oxidize the fuel. [120] proposed that the plasma should affect the pre-flame zone since the energy deposition in the discharge is much lower than the flame power.

An enhancement mechanism, based on stable intermediate species, was suggested by [86, 88, 89] who performed experiments with pulsed discharges of nanosecond duration in premixed flames and reported a dual-flame structure in which the non-equilibrium discharge, by radical production, produces a cool flame or acts as a reformer of the fuel into H_2 and CO (syngas) which in turn pilots the combustion of the rest of the (lean) mixture. For their burner, the blowout limit was extended by 10% in the presence of a discharge for methane/air mixtures and there was no impact for hydrogen/air mixtures.

Using the same counterflow experiment as in [202] (study of plasma on oxidizer stream), [203] also performed experiments of the impact of the plasma on a partially premixed flame. One of the two opposed jets had the fuel (methane) diluted in argon and the other a premixed mixture of oxygen doped with methane (2% in volume at 60Torr) and diluted in argon and helium. The plasma was produced in this second premixed stream. The main effect in this case was the rapid methane oxidation at low temperature in the presence of the plasma that resulted in a heat release that extended the extinction limits of the main combusting mixture; once again leading to a combination of non-thermal and thermal effects.

If the plasma overlaps with the flame, radicals can also play a role. In [87], the plasma was acting on the fresh stream but achieved anchoring of the flame to the electrodes, so that O radicals produced by the discharge could potentially reach the reaction zone. The enhancement, for a lifted methane jet flame, was that they could increase the speed of the flow by a factor of 2.5 when applying AC discharges using both DBD and what they called Single Electrode Diffuse Discharges (SEDD). [158] achieved stabilization and extension of the blow-out limits of a turbulent premixed flame using Repetitive Pulsed Nanosecond Discharges (RPND) at a power level less than 1% of the flame power and, although they identified the main active species produced by the plasma as O, H, and OH, they also measured a significant temperature increase suggesting again the dual effect of thermal and

non-thermal effects, specially when using radicals that need to be transported to the flame.

The last choice of plasma positioning is directly into the reacting zone. **In-situ energy deposition into the flame front** has been targeted especially using Micro-Wave (MW) energy [183, 198] and femto-second lasers [231]. The MW experiments explain the flame speed enhancement by a direct coupling of the MW energy to the flame front (via electron heating), whereas for the fs-laser experiments the creation of radicals (and in particular O atoms and hydrocarbon radicals) is the most likely explanation. The main advantage of using lasers is that it avoids the use of electrodes that can be eroded or even melt and also that the position of the plasma can be very precisely controlled, whereas its disadvantage is that, in most cases, it produces a localized spot of plasma that is difficult to scale to larger dimensions. The impact, however, when using such strategies was important: laminar premixed flame enhancements of $\sim 20\%$ [183, 198, 231].

Recently, [204] performed a counterflow flame experiment with a uniform discharge generated with the RPND technique between the opposed nozzles of the burner to study the direct coupling of the plasma and combustion kinetics. They studied the ignition curve of a methane/oxygen flame diluted in helium and observed they could significantly modify the ignition and extinction characteristics and stretch the conventional S-curve, reducing the ignition temperature to 900K (at a reduced pressure of 9600Pa) and removing the hysteresis of ignition and extinction. They attributed the modification to the creation of atomic oxygen by the discharge that could trigger the chain branching reactions at lower temperatures by decreasing the global activation energy. In this case, the discharge was not localized to the flame front but rather acted uniformly on the fuel and oxidizer streams as well as in the reaction zone. Apart from demonstrating the interest of using RPND directly placed in the flame, the interest of this work is that different experiments were performed with this same burner but the discharge placed in the oxidizer stream [202] and in a partially premixed mixture [203] making the impact of the positioning of the plasma evident. These previous studies showed that it is not easy to deliver excited species and radicals to the flame front when they are generated away from it due to their short lives (recombination, quenching..) and that, in general, a combination of thermal and non-thermal effects is required to increase the survival time of the reactive species unless the plasma is deposited directly into the flame.

Finally, localization of the discharge in the reaction zone was suggested by [116] using two different strategies. The first one is, as [183, 198], by using MW energy directly coupled to the flame front. In their experiments, the localized energy deposition was evident by the luminosity of the plasma superimposed to the flame. The second one, uses a sequential approach first *drawing* a pattern for the discharge propagation by pre-ionizing with a laser and then depositing the energy using MW; although the complexity of this approach is evident, the main advantage of this method is that the positioning of the plasma (and its shape) can be very finely controlled using lasers, and it is more or less decoupled from the environment properties, and then the energy level can be chosen independently using microwaves.

The **impact of the flame presence on the plasma properties** has been less explored although the combustion-discharge coupling has been observed by several researchers. [206, 218–221] performed experiments using a coaxial dielectric barrier discharge applied to a methane diffusion flame and, additionally to achieving a reduction in its detachment height and an extension of its flammability limits (velocity increases of $\sim 50\%$ until blow off), they observed a plasma channel anchoring the flame to the burner and filamentary discharges *slipping* from the plasma to the flame. Under their conditions in which a bright plasma filament anchored the flame to the nozzle of the burner, the flame behaved like a virtual ground; proposing a configuration in which the plasma is not constrained by the electrodes (e.g. point-to-point electrode system defines the positioning of the discharge) but instead *adapts* freely to the environment. A similar observation was made by [87] who witnessed that, when using a single electrode (SEDD), the discharge and impact on the flame were independent of the electrode position as the discharge has the tendency to anchor the flame which serves as a virtual ground.

1.5 Dynamics of electrically assisted flames

For completion of this discussion, it must be recognized that flames are weakly ionized plasmas per se so that, even electric fields below the breakdown threshold, can modify their properties (without the need to produce additional electrons through an electric discharge).

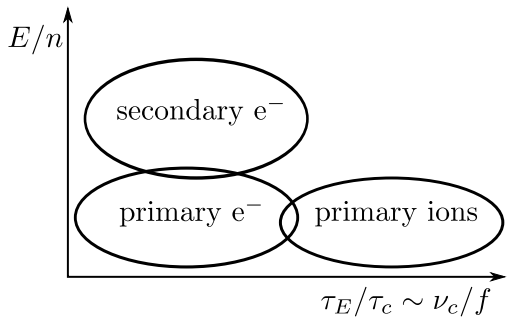

Figure 1-4: Energy coupling for an electrically assisted flame.

In general, depending on the time-scale of the electric field variation to the time response of the different charged particles involved, as well as on the voltage amplitude used, the electrical energy will be coupled to the flame's pre-ionization electrons (primary electrons), for fast sub-breakdown fields; to the flame's pre-ionization ions (primary ions), for slow sub-breakdown fields; or to the electrons produced by the gas discharge (secondary electrons), for fast fields above the breakdown threshold (see Figure 1-4).

Moreover, depending on whether the energy is coupled to the electrons or the ions, the transfer of energy to the neutral gas will be different. On the one hand, when the energy is transferred to the electrons, kinetic effects on the combustion process will dominate (either through non-thermal chemistry activation or through a temperature increase). On the other hand, when the energy is transferred to the ions, a non-thermal dynamic effect, based on a momentum transfer from the mobile ions to the neutral gas molecules (ionic winds), is the most likely way of affecting the combustion process.

The works reviewed in Section 1.4 refer to coupling of the energy to the electrons (with gas discharges generated by DBD, pulsed voltage, MW fields...), mainly for conditions above the breakdown voltage. Coupling to the primary electrons was observed as early as the 1970s, by H. C. Jaggers and A. von Engel [78] using high frequency sub-breakdown voltage (∼1-10MHz) that promoted vibrational excitation of the mixture without any further ionization, and also in the MW frequency range [112].

In addition, the ions present in flames have been used to manipulate flames since the early works of researchers like H. F. Calcote, J. Lawton, F. J. Weinberg, R. J. Heinsohn and S. K. Dayal and T. P. Pandya [30, 39, 40, 79, 100], primarily by the application of DC fields

that drive ionic winds in the flow. This coupling of the energy refers to the ions acquiring momentum, while moving down the potential gradient, which is on average lost in collisions with the neutral atoms and molecules, resulting in a body force on the fluid that modifies the flow field. These ionic winds can improve or deteriorate flame stabilization depending on the polarity of the applied electric fields and the orientation of the wind with respect to the undisturbed flow field. If the ionic wind is well oriented, stabilization can be achieved, as seen by increases of the blow-off velocity of the flame [7, 83]. In addition, modifications in the emission of nitrogen oxides, carbon oxides and soot formation (both reductions and increases have been measured) have also been reported when using slow, sub-breakdown fields [92, 93, 214, 234]. Despite having measured clear benefits when using these strategies, detailed theoretical models of the energy coupling and electrical interaction with the flame (ionic winds, electron heating ...) are scarce, and are mainly due to the initial efforts of J. Lawton and F. J. Weinberg [100, 102].

Recently, A. M. Drews et al. [47] reported that AC fields can also drive steady flows in flames and observed in their experiments static gas jets, created upon application of a sub-breakdown field at frequencies up to 1kHz, using Schlieren imaging. In addition, they proposed a theoretical explanation for the rectification of the force for the Bunsen burner-type flame under study. In general, studies on the effects of high-frequency alternating fields, in the range ∼1-10kHz, are more limited than for other ranges and, again, in many cases present experimental trends without offering a detailed theoretical explanation [228,229,234].

1.6 Scope and outline of this thesis

All in all, it is clear from the review of the literature that the impact of a particular energy path depends on where the plasma is being produced, the composition of the mixture and the combustion mode; and, unless placed close to the flame, radicals and short-lived species will not play the dominant role and combined thermal-kinetic effects or longer lived species will be required. Additionally, the impact of the combustion or flame environment on the discharge has not been extensively explored and, in many cases, the discharges used are highly constrained by the electrodes which are in contact with the discharge (risking erosion

by high current modes), and the dynamics of the plasma is not considered either because the study is performed using a uniform discharge or because the non-uniformity of the discharge is modeled as a *localized* energy deposition in a plasma channel.

The problem of the *unconstrained* development of the non-thermal plasma under a realistic turbulent combustion scenario is yet to be explored and is important in terms of determining where the plasma species will be deposited and even how to taylor their appearance to the region where they are most effective. Filament-like discharges occur very frequently when using non-thermal strategies and are in some applications the only way of affecting the combustion process [150]; so the full plasma dynamics problem under realistic conditions is an important fundamental problem. The literature on non-thermal plasma development for other applications already provides some insight on how these plasmas will develop under flame conditions but a dedicated study is required.

In summary, the three main goals of the research presented here are to:

1. Propose a novel platform for the study of the development of Repetitive Pulsed Nanosecond Discharges (RPND) in highly non-uniform gases. Analyze the development of the plasma under *local* streamer breakdown conditions and explore the possibility of exploiting the structure of the gaseous environment to obtain a *localized* effect.

2. Extend the analysis to explore the *unconstrained* development of RPND in nonpremixed counterflow flame conditions. Determine if selective breakdown of the flame by use of an electric discharge can be achieved as well as coupling of the plasma near the start of the reaction zone, where the reactions are just beginning and decay of the plasma-created species during transport should not be an issue.

3. Explore the impact of the non-uniformities of a flame: gradients in temperature, composition, pre-ionized regions as well as finite size effects; and how deviations from the 0D studies, and even the 1D counterflow nonpremixed platform, are required to explain the dynamics and structure of the charged species present.

The outline of this dissertation is as follows:

Chapter 2 overviews the experimental platforms developed for this work, namely a three

parallel jets device and a counterflow jets setup, both integrated with a discharge cell for RPND and AC experiments. In addition, the experimental diagnostics used are reviewed.

Chapter 3 presents a simplified model, based on a non-reacting *layered* gas configuration, proposed to explore the breakdown characteristics of short duration electrical discharges in inhomogeneous gases. An analytical model is developed which is then tested experimentally using sharp gradients in composition and temperature.

Chapter 4 provides a phenomenological description of the novel experimental observations of the previous Chapter based on the results of a numerical model of the electric discharge that incorporates the particularities of the environment at hand.

Chapter 5 discussed the coupling of a pulsed-nanosecond duration plasma to a counterflow nonpremixed flame, building upon the analysis for the non-reacting gas environment.

Chapter 6, deals with the effect of high frequency ∼kHz AC fields on the same counterflow nonpremixed flame platform. This problem is fundamentally different but also exploits the inhomogeneities in the flame environment, in this case pre-ionization at the flame front and finite size of the flame, to achieve a localized effect on the flame region. Experimental observations are complemented by an analytical model to explain the physics involved.

Chapter 7 gives an overview of the main findings of this thesis and gives recommendations for future work.

Chapter 2

Experimental methods

2.1 Introduction

In this Chapter, the different experimental platforms that have been used in this work to investigate the development of a non-thermal plasma under inhomogeneous conditions are described (Table 2.1). Two different setups have been designed and built for this thesis: a three plane parallel jets experiment (Section 2.2) and an opposed jets platform (Section 2.3). The latter has been used with opposed non-isothermal jets and as a counterflow nonpremixed burner. In both setups, two parallel electrodes were placed in the flow field that provided a quasi-1D, time-dependent, electric field aligned with the dominant gradients in the flow. The electrical setup including the discharge cells used and the power generation system are described in Section 2.4. The diagnostics and measurement techniques used are detailed in Sections 2.5 through 2.8.

Table 2.1: Platforms for the study of non-thermal plasmas in inhomogeneous environments.

Nature of the inhomogeneity	Platform	Results are reported in
Composition	Three parallel jets	Section 3.3
Temperature	Opposed jets	Section 3.4
Flame front	Counterflow burner	Sections 5.4, 6.2

2.2 Three plane parallel jets

The experiment reported in Section 3.3 concerns the study of repetitive pulsed nanosecond-duration discharges under a gradient in composition, which was obtained using three plane parallel jets. Helium and nitrogen were selected as the working fluids since, from the readily available gases, they have the most different ionization properties (Section 3.2). Unless otherwise indicated, helium was injected in the center stream and nitrogen was used in the side streams. The three jets were isobaric and isothermal (at atmospheric pressure and ambient temperature) and the orientation of the jets was vertical. A schematic of the setup is shown in Figure 2-1.

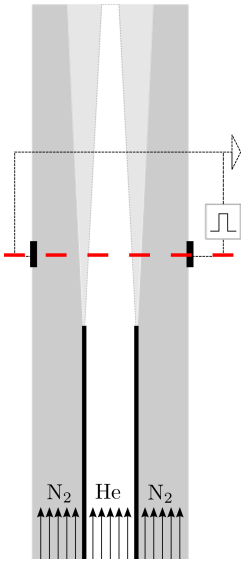

Figure 2-1: Three plane parallel jets schematic (steep gradient in composition).The red dashed line indicates the plane in which the study is performed.

2.2.1 Design criteria

Listed below are the criteria used for the design of the setup. Since the transport properties of the streams are fixed by the choice of gases, they affect the geometry and the flow velocities.

The width of the three exit slots was selected as d=2mm (all equal) in order to have the predicted electrical breakdown of the gases within the voltage limitations of the power supply (Section 3.2) and still be large enough for ease of fabrication. The length of the exit slots was 35mm to ensure planar jets.

All three jets had the same exit speed, and its value was chosen as high as possible to limit the growth of the mixing layers while ensuring laminar flow and negligible buoyant forces arising from the large difference in density of the two gases, $\rho_{He}/\rho_{N_2} = 0.14$. The main constraint, in terms of transition to turbulent flow, is set by the nitrogen jets due to their lower kinematic viscosity ($\nu_{N_2} = 1.6 \cdot 10^{-5} m^2 s^{-1}$ as compared to $\nu_{He} = 1.2 \cdot 10^{-4} m^2 s^{-1}$, both at standard conditions). A speed of u=5m s^{-1} was chosen for the experiments, which satisfied:

$$\mathrm{Re} = \frac{2du}{\nu_{N_2}} < \mathrm{Re}_c = 2000,$$
$$\mathrm{Fr} = \frac{u^2}{gd(\rho_{N_2}/\rho_{He} - 1)} >> 1,$$

where Re is the Reynolds number, Fr the Froude number, and g the gravity acceleration. The subscript c refers to the critical condition for transition to turbulence.

Finally, the electrodes were placed at 4mm of the jet exit, close enough to be within the potential core, have a sharp composition gradient, with minimal mixing, and be within the non-buoyant region of the jet. To ensure this last condition, general scaling laws require that (z is the length along the jet measured from the exit) [29]:

$$\mathrm{Fr}^{-2/3} \left(\frac{\rho_{He}}{\rho_{N_2}}\right)^{-1/3} \frac{z}{d} < 0.5.$$

2.2.2 Experimental setup

To avoid unwanted shorts, the setup had to be fabricated with insulating materials. The device was 3D printed in ABS plastic and was made of several parts that constituted the plenum chambers and two walls, parallel to the jets, that provided confinement and served as electrode holders. The exit slots were machined to surpass the tolerances of the 3D printer. Sponges were placed inside the plenum chambers to serve as turbulence suppression elements. Nitrogen and helium could be injected in the three independent plenum chambers, bottled gases were used, and the flow rates were measured with variable area flowmeters and varied using needle valves. Figure 2-2 shows a schematic of the setup and CAD model of the device.

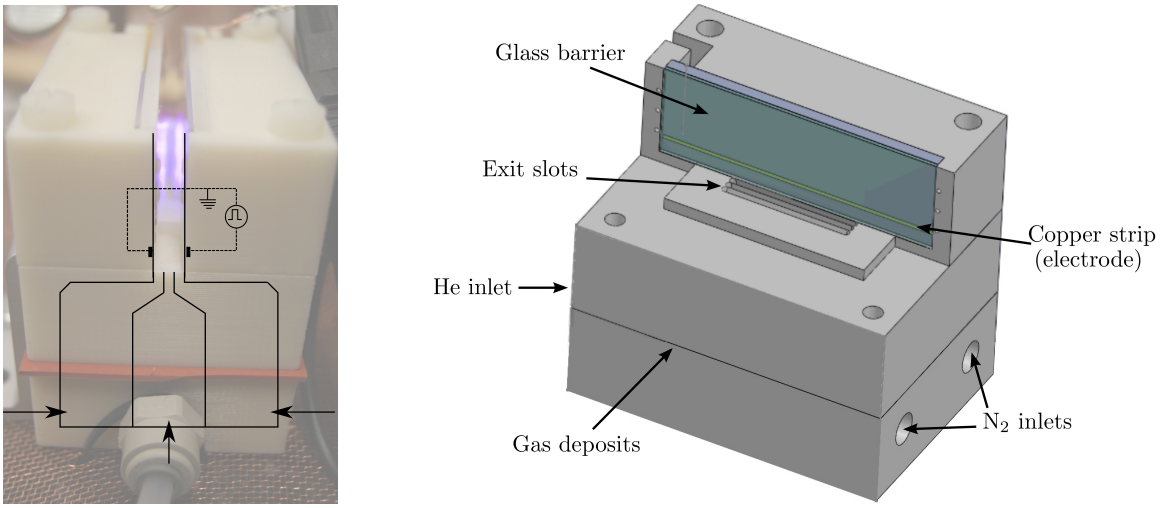

(a) Schematic. (b) CAD model.

Figure 2-2: Parallel jets experimental setup. The CAD drawing has one electrode and its support removed for ease of interpretation.

2.3 Opposed jets facility

The opposed jets facility was designed having in mind that it would be used for two different experiments: an opposed non-isothermal jets of uniform composition platform and as a counterflow nonpremixed burner (see Figure 2-3). The design had to meet the requirements of both experiments, the burner posing more restrictions than the non-reacting flows. All experiments were performed at atmospheric pressure.

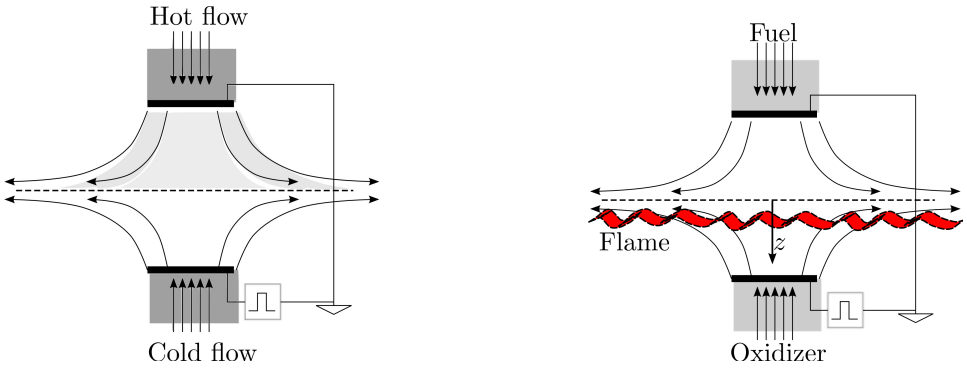

(a) Non-isothermal jets. (b) Nonpremixed flame.

Figure 2-3: Opposed jets schematic.

2.3.1 Design criteria

The design follows the guidelines given by other researchers that have worked with counterflow nonpremixed burners [56, 57, 136, 178, 180] and will be summarized in what follows.

The burner was comprised of two concentric tubes of Φ_i =15 mm inner diameter. The burner diameter was chosen large enough compared to the flame thickness (∼1mm) to ensure one-dimensionality close to the axis and as small as possible to work with low flows. The tubes were separated by L=17mm, since stability of the counterflow flame requires:

$$0.5 < L/\Phi_i < 2.$$

Once the geometry is fixed, the flow field is characterized by the choice of strain rate [1] defined as (oxidizer side) [178, 180, 181]:

$$a = \frac{2u_o}{L}\left(1 + \left(\frac{u_f^2\rho_f}{u_o^2\rho_o}\right)^{1/2}\right), \tag{2.1}$$

where a is the strain rate, u the exit speed, ρ the exit density and L the distance between tubes. The subscripts o and f refer to the oxidizer and fuel flows respectively (total mixture including dilutants). An equivalent definition can be easily written for the fuel side strain rate.

The exit velocities of the opposed jets were chosen to be momentum-balanced, in order to have the stagnation plane for the colliding flows sitting at the center of the burner gap (and the flame close to it). The condition is:

$$\frac{u_o}{u_f} = \sqrt{\frac{\rho_f}{\rho_o}}. \tag{2.2}$$

Once the composition is fixed, the only free experimental parameter is the strain rate, which can be varied in principle over a broad range. The upper limit of the strain rate is given by transition to turbulence or extinction of the flame, whichever comes first. The

[1] In reality the strain rate, defined as the normal gradient of the normal component of the flow velocity relative to the flame, changes from the fuel boundary to the oxidizer boundary. However, it is customary to refer to this global parameter (representative of the value close to the stagnation plane) as the strain rate of the flame with no further clarification.

lower limit is set by the maximum admissible flame thickness ($\delta_T \sim a^{-1/2}$), which needs to be small enough to satisfy adiabatic conditions at the boundaries. Additionally, the flame thickness impacts the way the electrical discharge develops, as described in Section 5.3.1. With all this in mind, a typical strain rate used in the experiments reported in Chapters 5 and 6 is $a = 40s^{-1}$.

For the flame experiments, the fuel of choice is methane and it is diluted either in nitrogen, argon or helium, in order to avoid excess unburnt fuel and soot formation (Figure 2-4). The oxidizer of choice is either oxygen diluted in nitrogen, argon or helium, or air. The specific mixtures used will be quoted with the results. Unless otherwise stated, the fuel flow was injected from the top nozzle and the oxidizer from the bottom, since stability was improved when injecting the denser stream from below. Composition will be reported in terms of the stoichiometric mixture fraction, Z_{st} [48]:

$$Z_{st} = \left(1 + \frac{Y_{CH_4,-\infty} M_{O_2} \nu_{O_2}}{Y_{O_2,\infty} M_{CH_4} \nu_{CH_4}}\right)^{-1}, \tag{2.3}$$

where $Y_{\pm\infty}$ is the local mass fraction at the nozzle far from the flame front (gives the degree of dilution of the injected streams), M the molecular weight and ν the stoichiometric coefficients of the global combustion reaction. For a momentum-balanced case, the value of Z_{st} decides where the flame sits with respect to the stagnation plane [107]. For $Z_{st} < 0.5$ the flame sits on the oxidizer side; this is usually the case when using methane as the fuel [48].

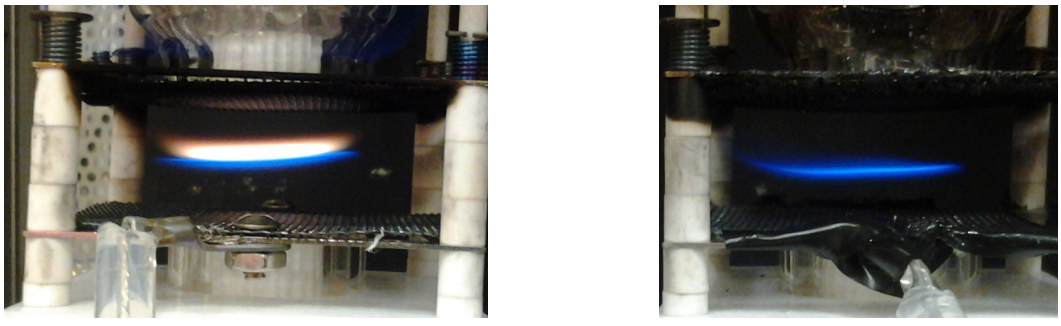

(a) Pure fuel, $X_{CH_4,-\infty}$=1 ($Z_{st} = 0.055$).

(b) Fuel diluted in nitrogen, $X_{CH_4,-\infty}$=0.19 ($Z_{st} = 0.33$).

Figure 2-4: Photographs of flames with and without fuel dilution, $a \approx 40s^{-1}$, and air as the oxidizer. Soot can be appreciated in the undiluted fuel case (a).

To quench the periphery of the flame, avoid recirculation and mixing with the stagnant gas, provide isolation from the environment and improve the flatness of the flame (reduce flame curvature), a coflow of inert gas, and in particular nitrogen, was used in both tubes. The velocity of the coflow was chosen to be approximately the same as that of the main flow.

Note that the guidelines have been here defined for the flame experiment. For the non-reacting non-isothermal jets, similar guidelines apply. In this case, the same gas was injected in both tubes. The upper nozzle had an internal heater inserted in it that increased the temperature of that stream up to 1000K. The bottom gas was at ambient temperature. The exit speeds still had to satisfy equation 2.2, so that the stagnation plane was in the middle of the gap; where now subscripts o and f refer to the ambient and heated flows respectively. The speeds were chosen to have laminar, non-buoyant jets. In addition, the higher the exit speed of the jets, the sharper the temperature gradient. For these experiments, no coflow was used.

2.3.2 Experimental setup

The counterflow jets apparatus consisted on two opposed quartz nozzles facing each other (the design was made as part of this work and sent to James Glass, Inc. for fabrication). Quartz was used to withstand the high temperature imposed by the heated flow and to ensure electrical insulation. Both nozzles were concentric quartz tubes of inner diameter 15mm and were surrounded by a coflow ring of inner diameter 18mm and outer diameter 22mm.

The top quartz tube had a SiC heater (SER Starbar) inserted in it, powered by a variable autotransformer (Powerstat 116B). Whenever the top jet was heated, the top quartz tube was insulated with a ceramic blanket (from CeraMaterials).

The bottom nozzle was placed on a two-axis translation stage, the two axis being in the plane parallel to the nozzle exit, and with control over the inclination of this plane for precise positioning of both nozzles relative to each other, see Figure 2-5(b).

The respective fuel, oxidizer and dilutant streams in the inner tubes were supplied via upstream sonic nozzles from compressed gas bottles and the flow rate was varied using the upstream pressure. For the coflows, the flow rate was measured using variable area flowmeters

and varied using needle valves.

Glass beads and ceramic honeycomb were inserted in the tubes as flow straighteners and turbulence suppressor elements. The electrodes were two stainless-steel meshes placed at the nozzle exits that also served this purpose.

Figure 2-5 shows a schematic, CAD model and photograph of the final setup.

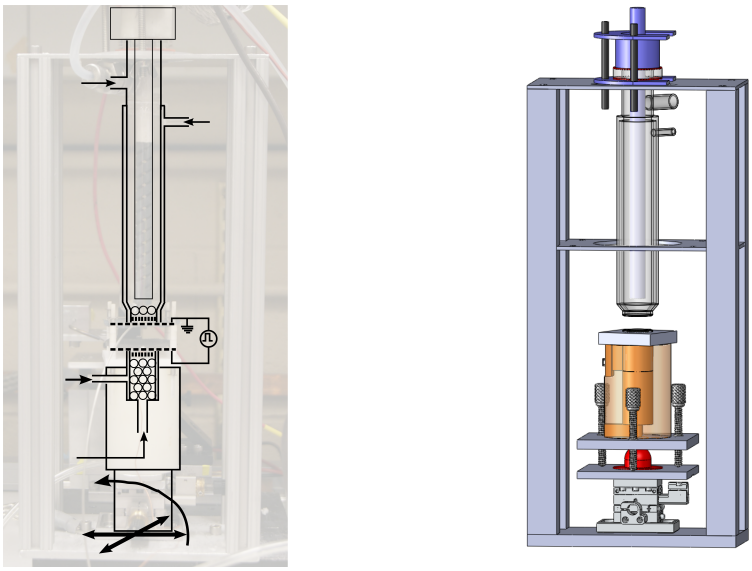

(a) Schematic. (b) CAD model.

Figure 2-5: Opposed jets experimental setup.

2.4 Electrical system

2.4.1 Discharge cells

In both the parallel jets and the opposed jets setups, the electrodes were placed so that the applied electric field was mainly in the direction parallel to the dominant gradients (composition or temperature gradients respectively) and as close to uniform as possible. The electrodes were directly connected to the power supply and no circuit elements were added to better match the transfer of power to the gas.

In the case of the parallel jets experiment, the electrodes consisted on two copper strips of 2mm width placed at 4mm of the jet exit and 6-7mm apart. Results using copper wire electrodes of 0.5 mm diameter placed on the same location did not significantly change the

appearance of the discharge. A glass microscope slide of 1mm thickness was used as a safety dielectric barrier attached to the cathode for some of the experiments, studies without the slide were also performed. The electrodes and electrode-holders are shown in Figure 2-6(a).

For the opposed jets experiment, two stainless-steel square meshes (50mm width) placed at the exit of the nozzles were used as the electrodes. Unless otherwise noted, the bottom mesh was powered (and corresponded to the anode when using unipolar pulsed voltage) and the top mesh was grounded. Accurate positioning of the electrodes at a distance 17mm from each other was achieved using alumina spacers (eV Parts from Kimball Physics). A closeup view of the discharge cell is shown in Figure 2-6(b).

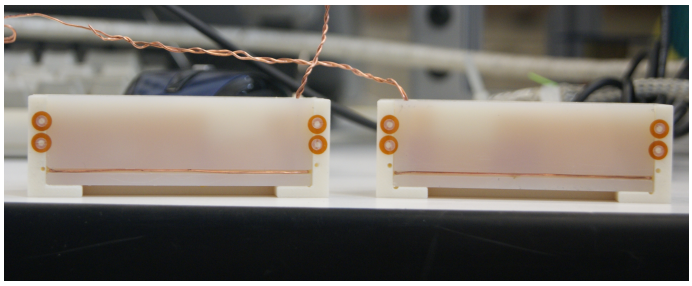

(a) Parallel jets.

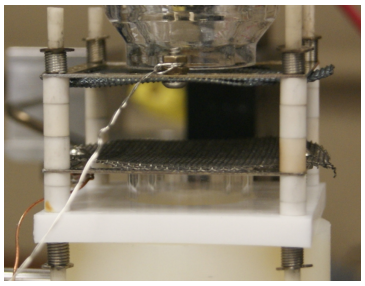

(b) Opposed jets.

Figure 2-6: Electrodes and discharge cells for the two setups.

2.4.2 Repetitive pulsed nanosecond discharge generation

In this research, the non-thermal plasma was generated by a nanosecond-duration high voltage pulse generator. The main characteristics of this type of discharges are high reduced electric fields, which can efficiently generate ionization, electronic excitation and dissociation of molecules by electron impact reactions; short duration, which avoids transition into a thermal spark; and high repetition frequencies, which enable the use of a transient discharge in a steady state setting [143] (Section 1.3.2).

Repetitive pulsed nanosecond discharges were produced using a high voltage pulse generator (FID Technologies FPG 10-30NKS10). The voltage pulses were unipolar (positive), had a maximum amplitude ranging from 2 to 10 kV into a 100-500Ω load, rise time of 2ns and duration of around 10ns at 90% of maximum voltage, and could be generated in a continuous mode with repetition frequencies from 2-30kHz or in bursts of pulses. The high voltage pulse

generator was externally triggered using a function generator (Agilent 33220A).

The pulse generator was connected to the electrode system through a 15m coaxial cable (RG 302/U) with an impedance of 75 Ω. The length of the coaxial cable allowed to separate the applied pulses from possible reflected pulses [150]. Reflected pulses appear as the coaxial cable connecting the high voltage pulse generator to the discharge cell is mismatched at both ends. A signal velocity of ∼70% the speed of light leads to the first reflected pulse appearing around 145ns after launching the incident pulse. Additionally, the pulse generator triggers a spurious secondary pulse around 600ns after the main pulse of non-negligible and variable amplitude. For the highest repetition rate (30kHz), the time between incident pulses is sufficient to damp out the subsequent reflections.

High voltage short duration discharges pose important challenges when using other electronic equipment for diagnostics due to the electromagnetic interference (EMI) they cause. Good grounding and proper shielding are crucial to make this type of measurements. Shielding was obtained by enclosing both the power supply and the experimental setup in separate Faraday cages and placing ferrite cores at all DC connections to act as common mode chokes. Power and data cables were shielded with metallic sleeves and aluminum foil. Grounding was provided using an equipotential plane, for the combustion experiments this was a metallic optical table, and using grounding copper braid (1 inch thick) to make the ground connections. Whenever possible, wireless connections were used (mouse, keyboard, etc).

2.4.3 AC voltage

The response of a flame to high frequency AC voltage was studied in the experiments of Chapter 6. In this case, a high-voltage amplifier and supply system, Trek Model 664, was used. Its output voltage range is up to ±10kV peak AC (output current peak ±20mA). The waveform to be amplified was generated using an Agilent 33220A function generator. Maximum amplification of the signal could be obtained for frequencies up to 10kHz. For higher frequencies, amplification was limited. The AC tests at higher frequency (60kHz) of Section 3.3.4 were thus made using a driving resonant circuit power supply (PVM12) with open circuit voltage of 1-20kV and short circuit current of 20mA. The frequency range of this power supply was 20-60kHz and, as well as the voltage level, it was set by the capacitive

load present (could not be varied).

2.5 Diagnostics

For the experiments reported in this work, three levels of characterization were required: characterization of the medium in which the plasma develops (Section 2.6), description of the gas discharge and plasma (Section 2.7) and measurements related to the plasma-flame interaction (Section 2.8). A summary of the diagnostics used is given in Table 2.2.

Table 2.2: Measurement techniques used and parameters diagnosed.

	Measurement technique	Parameter diagnosed
Medium	Schlieren	Composition
	Thermocouple	Temperature
	Photography	Flame position, luminosity
Plasma	Current, voltage	Energy, electrical behavior
	Photography	Position, confinement
	Fast photography	Uniformity, development dynamics
	Optical emission spectroscopy	Plasma species
Plasma-flame interaction	Laser Rayleigh scattering	Temperature modifications
	Video recording	Flame dynamics

2.6 Diagnostics: characterization of the medium

In all cases analyzed, the background gas in which the plasma developed was characterized by non-uniform composition and temperature. The pressure could be assumed atmospheric.

For no applied voltage, a global picture of the flow for the non-reacting experiments was obtained using a Schlieren system borrowed from the Gas Turbine Lab at MIT. It was used to verify that the flow was laminar in the region of interest and to have direct visualization of the jets. Quantitative information for the parallel jets experiment was also obtained. Temperature fields were measured using thermocouples and laser Rayleigh scattering (Section 2.8.1).

2.6.1 Schlieren flow visualization

Schlieren flow visualization is based on the deflection of light by a refractive index gradient [64, 182]. It can both be used to obtain a qualitative description of the flow field (transition to turbulence as exemplified in Figure 2-7, mixing characteristics of two fluids, etc) and, after proper calibration, to quantify refractive index distributions and related quantities [5,73,114]. In this work, a Schlieren system has been used to measure the composition profiles in the three parallel jets experiment.

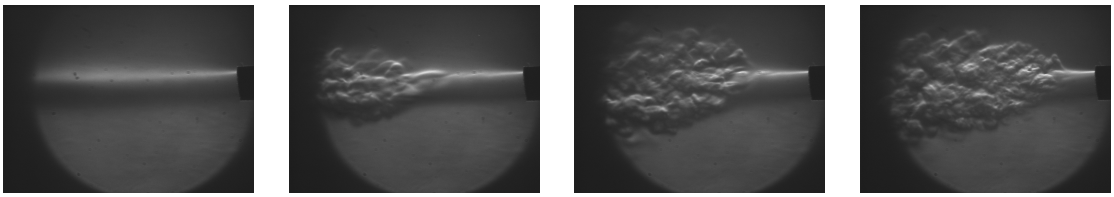

(a) Re=370. (b) Re=530. (c) Re=690. (d) Re=1060.

Figure 2-7: Schlieren visualization of a helium jet discharging into ambient, effect of Re.

Light refraction in gases

For a detailed derivation of the theory and mathematical description of the Schlieren technique, the reader is referred to the dedicated literature [64, 182], in what follows the main formulation needed for the purposes of this work is summarized.

When a light ray traverses a medium with non-uniform refractive index, it is deflected proportionally to the existing refractive index gradients. That is, a light ray traveling in the z-direction through a medium with a refractive index n which is a function of x and y, is deflected by an angle α_y (in the y-direction) according to:

$$\alpha_y = \int \frac{1}{n}\frac{\partial n}{\partial y} dz = \frac{L_z}{n}\frac{\partial n}{\partial y},$$

where L_z is the length of the refracting medium and the integration has been performed assuming no variations along the direction of propagation of the ray. An equivalent formula can be written for a deflection in the x-direction.

For a mixture of gases, the refractive index is given by the Gladstone-Dale relation:

$$n - 1 = \rho \sum_i G_i \frac{\rho_i}{\rho},$$

where G_i is the Gladstone-Dale constant of species i and varies slightly with the wavelength of the light, ρ is the density of the gas and ρ_i/ρ is the mass fraction of each component in the gas mixture. The summation is over all species present.

In the setup described in Section 2.2, the temperature and pressure can be assumed uniform and so the refractive index gradients can be directly related to gradients in composition. Additionally, the experiment is intrinsically two dimensional so that the 2D field can be directly obtained from a single non-intrusive measurement. Particularizing for uniform, given temperature and pressure, and in terms of the mole fractions of each species, X_i, the Gladstone-Dale equation becomes:

$$n - 1 = \frac{p}{R_u T} \sum_i G_i X_i M_i,$$

where p is the pressure, R_u the universal gas constant, T the temperature and M_i the molecular mass of species i. So, for a binary mixture (like the helium-nitrogen one here considered), n is a function of the mole fraction of one of the components, and thus, the composition-gradient field can be directly obtained from the refractive index gradient field. The calibration procedure used to obtain the refractive index gradient field from the Schlieren images is Schardin's method as described in [73] and the implementation for this work and calibration curves are summarized in Appendix A. The work in [73] uses the calibration to obtain a temperature field, in the present work the method has been modified to derive a composition field.

Schlieren system

Referring to Figure 2-8, from right to left (corresponding to the direction of travel of the light) the elements in the Schlieren system are described in what follows.

A blue LED with 360mlm of intensity and 470nm in wavelength was used to provide a

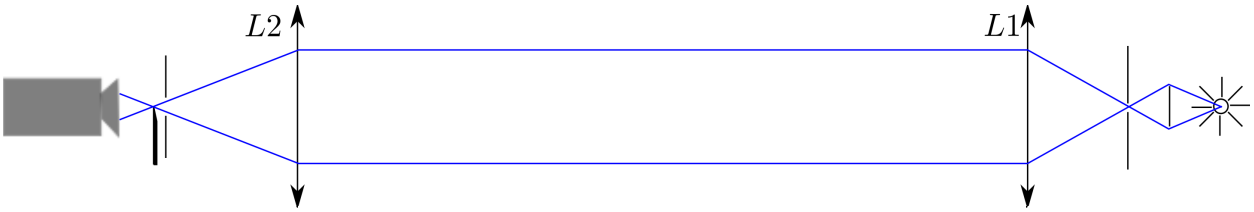

(a) Schematic.

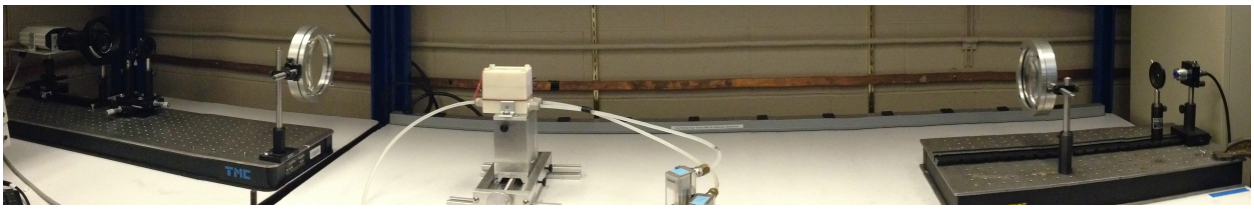

(b) Panoramic view.

Figure 2-8: Schlieren setup.

uniform, monochromatic source of light. In front, a condenser lens (microscope objective) focused the light to a point that coincided with the focus of lens L1. A diaphragm was also placed at this location to eliminate reflections.

Lens L1 creates a parallel beam of light in the test section between L1 and L2. The separation between these two lenses was arbitrary and the object under study was placed in this region. For no Schlieren object, the light travels as parallel rays. Lenses L1 and L2 had focal lengths of 28cm and 51cm respectively and diameters of roughly 15cm.

A knife-edge was placed at the focus of L2, this is an essential element in any Schlieren setup and its purpose is detailed in [64]. The orientation of the blade decides the refractive index gradients that are visualized (those normal to the blade), so that gradients in different directions can be revealed by suitably orienting the knife-edge. In short, the purpose of the knife edge is to block part of the refracted rays so that the disturbances due to the inhomogeneous medium show up as a modulated intensity in the Schlieren image. Thus, the deflection angle, or n gradient, is directly proportional to the contrast of the image (change in light intensity).

Another diaphragm was placed close to the knife-edge to eliminate reflections.

To capture the Schlieren image, a CoolSnap cf CCD from Photometrix was used, mounted with an objective lens (Canon Zoom Lens FD 70-210mm) for zooming and focusing. The flows measured were steady so no synchronization of the camera was needed.

2.6.2 Temperature measurements

Although in principle the temperature field of the non-isothermal jets experiment could also be measured using the quantitative Schlieren setup described (the 2D field for this axis-symmetric flow could be obtained using Abel-inversion techniques), in practice, mixing of the working fluid with the ambient air significantly contaminated the results. In the end, a K-type thermocouple, mounted on a translation stage, was used to measure the axial temperature profile along the axis of the jets. Considering that the peak temperatures reached are not too high ($\sim$ 900K), the measurement is representative of the gas temperature.

For the flame experiments, the high temperatures present ($\sim$1600-2100K) made the thermocouple measurements very inaccurate even when including a radiation correction [57]. For more accurate measurements, the laser Rayleigh scattering technique (Section 2.8.1) was used.

2.7 Diagnostics: electrical discharge

The diagnostics used on the electric discharge and plasma were optical and electrical. Electric parameters were obtained from the time-resolved current and voltage waveforms (Section 2.7.1). Initially, the nature of the discharge (homogeneous, filamentary) and its positioning within the flow field, was determined by direct imaging using standard photography. The imaging was later improved during the stay at the Applied Physics Group in Princeton University and with the help and equipment of Dr. A. Starikovskiy by performing time-resolved fast photography of the plasma at its own time-scale (Section 2.7.2). Optical emission spectroscopy was used to determine the dominant emissions of the discharge (Section 2.7.3).

2.7.1 Current and voltage waveforms

The electrical properties of the discharge were measured through time-resolved current and voltage waveforms. The voltage probe used was a LeCroy PPE 20kV and the current probe a Pearson 2877, coupled to a 20dB attenuator (Agilent 8493A-20) when needed. Both voltage

and current were displayed in a large bandwidth oscilloscope (1GHz Infiniium 54835A or 3GHz LeCroy Wavepro 7300A). These measurements were used to determine the energy deposition in the gas as well as to interpret the electrical behavior of the experimental setup. In what follows, the method used to estimate the electric energy deposition for the pulsed nanosecond-duration discharges is summarized.

Energy determination for the pulsed nanosecond-duration discharges

According to [143], the measured current of a pulsed nanosecond-duration discharge includes displacement (or purely capacitive), conductive (or purely resistive) and parasitic (noise) components:

$$I_{meas} = I_{disp} + I_{cond} + I_{paras}, \tag{2.4}$$

where the parasitic currents are mainly due to common-mode currents and probe loading.

Implicit in this decomposition of the current is that the capacitive and resistive components of the discharge cell are connected in parallel (additive currents). As will be discussed in Section 6.5.1, this requires that the existing charge bridges the inter-electrode space.

For the measured waveforms, the parasitic component was much lower than the displacement contribution. The capacitance of the system could thus be estimated from the current and voltage waveforms, if the voltage was below electrical breakdown, from:

$$I_{meas} \approx I_{disp} = C\frac{dV}{dt}. \tag{2.5}$$

Only the conduction component of the current contributes to the energy deposition in the gas. Thus, if it is measurable, the energy can be estimated by integrating the power:

$$\text{Energy} = \int_t I_{cond}(t)V(t)dt.$$

Unfortunately, for many of the discharges studied in this work, the conduction component was negligible and an alternative way of estimating the energy deposition had to be used.

[143] estimated the energy deposition, during application of an RPND voltage pulse,

for a diffuse plasma with very low conduction current by evaluating the difference between the energy calculated using the total measured current, for a case with the plasma, and a similar case, without the plasma. He argued that, for the no-plasma case, this energy represents parasitic losses since the integral of the displacement current times the voltage cancels out[2], whereas, for the plasma case, it also includes the small conduction contribution. By subtracting the two values, the parasitic losses can be eliminated:

$$\text{Energy} = \left(\int I_{meas} V dt\right)_{\text{plasma}} - \left(\int I_{meas} V dt\right)_{\text{no plasma}}. \tag{2.6}$$

It must be emphasized that this is a rough estimation of the current (the parasitic current is higher than the conduction current!) and that this method will at most give an order of magnitude for the real energy deposition. However, for lack of a better estimate, it has been used. To lower the error bound, the mean value of $\left(\int I_{meas} V dt\right)_i$ (i=plasma, no plasma) using 500-1000 pairs of waveforms was used, so that the energy deposition in the gas becomes:

$$\text{Energy} = \left(\bar{E}_{\text{plasma}} - \bar{E}_{\text{no plasma}}\right) \pm \sqrt{\sigma^2_{\text{plasma}} + \sigma^2_{\text{no plasma}}}. \tag{2.7}$$

The approximation given by equations 2.6 and 2.7 is more general than the circuit model implied by equation 2.4. For consistency with the circuit models later proposed for the plasmas observed in this dissertation (Sections 6.5.1 and 6.5.2), it must be said that, if the resistance and capacitance are connected in series instead of in parallel, the contribution of the capacitance still cancels out and the estimate of equation 2.7 still holds[3].

2.7.2 Ns-resolved photography

To resolve the plasma dynamics of the nanosecond-duration discharge coupled to a flame front, a PicoStar HR12 (La Vision) intensified CCD camera was used. The timing between

[2]When integrating over a voltage pulse, the contribution of the displacement current cancels out: $\int_{\Delta t} I_{disp} V dt = \int_{V_i}^{V_f} CV dV = \frac{C}{2}(V_f^2 - V_i^2) = 0$ (for $V_f = V_i = 0$).

[3]Referring to the symbols in Figure 6-20, the integral for $\bar{E}_{\text{plasma}}$ becomes: $\bar{E}_{\text{plasma}} = \int I_{meas} V dt = \int I_{paras} V dt + \int I_\sigma V_\sigma dt + \int I_\sigma (V - V_\sigma) dt = \bar{E}_{paras} + \int I_\sigma^2 R_\sigma dt + \int C(V - V_\sigma) d(V - V_\sigma) = \bar{E}_{paras} + \int I_\sigma^2 R_\sigma dt$. Thus, when subtracting the no-plasma energy, the parasitic loss is eliminated, and only the conduction contribution survives.

the CCD, the electronic shutter and the high voltage pulse generator was controlled with a delay generator (BNC Model 575). The images correspond to the integrated emission over a broad wavelength range. The emission captured corresponds almost exclusively to transitions of the second positive system of molecular nitrogen due to the short camera gate used, 0.5ns, and the presence of nitrogen. Different delays of the camera are introduced with respect to the application of the voltage pulse to obtain the discharge evolution in time. This time-resolved visualization assumes that the discharges are repeatable since the sequential images correspond to different applied voltage pulses. Images are delayed by 1ns between them.

2.7.3 Optical emission spectroscopy

For the non-reacting experiments of Section 3.3.3, exploratory optical emission spectra of the pulsed nanosecond-duration discharges, triggered in continuous mode, were recorded for emission in the range from 300 to 800nm. In this case, the spectra were spatially and temporarily integrated (no synchronization of the detector with the applied voltage pulses was used). The light emitted at the center of the plasma was focused by means of an optical fiber into the entrance slit of a 750mm focal length spectrometer (Acton Research Spectra Pro 2750, Princeton Instruments) and two different gratings were used: 300grooves/mm and 1800grooves/mm both blazed at 500nm for dispersion of 4.36nm/mm and 0.62nm/mm respectively. The detector used was a CoolSnap cf ICCD connected directly to the exit of the spectrometer. For these time-integrated images, a long exposure time of the camera was used ($\sim$1-5s). Calibration in wavelength was performed using a Hg lamp.

Similar exploratory spectra for the plasma-flame interaction experiments of Section 5.4 were obtained. In this case, the time-accumulated emission spectra from the center of the flame without the plasma and when applying high voltage pulses in either continuous mode or in bursts was recorded. To spatially resolve the emission in the direction across the flame, light from the plasma was focused using a 75mm UV focusing lens (no amplification) directly onto the entrance slit of an Acton Research Spectra Pro 500i spectrometer with a 500mm focal length and a grating of 600grooves/mm blazed at 500nm. A diagram of the setup is shown in Figure 2-9. The detector used was an ICCD (either a Princeton Instruments Roper

Scientic PI-MAX for the continuous mode measurements, in Section 5.4.5, or a PicoStar HR12 for the bursts of pulses measurements, in Sections 5.4.2 and 5.4.3). Images for the continuous mode were taken using 20ms camera exposure time. Images when capturing the emission for a given burst of pulses were triggered by the first incident voltage pulse and had exposure time corresponding to the whole duration of the burst (e.g. 100 pulses at 25kHz would require an exposure of 4ms). Calibration in wavelength was performed using an argon lamp.

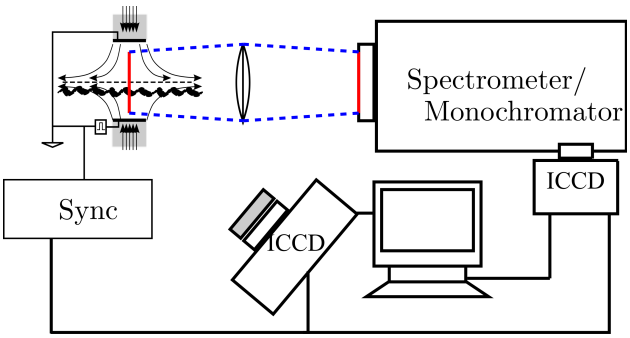

Figure 2-9: Imaging setup: photography and spectroscopy.

2.8 Diagnostics: plasma-flame interaction

Although the bulk of this dissertation is centered on determining how an inhomogeneous environment impacts the development of rapid gas discharges, two of the experiments performed were devoted to quantify the impact of the strategy on the flame itself.

To this end, the temperature fields with and without the pulsed nanosecond-duration plasma were compared, in order to measure a possible temperature increase associated to the electrical energy deposition (due to thermalization of the plasma or to an extension of the burning region). These results are reported in Section 5.4.6. The temperature measurements were performed using the Laser Rayleigh scattering technique, Section 2.8.1.

Additionally, the response of the flame to high frequency AC fields (100Hz-10kHz) was monitored by video recording as explained in Section 2.8.2. These results are reported in Section 6.2.

2.8.1 Laser Rayleigh scattering

Rayleigh scattering principles

Rayleigh scattering refers to the elastic scattering of light by particles much smaller than the wavelength of the incident radiation (individual atoms and molecules as well as small solid particles and clusters) due to induced electric dipole radiation.

Laser-illuminated Rayleigh scattering is a flow diagnostics tool that makes use of this principle by recalling that all species scatter light at the same wavelength as the incident radiation, so that the use of a monochromatic light source (e.g. a laser beam) greatly simplifies the interpretation of the observations. A detailed review of the laser Rayleigh scattering technique can be found in [118].

In this dissertation, laser-illuminated Rayleigh scattering was used to determine the temperature field in a counterflow flame experiment with and without plasma application. If the presence of solid particles (e.g. dust) can be neglected, Rayleigh scattering can be used to measure density, since the signal is linearly proportional to the number of scatterers. Moreover, if the pressure is uniform and known, the temperature field can be determined. If such is the case, the detected Rayleigh-scattered intensity when a laser beam traverses the medium to be probed is given by:

$$I_R = I_L N l \Omega \varepsilon \left(\frac{\partial \sigma}{\partial \Omega} \right)_{\text{eff}} \propto N \propto \frac{1}{T},$$

where I_R is the detected Rayleigh-scattered intensity, I_L is the laser intensity, N is the gas number density (number of scatterers per unit volume), l is the probed length, Ω is the solid angle of detection, ε is the optical transmission efficiency of the detector and optical elements and $\left(\frac{\partial \sigma}{\partial \Omega}\right)_{\text{eff}}$ is the differential Rayleigh scattering cross section of the gas mixture at the probed point.

For the application at hand, the main challenges that had to be addressed, in order to obtain the counterflow flame temperature field, were dealing with an inhomogeneous and unknown gas composition and eliminating stray light from optics and surfaces.

Appendix B overviews the method used to extract the temperature from the Rayleigh-

scattering images, the calibration method used is that of [13].

Rayleigh scattering setup

The laser Rayleigh scattering platform used is that of the Applied Physics Group in Princeton University [116] and was arranged with the help of C. M. Limbach. A schematic is shown in Figure 2-10. Following the propagation of the laser beam and referring to the diagram, the elements in the setup are described in what follows.

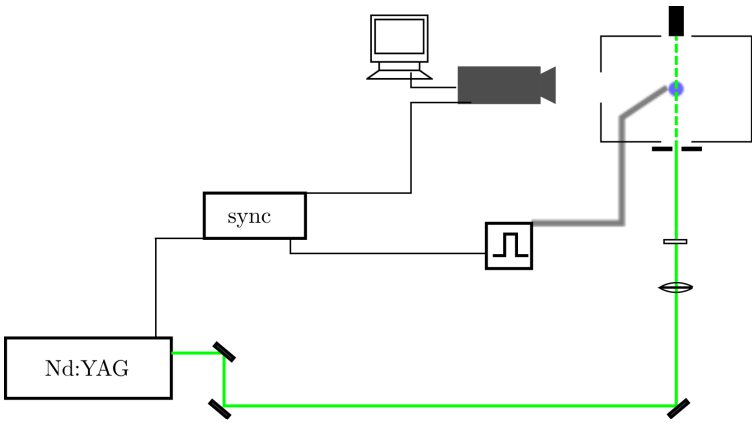

Figure 2-10: Laser Rayleigh scattering setup (top view). The green lines correspond to the laser beam.

A frequency doubled Nd:YAG laser, $\lambda = 532nm$, (Spectra-Physics Model GCR170) with 10ns output pulses at 10Hz provides the incident light. Next, three mirrors direct the laser which is then focused by a plano-convex 500mm focal length lens into the measurement region. A polarizer then ensures that the polarization of the laser is orthogonal to the observation direction in order to maximize the Rayleigh scattering signal detected. The light passing through the measurement region is finally disposed in a beam dump. In order to minimize stray light from optics and other surfaces, several diaphragms were placed. Additionally, the metallic surfaces of the Faraday cage enclosing the experiment, the metallic poles serving as structural support for the burner, and the reflecting quartz of the nozzles, were all covered with black tape.

Images were collected by an ICCD camera (Princeton Instruments Roper Scientic PI-MAX) mounted with an objective lens for zooming and focusing and a 532nm filter placed before the lens. The timing between the probe laser, ICCD camera and the high voltage pulse

generator could be controlled with a delay generator (Quantum Composers Model 9514).

Note: as described, the measurement was a 1D profile along the beam direction (which coincided with the direction *along* the flame, close to the peak temperature region, so that the radial temperature profile could be obtained). The setup could be modified to have a 2D temperature map by introducing the optics required to form the laser beam to a thin light sheet.

2.8.2 Monitoring flame dynamics

The dynamic response of the counterflow nonpremixed flame to AC voltage has been studied in Chapter 6.

To that end, the motion of the flame in the presence of an AC field was recorded by a Bonito 400-CL 200 fps camera mounted with an objective lens for zooming and focusing. For the experiments performed, the exposure time was set to 2ms and the frame rate to 200Hz. For each case, a total of 0.5s were recorded (100 sequential frames). For each frame, the flame contour was obtained as the locus of points of maximum intensity, e.g. in Figure 2-11 the flame is shown by the cyan curve. The flame position and shape as a function of time, with and without applied voltage, were determined from these measurements.

Figure 2-11: Obtaining flame dynamics from video recording. The images show two frames, at different times upon AC voltage application, in which the position and shape of the flame (indicated by the cyan curve) are affected by the instantaneous voltage conditions.

Chapter 3

Repetitive pulsed nanosecond discharges in non-reacting gradients

3.1 Introduction

In this Chapter, the breakdown characteristics of short duration electrical discharges in non-reacting, inhomogeneous gases, are studied.

In addition to the application of plasma assisted combustion, there are several situations in which non-thermal plasmas are produced, or appear naturally, in a highly non-uniform environment (Section 1.3.4). Typical technological applications would be those of plasma development in mixing layers, for aerodynamic actuation [119], or atmospheric pressure plasma jets (APPJ), used in thin film deposition and plasma medicine [99,177]. For naturally occurring phenomena, streamer plasmas propagating in the upper atmosphere do so in gradient density air [109]. Despite its importance, the fundamental problem of understanding non-thermal plasma development in a non-uniform gas is a fairly unexplored one, although there has been recent work in the area of non-thermal plasmas in the upper atmosphere [109, 140] and APPJ [24, 129].

For that reason, the first contribution of this dissertation is to propose a novel platform for the study of the impact of strong inhomogeneities in the development of Repetitive Pulsed Nanosecond Discharges (RPND). The platform was chosen to be non-reacting, to simplify the physics as much as possible, and to have some similarities to the flat flame (analyzed in

Chapter 5), in terms of the structure of the inhomogeneities present. Inhomogeneities both in the composition and temperature fields have been considered.

The model proposed is detailed in Section 3.2. Experimental confirmation of the hypothesis presented are given in Sections 3.3 and 3.4, for composition and temperature gradients respectively. Section 3.5 summarizes the main findings of this Chapter.

Part of the work included in this Chapter has been published in *Journal of Physics D: Applied Physics* [67] (Sections 3.2 and 3.3).

3.2 Non-reacting model: Gas-confined Barrier Discharge

3.2.1 Simplified model

A simple model is proposed to analyze the different breakdown modes of a pulsed nanosecond-duration discharge under very inhomogeneous conditions. Because of the analogous physics, this discharge is here named the Gas-confined Barrier Discharge (GBD). The model is pictured in Figure 3-1 and consists on a sandwich-like structure of two or three layers of gases with very different electrical properties, e.g. a layer of a gas that can be easily broken down (from here onwards, this layer will be referred to as the *hot* layer) surrounded by one or two layers of highly insulating gas (the *cold* layers). *Hot* and *cold* need to be understood from an electrical point of view: a gas can be more easily ionized either because of a lower number density or because of a favorable composition.

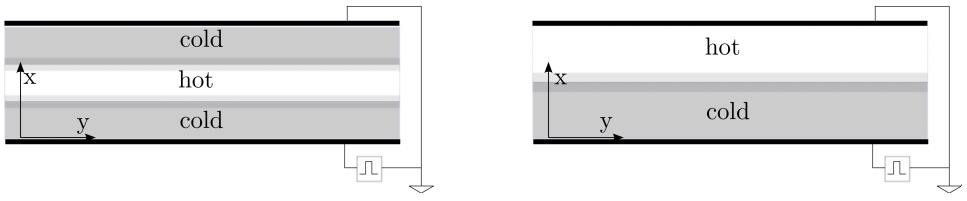

(a) Two *cold* layers ($N_c = 2$). (b) One *cold* layer ($N_c = 1$).

Figure 3-1: General structure of the GBD.

An analytical model is derived for this sandwich-like structure, which predicts that, depending on the selection of the electrical and geometrical parameters, the discharge can be produced in the whole gap or just in the *hot* layer with the *cold* layers acting as a

pseudo-dielectric (with important differences that are explored).

3.2.2 Analytical evaluation

An analytical evaluation of the GBD model, based on differences in the ionization coefficients of the gaseous layers, that uses the well-known criteria for Townsend and streamer breakdown [166] (Section 1.3.1), is here presented.

The main assumptions made are that there is only variation of the temperature and composition with x (Figure 3-1), the pressure and the applied electric field are uniform, and the reduced ionization coefficients for the *hot* and *cold* gases follow Townsend's semi-empirical formula ($i = h, c$):

$$\frac{\alpha_i}{n} = F_i \exp\left(-\frac{G_i}{E/n}\right), \tag{3.1}$$

where α_i/n is the reduced ionization coefficient (inverse of the mean free path for ionization divided by the number density of the gas), E/n the reduced electric field, the subscripts h and c refer to the properties of the *hot* and the *cold* layers respectively, and F_i and G_i are constants for each gas.

The uniform pressure will be named p_0, the thicknesses of each layer d_h and d_c respectively, and their ratio $r = d_h/d_c$. The temperature of the *hot* layer will be K times the temperature of the *cold* layer, T_0. The density in the *cold* layer will then be $n_c = \frac{p_0}{k_B T_0} = n_0$ and in the hot layer $n_h = n_0/K$. Also there can either be one or two cold layers, $N_c = 1, 2$, with the same thickness and properties.

Since the streamer breakdown mechanism has no direct relation to electrode phenomena [58], it seems reasonable to assume that the first electron avalanche will occur in the region where the conditions for ionization are most favorable. For a structure like the one in Figure 3-1, this will be the *hot* layer. The electric field before the first breakdown will correspond to the externally applied field and, for the geometry considered, is constant throughout the layers:

$$E = \frac{V}{d_h + N_c d_c}, \tag{3.2}$$

where V is the applied voltage.

Moreover, the propagation of the first electron avalanche across the *hot* layer alone might be enough to satisfy Meek's breakdown condition for streamer formation[1] ($\alpha_h d_h \approx 20$). Thus, combining these two expressions, the minimum applied voltage (in the full gap) to reach Meek's criterion within the *hot* layer will be:

$$V_{str,h}(\text{gases}, N_c, r, K, n_0 d_h) = G_h \frac{n_0 d_h}{rK} \frac{N_c + r}{\ln\left(F_h n_0 d_h/(20K)\right)}. \tag{3.3}$$

Once a streamer channel has formed, the potential drop along its body will be small (a quasi-neutral plasma is left behind) and so the electric field in the *cold* layer will increase, at least locally. In order for the discharge to be confined to the *hot* layer, this amplified electric field in the *cold* layer needs to be below its own breakdown condition.

For the case of a single *cold* layer ($N_c = 1$), and for perfect conduction by the plasma after breakdown of the *hot* layer, the full potential drop will occur in the *cold* layer. If the shorting of the *hot* layer is not complete, then the electric field in the *cold* layer will be lower and the avoidance of breakdown will be facilitated. Therefore, a shorted *hot* layer is the most restrictive condition.

For the case of a *hot* layer sandwiched between two *cold* layers ($N_c = 2$) there will be an asymmetry in the electric field and the potential drop in one of the *cold* layers (at the cathode-side) will most likely be greater than in the other. I.e., there will be a non-symmetrical accumulation of charge that will modify the electric field on each side: on the anode-side the electrons are free to move towards the anode whereas the ions will start piling up in the cathode-side mixing layer due to their slower motion. The worst-case scenario (highest electric field in one of the cold layers) would then be that the full potential drop occurs in the cathode-side layer alone. This is an under-prediction of the region of confinement of the discharge to the *hot* layer and in reality a higher applied voltage is possible as there can be

[1]The criterion for streamer formation, or Meek's breakdown condition, is obtained by stating that the electric field induced by the space charge in the electron avalanche is of the same order as the external field. This criterion is representative of the formation of a sharp ionization front propagating into a non-ionized gas and leaving a non-equilibrium plasma behind. The condition becomes: $\alpha d = \ln\{4\pi\varepsilon_0 E/(e\alpha^2)\}$, the logarithm in the expression attenuates the dependencies inside it, and so it is customary to make the approximation $\alpha d \approx 20$, for most cases of interest.

some potential drop both in the anode-side *cold* layer and in the *hot* layer itself.

For the most restrictive situation in which the full potential drop occurs in the cathode-side *cold* layer, the electric field in it will be:

$$E = \frac{V}{d_c}, \tag{3.4}$$

and the breakdown can be assumed to be of the Townsend type, which is more restrictive than the streamer breakdown and there is direct contact of the breakdown region with the cathode so that secondary emission from its surface can feed the discharge.

The onset of breakdown of the cathode-side *cold* layer will be given by $\alpha_c d_c = \ln(1/\gamma + 1)$ [166], with γ the secondary emission coefficient.[2] Combining, the total voltage to avoid breakdown of the cathode-side *cold* layer, needs to be lower than:

$$V_{\text{Paschen},c}(\text{gases}, N_c, r, K, n_0 d_h) = \frac{n_0 d_h G_c / r}{C_c + \ln(n_0 d_h / r)}, \tag{3.5}$$

$$\text{where,} \quad C_c = \ln(F_c / \ln(1/\gamma + 1)).$$

This region is labeled, in Figure 3-2(a), as 'Confined to hot layer (a)' (a=asymmetry). Note that, if the potential drop is equally shared between both *cold* layers, the applied voltage can be doubled before breakdown of the *cold* layer occurs (labeled in Figure 3-2(a) as 'Confined to hot layer (s)', s=symmetry). In reality, an intermediate situation is more likely.

Additionally, the least restrictive situation would be when the shorting of the *hot* layer is not complete and can be neglected. In that case, the breakdown of the *cold* layer occurs for applied voltages a factor $(N_c + r)$ higher, $V^*_{Paschen,c}$. In reality, there will be a finite resistive component and the condition will lie between these extremes, Figure 3-2(b).

Equation 3.3 has a vertical asymptote at $n_0 d_h = 20K/F_h$ and equation 3.5 at $n_0 d_h =$

[2]The Townsend breakdown mechanism assumes, not only exponential growth of the electron avalanche, but also undisturbed electric field by the space charge and that the self-sustained current is controlled by secondary electron emission from the cathode. Combined with Townsend's semi-empirical formula, equation 3.1, it gives the well-known Paschen curves for the breakdown voltage.

$r \ln(1/\gamma + 1)/F_c$.

The point for which equations 3.3 and 3.5 are equal gives the envelope for the minimum voltage and $n_0 d_h$ for any geometry for which confinement of the discharge to the *hot* layer is assured (for streamer breakdown condition of *hot* layer) (in red on Figure 3-2(a)):

$$n_0 d_h|_{env}(\text{gases}, N_c, r, K) = r \exp\left(\frac{G_c/G_h \ln(F_h r/(20K)) - C_c(N_c + r)/K}{(N_c + r)/K - G_c/G_h}\right). \tag{3.6}$$

Finally, at the left branch of the curve in equation 3.3, the contribution of the cold layers may enable the streamer criterion to be met when the ionization in the *hot* layer alone does not suffice. In this case, the first breakdown will occur in the full gap if Meek's condition is reached:

$$N_c \alpha_c d_c + \alpha_h d_h \simeq 20, \tag{3.7}$$

$$\text{with,} \quad E = \frac{V}{d_h + N_c d_c}.$$

Introducing the values for the ionization coefficients, for voltages over $V_{str,h+c}$, there will be breakdown in the full gap:

$$V_{str,h+c}(\text{gases}, N_c, r, K, n_0 d_h) = \frac{1}{Kr} \frac{G_h n_0 d_h (N_c + r)}{\ln(1/\beta)}, \tag{3.8}$$

with β being the solution to equation 3.9:

$$\beta + N_c \frac{K F_c}{r F_h} \beta^{K G_c/G_h} = \frac{20K}{F_h n_0 d_h}. \tag{3.9}$$

For large $n_0 d_h$, $V_{str,h+c} \to V_{str,h}$, and the contribution of the cold layer is not needed.

3.2.3 Test cases

Two different test cases are analyzed and the analytical prediction is presented in Figure 3-2.

The first case presents different composition in the layers: a *hot* layer of helium surrounded by two *cold* layers of nitrogen, Figure 3-2(a). Helium and nitrogen were chosen

since they have fairly distinct coefficients in the Townsend ionization formula: e.g. for helium, $F = 9.32{\cdot}10^{-21}m^2, G = 105Td$, and for nitrogen, $F = 3.73{\cdot}10^{-20}m^2, G = 1062Td$ [166]. The temperature in this case was uniform, $K = 1$, and the thickness of the layers equal, $r = 1$.

The second case considers uniform composition but two layers at different temperatures, Figure 3-2(b). Helium was chosen as the working fluid since it requires lower applied voltages to create the electrical discharge (compatible with the available equipment, for experimental comparison) and also facilitates the production of more uniform discharges. In this case, the temperature ratio between the *hot* and *cold* layers is chosen as $K = 3$, and the thickness of both layers is again taken equal, $r = 1$.

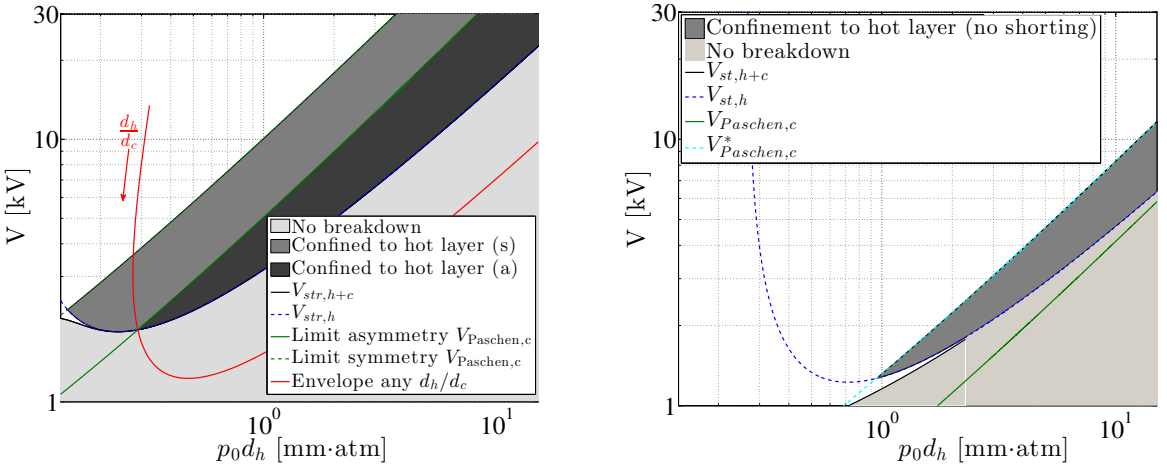

(a) Composition: N_2-He-N_2 ($N_c = 2$, r=1, $K = 1$). (b) Temperature: He ($N_c = 1$, r=1, $K = 3$).

Figure 3-2: Breakdown as a function of voltage and pressure times *hot* layer thickness.

In the plots, p_0 is used instead of n_0 as the values are easier to interpret ($T_0 = 293K$ is used for the conversion). The dark gray shade corresponds to the region in which the discharge can be confined to the *hot* layer; the light gray shade refers to no breakdown; and the white shade indicates electrical breakdown in the full gap. The red envelope indicates the most restrictive limit of gas-confined discharge for any r.

All in all, the model predicts that, depending on the temperature ratio of the layers, the gases present, the ratio of thicknesses of the layers and the applied voltage, three different situations can take place: no breakdown, breakdown of the hot layer alone and breakdown of the full gap. Although the model is crude, the trends are expected to hold and the

parameters are used to guide the experiments in Sections 3.3 and 3.4.

3.3 Experiments in N_2-He layers

To validate the hypothesis of selective breakdown of a region of gas by choice of composition and electrical parameters, an experiment using the nitrogen-helium-nitrogen structure analyzed in Figure 3-2(a) is here presented. The experimental setup used is that described in Section 2.2. The experiment is performed at atmospheric pressure and $d_h = 2mm$ so that, for applied voltages somewhere in the region between ∼5-18kV, selective breakdown of the helium layer alone should be achieved.

The plasma was created using repetitive pulsed nanosecond discharges, RPND (Section 2.4.2). The high voltage and the short duration of the discharge favor the streamer breakdown mechanism, while ensuring its transient nature.

3.3.1 Selective breakdown of the helium layer: observations

The structure of the plasma, when using positive voltage pulses of 15kV amplitude as seen by the discharge cell, ∼20ns duration, at a repetition rate of 3kHz, is shown in Figure 3-3.

It can be appreciated how the discharge was confined to the helium layer, as predicted. In the figure, the anode is the bottom electrode and the grounded cathode, with a glass dielectric in front, is the top one. There is no glass dielectric in front of the anode, which is directly in contact with the gas jet. The direction of the gas streams is coming out of the photograph and the image corresponds to the plane of the electrodes, that is looking from downstream of the flow to the jets (as represented by the red line in Figure 2-1).

The discharge had a filamentary appearance, with filaments traveling along x or streamwise of the bulk flow (referring to the axis in Figure 3-1(a)), and the filaments were clearly seen to change direction as much as 90° to y-directed or streamwise, when they reached the He-N_2 mixing layer. Filaments traveling upstream of the bulk flow were the most common since the composition profile is sharper and there is a higher concentration of helium (downstream mixing is enhanced and the composition profile is more diffusive).

Even though the discharge developed in the helium layer alone, the filamentary structure

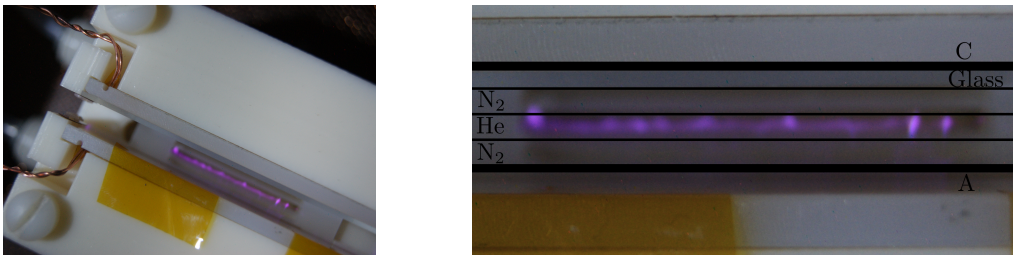

(a) Direct photo. (b) Zoom in discharge region.

Figure 3-3: Helium confined plasma in a N_2-He-N_2 structure, using RPND of 15kV amplitude at 3kHz. The lines between the helium and nitrogen regions have been added for ease of visualization. In reality, no physical boundary exists there.

can be explained by some mixing with nitrogen. This is not something unexpected: [58] cites how even if only ∼1% of air is added to helium, the discharge transitions from uniform to filamentary. Measurements of the actual composition are presented in Section 3.3.5.

Further confirmation of the phenomenom was obtained by varying the roles of the nitrogen and helium layers. The applied voltage pulses were as in the previous case. Photographs of the different combinations tested are shown in Figure 3-4, the confinement of the discharge to the helium layer can be appreciated in all cases.

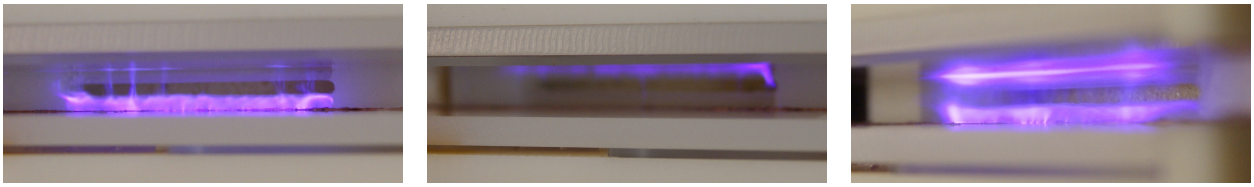

(a) N_2-N_2-He. (b) He-N_2-N_2. (c) He-N_2-He.

Figure 3-4: Helium confined plasma for different N_2/He combinations, using RPND of 15kV amplitude at 3kHz. Labeling of the gases starts from the top electrode, the cathode.

Removing the glass slide from the cathode did not change the results, Figure 3-5. In these photographs, the applied voltage amplitude, as seen by the discharge cell, was 10kV.

Tests replacing nitrogen by air led to the same observations. However, if the flowing air was replaced by stagnant (ambient) air, the *cold* layers were perforated by a nanosecond spark that spread along the cathode-side glass barrier once it reached it (characteristic of the impact of a streamer upon contact with a cathode dielectric [152]). This is shown in Figure 3-6, using 15kV applied voltage at 3kHz. Therefore, there is an essential role of the convective transport, both of charged species and heat when the repetitive unipolar strategy

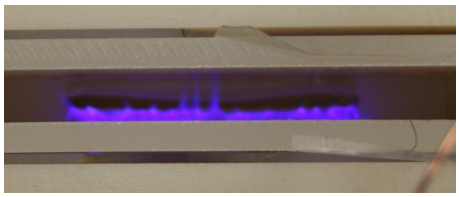

(a) N_2-N_2-He.

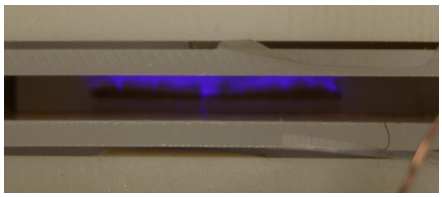

(b) He-N_2-N_2.

Figure 3-5: Effect of removing the glass slide for different N_2/He combinations, using RPND of 10kV amplitude at 3kHz. Both electrodes are directly in contact with the gas jets.

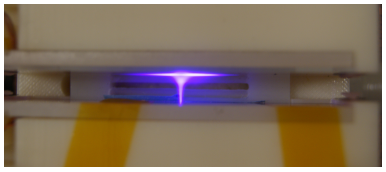

Figure 3-6: Helium injected into stagnant air: nanosecond spark. In this case, there was no flow of nitrogen.

is used, in addition to the need of sharp gradients.

3.3.2 Electrical measurements of the RPND strategy

Representative voltage and current waveforms of these experiments are shown in Figure 3-7.

In all cases, the current measured for these *floating* plasmas, is mainly capacitive, since the discharge does not bridge the gap and the conduction current becomes negligible compared to the high value of the capacitive current measured (∼30A).

The estimated capacitance from these measurements, is C ≈8pF. As expected, the capacitance is independent of whether or not there is a plasma, of the voltage and of the pulse repetition frequency.

This capacitance includes, not only the capacitance of the discharge cell, but also that of the wires connecting the electrodes to the coaxial cable from the power supply, the voltage probe and the uncompensated part of the oscilloscope itself. Note that all these capacitances are connected in parallel so they add up. Actually, the contribution of the discharge cell is very small as compared to the capacitance of say, the voltage probe alone (3pF).

A theoretical estimate of the capacitance of a long rectangular plate strip capacitor

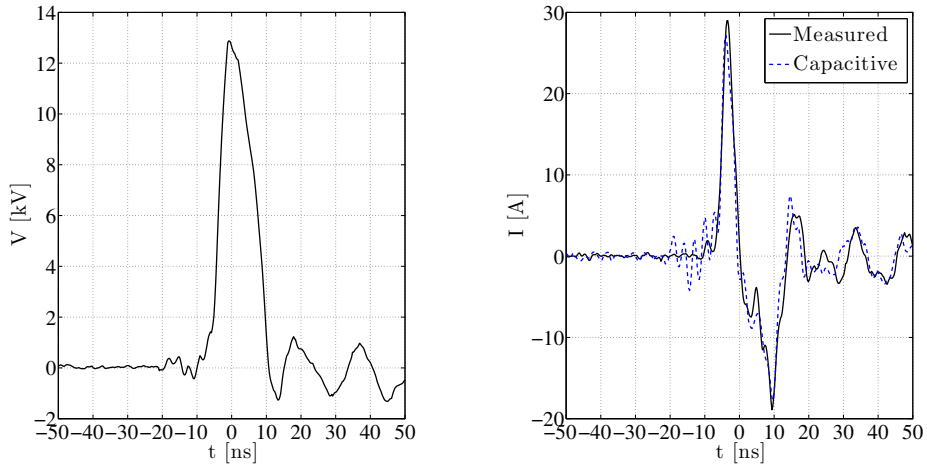

(a) Voltage. (b) Current.

Figure 3-7: Representative measurements of voltage and current as a function of time using RPND. The capacitive contribution of the current is plotted in blue for comparison.

including fringing fields (correction for the finite width) is given by [133] as:

$$C = C_0 C_f = \varepsilon_0 \frac{wL}{d} \cdot C_f \left(\frac{d}{w} \right), \tag{3.10}$$

where C_0 is the infinite parallel plate capacitance, L and w are the length and width of the electrode strips respectively, d is the distance between plates, and C_f is the correction to account for fringing effects, which is a function of the aspect ratio d/w and is tabulated in [133]. For the experimental parameters here considered, $C \approx 0.6pF$, and the maximum energy that can be stored by this capacitor (for voltage pulses of 15kV) is $\sim 70\mu$J/pulse.

3.3.3 Exploratory optical emission spectroscopy measurements

An exploratory time-integrated spectrum of the emission of the helium-confined discharge in the range 300-800nm is shown in Figure 3-8, using the 300grooves/mm grating (Section 2.7.3). The emission corresponds to the center of the helium-rich layer (N_2-He-N_2 case).

The dominant emission comes from the second positive system (SPS) of molecular nitrogen, $C^3\Pi_u - B^3\Pi_g$, since even a small fraction of nitrogen in the helium stream makes this emission dominant. The first negative system (FNS) of N_2^+, $B^2\Sigma_u^+ - X^2\Sigma_g^+$, is also observed; which occurs readily in the presence of excess helium [154]. The helium lines are weaker than

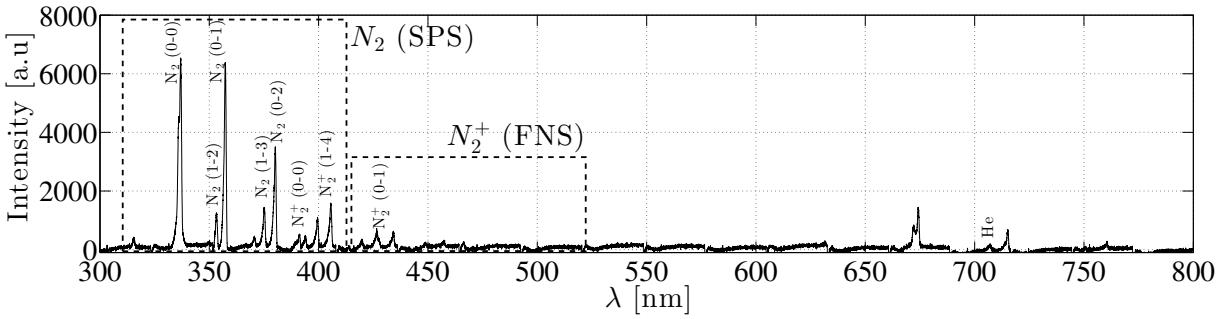

Figure 3-8: Time-integrated spectra of the helium-confined discharge (using RPND).

the nitrogen bands [32], and only the line at 706.5nm could be identified using the present grating and exposure of the camera. Using the 1800grooves/mm grating and increasing the exposure, the helium lines at 587.5nm and 667.8nm could also be distinguished.

When using air instead of nitrogen, the OH $(A-X)$ band, ∼306nm, and the OH Meinel band, ∼728nm, which usually indicates the presence of ozone [154], could also be seen.

The spectra here measured can be compared to spectra for atmospheric pressure helium plasma jets (APPJ) emerging into ambient air, as reported by [235]. As in the present work, the emission spectrum reported in [235] was dominated by the SPS of molecular nitrogen and the N_2^+ bands, and the only helium line detected was that at 706.5nm.

These measurements confirm that the center of the jet cannot be considered pure helium, although the confinement to the helium-rich layer is still achieved. This will be further explored in Sections 3.3.5 and 3.3.6.

3.3.4 Experiments using AC voltage

A final test, to illustrate that gaseous insulating layers can act as a barrier to the discharge, was performed using AC voltage instead of nanosecond-duration pulses. This strategy is the one generally used with traditional dielectric barrier discharges (DBD).

Experiments with and without the glass slide were performed and analogous conclusions were reached. For these experiments, sinusoidal voltage is applied to the bottom electrode and the top electrode is grounded. The peak-to-peak AC voltage is 9kV (Figures 3-9(a) and 3-9(b)) and 7kV (Figures 3-9(c) and 3-9(d)), both at ∼60kHz.

Since for the configuration with two layers (N_c=1, Figure 3-1(b)) used in this part, and

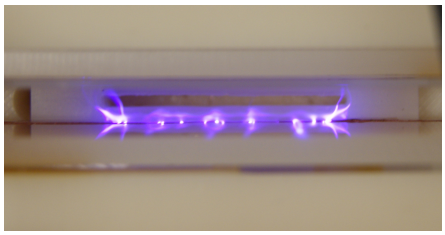

(a) N_2-N_2-He, glass dielectric on top.

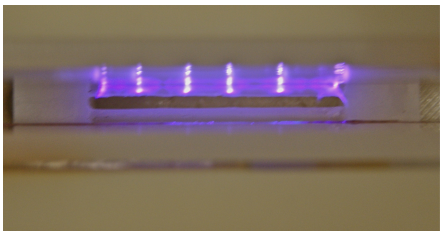

(b) He-N_2-N_2, glass dielectric on top.

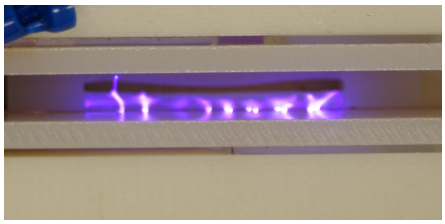

(c) N_2-N_2-He, no glass dielectric.

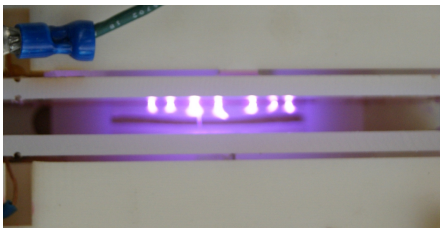

(d) He-N_2-N_2, no glass dielectric.

Figure 3-9: N_2/He layers with AC voltage (at 60kHz and 7-9kV peak-to-peak). Labeling of the gases starts from the top, grounded, electrode. The bottom electrode is the powered one.

when applying AC voltage, the helium layer will be for every half-cycle in contact with the cathode, the conditions were selected to have *local* Townsend breakdown in the helium layer instead of *local* streamer breakdown. That is, when using an applied voltage of 3.5kV and 4.5kV (peak values) over the 6mm gap at ambient temperature and atmospheric pressure, the reduced electric field takes values of 24Td and 31Td respectively so that $\alpha_h d_h$ is below Meek's criterion ($\alpha_h d_h$=20) but above Townsend's condition ($\alpha_h d_h = \ln\left(\frac{1}{\gamma}+1\right)$) for any γ in the range [0.01,1]. Due to the very different ionization coefficients, in the nitrogen layer the condition is far from met so that it should act as a barrier to the discharge as desired.

Photographs of the discharge are shown in Figure 3-9.

For the case of the nitrogen in contact with the powered electrode, Figures 3-9(b) and 3-9(d), the discharge appeared to be self-organized and pattern glow-like [49]. The self-organized pattern, which remained stable over a long time of continuous operation, consisted on several mm-sized plasma channels (the width of the individual emission regions is of the order of the discharge gap), which were spatially symmetric. Their length (in the direction of the field) was that of the helium stream, the emission ending abruptly at the interface with the nitrogen jet, showing the analogous behavior to a traditional DBD.

For helium in contact with the powered electrode, Figures 3-9(a) and 3-9(c), some unorga-

nized filaments with much thinner luminous regions and a random-looking pattern appeared. These *streamers* were anchored to the *edge* of the strip electrodes. It is not far-fetched to postulate that this is a consequence of the finite size of the electrodes, since the field enhancement at those borders could result in the Meek criterion being reached locally.

Thus, by positioning the insulating nitrogen barrier on the powered side, streamer formation at the sharp electrode border can be avoided and the formation of a patterned-glow is more easily put into practice. Still, in both cases the full confinement of the plasma emission to the helium-rich layer was achieved, and the nitrogen side was *clean*.

When using AC, as compared to RPND, the slower rate of change of the applied voltage translates into a lower magnitude of the displacement current measured. This makes the current waveforms, for a case without plasma and a case with plasma, differentiable.

Representative current and voltage waveforms, for a case without plasma, are shown in Figure 3-10. In this case, the measured current is again mainly capacitive. The measurement was made by injecting nitrogen in all three ports.

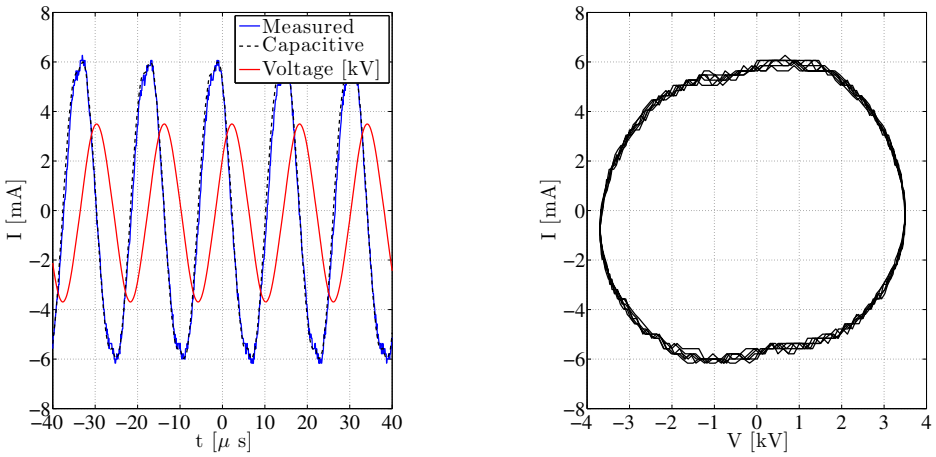

(a) Waveforms in time.

(b) Current vs. voltage.

Figure 3-10: Current and voltage plots with AC power and no discharge.

Representative current and voltage waveforms, for a case with breakdown in the helium-rich layer, are shown in Figure 3-11. In this case, the helium layer was in contact with the grounded electrode (to avoid border effects) and the nitrogen with the powered electrode, as shown in Figure 3-9(d). The current shown is including the displacement contribution (total measured current). It can be appreciated how there is only one current peak superimposed to

the sinusoidal contribution per voltage-cycle, suggesting that the distinct plasma channels of Figure 3-9(d) occur simultaneously, consistently with the operation of patterned-glow discharges. Also note the asymmetry in the operation for the positive and negative voltage (the conduction current pulses are marked by arrows). The discharge is on (conduction current pulse) for the positive polarity, when the cathode is in contact with the helium layer.

If the helium is instead placed in contact with the powered electrode (e.g. Figure 3-9(c)), the curves are as the ones presented but inverting the roles of the positive and negative voltages, i.e. they look symmetric with respect to V=0V and I=0A and the conduction current pulses occur for the negative polarity.

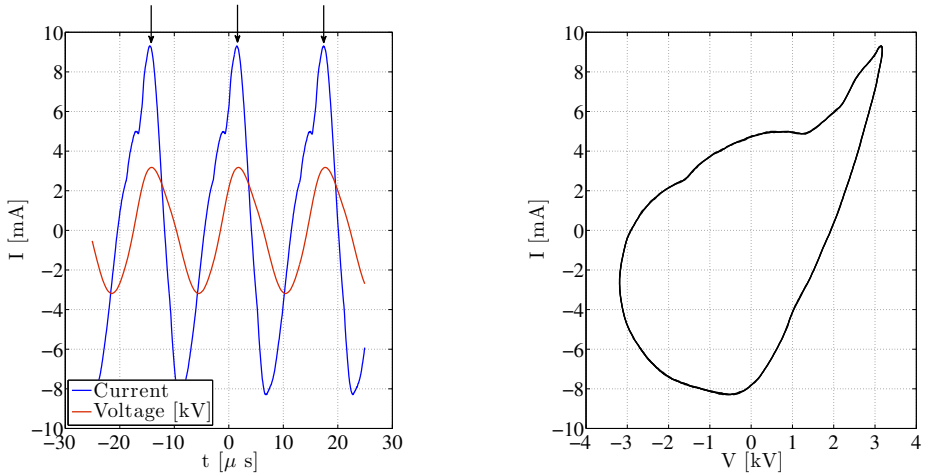

(a) Waveforms in time.

(b) Current vs. voltage.

Figure 3-11: Current and voltage plots with AC power and visible discharge. Case with the helium-rich layer in contact with the grounded electrode, as shown in Figure 3-9(d).

The asymmetry in the operation with the voltage polarity, when operating under local Townsend breakdown conditions, may be explained by the differences between gas barriers as compared to solid barriers. More specifically, the mechanism of *secondary electron emission* at the mixing layer interface between the working gas and the dielectric gas is unclear, or may even be inexistent, and it is required for the discharge to be self-sustained. Without it (or a replacement phenomenon), a Townsend discharge will decay. If there is no secondary emission (or equivalent) at the mixing interface between the two gases, when using a single-barrier discharge, the discharge will only be ignited every other half-cycle, when the electrode directly exposed to the helium is the cathode so that secondary emission from the metallic surface

can ensure self-sustainment. In the other half-cycle, when the electrode directly exposed to the helium is the anode, there is no secondary emission and therefore no discharge. This explanation is consistent with the current measurements but it should be further explored.

3.3.5 Environment measurements

The spectroscopy measurements (Section 3.3.3) reveal that there is some mixing with nitrogen in the region where the discharge develops. Measurements of the actual composition were obtained, using the Schlieren technique described in Section 2.6.1 and Appendix A, for the two cases considered in the experiments: N_2-N_2-He and N_2-He-N_2.

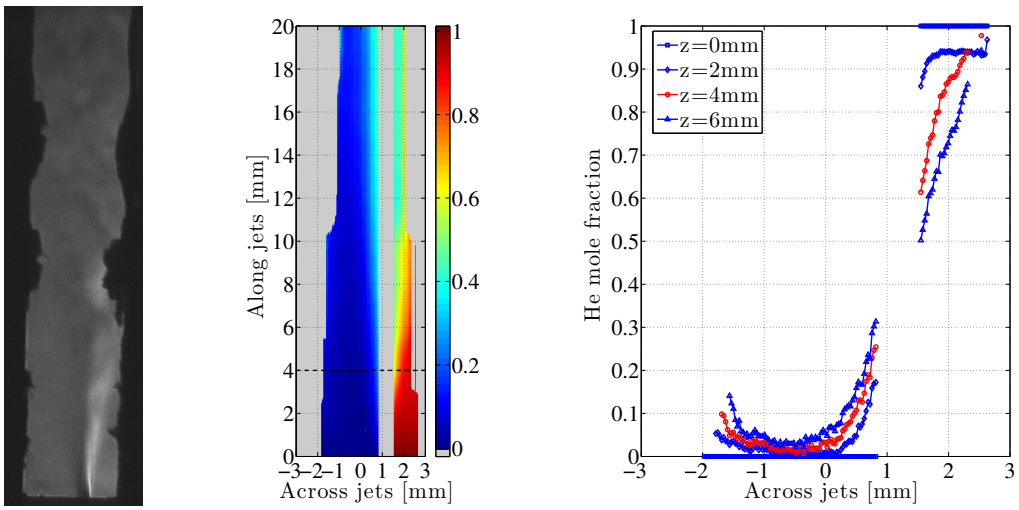

(a) Raw. (b) He mole fraction map. (c) X_{He} profile across jets, different z.

Figure 3-12: Helium mole fraction, from Schlieren imaging, for N_2-N_2-He sandwich.

For the case of the N_2-N_2-He jets, a 2D map of the helium mole fraction is shown in Figure 3-12(b). The gray regions are areas where the composition could not be determined, either because integration along the jets was interrupted by the presence of a solid structure (e.g. bolts in the walls) or because a saturated gradient was encountered. It can be seen that the potential core is pretty long and, at the exit of the device, the composition cannot be considered uniform yet. Composition profiles across the jets, at different positions in the streamwise direction z (distance from the exit of the jets), are plotted in Figure 3-12(c). The one corresponding to the position of the electrodes is indicated in red (z=4mm): the composition in the center of the helium-rich layer is close to pure helium (X_{He} ~95%).

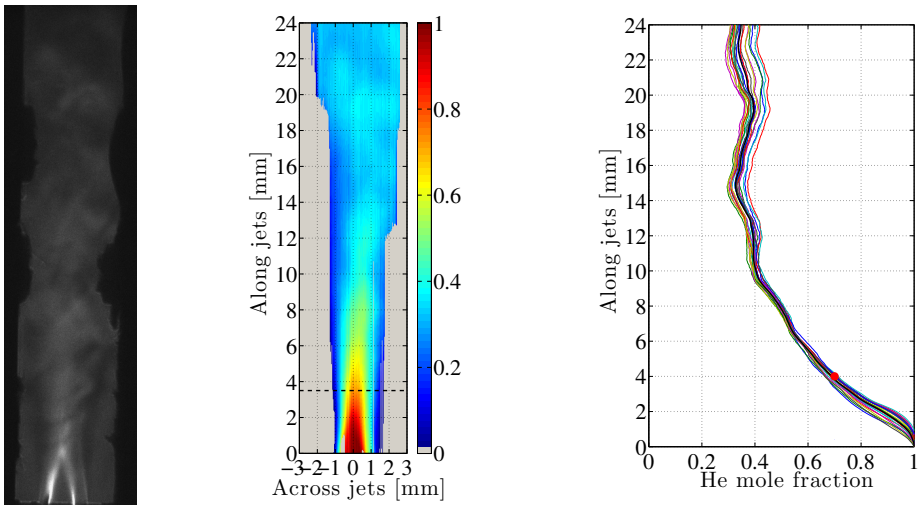

(a) Raw. (b) He mole fraction map. (c) X_{He} along jets, gap center.

Figure 3-13: Helium mole fraction, from Schlieren imaging, for N_2-He-N_2 sandwich.

For the case of the N_2-He-N_2 jets, a 2D map of the helium mole fraction is shown in Figure 3-13(b). Different profiles of the helium mole fraction along the jets, for a region 0.7mm wide in the center of the gap, are shown in Figure 3-13(c). At the jet exit, pure helium has been assumed (X_{He}=1) and, at the exit of the device, the composition obtained through the integration gives X_{He}=0.35, which is very close to the theoretical mixture obtained with the experimental parameters used. For these experiments, the potential core was shorter ∼1mm, and the composition at the electrodes position was ∼ 70% helium.

In short, for the N_2-N_2-He case, the ideal situation of pure gas (helium or nitrogen) in each layer is close to the experimental reality. For the N_2-He-N_2 case, the experimental composition profile is far less favorable than the ideal assumption. Still, confinement of the discharge to the helium-rich layer was observed (see Section 3.3.6 for further discussion).

3.3.6 Discussion

All in all, the convective nitrogen-rich layers *stopped* the filamentary discharges, behaving like a barrier to the discharge, and their appearance were reminiscent of a regular DBD where the *cold* layers played the role of the dielectrics. For helium-rich layers, with mole percentage of helium ∼70-100%, confinement to the helium layer was achieved when using both RPND and AC voltage.

Although it is tempting to compare these gas-confined barrier discharges to a regular DBD, it is important to recall the main differences that exist, as compared to solid dielectrics (an example of a repetitive unipolar nanosecond-pulse DBD can be found in [108, 205]).

First of all, for the case of gaseous layers, there is a resistive component introduced, since the charged particles can drift through them, albeit not producing any further ionization. This introduces a notable asymmetry in the behavior of the nitrogen layers as compared to solid dielectrics, which is due to the difference in mobility of the electrons and the ions. More specifically, for the nitrogen layer in contact with the cathode, positive charge can accumulate in the He/N_2 mixing layer (Figures 3-4(a) and 3-5(a)), whereas for the nitrogen layer in contact with the anode, the electrons drift away at a shorter time scale (Figures 3-4(b) and 3-5(b)).

Second, when using gaseous dielectrics, bulk transport of the flow (convection) and charge transport (drift and diffusion across the *cold* layers) contribute to the depolarization before the next pulse is applied. For the experiments here performed, the flow residence time within the extent of the electrodes ($\sim$0.4ms) is of the same order as the inverse of the pulse repetition frequency (3kHz) so that a given volume of gas only *sees* one applied voltage pulse.

From the experimental results, another aspect that requires explanation is the ionization properties of the helium-rich layer when there is mixing with nitrogen; as well as the dominant nitrogen emission in all cases. To that end, the Boltzmann equation for the electron energy distribution function (EEDF) was solved, using BOLSIG+ [72], for the case of 120Td and as a function of the helium mole fraction. The results are shown in Figure 3-14.

On the one hand, from this figure, it can be appreciated how most of the energy is spent in the excitation of N_2 even for helium mole fractions as high as $X_{He} \simeq 0.95$. Therefore, the dominant emission comes from nitrogen even when there is very little nitrogen present.

On the other hand, in the analytical model of Section 3.2, used to guide the experimental parameter choice, the ionization in each layer was assumed to be that of helium, in the helium-rich layer, and that of nitrogen, in the nitrogen-rich layer. However, in some of the actual experiments, mixing could not be avoided.

Actually, for $\sim$70% helium, Figure 3-14(a) shows that ionization of nitrogen molecules is more likely than ionization of helium atoms. Moreover, the energy spent in ionization of

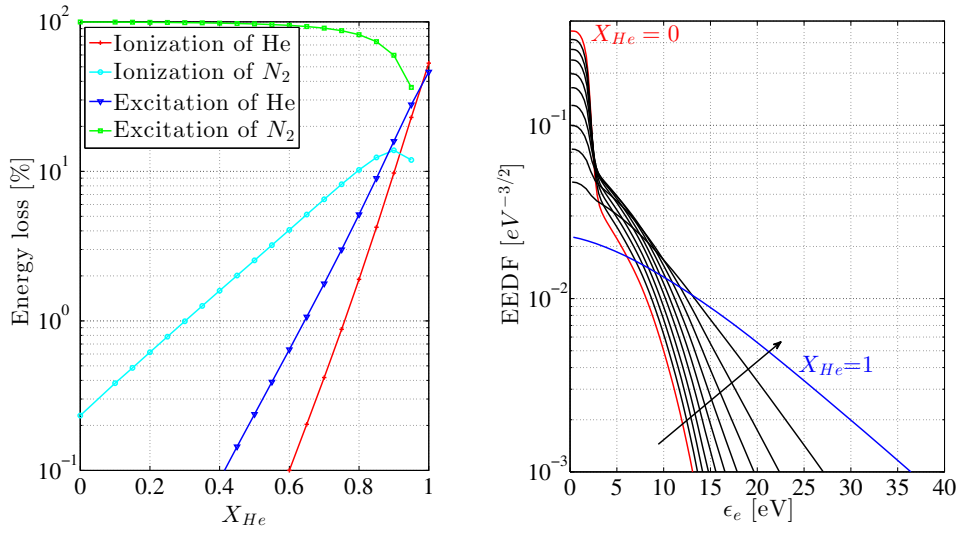

(a) Electron energy loss fraction.

(b) EEDF.

Figure 3-14: Electron impact processes in He-N_2 mixture as a function of the mole fraction of helium in the mixture, at 120Td. Calculations have been performed using BOLSIG+.

nitrogen is greatly enhanced by the presence of excess helium: for pure nitrogen only ∼0.2% of the energy goes to ionization of nitrogen, whereas for 70% helium, this fraction amounts to ∼7% (explanation below). Therefore, the helium-rich layer still presents significantly enhanced ionization with respect to the nitrogen-rich layers, albeit the ionization being of the nitrogen molecules and not the helium atoms.

Finally, the fact that nitrogen ionization is enhanced with respect to that of pure nitrogen, when helium is added, may be surprising but can be explained looking at the EEDF for the different mixtures, see Figure 3-14(b). The EEDF in pure He has a higher mean energy than in pure N_2, where the strong vibrational excitation at about 2eV clips the distribution beyond that energy. Hence, the ionization of nitrogen molecules presents a maximum at some non-zero value of X_{He}: as a result of the competing effects of the number of available targets and the number of electrons at high energy (longer tail).

Note that, in addition, there will be Penning ionization that has not been considered, and whose rate depends on X_{N_2} and the excited helium produced.

All in all, the chemistry of the helium layer is strongly influenced by the nitrogen that has leaked in, which significantly complicates the interpretation of the results. To eliminate this unnecessary complication, additional experiments with uniform composition but layers

at different temperatures are presented in Section 3.4.

3.4 Experiments in a temperature gradient

Non-isothermal experiments with uniform composition are reported in this Section, in order to eliminate the effect of the helium-nitrogen chemistry discussed. Helium was chosen as the working fluid since the applied voltage required for atmospheric breakdown is lower (and compatible with the available equipment). The parameters used are the ones in Figure 3-2(b): in this case there is only one *cold* layer (Figure 3-1(b)) and the temperature ratio between the two layers is $K = 3$. The experimental setup used is that described in Section 2.3, where the opposed jets are momentum balanced so that the stagnation plane lies in the middle of the gap ($r = 1$), the exit velocity of the cold stream is 2.5m/s, and the top jet is heated to 900K. RPND, of different amplitudes, at 3kHz, are applied to the bottom electrode (*cold* side) and the top electrode (*hot* side) is the grounded cathode[3].

The guidelines from Figure 3-2(b) can be used to choose the experimental region to be studied: the actual region of confinement to the heated layer will be somewhere in between the two considered extremes. On the one hand, perfect shorting of the *hot* layer does not allow to sustain confinement; on the other, an infinite resistance gives an overestimated region of confinement of ∼4-8kV.

The transition from confined discharge to the heated layer, to breakdown of the full gap, was experimentally observed by increasing the applied voltage, as shown in Figure 3-15.

In all cases, the discharge observed had a diffuse and uniform glow-like appearance (at least to the naked eye) as the working gas was helium. The plasma emission was confined to the helium jets, and the limiting streamlines (between the helium opposed jets and the ambient air) could be sharply identified visually.

For low enough voltages, the plasma emission was limited to the top hot jet (Figure 3-15(a)) and it extended to the approximate position of the stagnation plane. By increasing the applied voltage, the emission suddenly bridged the full gap although the two regions,

[3]The roles of the cathode and anode could not be inverted due to the heater inserted in the top tube: the top electrode always had to be grounded, since it was very close to the powered heater, to avoid sparking between them.

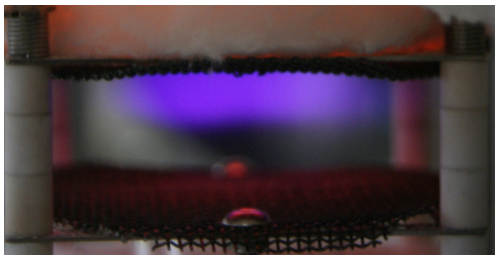

(a) 7kV peak voltage.

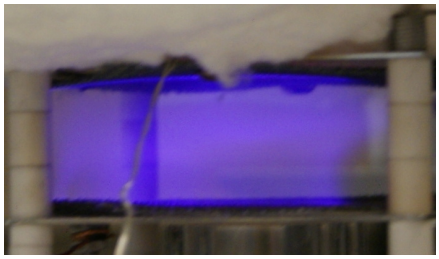

(b) 8.9kV peak voltage.

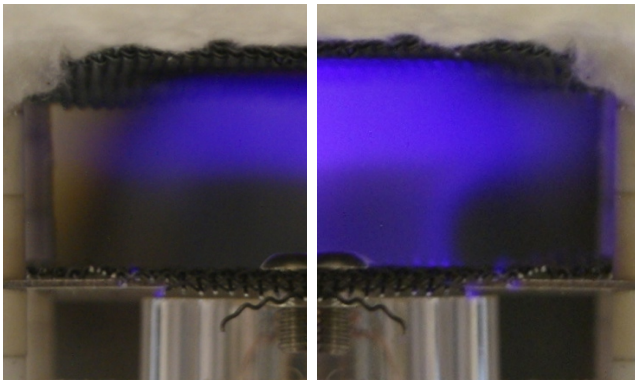

(c) 7.4kV → 12kV.

Figure 3-15: Effect of increasing the applied voltage for RPND in temperature gradient. Top jet is at 900K and bottom jet at ambient temperature. Experiments in helium. Pulse repetition frequency is 3kHz.

of the *hot* and *cold* jets, could still be clearly identified due to the stronger emission of the heated region (Figure 3-15(c)). If the voltage is decreased to the initial value, confinement to the *hot* stream is recovered.

Measured voltage and current waveforms were of the form of the ones shown in Figure 3-7, and so are not duplicated here. The measured current was mainly capacitive, even for full breakdown of the gap: this is a well known characteristic of diffuse discharges when using RPND (e.g. [143] observed a glow-like discharge when applying RPND to a point-to-point electrode system in air at atmospheric pressure and 1000K, which he named the D-regime, that had negligible conduction current as compared to the displacement one). The capacitance estimated from these waveforms was again higher than the one corresponding to the discharge cell alone. An estimate for this square parallel plate capacitor (including fringing effects), also due to Nishiyama et al. [134], gives $C \approx 2.4pF$. This capacitance corresponds to a maximum stored energy (for voltage pulses of 7kV) of $\sim 60\mu$J (this value will be verified in Section 6.3.2, since the electrical response of this system is of interest in

Chapter 6).

Experiments with AC voltage, substituting the RPND strategy (as in Section 3.3.4), were attempted but the appearance of an AC arc, that rotated around the rim of the nozzle, could not be avoided. This is most likely due to the less sharp gradient (Figure 3-16), compared to the experiments with He-N_2 layers, the smaller difference between ionization coefficients in the different regions, and the existence of a stagnation region (close to the rim) in which heat and ionized species could accumulate.

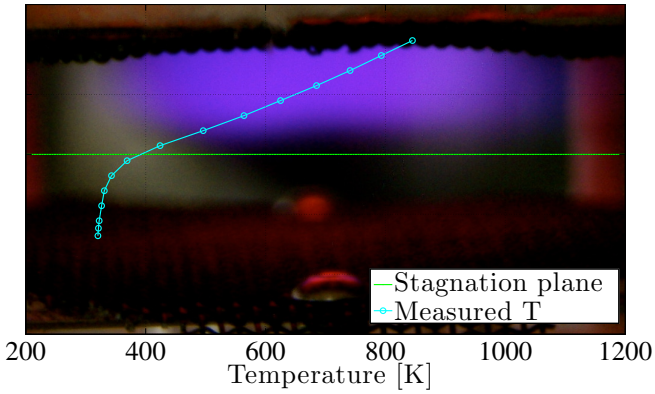

Figure 3-16: Thermocouple measurement of the temperature field superimposed to direct photo of the plasma emission. Measurement is shown by the cyan line.

3.5 Summary of findings and implications

In this Chapter, a novel model for the study of RPND in non-uniform gases was presented. It was proposed that, in such a situation, electrical breakdown could be confined to regions of favorable ionization and that *cold* regions of gas (in a generalized sense) could behave as barriers to the discharge.

The hypothesis was confirmed experimentally using differences in composition (helium and nitrogen) and differences in temperature (with uniform helium composition). The experiments in helium/nitrogen layers confirmed that filamentary-like breakdown using RPND could be confined to the helium stream even for high degree of mixing (purity of the helium stream going from ∼70-100%). The experiments in uniform helium composition but with

opposed non-isothermal jets, showed that the same idea applied to glow-like discharges (uniform at least to the naked eye), that could be confined to the high temperature region for low enough applied voltages. The transition from *hot* layer confinement to breakdown of the full gap occurred sharply by increasing the applied voltage.

For the helium/nitrogen experiments, the confinement to the helium-rich stream was also observed when applying AC voltage at high frequency (60kHz).

Interesting properties of these *floating* plasmas are related to the fact that contact with the electrodes is avoided. This allows to couple the energy to a specific region of the gas (by choice of fluid properties) and to have a purely non-thermal plasma with little heating and no erosion of the electrodes. Amongst other applications, which can benefit from a selective breakdown of a region within the flow field, is the application of RPND to a flame (this point is explored in Chapter 5). In the case of a flame, the flame front is the region of favorable ionization where the plasma can be coupled, which is precisely the region where the combustion reactions are taking place.

The main limitation of this structure with non-ionizing layers of gas, is the inherently low energy deposition per pulse; although it can possibly scale up by increasing the capacitance of the electrode system (in this case, the capacitance that matters is that of the pair of *effective plates* at the edges of the hot layer). More energy could also be coupled by using longer voltage pulses. In addition, the power can be increased by using a higher pulse repetition frequency.

All in all, these gas-confined barrier discharge plasmas can be interesting for applications that require a non-thermal nature, that avoids the nanosecond-spark. In this study we have provided a proof of concept, tailoring to a specific application will require detailed spatially and temporarily resolved studies of the chemistry induced and the species ionized. Recommendations for future work include detailed measurements of the spatial structure of the discharge including the time-dependent electric field and ions in the gap: confinement in this work has referred to the spatial structure of the emission, a more precise determination would rely on the rate of ionization.

Chapter 4

Model of the discharge development in a non-uniform environment

4.1 Introduction

In Chapter 3, experimental evidence of filamentary-like breakdown of a helium jet sandwiched between two nitrogen streams was presented, and it was argued that the differences in the ionization properties of the layers were sufficient to explain the experiments. In this Chapter, a numerical model of such a configuration is developed in order to provide a phenomenological description of the discharge evolution and help explain the experimental observations.

The structure of this Chapter is as follows. The self-consistent fluid model used for the development of the gas discharge is detailed in Section 4.2. Next, Section 4.3 presents 1D results of the numerical model for a nitrogen-helium-nitrogen GBD configuration. Finally, Section 4.4 links the model results to some of the experimental observations in Chapter 3.

Part of the discussion included in this Chapter was published, alongside with the composition gradient experiments of Chapter 3, in *Journal of Physics D: Applied Physics* [67].

4.2 Fluid model of the electric discharge

Although different models have been proposed for the numerical simulation of gas discharges, the most popular and widely used is based on a fluid model for, at least, each of the main

charged species present (electrons and dominant positive ions) coupled to Poisson's equation for the electric field. This fluid model is valid for both Townsend and streamer breakdown conditions and has been extensively used to describe discharges in homogeneous gases.

In the case of Townsend breakdown, numerical solution of dielectric barrier discharges (DBD) has been pursued by many researchers, specially within the Plasma Display Panel (PDP) community [15, 69, 70, 163, 164]. More recently, the same model was used to explore self-organized pattern formation under Townsend breakdown conditions [21,22,49,65,68,199].

In the case of streamer breakdown, first filament studies of individual streamers follow the same governing equations. However, numerical simulation is more complex as streamers are multi-scale phenomena that involve very non-linear dynamics [41, 71, 149]. In this field, work has been performed both for volumetric streamers and surface streamers upon impact with an electrode or dielectric barrier [152].

The fluid models proposed in the literature differ in the level of simplification introduced: e.g. number of species and reactions, model for the transport and reaction parameters, dimensionality... [50]. However, it has been shown that first order features, based on the drift-diffusion approximation, ionization by electron impact, and the local field approximation (see Section 4.2.1 for definitions) are sufficient to describe complex phenomena such as self-organized patterns in the glow mode [14] or the dynamics of streamer development in a non-attaching gas like nitrogen or helium [51]. This will be the approach taken in this work since the aim here is to clarify whether or not a streamer plasma can be blocked or deflected by an adverse ionization region (lower density or higher G in equation 3.1) and not to quantitatively reproduce the experimental results. The specifics of the model will be detailed in what follows.

4.2.1 The drift-diffusion approximation

The phenomena observed in Section 3.3 are three dimensional and the role of the bulk transport processes is essential to describe the repetitiveness and periodicity of the process (e.g. convection removes heat and avoids charge accumulation). However, at the timescale of a single voltage pulse, the bulk flow properties can be assumed frozen and the discharge evolution can be studied in the plane of the electrodes (ignoring the streamwise direction).

The governing equations that describe the discharge evolution, in the drift-diffusion approximation, are the ion and electron continuity equations (zeroth-order moment of the Boltzmann equation) coupled to Poisson's equation for self-consistency [41, 61]. The system of equations to be solved is given by:

$$\frac{\partial n_p}{\partial t} + \nabla \cdot \vec{\Gamma}_p = S_p, \tag{4.1}$$

$$\nabla \cdot (\epsilon_r \varepsilon_0 \nabla V) = -e(n_i - n_e), \tag{4.2}$$

where, the electron and ion fluxes $\vec{\Gamma}_p$, $(p = e, i)$, are given by the first-order moment of the Boltzmann equation in the drift-diffusion approximation, as:

$$\vec{\Gamma}_p = \text{sign}(q_p) n_p \mu_p \vec{E} - D_p \nabla n_p, \tag{4.3}$$

and n_p are the electron $(p = e)$ and ion $(p = i)$ densities, S_p is the source or net production term, V is the electric potential, $\vec{E} = -\nabla V$ is the electric field, μ_p are the mobilities, D_p are the diffusion coefficients, ϵ and ε_0 are the relative and the vacuum permittivities respectively and e is the electron charge (assuming singly charged ions).

The transport coefficients for the electrons, μ_e and D_e, are evaluated in the local field approximation [149, 166] as a function of the reduced electric field using BOLSIG+ [72]. The local field approximation assumes that the electron energy gain from the electric field is balanced by collisional losses *locally*, so that there is a one-to-one relation between the electron mean energy and the local electric field.

The mobility of the ions, μ_i, is taken as a constant from the literature [53] and the diffusion coefficient, D_i, is evaluated from the Einstein relation, $D = k_B T \mu / e$, in the assumption that the temperature of the ions is equal to the temperature of the gas.

For the source term, only direct electron impact ionization from the ground state is considered and the ionization coefficient's, α, dependence on the local electric field is given by Townsend's formula (equation 3.1), so that the source term becomes:

$$S_e = S_i = \alpha |\vec{\Gamma}_e|,$$

if $(-\vec{\Gamma}_e \cdot \vec{E} > 0)$, and zero otherwise, since, in the latter case the electrons are diffusing in the direction opposing the electric force and thus are losing energy [163].

In this analysis, the dynamics of the ionization front will be evaluated presuming that the electrical properties can be decoupled from the excited species kinetics. Although for a helium-nitrogen mixture other ionization processes such as Penning will also be taking place, the insight given in [17, 24, 126], for plasma bullets in helium-nitrogen (or air) mixing layers, showed that including Penning reactions provides slight quantitative differences in the results but is not critical for the streamer to propagate. Use of nitrogen, as compared to air, greatly simplifies the modeling since only one type of ion can be considered (N_2^+) and electron loss by attachment can be neglected (the fast attachment rate of electrons to oxygen in weakly ionized plasmas needs to be considered in air [44]).

In addition, the minimal streamer model is used [51] and the effect of photoionization and pre-ionization from previous pulses (required for cathode-directed streamer propagation) is substituted by a minimum background plasma density, which is common practice in the literature [149, 151]. Further justification in using this approximation is that, whereas it is generally accepted that the source of free electrons in nitrogen comes from photoionization, it is unclear where they come from in helium [17], where the discharge development was experimentally observed for the configuration under study (Section 3.3).

4.2.2 Layered gas environment

The propagation of streamers in non-uniform gases is a far less explored problem than in homogeneous gases or non-uniform electric fields [12]. Most of the numerical work on inhomogeneous media is due to the research on Atmospheric Pressure Plasma Jets [17, 23–25, 125, 126, 128, 130]; recently, to studies of streamer and sprite development in the upper atmosphere [109]; and, finally, to the literature on streamers in two-phase media [10, 27].

In principle, the presence of an inhomogeneous medium can be easily included into the drift-diffusion model as the timescales of the fluid flow are much slower than the streamer propagation time [110]. In this study the presence of a *layered* gas, such as the one pictured in Figure 3-1(a), is built in by prescribing frozen density and composition profiles, which affect only the transport and ionization coefficients. For the numerical evaluation, the boundaries

of the *hot* and *cold* layers do not need to be sharp, as in the analytical description of Section 3.2.2, and the impact of a diffusion profile can be introduced.

More precisely, the transport and ionization coefficients are no longer a function of the local electric field only, $E(x, y, t)$, but also of the composition and density of the gas at that point [129]. For a binary mixture, with mole fraction of the more easily ionizable species and density profile given by $X_h(x)$ and $n(x)$ respectively (coordinates refer to Figure 4-1), the dependencies have been assumed of the form ($p = i, e$):

$$\mu_p n = \left(\frac{X_h}{\mu_{h,p} n\,(E/n)} + \frac{1 - X_h}{\mu_{c,p} n\,(E/n)} \right)^{-1},$$

$$D_p n = \left(\frac{X_h}{D_{h,p} n\,(E/n)} + \frac{1 - X_h}{D_{c,p} n\,(E/n)} \right)^{-1},$$

$$\frac{\alpha}{n} = X_h \frac{\alpha_h}{n}\,(E/n) + (1 - X_h) \frac{\alpha_c}{n}\,(E/n)\,,$$

where local values apply. These forms are a direct consequence of the additivity of collision frequencies since $\mu,\ D \sim \nu^{-1}$ and $\alpha \sim \nu$. A smooth curve is used for both $X_h(x)$ and $n(x)$ with a thin mixing region so that the simplest models for the transition zone, i.e. Blanc's law for the transport coefficients [115] and Wieland approximation for the ionization coefficients [33], do not introduce significant modifications to the results (see discussion in Section 5.3.1).

4.2.3 Geometry of the problem

The discharge geometry and simulation domain is shown in Figure 4-1. The structure is similar to the geometry of the experiments reported in Section 3.3.1 but in the numerical experiment solid dielectric barriers are attached to both electrodes, in order to help highlight the similitudes between the *gaseous pseudo-dielectrics* and the solid dielectrics (removal of both solid dielectrics is explored in Section 4.3.4). The gaseous gap has the structure of the GBD, with either a sharp gradient in composition, $X_h(x)$, or in temperature, $n(x)$.

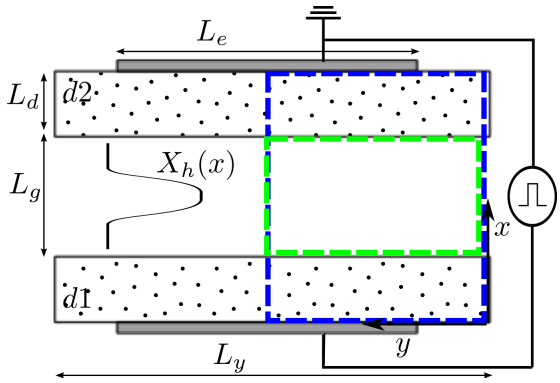

Figure 4-1: 2D geometry of the discharge cell. The blue region corresponds to the domain in which Poisson's equation is solved (gas gap plus solid dielectric barriers) and the green area to the region where the charged species equations are solved (gas gap alone).

For the 2D solution, symmetry is assumed and only half of the domain is solved for, for the 1D solution only the dependence on x is modeled. The simulation domain is divided into two. First, the domain constituted by the gaseous gap and both dielectrics is where Poisson's equation is solved (indicated in blue in Figure 4-1). Second, the gas gap alone is where the electron and ion continuity equations are evaluated (indicated in green in Figure 4-1).

4.2.4 Boundary conditions

Species continuity

The boundary conditions for the charged species' continuity equations are written in terms of the flux of particles.

In general, close to the wall and for distances comparable to the mean free path length, the fluid model fails and a kinetic description of the flux of particles to the wall becomes more appropriate. For an absorbing wall, such as the solid dielectrics in Figure 4-1, the expression for the flux normal to the wall is given in [49, 163, 164, 173, 199] as ($p = i, e$):

$$\vec{\Gamma}_p \cdot \vec{n} = a n_p \left(\text{sign}(q_p) \mu_p \vec{E} \right) \cdot \vec{n} + \frac{1}{4} v_{th,p} n_p, \tag{4.4}$$

where $\vec{n}$ is the normal vector pointing towards the wall, $v_{th,p}$ is the thermal velocity given by $v_{th,p} = \sqrt{\frac{8 k_B T_p}{\pi m_p}}$, and a is a switching function that is one when the drift velocity points towards the wall and zero otherwise. Note that this expression assumes a collisional sheath,

which is resolved with the fluid model.

Secondary emission is captured by adding a term to the electron flux given by equation 4.4, which is proportional to the ion flux arriving at the wall, that is:

$$\vec{\Gamma}_e \cdot \vec{n} = a n_e \left(-\mu_e \vec{E}\right) \cdot \vec{n} + \frac{1}{4} v_{th,e} n_e - \gamma_s \vec{\Gamma}_i \cdot \vec{n}, \tag{4.5}$$

where the constant of proportionality, γ_s, is the secondary emission coefficient of the surface.

At the left hand-side boundary (referring to Figure 4-1), symmetry conditions are imposed, since, by symmetry $\frac{\partial n_p}{\partial y} = 0$ and $E_y = 0$, the particle flux in the y direction becomes:

$$\vec{\Gamma}_p \cdot \vec{i}_y = 0. \tag{4.6}$$

This is the same condition as for the right hand-side boundary (referring to Figure 4-1), for no particles allowed to leave the discharge cell (not necessarily a physical condition).

Note that no boundary conditions are imposed at the mixing layers between the different gas streams and the equations are solved continuously in all the gas gap.

Electric potential

Poisson's equation, equation 4.2, needs to be solved within the gas region where a net space charge, $e\left(n_i - n_e\right)$, exists and, within the solid dielectrics, where it is simplified to Laplace's equation. The boundary conditions at the electrodes are given by the imposed potentials, $V = 0$ at the grounded cathode, and $V = V_{\text{app}}(t)$ at the powered anode.

As was the case for the fluid equations, boundary conditions at the left hand-side are given by symmetry and at the right-hand side (referring to Figure 4-1) by zero electric flux coming out of the discharge cell (not necessarily a physical condition). Both conditions are reduced to: $E_y = 0$.

In addition, at the solid dielectric-gas interfaces, Gauss's law needs to be satisfied:

$$\left(\epsilon_d \varepsilon_0 \vec{E}^{\text{dielectric}} - \varepsilon_0 \vec{E}^{\text{gas}}\right) \cdot \vec{n} = \sigma_{\text{s}}, \tag{4.7}$$

where $\vec{E}^{\text{gas}}$ and $\vec{E}^{\text{dielectric}}$ are the electric field, at the interface, in the gas and solid dielectric

sides respectively and σ_s is the surface charge accumulating on the solid dielectrics. σ_s is given by the flux of particles arriving to the wall:

$$\sigma_s = \int_0^t e \left(\vec{\Gamma}_i \cdot \vec{n} - \vec{\Gamma}_e \cdot \vec{n} \right) dt, \tag{4.8}$$

where it has been assumed that the surface charge stays where it is deposited and the integrand corresponds to the conduction current density.

4.2.5 Numerical solution of the equations

The three partial differential equations (equations 4.1 (2) and 4.2) have been discretized using a finite element approach, for the continuity equations, and a finite differences approach, for Poisson's equation; where the particle fluxes have been modeled using a Scharfetter-Gummel exponential representation [176].

The system of equations has been solved by alternating the solutions of the continuity and Poisson's equations using a semi-implicit scheme as proposed by [71]. A rectangular cartesian grid has been used in the discretization of the equations. Further details of the numerical model, as well as numerical verification and physical validation by comparison with some cases reported in the literature, are presented in Appendix C.

4.3 Numerical results of the GBD model

In this Section, the fluid model described in Section 4.2 (the numerical implementation is detailed in Section C.1) is used to simulate the gas-confined barrier discharges experimentally observed in Chapter 3. In particular, the model evaluates the evolution of a first filament during the high voltage pulse application and immediately after the voltage pulse ends. Since the goal of this part is to provide a phenomenological description of the discharge development, and not to reproduce the experimental results, the dimensions of the discharge cell used are smaller than in the experiments to reduce computational time. Additionally, a longer voltage pulse was selected to clearly observe the propagation dynamics of the ionization front once it reaches the helium/nitrogen mixing layer.

4.3.1 Parameters for the numerical experiment

The geometry used for the numerical evaluation is that presented in Figure 4-1, where the gas gap is L_g=3mm long and the solid dielectrics are L_d=0.5mm thick, with a relative permittivity of $\epsilon_d = 5$ and a secondary emission coefficient of $\gamma_s = 0.1$.

The gas is at atmospheric pressure and ambient temperature, $n(x)$ is uniform, and the gas composition varies across the gas gap from pure nitrogen, to pure helium, and back to pure nitrogen, according to the profile for $X_h(x)$ shown in Figure 4-2. The nitrogen/helium mixing thickness at the position of the electrodes was estimated as $\delta x_{mix} \sim \sqrt{z_e D_{12}/u_\infty} \sim 0.2mm$, for z_e=4mm, $u_\infty = 5m/s$ and $D_{12} \sim 7 \cdot 10^{-5} m^2/s$ (binary diffusion coefficient of an equimolar mixture of nitrogen and helium at ambient conditions [82]).

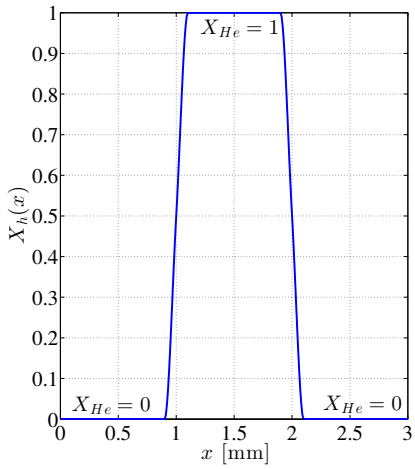

Figure 4-2: Variable composition profile across the gas gap: nitrogen-helium-nitrogen. The profile is continuous and smooth.

The boundary conditions given by equations 4.4 and 4.5 are simplified by assuming that the thermal speeds are constant at the wall: for the ions, $v_{th,i} = 470m/s$, and, for the electrons, that corresponding to 1eV.

For the transport coefficients, the ion mobility in helium was taken to be $10.2\text{cm}^2\text{s}^{-1}\text{V}^{-1}$ (He^+/He), and in nitrogen $1.87\text{cm}^2\text{s}^{-1}\text{V}^{-1}$ (N_2^+/N_2) [53]. Note that, although this is not an accurate description of the mobility of the ions (the model assumes one *effective* type of ion), at the short time scales considered they are pretty much stationary and unaffected by the electric field. The transport coefficients of the electrons, μ_e and D_e, are evaluated in the

local field approximation as a function of the reduced electric field using BOLSIG+ [72], and are shown in Figure 4-3 (in practice, a polynomial fit to the data is used).

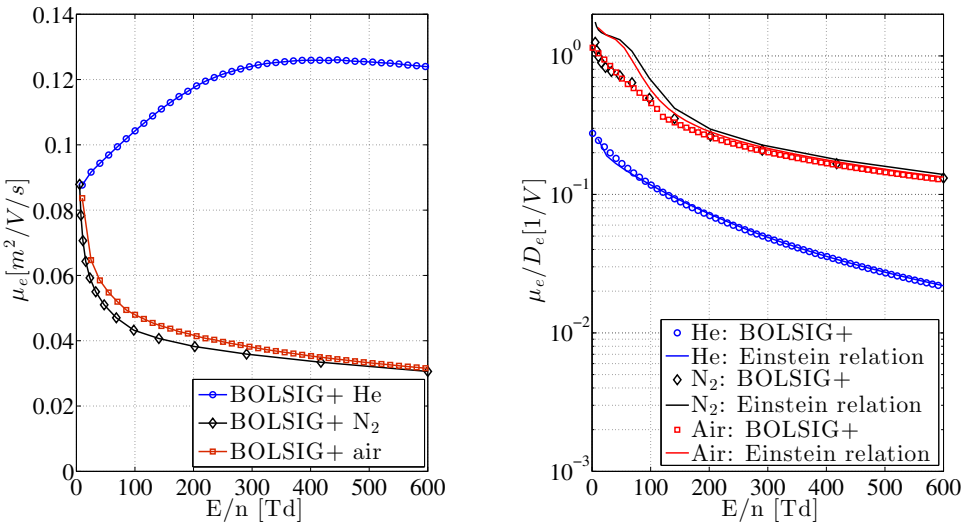

(a) Mobility.

(b) Mobility / Diffusion.

Figure 4-3: Electron mobilities and diffusion coefficients in helium, nitrogen and air as a function of the reduced electric field (atmospheric pressure and ambient temperature). Data calculated using BOLSIG+ [72].

The coefficients in the Townsend ionization formula were taken as: $F = 9.32{\cdot}10^{-21}m^2, G =$ 105Td, in helium, and $F = 3.73 \cdot 10^{-20}m^2, G = 1062$Td in nitrogen [166].

The minimum background density was selected to be $n_{min} = 10^8 cm^{-3}$, following the guidelines of [17,31]. The impact of this parameter is explored in Appendix C (Section C.2.3).

For the analysis in this part, 1D results are presented. Results in 2D lead to the same conclusions and are summarized in Appendix D. The grid has N_{xg}=1000 grid points, in the gas gap, and N_{xd}=160, in each dielectric (the adequacy of the resulting spacing is discussed in Section C.2). The maximum time step used is Δt=0.1ns.

The applied voltage pulse amplitude was 3kV. With these conditions, the discharge should be within the region of confinement to the *hot* (helium) layer of Figure 3-2(a). The voltage pulse duration was set to 150ns.

The initial condition for the simulation of the first filament was a gaussian spot of plasma placed on the helium/nitrogen mixing layer, at the cathode side (x=2mm). This type of initial condition has been found to produce a fast formation of a cathode directed streamer

[152]. The voltage level was selected so that the electron avalanche formed would satisfy Meek's criterion when it reached the anode-side mixing layer. The gaussian curve had a peak amplitude of $n_0 = 10^9 cm^{-3}$ and a standard deviation of $\sigma = 30\mu m$. The initial surface charge on the solid dielectrics was set to zero.

4.3.2 Discharge evolution during application of the voltage pulse

This Section discusses the results of the simulation of the discharge during application of the voltage pulse (total time 150ns).

Starting from the gaussian spot of plasma on the cathode-side helium/nitrogen mixing layer, an anode-directed electron avalanche is formed. The conditions are such that, when the avalanche reaches the anode-side mixing layer, the electric field is sufficiently distorted by the space charge that a cathode-directed streamer can start propagating. In theory, an anode-directed streamer could also develop from this mixing layer but the reduced electric field in the nitrogen side is insufficient to provide the ionization mechanism. Thus, only a volumetric cathode-directed streamer is formed, which propagates *seeded* by the forced background density.

Once the cathode-directed streamer reaches the cathode side helium/nitrogen mixing layer, its propagation is impeded, as the field is not high enough to penetrate the nitrogen. Instead, the volume streamer stagnates at the interface. A snapshot of the electron and ion number densities and the electric field is shown in Figure 4-4, at 50ns after pulse onset, when the streamer has already reached the end of the helium zone.

In this situation, the electrons are still free to drift towards the anode but the ions are pilling up on the cathode-side mixing-layer due to their slower drift, creating a positively charged layer on it.

No (or little) ionization occurs outside the helium layer, confirming the localization of the discharge to the center of the gap. Inside the body of the streamer, the electric field is very low, as is expected within the plasma. The reduction of the field in the helium layer results in an increase of the electric field in the nitrogen layers, which is still not high enough to make them ionizing. The numerical results confirm the analytical hypothesis of Section 3.2.2: the non-symmetrical accumulation of charge results in an asymmetry in the behavior of the two

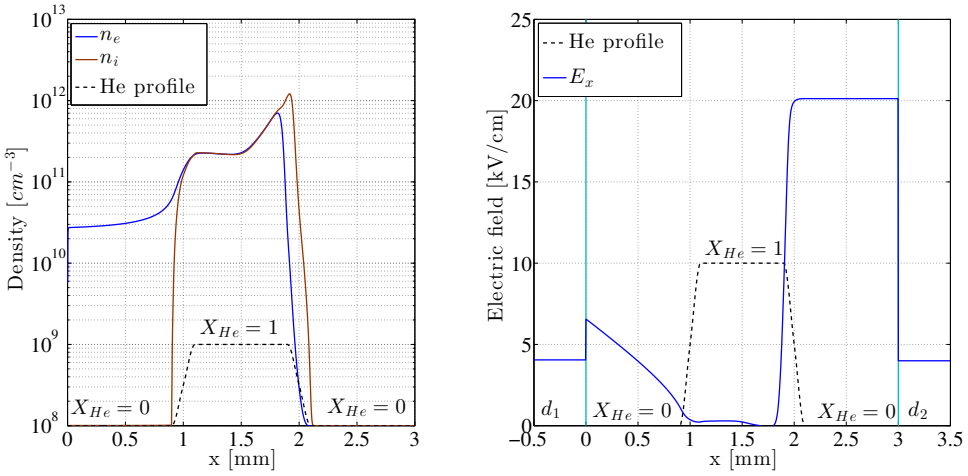

(a) Electron and ion number density.

(b) Electric field.

Figure 4-4: Snapshot of streamer stagnating at the mixing layer (50ns after pulse onset). Anode is at x=-0.5mm and cathode at x=3.5mm. The helium fraction profile is plotted in both graphs for reference.

nitrogen layers, which presents a larger magnitude of the electric field at the cathode-side.

Figure 4-5(a) shows the conduction current density evolution in time. The duration of the current pulse (FWHM∼20ns) is shorter than the voltage pulse duration (150ns). A short time after the voltage pulse is applied, the electrons start arriving to the anode and keep arriving as long as the streamer is propagating towards the cathode. The anode-side solid dielectric starts charging to negative values, whereas the cathode-side solid dielectric remains essentially *uncharged*, Figure 4-5(c).

Once the ionization front reaches the cathode-side helium-nitrogen mixing layer two effects limit the current spike: first, the plasma created shields the electric field so that the ionization in the helium layer gradually decreases; second, no (or little) ionization occurs outside the helium layer so that ions start piling up at the interface at the cathode-side which starts to accumulate positive charge, Figure 4-5(b). For this second effect to be significant, the charge in the mixing layer, $\frac{Q}{A} \sim e(n_i - n_e)\delta x_{mix}$, needs to be:

$$\frac{Q}{A} \approx \frac{\epsilon_0 V}{d_h + d_c} \sim 1nC/cm^2,$$

which is the case for the model within the tested case. Note that, in this configuration,

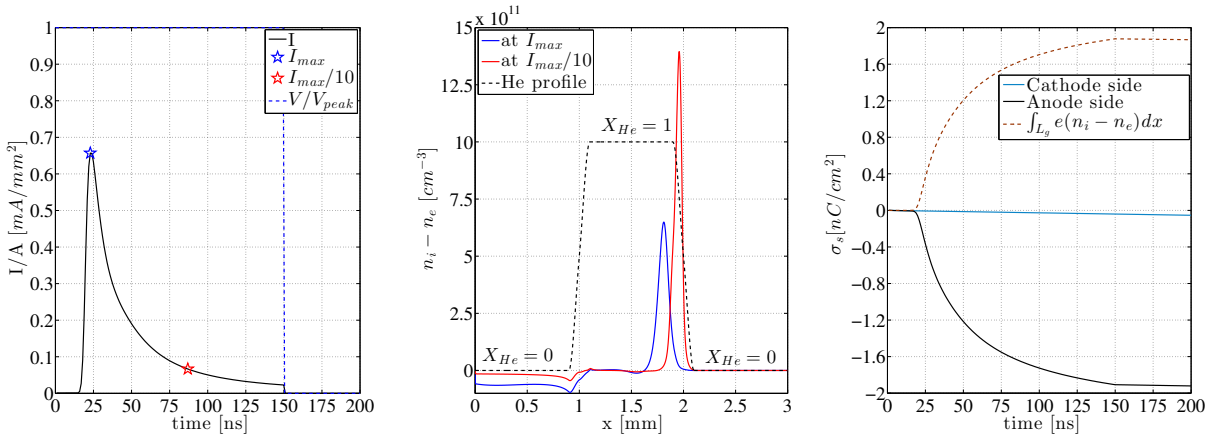

(a) Conduction current. (b) Space charge (mixing layers). (c) Surface charge (dielectrics).

Figure 4-5: Calculated current, net space charge at the time of peak conduction current and when the current has dropped to $1/10^{th}$ of its peak value, and surface charge on the dielectrics.

the *effective* DBD has, as the anode-side dielectric, the solid dielectric and, as the cathode-side dielectric, the corresponding nitrogen layer. Moreover, the negative surface charge accumulated at the anode-side dielectric is of the same order as the positive surface charge on the cathode-side helium/nitrogen interface (charge conservation, see Figure 4-5(c)). In addition, it is interesting to see how the ion layer in the helium-nitrogen cathodic interface, Figure 4-5(b), is drifting as it amplifies. A cartoon of the operation is presented in Figure 4-6.

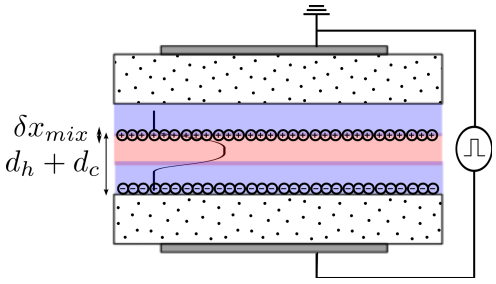

Figure 4-6: Cartoon of the operation of the *effective* DBD. The nitrogen layer plays the role of the cathode-side dielectric (net space charge in the thin mixing interface).

All in all, the current spike duration is of the order of the electron drift time to the anode ($\frac{d_h+d_c}{\mu_e E} \sim 40ns$) as long as there is an applied voltage during that time. Also, note that the voltage pulse duration should be selected much shorter than the life-time of the charged layer on the helium-nitrogen interface, which is given by the ion drift/diffusion time $\sim 1\mu s$.

4.3.3 Afterglow shortly after the voltage pulse is turned off

Figure 4-7 shows the electron and ion density as well as the electric potential at t=200ns, 50ns after the pulse is switched off.

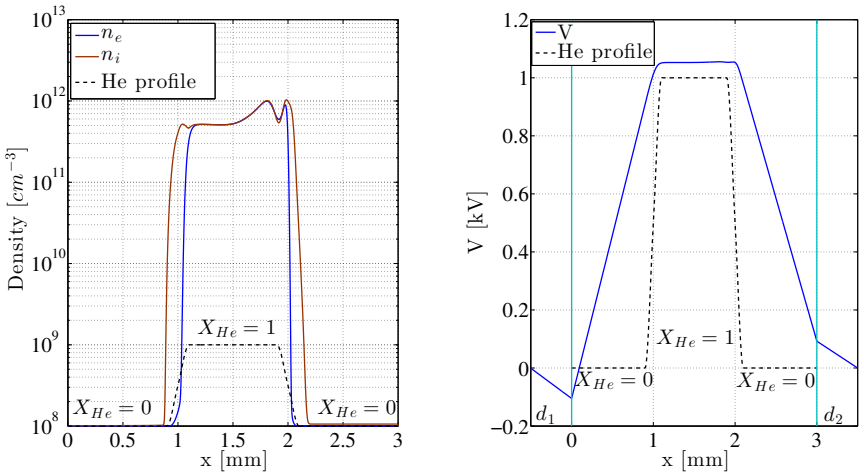

(a) Electron and ion number density. (b) Electric potential.

Figure 4-7: Snapshot of the charge densities and electric potential during the afterglow phase (200ns after pulse onset, 50ns after the pulse is switched off). The helium fraction profile is plotted in both graphs for reference.

At the end of the voltage pulse, within the assumptions of the model (e.g. the only electron loss mechanism considered is transport to the walls), due to the configuration of the potential at this point, the excess electrons stop escaping towards the anode and start drifting towards the center of the gap. This contributes to a positive feedback mechanism for the concentration of successive discharges in the helium layer if the repetition frequency of the voltage pulses is faster than the flow residence time. The excess ions are escaping by their drift towards both electrodes and the quasi-neutral electron and ion mixture is governed by ambipolar diffusion.

4.3.4 Results removing the solid dielectrics

In the numerical results presented so far, solid dielectrics were attached to both electrodes. This helped highlight the similitudes between the *gaseous pseudo-dielectrics* and the solid dielectrics. From the model it was seen that the behavior was similar to an *effective* DBD

where the role of the cathode-side dielectric was played by the cathode-side nitrogen layer.

However, in the actual experiments, either no solid dielectrics or a single solid dielectric attached to one of the electrodes were used and, still, the plasma-emission was confined to the helium-rich stream. Moreover, the experiments revealed little effect on having or not the solid dielectric barrier attached to the electrode.

In view of the numerical results, it can be argued that the operation will not be qualitatively affected (within the approximations of the model) when removing the solid dielectrics.

On the one hand, removing the cathode-side solid dielectric should have little effect, since the nitrogen layer on that side is *clean* (there is no volumetric charge except for the forced background density). This is true as long as the increase of the electric field in the cathode-side nitrogen layer due to the solid dielectric removal is still below that required for nitrogen ionization (even though there is no surface charge, the different permittivities result in a discontinuity in the electric field, equation 4.7).

On the other hand, removing the anode-side dielectric would modify the electric field in the anode-side nitrogen layer, as there would not be a negative surface charge at its boundary, but this would only modify the value of the electron drift towards the anode (and consequently the current pulse width) but not the profile of electron and ion densities since no ionization is occurring within the nitrogen layer anyway.

To validate this reasoning, the model described in Section 4.2 was modified to remove the solid dielectrics. The results, both during pulse application and shortly after the voltage pulse is turned off, are very similar to the case with solid dielectrics for the reasons discussed above. Figures 4-8(a) and 4-8(b) show comparison of the electron and ion number density and the electric potential for the cases with and without solid dielectrics at 50ns after pulse onset. It can be appreciated how the streamer still stagnates at the helium-nitrogen interface and the densities of the charged species are pretty much unaffected (aside from the slightly higher ionization due to the slightly higher electric field when removing the solid dielectrics). In the case of no solid dielectrics, the *surface charging* is substituted by the positive volumetric charge accumulation at the helium/nitrogen mixing interface, Figure 4-8(c).

At this point, it is interesting to point out that, as for traditional DBD structures, *at least* one dielectric barrier [91] is required, so that operation with a single dielectric barrier

is possible: in this case, the cathode-side nitrogen layer.

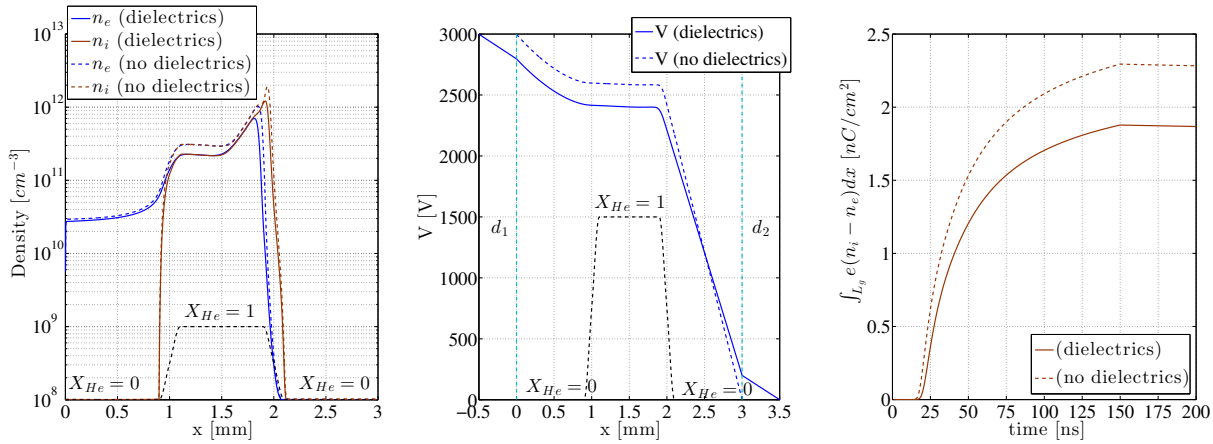

(a) Electron and ion number density.

(b) Electric potential.

(c) Net charge accumulation.

Figure 4-8: Comparison of numerical evaluation with solid dielectrics attached to both electrodes (solid lines) and no solid dielectrics (dashed lines). Snapshot of the streamer at 50ns after pulse onset and time evolution of the net space charge integral.

4.4 Discussion and link to the experimental observations

In this Chapter, results of a numerical model for the GBD proposed in Chapter 3 have been presented. The geometry considered for the numerical evaluation was similar to the nitrogen/helium layered gas configuration in the experiments of Section 3.3.1.

The numerical results were consistent with the experimental observations. On the one hand, in the model, the ionization was confined to the helium layer and no (or little) ionization occurred outside of it. Although in the experiment, the spatial structure of the ionization rate could not be measured, the plasma emission was, in all cases, clearly confined to the helium-rich stream.

On the other hand, a 1D positive streamer ionization front (triggered in the simulation by the choice of initial conditions) stagnated at the interface of the helium-nitrogen streams, since the electric field was not high enough to penetrate the nitrogen. In the 2D simulations (see Appendix D), lateral streamers appeared that followed the mixing layer. These results of the streamer dynamics are consistent with the experimental observations: the discharge

filaments were seen to stagnate or deflect once they reached the mixing layer between the two gases.

In addition, the model provided a phenomenological description of the discharge evolution and confirmed the asymmetry discussed in Chapter 3. In the numerical model, positive charge accumulated in the cathode-side mixing layer whereas, the electrons were free to drift across the anode-side nitrogen layer, so that the net charge accumulated in the anode-side mixing layer was much lower.

Chapter 5

Repetitive pulsed nanosecond discharges in counterflow nonpremixed flames

5.1 Introduction

In Chapters 3 and 4, it was shown that electrical breakdown triggered by RPND in a non-uniform gas could be confined to regions of favorable ionization; and that the spatial extent of the discharge was defined by the geometry, the temperature and composition fields, as well as the applied voltage.

The application of RPND to assist flames takes place in such a highly non-uniform environment, characterized by sharp gradients in temperature and composition, as well as isolated pre-ionized regions. The literature review on the chemical effects of plasma-assisted combustion (Section 1.4.2) revealed that the impact of a particular plasma-triggered energy path is highly dependent on where the plasma is produced [120, 136, 171] and therefore, knowledge of the spatial structure of the plasma is required to understand the plasma-activation strategy.

In addition, previous research [202–204] has shown that, unless placed close to the flame front, radicals and short-lived species will not survive and, combined thermal-kinetic effects or longer lived species will play the dominant role. Therefore, a purely non-thermal strategy, based on *active species* injection alone, requires that the plasma be placed *close* to the flame front. Previous work on localized energy deposition to the flame is due to [116, 183, 198]

using MW energy and to [231] using fs-lasers; in the present Chapter, direct coupling of an RPND plasma to a flame is targeted following the concepts explored in Chapter 3.

The structure of this Chapter is as follows. Section 5.2 motivates the selection of the laminar counterflow nonpremixed flame as the platform of choice for the flame studies presented in Chapters 5 and 6. Next, in Section 5.3, an analysis of the dependency of the parameters that drive the breakdown, on the flame parameters, is performed. Finally, experimental evidence[1] of the RPND plasma coupling to a flame is given in Section 5.4. Section 5.5 summarizes the main findings of this Chapter.

5.2 The laminar counterflow nonpremixed flame platform

5.2.1 Motivation

Nonpremixed flames (historically known as diffusion flames), occur when fuel and oxidizer are injected separately in the combustor, and mixing and burning take place simultaneously. The laminar counterflow nonpremixed flame is the platform chosen for the studies in Chapters 5 and 6 of this dissertation for three reasons.

First, the understanding of laminar nonpremixed flames forms the basis for the understanding of turbulent nonpremixed flames, which readily appear in many applications of interest, such as jet engines, diesel engines or bipropellant rocket engines. Many models for turbulent combustion use the *flamelet approach* [161, 224, 226], which views the turbulent flame as an ensemble of laminar flame elements embedded in a turbulent flow field (Figure 5-1). Therefore, comprehensive studies of realistic problems need to be preceded by the analysis of the laminar counterflow nonpremixed case.

Second, the counterflow nonpremixed flame presents an essentially one-dimensional structure, which can be described in terms of a conserved scalar, the mixture fraction, and therefore constitutes an analytically simple platform (Section 6.4.1) very attractive for comparison with experiments.

Third, the opposed jet nonpremixed burner with two electrodes parallel to the flame,

[1]The experiments in this Chapter were performed during a three month stay in Professor R. Miles' Applied Physics Group, Princeton University.

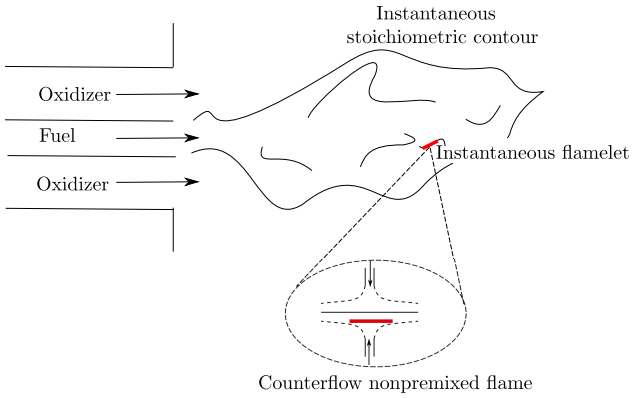

Figure 5-1: The flamelet concept for turbulent nonpremixed flames.

such as the one implemented in this work, was proposed as the most suitable platform for electrical studies of flames already during the early research on the effects of electric fields upon flames [40, 79, 159]. In this case, the applied electric field is aligned with the direction of variation of the flame properties, respecting the one-dimensionality of the platform.

5.2.2 Experimental platform and 1D approximation

Nearly flat counterflow nonpremixed flames were established using the setup described in Section 2.3. The parameters that could be varied were the choice of dilutant, the degree of dilution of the fuel and oxidizer streams, as well as the strain rate.

The typical appearance of the flames used is that of a blue flat flame sitting close to the center of the gap, Figure 2-4(b). The flatness of the flame ensures the one-dimensionality close to the centerline.

A representative temperature profile of the flames under study is shown in Figure 5-2, for a flame with parameters summarized in Table 5.1.[2] The temperature was measured using the laser Rayleigh scattering strategy described in Section 2.8.1 and detailed in Appendix B (Section B.2), and is compared to a 1D calculation.

The 1D approximation for these types of flames predicts well parameters such as the

[2]For the flame parameters quoted: the strain rate and the stoichiometric mixture fraction are calculated from equations 2.1 and 2.3 respectively, the global stoichiometry ϕ (by mass) is evaluated from the mass flow measurements, the power is estimated using the heat value of methane and the flame temperature is evaluated from 1D calculations using Cantera [66]. The sign convention for the top and bottom nozzles is that of Figure 2-3(b), so that, in most cases the fuel is on top ($-\infty$).

Table 5.1: Flame parameters for the temperature profile of Figure 5-2.

a $[1/s]$	Dilutant	$X_{O_2,\infty}$	$X_{CH_4,-\infty}$	Z_{st}	ϕ	Power $[W]$	T_{max} $[K]$
35	N_2	0.21	0.19	0.33	1.92	116	1630

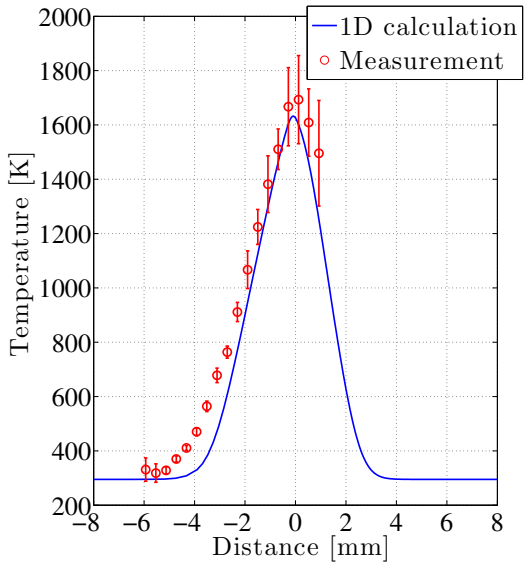

Figure 5-2: Measured temperature profile, across flame, compared to 1D calculation. Flame with parameters given in Table 5.1. Fuel side is on the left and oxidizer on the right.

peak temperature or the full width at half maximum of the temperature profile, and will be used for the parametric analysis in Section 5.3.

All the flame profiles presented have been calculated using Cantera [66] and the chemical kinetic mechanisms used were the GRI 3.0 mechanism [54], when using nitrogen or argon as the dilutant, and the San Diego mechanism [211], when using helium as the dilutant.

5.2.3 A note on finite length effects and edge-flames

Although the counterflow nonpremixed flame is generally described through a similarity solution that allows the problem to be treated one-dimensionally (dominant gradients occur *across* the flame), in some instances, it is important to account for finite size effects.

In general, turbulent nonpremixed flames can be viewed as a sequence of flame patches

(isolated burning islands) and extinction holes (extinguished islands) [223], so that, the edges of those regions can be important in describing extinction and ignition processes [104, 106, 131, 175]. Looking at a small segment of such a flame (a counterflow nonpremixed flame), this becomes more evident for low strain rate and small diameters [37].

The characteristic feature of the edge flame is that it behaves as a partially premixed flame. As such, it has the ability to propagate (preferentially along the stoichiometric iso-surface) even when the flame, of which it is an edge, cannot [60, 153]. The parameter that controls its propagation speed, i.e. decides whether the edge-flame behaves as an extinction or an ignition front or is stationary, is the Damköhler number (ratio of the mixing time scale to the reaction time scale). Thus, by varying either the chemical rates or the flow residence time, the propagation characteristics of the edge-flame can be modified.[3] For plasma-assisted strategies, the first can be affected by radical injection or temperature increase and, the second, through induced ionic winds or shock wave generation.

For the flame experiments in this dissertation, coupled to either RPND plasmas (Chapter 5) or AC fields (Chapter 6), finite size effects were needed to explain some observations. In Section 5.4.6, a RPND plasma confined to the flame region did not modify the main flame properties but led to a slight curving of the flame edge[4]. Moreover, the finite diameter of the flame was thought to be imperative to explain the flame dynamics under an AC field, as will be discussed in Section 6.4.4.

5.3 Flame as an environment for plasma development

In terms of its electrical properties, the structure of the counterflow nonpremixed flame is partly similar to the model presented in Figure 3-1(a): it consists of a high temperature layer surrounded by gas at a much lower temperature. The parameters that appear in the model of Section 3.2.2, namely the temperature ratio $K = T_{max}/T_0$, the geometry ratio $r = d_h/d_c$ and the ionization coefficients F and G, are related to the flame parameters (strain rate and

[3]The mathematical description of the end of a flamelet can be found in [28, 45].

[4]For the experiments presented in Section 5.4.6, the interpretation is hindered by the presence of the inert coflow curtain. In the presence of a shroud flow, the extinction at the periphery is controlled by dilution with the inert gas, limiting the possibility of existence of the edge flame [60, 103].

dilution) in Section 5.3.1. In addition, the impact of the flame front natural pre-ionization will be discussed in Section 5.3.2.

5.3.1 Dependencies with strain rate and dilution

Flame thickness

The thickness of the thermal mixing layer (high temperature region) of a strained non-premixed flame scales as [56]:

$$\frac{\delta_T}{\delta_T^{\text{ref}}} = \sqrt{\frac{a_{\text{ref}}}{\alpha_{\text{ref}}}\frac{\alpha}{a}} \sim \sqrt{\frac{a_{\text{ref}} p_{\text{ref}}}{ap}}, \tag{5.1}$$

where α is the thermal diffusivity, p is the pressure, a the strain rate, and δ_T^{ref} a reference thickness. Thus, for the experimental platform at hand, thinner flames can be obtained increasing the strain rate or using a dilutant with a lower diffusivity. Using the notation of Section 3.2.2, and defining the flame thickness as the full width at half maximum (FWHM) of the temperature profile, the ratio $r = d_h/d_c$ for the flame geometry becomes:

$$\frac{d_h}{d_c} = 2\left(\frac{L}{d_h^{\text{ref}}}\sqrt{\frac{ap}{a_{\text{ref}} p_{\text{ref}}}} - 1\right)^{-1} \approx \frac{d_h}{d_c}(a, \text{gas}). \tag{5.2}$$

Figure 5-3(a) shows the dependency of the flame geometry with the strain rate, for atmospheric flames and the parameters of the experimental burner, as calculated with Cantera. Cases presented correspond to CH_4-air flames, flames diluted in helium (equal dilution of fuel and oxidizer ranging from X_{He} =0.1-0.77) and flames diluted in argon ($X_{Ar} = 0.7$). It can be appreciated that the scaling of equation 5.2 holds when using the detailed chemistry [54,211].

From this plot, the minimum strain rate is selected to ensure adiabatic conditions at the boundaries. Since the flame thickness scales as $a^{-1/2}$, low values of the strain rate lead to a temperature profile that is not flat at the nozzle exit, increasing the heat transfer to the burner. The maximum strain rate is limited by transition to turbulent flow (Section 2.3.1). These conditions give a range of variability of $d_h/d_c \approx [0.25, 1]$, which corresponds to a FWHM of the temperature profile between $d_h \approx [1.9 - 5.8]$mm. For nitrogen and argon diluted flames, having $d_h/d_c < 1$ translates to the strain rate being above 20s^{-1}.

Temperature ratio

The peak flame temperature depends on the degree of dilution and the strain rate.

For the highly diluted mixtures here used (air-like but with different inert gases), the maximum temperature will be of the order of ∼2200K.

The minimum peak temperature will correspond to a flame close to extinction. The review on counterflow nonpremixed flames by H. Tsuji [209] reports the limit fuel concentrations and corresponding flame temperatures for methane flames diluted with various inert gases. For methane diluted in nitrogen/air flames, the maximum dilution of the fuel before extinction is $X_{N_2,-\infty}$=0.84, and the corresponding peak temperature, 1460K. For an 'air' like mixture in which the nitrogen is substituted by argon, the maximum dilution of the fuel is $X_{Ar,-\infty}$=0.92. These values are consistent with flame-extinction calculations using Cantera [66] as shown in Figure 5-3(b) (extinction corresponds to the sudden temperature drop).

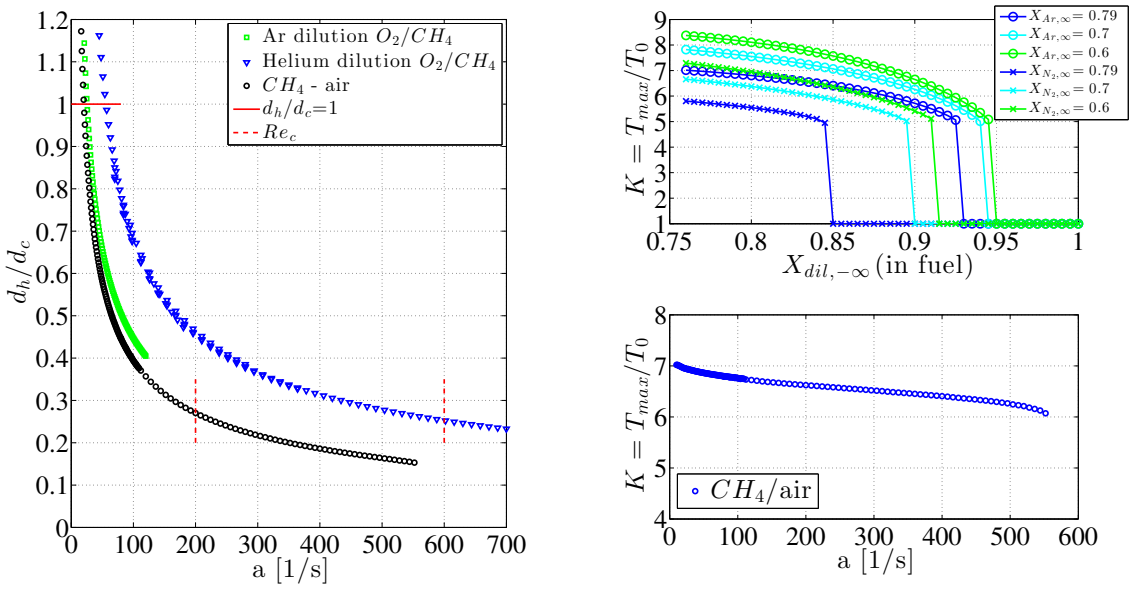

(a) d_h/d_c. (b) $T_{\max}/T_0$.

Figure 5-3: Flame geometry and temperature ratio as a function of dilution and strain, for atmospheric flames and the parameters of the experimental burner, as calculated with Cantera.

Figure 5-3(b) shows the dependencies of the temperature ratio as a function of the strain rate (for a methane/air flame) and as a function of the degree of dilution of the fuel (for

same type of dilutant in both streams, different degrees of dilution of the oxidizer stream and a=40s^{-1}). The temperature ratio range that can be obtained is $K \approx$5-8.

Ionization properties of flame-like mixtures

The variability of the ionization properties of the gas with its composition is here analyzed. For the methane flames considered, the major species that appear are oxygen and methane (reactants); helium, nitrogen and argon (dilutants); and carbon dioxide and water (products). The ionization properties of the pure gases are very different and their ionization coefficients are usually given in different ranges of the reduced electric field that may not overlap (Table 5.2). In general, the Townsend semi-empirical formula (equation 3.1) cannot accurately describe the ionization behavior in a wide range of reduced electric fields, so it is of interest to compare the different gases and mixtures under similar conditions.

Table 5.2: Townsend ionization coefficients for major species in flame.

	Gas	F $[10^{-21}m^2]$	G $[Td]$	Range of E/n $[Td]$	Source
Reactants	O_2	19.7	646	257-642	[167]
	CH_4	25.1	624	80-600	[167]
Dilutants	He	9.32	105	60-470	[166]
	N_2	37.3	1062	310-1865	[166]
		27.3	854	84-620	[166]
	Ar	37.3	559	310-1865	[166]
Products	CO_2	62	1448	1550-3100	[166]
		8.23	478	80-155	[167]
	H_2O	40	900	470-3100	[166]

In addition, values of the ionization coefficients for mixtures are usually not readily available, and the Wieland approximation [33], which is the weighted molar average at each reduced electric field of the ionization coefficients of the pure substances (consistent with the definition of the mean free path), is used. Note however that this approximation is only valid for mixtures that have similar EEDF for the same reduced electric field [113] so that great discrepancies can be found, for example, for monoatomic/molecular mixtures. To illustrate this point, Figure 5-4 shows the EEDF at E/n=400Td of methane diluted in nitrogen, Figure 5-4(a), and in helium, Figure 5-4(b); the red curve represents pure methane

and the blue one pure dilutant. The greater modification of the EEDF from pure methane to pure helium can be appreciated as compared to the mixture of molecular gases (note the different energy range used in the plots).

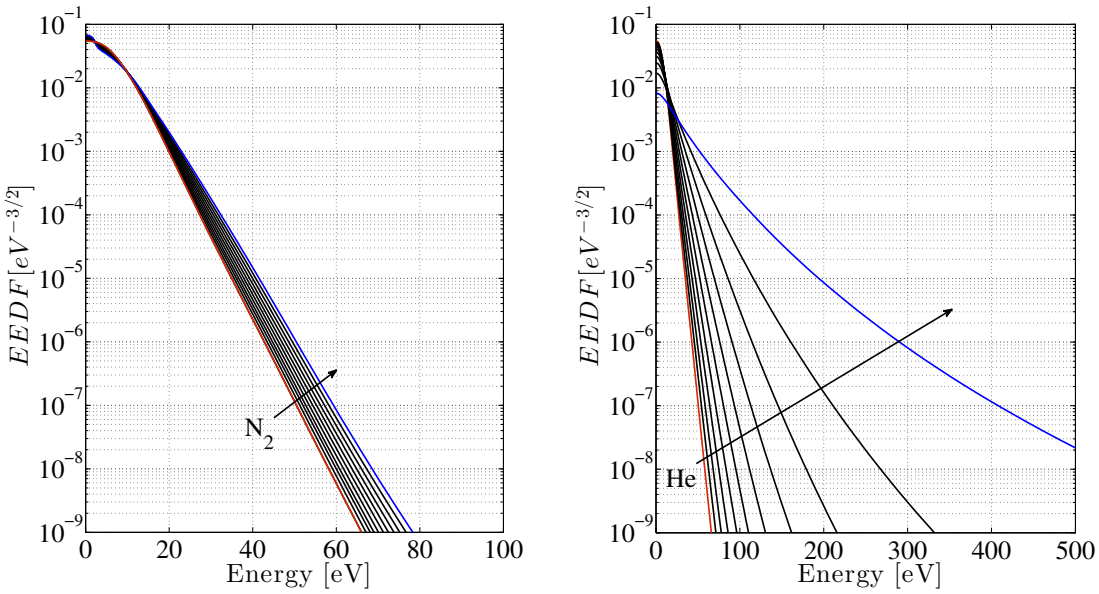

(a) EEDF, nitrogen dilution.

(b) EEDF, helium dilution.

Figure 5-4: Effect of diluting CH_4 on its EEDF, as calculated with BOLSIG+ (E/n=400Td, T=600K). The red curve represents pure methane and the blue one pure dilutant.

To account for the EEDF modification for a gas mixture and be able to compare the Townsend coefficients in the same range, the effective ionization coefficient has been evaluated solving the EEDF of the mixture and adding the individual coefficients (ionization minus attachment) of each species:

$$\alpha - \eta = \sum_{i}^{\text{species}} X_i \sum_{j}^{\text{reactions}} (\alpha_j - \eta_j)_i, \tag{5.3}$$

where η is the attachment coefficient and the other symbols have already been used. From the gases considered, CH_4, O_2, CO_2 and H_2O are the attaching gases. Only ionization by electron impact has been considered (e.g. no Penning).

Solution to the Boltzmann equation[5] has been obtained using BOLSIG+ [72]. The elec-

[5]Parameters used in BOLSIG+ calculations: effect of electron production not included; after impact, all energy is taken by one electron.

tron impact reactions used are those proposed by Morgan et al. [123] augmented by the rotational excitation of water, which was taken from the Itikawa database [75, 76].

The data obtained from this calculation were then fitted by the formula suggested by Townsend (equation 3.1) in the range 200-500Td, as shown in the example of Figure 5-5. The non-linear data fitting was performed in the least-squares sense.

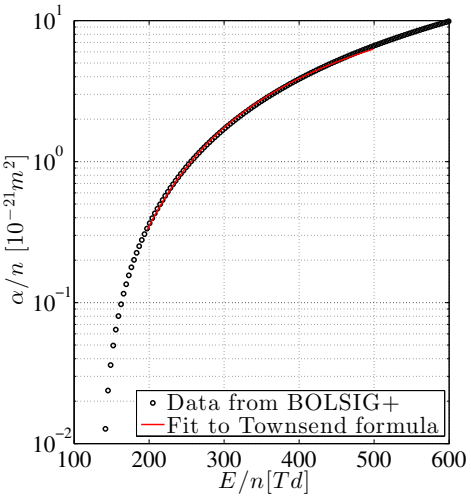

Figure 5-5: Fit of Townsend formula to data from BOLSIG+ (N_2:CO_2:H_2O=80:6.7:13.3).

Mixtures considered correspond to the reactants composition (diluted oxygen and diluted methane) as well as the products, in stoichiometric proportions (two moles of water per mole of carbon dioxide, diluted). The fit for the Townsend coefficients (F and G) in the range 200-500Td, as a function of the dilutant mole fraction, is shown in Figure 5-6. For nitrogen dilution, the mean deviation of the data from the formula is less than 3.5%; for argon dilution, less than 3%; and for helium dilution, less than 5%.

From Figure 5-6, it can be appreciated how the ionization properties can be favored by dilution in argon or helium (reduction in the G parameter, which has an exponential contribution). However, there is a compromise between lowering G and decreasing the peak flame temperature. In the case of nitrogen, a lower degree of dilution leads to a higher peak temperature and a reduction of the G parameter; both in the direction of favoring ionization. For this last dilutant, the effect of the increase in peak temperature is more important due

to the lower variability of the Townsend G coefficient with the composition.[6]

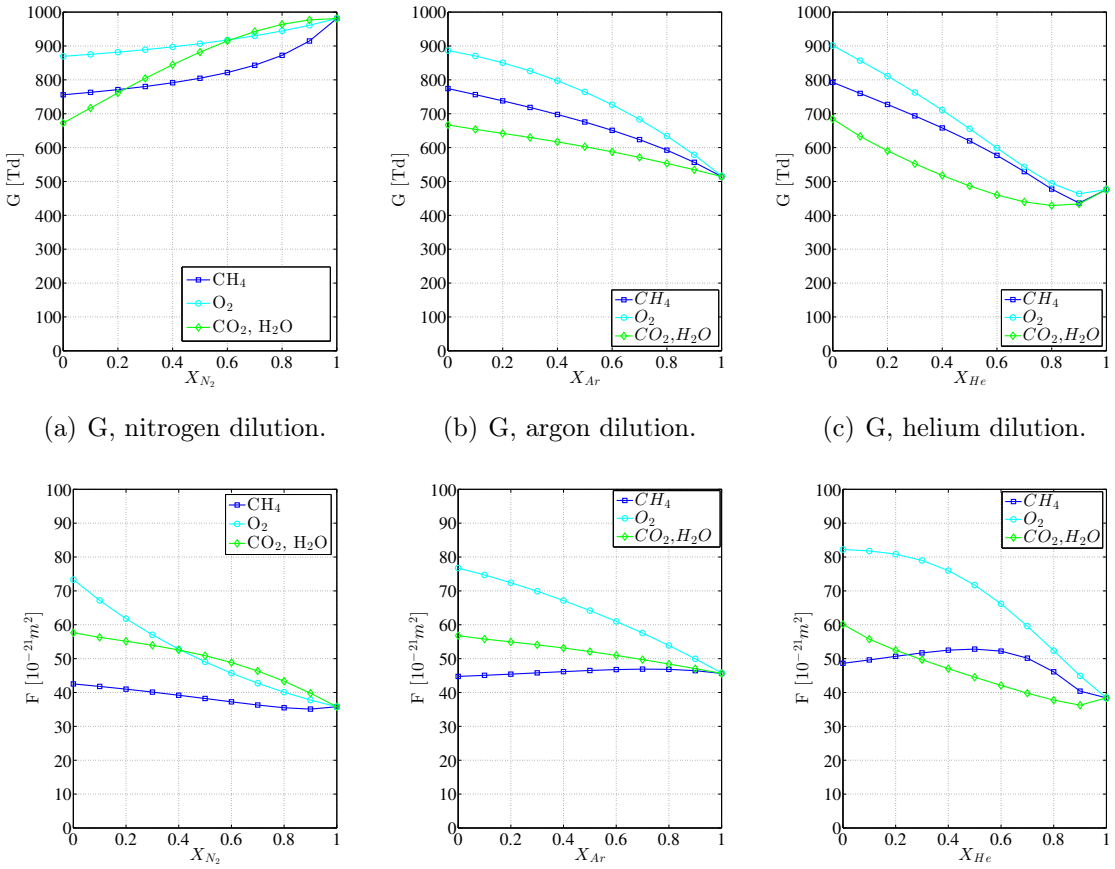

(a) G, nitrogen dilution. (b) G, argon dilution. (c) G, helium dilution.

(d) F, nitrogen dilution. (e) F, argon dilution. (f) F, helium dilution.

Figure 5-6: Townsend ionization coefficients for flame mixtures in the range 200-500Td, calculated fitting ionization data calculated with BOLSIG+.

5.3.2 Chemi-ionization

The main discrepancy of the flame environment with the non-reacting platforms of Chapter 3 is that the flame itself is a plasma. Even before applying an electric field above the breakdown threshold, ions and electrons are generated within the high-temperature zones of hydrocarbon flames in amounts much in excess of thermodynamic equilibrium values [101].

[6]The discrepancies between the calculated coefficients for the pure gases, and those reported in Table 5.2, can be explained by the range of E/n considered and the inclusion of attachment. E.g. for the non-attaching gas He, the range of E/n for the evaluation in both cases is very different: a fit of the BOLSIG+ data in the range 10-700Td gives $G = 134Td$, but the mean deviation of the data from the formula is very large $\sim 59\%$.

This excess ionization is due to chemi-ionization reactions, in which species undergo a chemical rearrangement that is sufficiently exothermic to ionize one of the products [102], the most important reaction being:

$$CH + O \longrightarrow CHO^+ + e^-,$$

where the CH is either in ground state or electronically excited [38]. Since the CH radicals are only present in the reaction zone of hydrocarbon flames, that is where high populations of charged species are encountered [179]. Although CHO^+ is the precursor ion, the dominant ion is usually H_3O^+.[7]

All in all, the electron and ion number densities peak within the reaction zone of the flame and the thickness of the region with charged species is of the order of the reaction zone thickness; e.g. the FWHM of the electron density profile has been reported to be $\delta_i \sim$0.6mm, for a stoichiometric premixed methane-air flame [80,111]. Note that this thickness may vary with the flame parameters but, in general, will be of the order of a fraction of a mm, which is much less than the thickness of the high temperature region (Section 5.3.1): $\delta_i < d_h$.

The dependencies of the ionization level of a flame with the flame parameters were studied by H. F. Calcote [30] who found that the mole fraction of ions present was practically independent of pressure, had little dependence on temperature, and the main dependency was with the equivalence ratio. The peak ionization was found close to stoichiometric conditions (slightly fuel rich) and, for methane-air flames, is $n_i/n \approx 10^{-7}$ (this fraction is consistent with other values reported in the literature [80, 102, 111, 155]). For equivalence ratios far from stoichiometry, this fraction could be an order of magnitude lower, leading to a range of variability of the ionization fraction of $n_i/n \approx 10^{-8}$-10^{-7} [30].

The existence of this natural ionization impacts the way the electrical energy can be coupled to the gas. On the one hand, the interaction of the chemi-ionization ions with static electric fields, below the breakdown threshold, was studied in the 1960s and 1970s and was used to drive ionic winds in the flow [102]. On the other hand, more recent work in Princeton

[7] A simplified chemical kinetic mechanism for ion formation, in methane/oxygen flames, can be found in [155]. It is augmented in [188] to include the negative ions, and in particular electron attachment to O_2, as well as nitrogen reactions and nitrogen-based ions.

University, has coupled sub-critical MW energy to the chemi-ionization electrons in the thin reaction-front region of a premixed flame [80, 116, 197, 200].

In the case of RPND above the breakdown threshold (at least locally), the presence of these chemi-ionization electrons will contribute to the sustainability (repetitive nature) and homogeneity of the discharge, to the non-uniformity of the medium and presumably modify the breakdown thresholds. These effects are briefly explored in what follows.

Sustained nature of the RPND discharge

The RPND strategy relies on the use of high frequency to achieve a cumulative and steady-state behavior from an inherently transient discharge [143]. The repetition frequency of the pulses, ∼10-100kHz, is chosen to match the recombination time of the electrons in order to sustain a minimum population at all times.

The existence of a sustained pre-ionization in the flame front provides this condition already. Moreover, the natural ionization level of a methane-air flame is of the same order as the minimum electron number density measured by researchers at Stanford University for a glow-like RPND in atmospheric-pressure air preheated to 2000K [98]. In their experiments, the plasma was created by applying 6kV peak-amplitude, 10ns duration voltage pulses at 100kHz to a point-to-point electrode system of gap-length 1cm, and the minimum electron mole fraction measured between pulses was $n_e/n \approx 1.9 \cdot 10^{-7}$.

Homogeneity of the pulsed avalanche discharge

The classical criteria for streamer and Townsend breakdown say nothing about the existing level of pre-ionization in the gas. These criteria only require the existence of free electrons in the medium, from which electron avalanches can be initiated upon application of an electric field, but are associated to an individual avalanche so that the number of existing electrons does not play a role. Implicit in the formulation for the streamer criterion is also that the individual avalanches can develop strong local gradients, i.e. the discharge is filamentary from its onset. This last condition may be compromised if the number of simultaneous primary avalanches is high, in which case one expects the adjacent avalanches to overlap, smoothing out the local gradients and leading to a homogeneous breakdown condition [105].

The minimum pre-ionization density, $n_{0,\min}$, required for overlap of the primary avalanches is given, as proposed in [105, 147], by:

$$n_{0,\min} = \frac{3}{4\pi R_{\text{crit}}^3},$$

where R_{crit} is the critical radius of the avalanche head when the induced electric field is of the order of the applied field, and can be estimated from [59]:

$$R_{\text{crit}} = \sqrt{\frac{4D_e}{\mu_e E_0} x_{\text{crit}}} \approx \sqrt{\frac{4D_e}{\mu_e E_0} \frac{1}{\alpha} \ln\left(\frac{4\pi\varepsilon_0 E_0}{e\alpha^2}\right)}.$$

In this expression, a first-order correction for the electron diffusion has been introduced, D_e and μ_e are the electron diffusion and mobility respectively, E_0 is the applied electric field and x_{crit} is the avalanche length at the moment of streamer formation. Through the Einstein relation, $D_e/\mu_e = kT_e/e = \frac{2}{3}\varepsilon_e$, where T_e is the electron temperature and ε_e the electron energy in eV. Both ε_e and α (equation 3.1) are, in the local field approximation, a function of the reduced electric field.

E.g. for a methane/air flame, with the parameters in Table 5.3, and a reduced electric field of $E_0/n = 246$Td (corresponding to an applied voltage of 15kV over the 17mm gap), the electron energy and ionization parameters for the air side, from the previous sections and using BOLSIG+ [72], are $\varepsilon_e = 6.1eV$, $F = 40.1 \cdot 10^{-21} m^2$ and $G = 944.5Td$. For these parameters, the critical radius becomes $R_{\text{crit}} = 330\mu m$ and the minimum pre-ionization density for overlap of the primary avalanches is $n_{0,\min} \approx 7 \cdot 10^9 m^{-3}$. This value is well below the natural pre-ionization of the flame, contributing to the homogenization of the discharge.[8]

Note that, since the pre-ionization region is thinner than the high temperature region, this condition implies a planar ionization front.

[8] Within this approximation, the avalanche length at the moment of streamer formation is $x_{\text{crit}} = 5.8mm$ (of the order of the high temperature thickness, evaluated from Figure 5-3(a)) and the time $t_{\text{crit}} = 25ns$. For the experiments, there will be a limitation by the fixed duration of the high voltage pulses. In addition, the critical time and length, at the moment of streamer formation, can be reduced by increasing the reduced electric field; again, ∼245Td is the practical limit with the available equipment.

Contribution to the non-uniformity of the medium

The presence of a high density plasma seed, precisely within the high temperature region, exacerbates the differences between the *cold* and *hot* regions of the gas. Electron avalanches will, most likely, be initiated where the electron density is higher (at the reaction zone) just where the avalanche multiplication is stronger due to the higher temperature. Therefore, this *ionization seed* contributes to the localization of the discharge.

Breakdown threshold modification

As has been discussed, Meek's condition is independent of the pre-ionization level. However, this seed will impact the initial phase of the charge evolution. Since the electron avalanches are close enough to overlap, a 1D model is here developed to evaluate the impact of an initial plasma Gaussian density on the electron avalanche and its implications on Meek's condition[9]. Note that this is not a criterion for streamer formation in the classical sense since the filamentary structure is replaced by a planar ionization front.

Starting from the 1D governing equations for the gas discharge described in Section 4.2.1, neglecting the diffusion terms and the ion drift, and defining the non-dimensional variables:

$$\tau = \alpha(E_\infty)\mu_e E_\infty t, \quad \xi = \alpha(E_\infty)x, \quad \bar{E} = \frac{E}{E_\infty}, \quad \bar{n}_{i,e} = \frac{e n_{i,e}}{\varepsilon_0 E_\infty \alpha(E_\infty)},$$

the non-dimensional equations to be solved become:

$$\frac{\partial \bar{n}_e}{\partial \tau} - \frac{\partial\left(\bar{n}_e \bar{E}\right)}{\partial \xi} = \bar{n}_e |\bar{E}| \exp\left(\bar{G}_\infty \left(1 - \frac{1}{|\bar{E}|}\right)\right) \tag{5.4}$$

$$\frac{\partial \bar{n}_i}{\partial \tau} = \bar{n}_e |\bar{E}| \exp\left(\bar{G}_\infty \left(1 - \frac{1}{|\bar{E}|}\right)\right) \tag{5.5}$$

$$\frac{\partial \bar{E}}{\partial \xi} = \bar{n}_i - \bar{n}_e, \tag{5.6}$$

where the parameter $\bar{G}_\infty = \frac{G}{E_\infty/n}$ is the exponential factor in Townsend's formula, equa-

[9]Throughout this dissertation the word breakdown is not being used in the classical Townsend breakdown sense in which there is a self-sustained current controlled by secondary electron emission at the cathode. In general, breakdown here is referred to having reached Meek's criterion, which does not require a conduction current to bridge the gap, but rather refers to an ionization front that is self-sustained.

tion 3.1, evaluated at $E{=}E_\infty$ far from the initiation seed. The initial conditions are a Gaussian plasma, with amplitude $n_{e,0}$ and width δ_i, and the unperturbed electric field:

$$\bar{n}_{e,i}(\xi, \tau = 0) = \lambda \exp\left(-\frac{4\xi^2}{\beta^2}\right), \qquad \bar{E}(\xi, \tau = 0) = 1,$$

where λ and β are the free parameters that depend on the initial conditions:

$$\lambda = \frac{e n_{e0}}{\varepsilon_0 E_\infty \alpha(E_\infty)}, \qquad \beta = \delta_i \alpha(E_\infty).$$

In addition, it is assumed that the inter-electrode distance is much larger than the reference length, $\alpha(E_\infty)^{-1}$, so that the seed propagates in an infinite medium and, far from the starting point, the variables $\bar{n}_e \approx 0$, $\bar{n}_i \approx 0$, and $\bar{E} = 1$, remain unperturbed.

With these assumptions, equations 5.4-5.6 are combined to yield an equation for $\bar{E}$:

$$\frac{\partial \bar{E}}{\partial \tau} - \bar{E}\frac{\partial \bar{E}}{\partial \xi} = F\left(\xi, \bar{E}\right) = -\lambda \exp\left(-\frac{4\xi^2}{\beta^2}\right)\bar{E} + \bar{E}\int_1^{\bar{E}} \frac{|\bar{E}'|}{\bar{E}'} \exp\left(\bar{G}_\infty\left(1 - \frac{1}{|\bar{E}'|}\right)\right) d\bar{E}',$$
$$\bar{E}\left(\xi, \tau = 0\right) = 1, \tag{5.7}$$

which can be solved using the method of characteristics, at least at an initial stage.

Equation 5.7 is used to derive a modified Meek's criterion in the presence of an initial Gaussian plasma with parameters λ and β.

For the streamer mode electric breakdown occurs when a sharp ionization front propagates into a non-ionized gas, leaving a non-equilibrium plasma behind. The formation of this ionization wave requires a non-linear balance between the ionization and the screening of the electric field. This condition is normally formulated by saying that the electric field induced by the space charge is of the same order as the external field, in the body of the ionized region, and gives Meek's criterion: $-\xi_{\text{crit}} \approx 20$ (with the sign criteria used, the anode directed ionization avalanche moves towards negative values of ξ).

Here, the condition will be imposed by stating that $\bar{E}\left(\xi^*, \tau_{\text{crit}}\right) = 0.1$ for the first time, so that the induced field *almost* cancels the applied field at some point ξ^*. Note that ξ^*, where $\bar{E} = 0.1$, and ξ_{crit}, ionization front position at τ_{crit}, are not equal, as the ionization

front will be ahead of the plasma left behind. The latter is given by the position where the distortion of the electric field, $|\frac{\partial \bar{E}}{\partial \xi}|$, is maximum.

Figure 5-7 shows the impact of the Gaussian amplitude, λ, on how fast the electric field is distorted by the space charge. There are two distinct regions depending on whether λ is greater or smaller than 1 (initial density of the order of the characteristic ionization density).

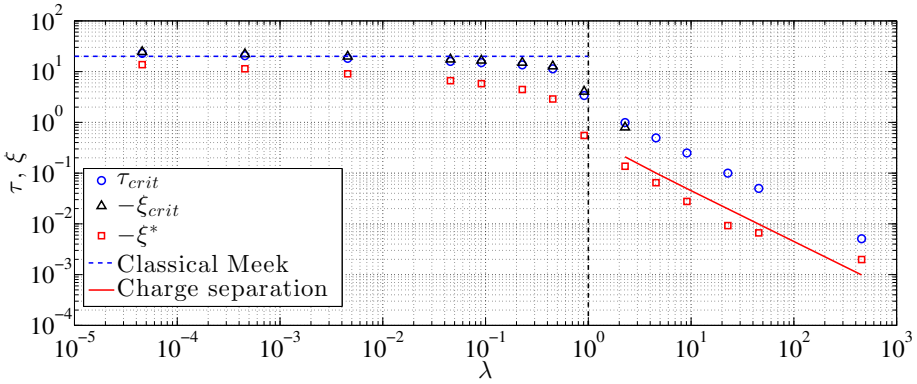

Figure 5-7: Meek's criterion modified to include a Gaussian seed of electrons and ions. Effect of the initial Gaussian density amplitude, λ, for parameters $\beta = 0.99$ and $\bar{G}_\infty = 4.42$.

For $\mathcal{O}(\lambda) << 1$, the charge created by electron impact ionization becomes greater than the initial charge for times lower than τ_{crit}, so that the distortion of the electric field is mainly due to the newly created charge and the criterion $\bar{E} = 0.1$ is representative of an ionization wave being formed, that leaves a quasi-neutral plasma behind. Increasing λ slightly expedites the avalanche evolution, but with a logarithmic dependence. Note that, since the ionization front travels at the drift velocity, $-\xi_{\text{crit}}$ and τ_{crit} are similar.

For $\mathcal{O}(\lambda) >> 1$, τ_{crit} rapidly decreases with λ. The charge that has been created by electron impact ionization at τ_{crit} is negligible, compared to the initial charge, so that the electric field shielding is mainly due to a displacement of the initial electron profile. The analytical solution for electric field shielding due to a separation, ξ_0, of two identical Gaussian profiles of opposite charge is plotted in Figure 5-7 for comparison. The condition is that, where the net space charge is zero, the induced electric field is -0.9, which simplifies to:

$$\xi^* = \frac{\xi_0}{2} = \frac{\beta}{2}\text{erf}^{-1}\left(-\frac{1.8}{\beta\lambda\sqrt{\pi}}\right) \underset{\lambda>>1}{\approx} -\frac{1.8}{4\lambda}.$$

Therefore, for $\mathcal{O}(\lambda) > 1$, the solution plotted in Figure 5-7 is not a criterion for the formation

of a planar ionization front but rather for shielding of the initial plasma. This does not mean that a planar ionization front will not form from a dense seed, rather that the criterion used is not representative of its initiation, which will occur at a later time.

Moreover, the solution to equation 5.7 far from the seed has no memory of the initial plasma (the term proportional to $\sim \exp\left(-\frac{4\xi^2}{\beta^2}\right)$ vanishes). The asymptotic solution is a front that propagates with unchanged shape, and is independent of the initial plasma density. The asymptotic anode-directed ionization front also has unchanged amplitude, and carries a constant excess negative charge near its forward edge. The ionization continues, but the new electrons stay behind to neutralize the ions, and a plasma *trail* is left behind.

The impact of the Gaussian width, β, is shown in Figure 5-8. Again, there are two distinct regions. For $\mathcal{O}(\beta) < 1$, there is little effect of increasing β, since the width of the seed is much smaller than the ionization mean free path and the behavior is essentially that of an initial sheet. For $\mathcal{O}(\beta) >> 1$, the solution collapses to the 0D solution as ionization is equally likely for all ξ, there is no planar ionization wave.

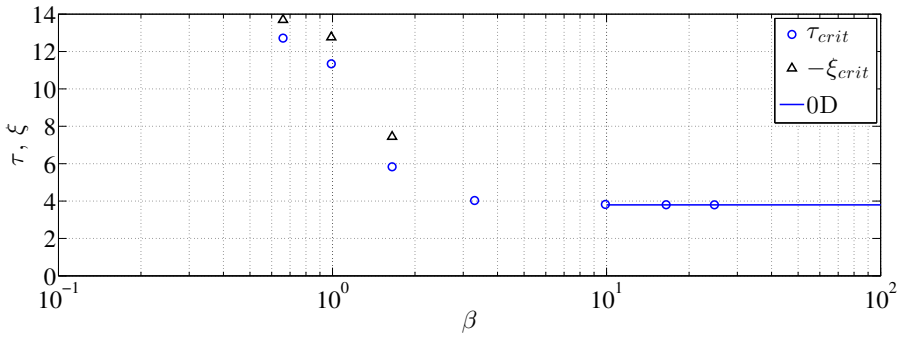

Figure 5-8: Meek's criterion modified to include a Gaussian seed of electrons and ions. Effect of the initial Gaussian density width, β, for parameters $\lambda = 0.456$ and $\bar{G}_\infty = 4.42$.

Note that, for the negatively charged planar ionization front in an unbounded domain considered, there is no amplification of the electric field in front of the ionization wave (which appears for filamentary streamers). This amplification requires the inclusion of 2D effects or boundary conditions.

Finally, in order to relate this analysis to the flame experiments the following conditions are used: $E_\infty = 8.82 \cdot 10^5$V/m, atmospheric gas at 2000K, $F = 3.73 \cdot 10^{-20} m^2$ and $G = 1062 Td$, Gaussian density width $\delta_i = 0.6mm$ and amplitude $n_{e0}/n = 10^{-8}$-10^{-7}. The relevant

parameters become: $\bar{G}_\infty$=4.42, $\beta = 0.99$ and $\lambda = 0.46$-4.6. A couple of comments can be made. First, Meek's condition will not be greatly influenced by the presence of an initial Gaussian density (in terms of length and time required for an ionization wave to form), although for very dense seeds shielding of the initial plasma will precede the formation of the ionization wave, which will develop from the displaced negative density. Second, for the experimental parameters used in Section 5.4.1, the expected chemi-ionization plasma density is of the order of the characteristic ionization density (by electron impact). Use of higher electric fields can lower the parameter λ, favoring the relative production of secondary electrons, and β, favoring a planar ionization wave instead of the 0D solution.

Note that the initial plasma thickness (chemi-ionization length-scale) is $\mathcal{O}(\beta)\sim 1$, whereas the length-scale for the formation of an ionization front is $\mathcal{O}(-\xi_{\text{crit}})\sim 10$. This latter scale needs to be of the order of the high temperature region thickness $d_h\alpha(E_\infty)$ for the ionization front to develop within the flame. In addition, the time for this condition to be reached, needs to be shorter than the width of the voltage pulse $\tau_{\text{crit}} < \alpha(E_\infty)\mu_e E_\infty \Delta t$.

5.3.3 Spatial structure of plasma-species creation

In addition, the enhancement of the reduced electric field in the high temperature zone provides a spatial structure to the electron impact excitation and dissociation reactions. Moreover, a temperature profile such as the one in Figure 5-2, translates into a similar profile for the reduced electric field so that, in general, E/n in the flame will be 5-8 times higher than outside.

The effect of the variation of E/n on the energy share between the different electron impact reactions has been evaluated by solving the Boltzmann equation using BOLSIG+ [72]. As in Section 5.3.1, the electron impact reactions used are those proposed by Morgan [123].

Figure 5-9 illustrates how the energy is spent, as a function of the reduced electric field, for a stoichiometric mixture of methane/oxygen with 73% dilution in nitrogen, argon and helium respectively. In the plots, the dissociation reactions (labelled *dis*) correspond to electronic excitation with energies in excess of those required to break the molecular bonds (i.e. 4.25eV for CH, 9.8eV for N_2 and 5.15eV for O_2), and the ionization of all species has been grouped. The blue and pink vertical regions correspond to reduced electric fields of

36Td and 246Td and highlight the positioning of the ambient and peak flame temperature regions respectively (for the experimental parameters later used).

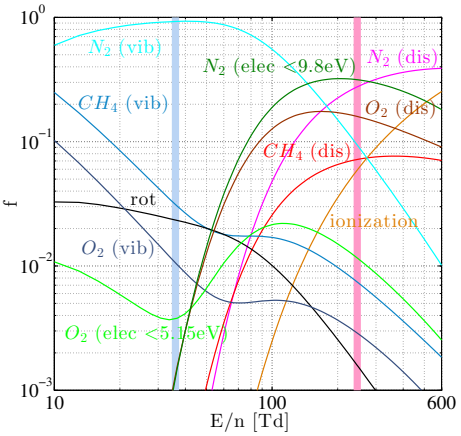

(a) Nitrogen dilution.

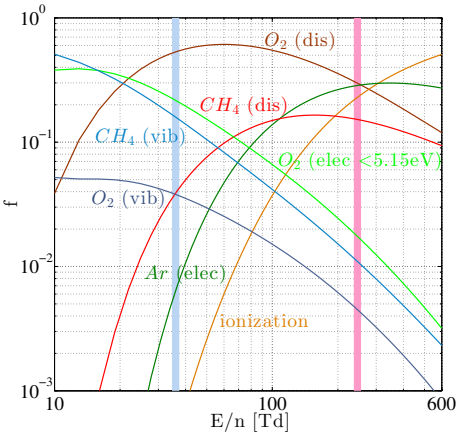

(b) Argon dilution.

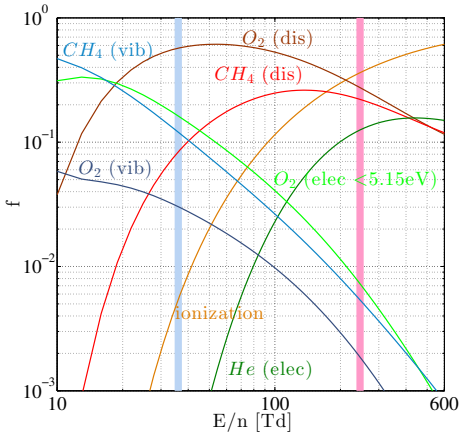

(c) Helium dilution.

Figure 5-9: Energy loss fractions, f, to different electron impact reactions for stoichiometric methane/oxygen diluted in different inert gases (73% dilution). Calculated using BOLSIG+.

Figure 5-9(a) shows that, for the most frequent case of dilution in nitrogen, there is low energy excitation in the *cold* sides whereas the high temperature region is situated close to the peak dissociation (and therefore radical formation) of both O_2 and CH_4. At low reduced electric fields, the vibrational excitation of nitrogen absorbs all the energy, so that to activate the dissociation reactions higher reduced electric fields are needed. In this case, which is precisely the practical case, the flame sits in an interesting region of species production so that, even if the gas discharge is not confined to the flame, the radicals and

active species are primarily produced close to the flame front.

Note that, although the fractional energy that goes to dissociation peaks at $E/n \approx$200-250Td, by increasing the reduced electric field the amount of ionization is increased, and more electrons are accelerated, increasing the energy that can be coupled to the gas while still being in a region where dissociation is important.

For dilution in the monoatomic gases, either argon or helium, a large part of the energy is again spent in vibrational excitation in the *cold* ends. However, the dissociation now peaks at slightly lower reduced electric fields, since there is no nitrogen to clip the EEDF from its high energy tail. Dissociation therefore happens in a broader region that extends to lower temperatures. Also, note that by using helium or argon, instead of nitrogen, ionization and dissociation are favored, with a greater share of the energy going to these processes.

5.4 Experiments of RPND in counterflow nonpremixed flames

In what follows, a series of experiments are presented to explore the selective breakdown of regions of favorable ionization within the flow field of a counterflow nonpremixed flame. As discussed in Section 5.3, the situation is similar to the GBD structure explored in Chapter 3 where the coupling is reinforced by the presence of the chemi-ionization electrons, that serve as an initial condition for the development of the electron avalanches upon application of a voltage pulse.

E.g. for the flame specifications of Table 5.3, the parameters that enter the GBD model of Section 3.2.2 are $K \approx 6.8$, $d_h/d_c \approx 0.9$, $p_0 d_h \approx 5.3 mm \cdot atm$, $F = 40.1 \cdot 10^{-21} m^2$ and $G = 944.5 Td$. Within the approximation, the applied voltage needs to be above 15kV to reach Meek's criterion in the *hot* zone alone. Note that, in reality, this is an underestimation of the required voltage level since the electron avalanches are initiated at the center of the flame so the effective length that the electrons can travel before reaching the *cold* region is only half d_h. Unfortunately, the power supply available could not go beyond this voltage level, which limited the exploration of the envelope of the confined emission. For that reason, the

approach taken has been to explore some meaningful examples to verify the different coupling options and their characteristics.

In Section 5.4.1, voltage pulses of ∼15.5kV amplitude were applied and indeed the excitation by the RPND was confined to the flame region.[10]

5.4.1 Plasma coupling to the flame: ns-resolved photography

Selective RPND excitation of the flame was experimentally observed for the flame parameters of Table 5.3. The appearance of the base flame was similar to the one shown in Figure 2-4(a). In these experiments, the applied RPND voltage pulses were of ∼15.5kV amplitude, as seen by the discharge cell, 20ns duration, and were delivered at a repetition rate of 25kHz.

Table 5.3: Flame parameters used in the ns-resolved photography experiments.

a $[1/s]$	Dilutant	$X_{O_2,\infty}$	$X_{CH_4,-\infty}$	Z_{st}	ϕ	Power $[W]$	T_{max} $[K]$
25	N_2	0.21	1	0.055	12.8	65	2050

Photographs of the evolution of the plasma, during application of a voltage pulse, were taken with an exposure time of 0.5ns and a delay between images of 1ns to record the emission evolution in space and time (Section 2.7.2)[11]. The mean of 10 images, with equal delay with respect to the start of the pulse, was used in the results presented in Figures 5-11 and 5-12.

Figure 5-10 shows representative sequential images of the emission evolution during application of the 1000$^{\text{th}}$ pulse in a train. With the exposure time used, the emission corresponds

[10]The estimates presented are consistent with experiments reported in the literature by W. Sun et al. [204] using RPND discharges across a counterflow nonpremixed flame. The experiments in [204] used a burner (with distance between nozzles of 16mm) at 9600Pa and helium-diluted flames, with a degree of dilution ∼70% in both streams, and a strain rate of $400s^{-1}$. These conditions led to very diffuse temperature profiles and the measured temperature at the electrodes was 600K. With these parameters, the estimated FWHM of the temperature profile is 7.25mm and the peak temperature 1615K, both obtained using Cantera [66]. The parameters for the GBD model then become $K \approx 2.7$, $d_h/d_c \approx 1.66$, $p_0 d_h \approx 0.7 mm \cdot atm$, $F = 50.1 \cdot 10^{-21} m^2$ and $G = 545 Td$. For the applied voltage of 7.6kV used in those experiments, the GBD model predicts breakdown of the full gap, as is reported in [204] (see Figure 2 of this reference). It is interesting to note that the possibility of confinement to the flame region is favored at higher pressures due to the tongue-like shape of the breakdown maps.

[11]The ns-resolved photography experiments, as well as the spectroscopy measurements of Sections 5.4.2 and 5.4.3, were performed with the help of Dr. A. Starikovskyi.

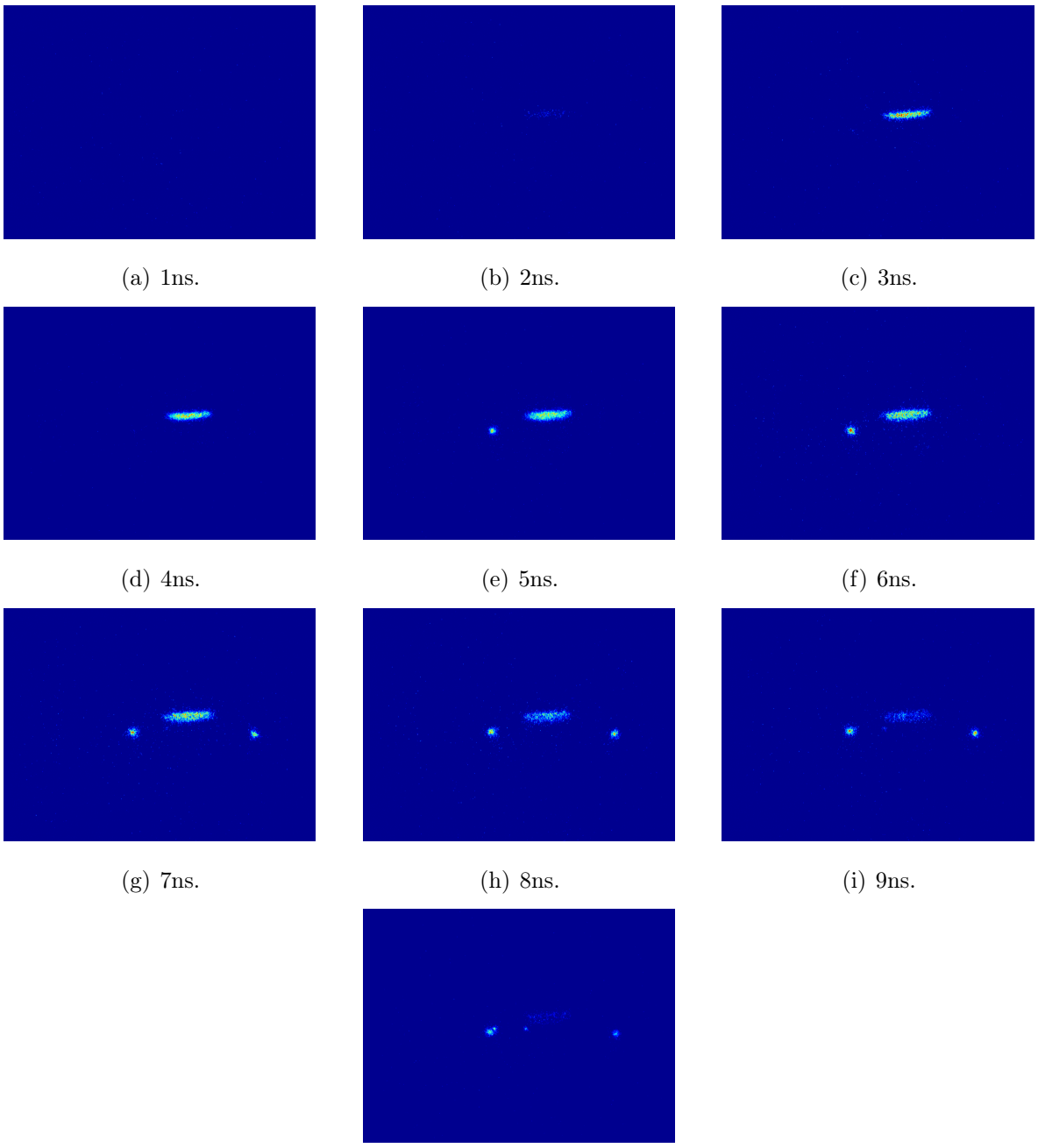

(a) 1ns. (b) 2ns. (c) 3ns.

(d) 4ns. (e) 5ns. (f) 6ns.

(g) 7ns. (h) 8ns. (i) 9ns.

(j) 10ns.

Figure 5-10: Time evolution of the plasma emission coupled to the flame. Images correspond to sequential photographs during pulse number 1000 in a train. The exposure time is 0.5ns.

almost exclusively to transitions of the second positive system of molecular nitrogen [193]. Note that, without voltage pulse application, no light is captured by the camera, even in the presence of the flame, so that the emission corresponds to the RPND excitation. The localization of the discharge to the regions of high E/n is clear in these images: the emission comes from either the flame region (low n) or from the sharp edges of the square electrodes (high E), seen by the circular emission regions. The emission is in all cases uniform.

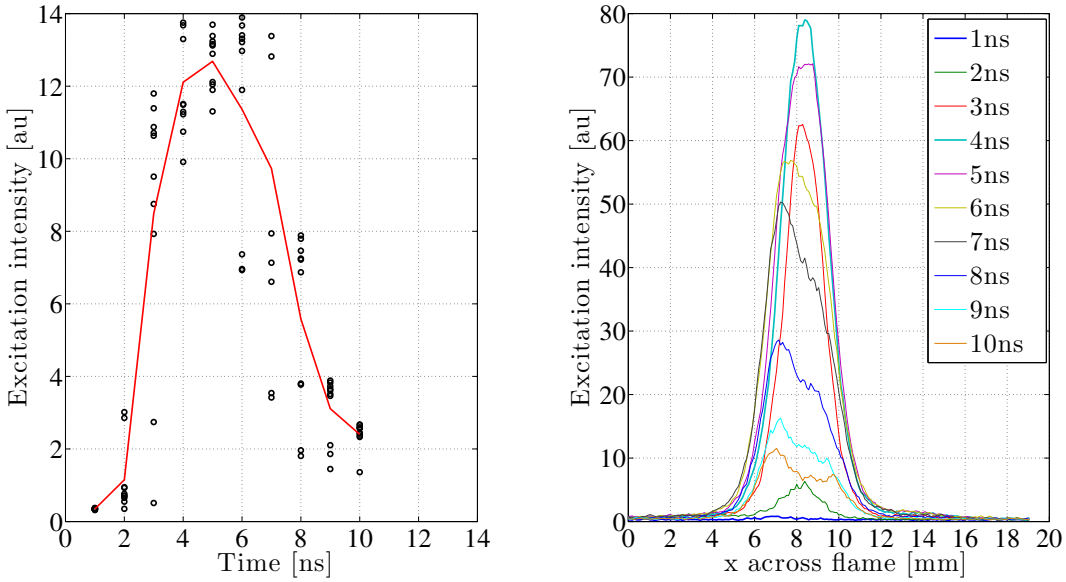

(a) Time evolution.

(b) Spatial profile.

Figure 5-11: Time evolution of the integrated plasma emission and spatial profiles across the flame (pulse number 1000). x is measured from the bottom jet. The black circles in (a) correspond to individual photographs and the red line is the mean of all images taken.

From these images, the evolution in time of the integrated emission of a region 9.5mm along the center of the flame and 17mm across the flame, is shown in Figure 5-11(a). The black circles correspond to the 10 individual photographs taken and the red line is the mean of those images. The emission lasts for ∼10ns, consistent with the time during which high voltage is applied. The evolution in time of the emission profiles *across* the flame are shown in Figure 5-11(b). The peak in emission occurs at 4ns and the localization of the profiles is evident: out of a region 6mm wide, there is no emission.

The experiment was repeated for pulses number 2, 100 and 10000 in a train. Figure 5-12 compares the evolution in time of the integrated emission and of the emission profiles across

the flame (at peak emission) for the different pulses. The profiles are very similar in all cases, indicating that all the pulses have an equivalent impact on the gas. Note that the slight shift of the profile of pulse 10,000 with respect to the other pulses can be attributed to slight regulations that were made during the length of the experiment to the flow of the nitrogen shroud. Table 5.4 summarizes the FWHM of the emission at 4ns.

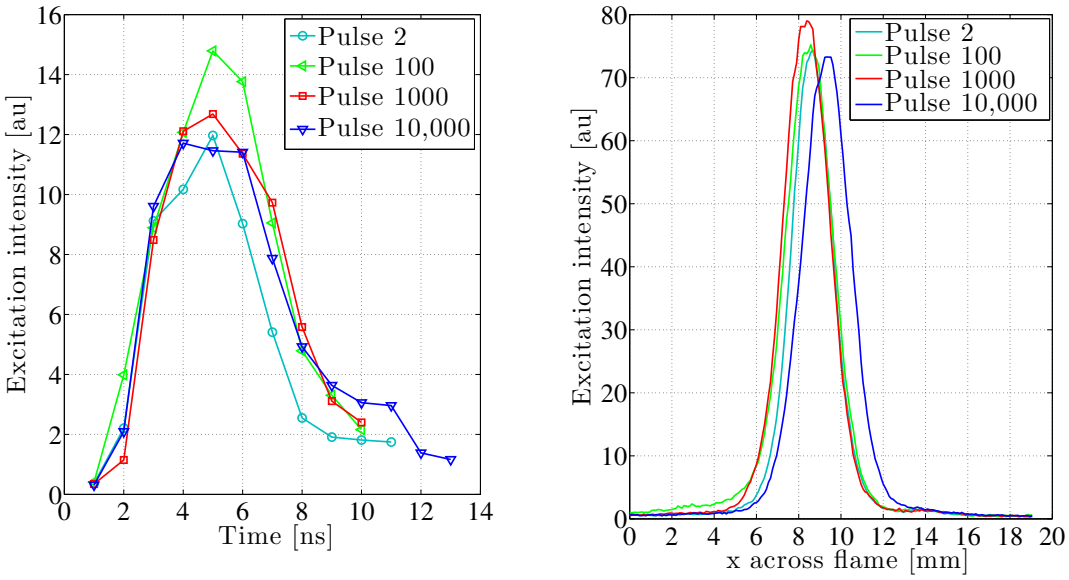

(a) Time evolution.

(b) Spatial profile at peak emission, 4ns.

Figure 5-12: Time evolution of the integrated plasma emission and spatial profiles across the flame (pulse numbers 2, 100, 1000 and 10000). x is measured from the bottom jet.

Table 5.4: Measured FWHM of plasma emission.

Pulse number	FWHM $[mm]$
2	2.2
100	2.6
1000	2.6
10000	2.7

A final comment must be made related to the, globally, very-fuel rich flame used in this experiment. In this case the fuel stream was pure methane, leading to a sooty flame (Figure 2-4(a)), and arising the doubt of whether there could be a possible reinforcement due to the presence of soot particles [117]. This point was addressed by using non-sooty,

highly diluted flames for the rest of the experiments presented in this Chapter for which, the same coupling was observed. Direct photographs of the coupling, using highly diluted and undiluted fuel, are shown in Appendix E.

5.4.2 Coupling to the fuel stream

Confinement to the flame front can be disturbed by using dilutants with different electrical properties for the fuel and oxidizer streams. E.g., by diluting the fuel in helium and the oxidizer in nitrogen, selective excitation of the full fuel stream is possible, as shown in Figure 5-13. The parameters used in this case are summarized in Table 5.5.

Table 5.5: Flame parameters for selective RPND excitation of the fuel stream.

a $[1/s]$	Dilutant	$X_{O_2,\infty}$	$X_{CH_4,-\infty}$	Z_{st}	Power $[W]$	Voltage $[kV]$	f $[kHz]$	Number of pulses
40	N_2 (oxidizer), He (fuel)	0.41	0.125	0.23	225	15.5	25	Continuous 100

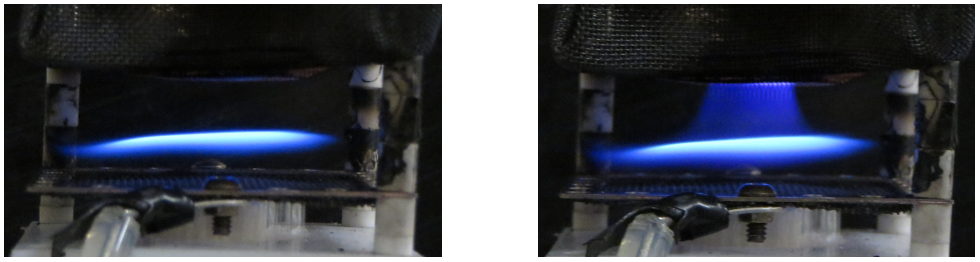

(a) Base flame. (b) RPND coupled to the fuel stream.

Figure 5-13: Selective RPND excitation of the fuel stream by choice of dilutants. Top jet (fuel) is diluted in helium, bottom jet (oxidizer) is diluted in nitrogen. Applied voltage pulses of 15.5kV at 25kHz.

Figure 5-14 shows the spatially resolved, across the flame, emission around the 431.4nm peak of the CH band without applied pulses and for the accumulation of 100 RPND pulses (integrated emission in 4ms). The experimental setup is the one described in Section 2.7.3.

The peak of excited CH marks the position of the flame front and it can be appreciated how the peak is ∼18% more intense after applying 100 voltage pulses. In addition, when applying the RPND strategy coupled to the fuel stream, the fuel is *activated*, shown by the

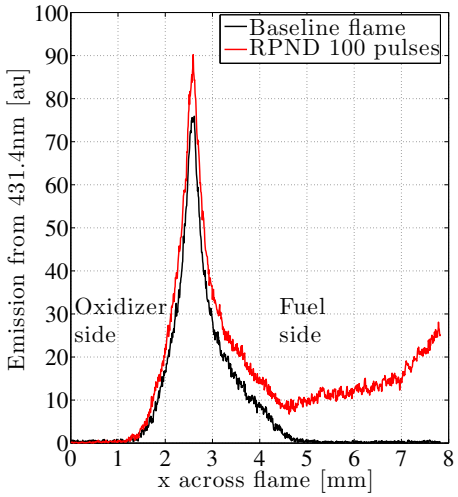

Figure 5-14: Spatially resolved emission from CH^* at 431.4nm, case of selective RPND excitation of the fuel stream by choice of dilutants. x is measured from the bottom jet, in this case, the origin of the measurement is arbitrary.

presence of excited CH out of the flame front region, and in the fuel side. This indicates that there is a pre-cracking of the fuel into smaller segments on the fuel side as a result of the high voltage pulses. This is consistent with the plasma species structure analysis of Figure 5-9(c) in which it was seen that, when diluted in helium, dissociation of CH_4 extends to lower temperatures.

5.4.3 Loss of confinement and transition into a ns-spark

If the electric field in the gap is above a certain threshold, confinement to the flame front, or one of the streams, can no longer be sustained and electrical breakdown occurs in the full gap. At atmospheric pressure, transition into a nanosecond-spark is difficult to avoid and high-conduction current discharges are usually characterized by constriction into an incipient arc, with significant gas heating involved [145].

With the mesh-to-mesh electrode system at hand, the appearance for full gap breakdown (and nitrogen as the dilutant of choice) is that of disorganized filamentary discharges, that bridge the gap between the anode and the cathode, and are scattered in the whole discharge volume.

To eliminate the randomness in the positioning of the discharge, in this section, a pin electrode was attached to the anode mesh so that the filamentary discharge was fixed in space. In this case, the pin provides the locally high electric field for the spark creation. The parameters used are those summarized in Table 5.6. Digital camera photographs of the baseline flame and during continuous application of RPND are shown in Figure 5-15. Figure 5-15(b) shows a nanosecond-spark that perforates the flame and modifies the flame structure: the emission front is displaced and visible soot emission appears, indicating fuel-rich burning.

Table 5.6: Flame parameters for ns-spark experiments.

a $[1/s]$	Dilutant	$X_{O_2,\infty}$	$X_{CH_4,-\infty}$	Z_{st}	Power $[W]$	Voltage $[kV]$	f $[kHz]$	Number of pulses
65	He	0.16	1	0.13	140	14	25	100, 1000

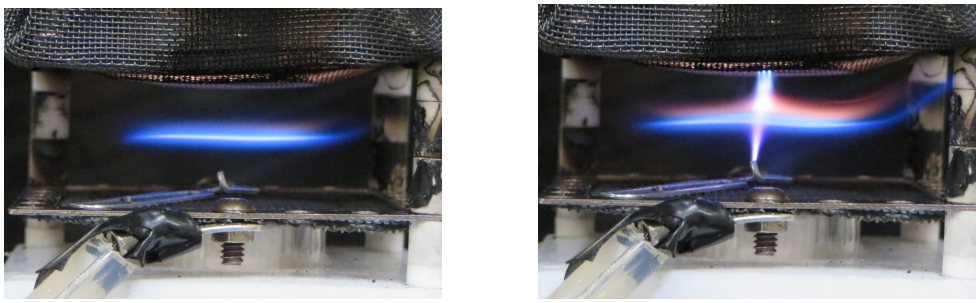

(a) Base flame. (b) RPND loss of confinement.

Figure 5-15: Nanosecond-spark across flame using pin-to-mesh electrodes (pin is on bottom, the powered anode). Applied voltage pulses of 14kV at 25kHz.

To illustrate the impact of the ns-spark on the flame structure, Figure 5-16 shows the spatially resolved, across the flame, emission around the 516nm peak of the C_2 Swan band. The emission is accumulated over the duration of the burst of pulses.

For no applied voltage pulses, the C_2^* emission is restricted to the flame front region. For 100 pulses ($\sim 4ms$), the C_2^* emission extends to the fuel side, demonstrating some kind of fuel reforming. For 1000 pulses ($\sim 40ms$), the time scale of the energy deposition is longer than the characteristic time of the flame flow field (~15ms), so that the flame has enough

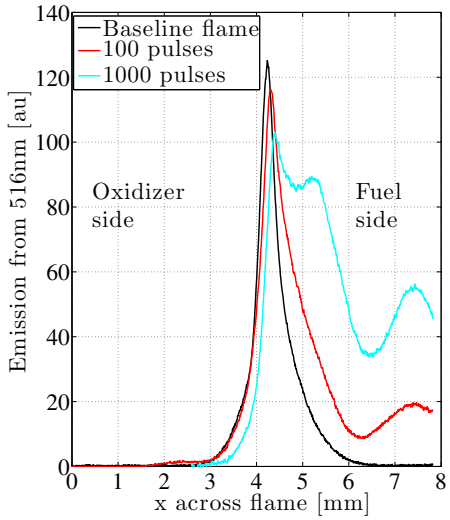

Figure 5-16: Spatially resolved emission from C_2^* at 516nm, case of ns-spark triggered by RPND. x is measured from the bottom jet, in this case, the origin of the measurement is arbitrary.

time to respond to the perturbation. As before, there is fuel reformation on the fuel side, as shown by the presence of excited C_2 in the fuel stream. In addition, the peak C_2^* emission (indicative of the position of the flame reaction front) has shifted to a new position closer to the fuel nozzle. This indicates that the ns-spark facilitates ignition of the surplus fuel through a combination of heating, pre-cracking of the fuel, and, most likely, local stirring of the fluid through shock wave generation. From this image, the flame displacement in the presence of the ns-spark is ~0.8mm.

5.4.4 Energy deposition versus confinement

Time-resolved current and voltage waveforms were recorded for the cases studied. As happened with the experiments in Section 3.3.2, for the *floating* plasmas in this Chapter, there was hardly any difference between the waveforms with and without plasma. The same can be said for RPND confined to the flame (Section 5.4.1) and for the selective excitation of the fuel half alone (Section 5.4.2). This complicates the estimation of the energy deposition in the gas from electrical measurements, as discussed in Section 2.7.1, since the conduction current becomes negligible as compared to the other contributions.

An estimate of the energy was obtained by integrating the product of the measured voltage and current in an interval of 50ns around the application of pulse number 1000 in a train, and comparing the measurements without and with the plasma, as proposed by [143]. The statistics for the energy estimated in this manner (500 waveforms were recorded in each condition), for different flame compositions and maximum applied voltage at 20kHz, are shown in Figure 5-17. The non-zero energy deposition without a flame is an artifact, maybe due to leakage currents, which is subtracted away when compiling the estimates in Table 5.7 (parasitic energy losses).

It has to be emphasized that this is a rough estimation (conduction current is much less than the noise in the measurement!) but some confidence in the measurement arises from the differentiable mean values for the plasma and no plasma cases. From these estimates, the energy deposition in the gas is summarized in Table 5.7.

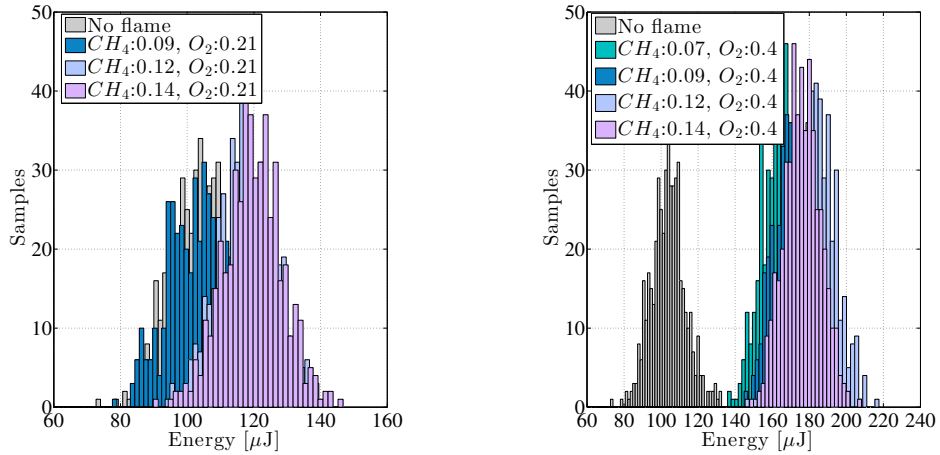

(a) $X_{O_2} = 0.21$. (b) $X_{O_2} = 0.4$.

Figure 5-17: Statistics of energy estimates for case of plasma confined to flame, for argon diluted flames. Histograms represent 500 cases in each condition. RPND of 15.5kV at 20kHz.

The energy deposited per pulse, for the RPND confined to the flame front, is $\sim$1-100μJ, which corresponds to $\sim$0.05-1% of the power of the flame itself. These estimates are consistent with measurements in [143] for a diffuse plasma at atmospheric pressure (what the group at École Centrale Paris called the D-regime) and applied voltage pulses of the same characteristics as the ones here used. The estimate is also lower than the maximum capacitive energy that can be stored in the discharge cell (using the capacitance estimate of

Table 5.7: Energy estimates for confined plasma strategy, upon RPND application.

Flame						Plasma			
a $[1/s]$	Dilutant	$X_{O_2,\infty}$	$X_{CH_4,-\infty}$	Z_{st}	Power $[W]$	Voltage $[kV]$	f $[kHz]$	Energy $[\mu J/\text{pulse}]$	Power $[W]$
40	Ar	0.4	0.14	0.59	155	15.5	20	75±29	1.5±0.6
40	Ar	0.4	0.12	0.63	132	15.5	20	81±29	1.6±0.6
40	Ar	0.21	0.14	0.42	116	15.5	20	16±31	0.3±0.6
40	Ar	0.21	0.12	0.46	116	15.5	20	15±29	0.3±0.6

Section 3.4) at the peak voltages considered, which is $\sim 285 \mu$J/pulse.

Therefore, the main limitation of a diffuse plasma that does not bridge the gap between electrodes is the low energy per pulse that can be deposited in the gas. A way to increase the power, while respecting the confinement, is to increase the pulse repetition frequency (Section 5.4.5) or to push the envelope of the confined strategy by increasing the applied voltage amplitude. These experiments could not be pursued since the available power supply was already being used at its maximum capabilities.

A circuit model for the *floating* discharge is proposed in Section 6.5.2.

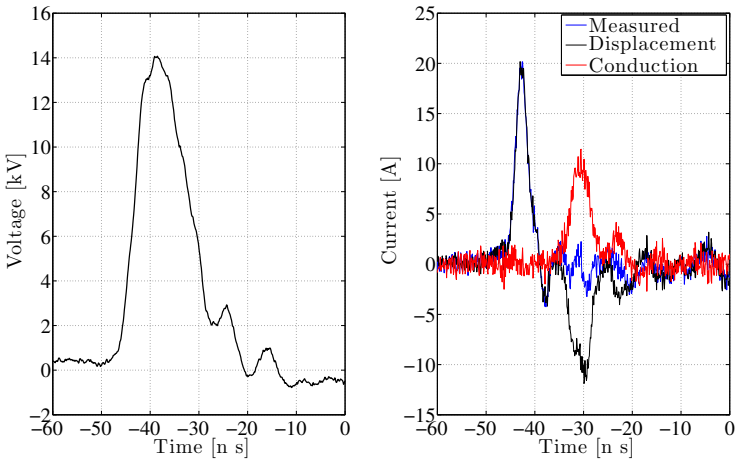

Figure 5-18: Current and voltage waveforms for ns-spark of Table 5.6. The measurable conduction current in this case is shown in red.

A completely different situation arises for the ns-spark of Section 5.4.3. In this case, the conduction current becomes measurable, as shown in Figure 5-18. The energy deposition, estimated in this case through the conduction component of the current, is $\sim 325 \mu J/$pulse

or a power of 8W, which corresponds to $\sim$ %6 of the flame power. This value can be greater than the maximum capacitive energy that can be stored in the discharge cell since the equivalent circuit becomes a resistance in parallel with the capacitance (see Section 6.5.1 for justification).

For this more energetic discharge, the results of Section 5.4.3 clearly showed a modification of the flame properties.

5.4.5 Frequency effect

The effect of increasing the electrical power, for the flame-confined strategy, by increasing the pulse repetition frequency is illustrated in this part. To this end, the impact on the emission spectrum of an argon-diluted flame is evaluated (the conditions used are summarized in Table 5.8).

Table 5.8: Flame parameters used to obtain the emission spectrum of Figure 5-19.

a $[1/s]$	Dilutant	$X_{O_2,\infty}$	$X_{CH_4,-\infty}$	Z_{st}	ϕ	Power $[W]$	T_{max} $[K]$	Voltage $[kV]$	f $[kHz]$
40	Ar	0.29	0.12	0.54	0.83	130	1980	15.5	20

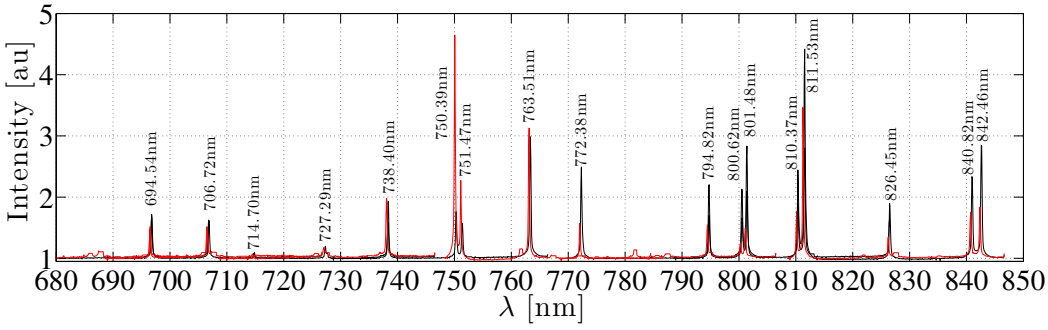

Figure 5-19: Time-integrated spectrum for RPND application to an argon diluted flame. The argon excitation in the flame by RPND is plotted in red, for comparison, the spectrum of an argon lamp is shown in black.

The time-integrated and spatially averaged spectrum from the center of the plasma is shown in Figure 5-19. The peaks observed, in the range 680-850nm, correspond to argon

excitation, which is illustrated by comparison of the RPND emission to that of an argon lamp in the same range. For the flame alone, without voltage pulses, the peaks are not seen.

The integrated emission of the most intense peaks is plotted against the pulse repetition frequency in Figure 5-20. The emission has been normalized with the values at 25kHz. The dependency is almost linear, showing that the effect of increasing the frequency is to accumulate more pulses within a given volume of gas. E.g., for an estimated residence time of the fluid within the region of emission of ∼12ms, a pulse repetition frequency of 10kHz means that ∼120 pulses are deposited in a given volume of gas, whereas for f=25kHz this number is increased by a factor of ∼2.5 (as the emission of Figure 5-20).

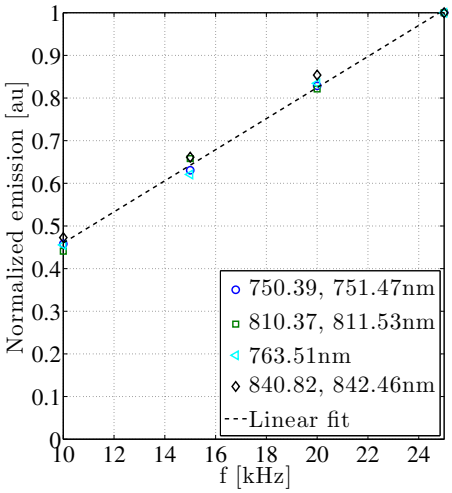

Figure 5-20: Effect of the pulse repetition frequency on the time-averaged argon excitation for an argon-diluted flame. The emission has been normalized with the values at 25kHz.

5.4.6 Flame modification for the RPND flame-confined strategy

Previous work in the field using RPND plasmas at atmospheric pressure for flame stabilization and inflammation, has shown little or no impact on the flame properties when using diffuse, low conduction current mode plasmas, and significant impact when applying filamentary, high conduction current discharges (or ns-sparks). For example, [157,158] achieved stabilization of a lean premixed propane-air intermittent flame by using ns-sparks and observed no effect when using a diffuse plasma. They attributed the different response to the large difference in energy deposition per applied pulse: $\sim 10\mu J$ for the diffuse regime as com-

pared to over $100\mu J$ for the filamentary plasmas. Flame inflammation studies, when using RPND, have also led to the same conclusion. [150] observed two types of discharges, with low and high conduction current respectively and, for the high conduction mode, measured a significant increase in both the production of atomic species and the gas heating (as well as electrode erosion). Again in this case, the high current mode was able to achieve ignition of a premixed propane-air mixture whereas the low current mode was not.

The main complication that arises, when using ns-sparks, is that the strategy is no longer purely non-thermal, since the discharge comes accompanied by significant gas heating (and shock wave generation) that also affect the properties of combustion. In this case, it is difficult to decouple the impact of the heating itself from the increase in energy deposition and, in general, a combination of both is what enables the flame modification (see literature review in Section 1.4). To fully decouple the non-thermal from the thermal contribution, high conduction currents (which come accompanied by heating) need to be avoided. Unfortunately, this comes at the expense of significantly decreasing the energy deposition.

For the plasmas in this Chapter, the relative energy deposition between the confined plasmas as compared to the ns-sparks, presents a similar picture. Moreover, from the experiments of Sections 5.4.1 through 5.4.3, there was a large modification of the flame structure for the ns-spark across the flame (accompanied by a shift in the position of the flame and soot formation) whereas for the confined plasma only the superimposed plasma emission was observed.

However, the difference between these confined plasmas, with respect to other diffuse plasmas presented in the literature, is that there is a localization of the plasma-created species close to the reaction zone (instead of being distributed in the whole volume). This leaves the question open of whether or not the low energy deposition can be compensated by the spatially-targeted energy coupling.

To answer this question, extension of the dilution limit by applying RPND was attempted. In this test, a fixed air-like mixture was used in the oxidizer and the mole fraction of methane, in the diluted fuel stream, was gradually decreased until extinction. No extension of the dilution limit was obtained when applying RPND within the limits of the available power supply.

Anyhow, a slight modification of the flame was observed when applying RPND coupled to the flame front. Aside from the plasma emission superimposed to the flame emission, in some instances, the edge of the flame was seen to curve downwards (towards the oxidizer jet exit, which also coincided with the powered anode). The edge-flame modification is here shown through the difference between radial temperature measurements along the flame, in a position close to the peak temperature region, without and with the applied voltage pulses.

The temperature was measured using the laser Rayleigh scattering strategy described in Section 2.8.1 and detailed in Appendix B (Section B.1). Details of the flame parameters used are summarized in Table 5.9.

Table 5.9: Flame parameters for the laser Rayleigh scattering measurements.

a $[1/s]$	Dilutant	$X_{O_2,\infty}$	$X_{CH_4,-\infty}$	Z_{st}	ϕ	Power $[W]$	T_{max} $[K]$	Voltage $[kV]$	f $[kHz]$
40	N_2	0.21	0.2	0.32	1.97	116	1650	15.5	25-30

Radial temperature profiles along the flame, for the baseline case and for RPND at different frequencies are shown in Figure 5-21(a).[12] Figure 5-21(b) shows the temperature increment when applying RPND, with respect to the baseline case, superimposed to a photograph of the flame (black region) to highlight the positioning of the temperature increase measurement.

From the temperature measurements, it can be concluded that the impact of the plasma on the flame structure is very limited. There is essentially no temperature increase in the main flame and there is a slight temperature increase at the flame edge.

In general, the temperature increase associated to the presence of the plasma, can be due to either a thermalization of the plasma or an extension (or spatial distortion) of the burning region, in which case, the temperature increment would be due to heat release by combustion reactions taking place in previously extinguished regions. In the present case, the latter is the most likely situation due to the spatial location of the temperature increment measured.

Note that the maximum temperature measured is ∼1500K, which indicates the profile

[12]The images were taken in an arbitrary order, avoiding increasing and decreasing frequencies, to limit a possible bias due to heating up of the equipment with time.

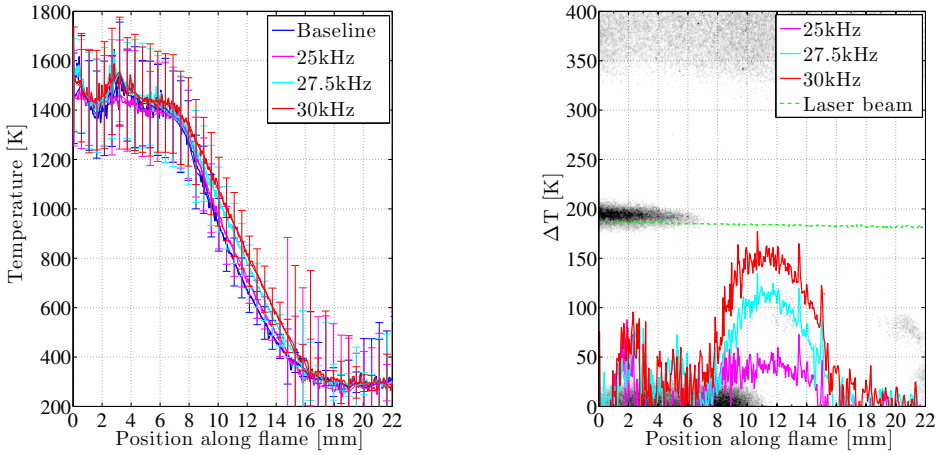

(a) $T(r)$.

(b) Temperature increase.

Figure 5-21: Radial temperature profiles along the flame without and with RPND. The temperature increase, with respect to the baseline case without the applied voltage pulses, is superimposed to a photograph of the flame to highlight the spatial structure. Only half of the flame is shown (symmetry). The radial position is measured from the center of the flame.

was measured close to the peak temperature region but not exactly. Also, the long (∼6mm) temperature drop region can be attributed to the presence of the coflow.

5.5 Summary of findings and implications

In this Chapter, a combination of analytical estimations and experiments has been used to explore the impact the counterflow diffusion flame environment has on the development characteristics of pulsed nanosecond discharges. The problem has been analyzed from the point of view of the gas discharge physics instead of the combustion.

The role of the main flamelet parameters, i.e. choice of dilutant and degree of dilution as well as the strain rate and pressure, has been discussed and the impact on the possible electrical breakdown modes has been explored. From the analytical analysis, it was proposed that the concentration of the discharge to the flame region can be favored by using higher strain rates (that lead to thinner flames) and by the choice and degree of dilution. The substitution of the nitrogen, by helium or argon, facilitates the breakdown, and, a lower degree of dilution, increases the temperature ratio facilitating the confinement. However,

whereas for nitrogen dilution decreasing the degree of dilution also potentially decreases the G parameter in the Townsend formulation (i.e. enhances ionization), for helium and argon dilution an optimum exists in terms of increasing the peak temperature and lowering G. In addition, the use of helium and argon extend the peak of dissociation to lower temperatures (for fixed voltage), by avoiding the nitrogen vibrational modes that absorb most of the energy at the lower fields.

Experiments confirmed that emission triggered by RPND could be fully coupled to the flame region, demonstrating that selective excitation of the flame and in-situ plasma coupling is possible when using pulsed voltage within a range of parameters. In this case, the plasma focusing was due to a combination of the inhomogeneity of the medium and the presence of chemi-ionization electrons. Ns-resolved photography showed that the emission was in the case tested uniform, which was attributed in part to the high level of pre-ionization existent in the flame.

It is interesting to note the tongue-like regions of confinement (for a $p_0 d_h$-applied voltage map) that were presented in Section 3.2.3, indicating the existence of a minimum pressure for confinement to the *hot* zone to be possible. The experiments in this Chapter were all performed with atmospheric pressure flames, which facilitates the confinement, as compared to the experiments at 9600Pa in [204], in which breakdown of the full discharge gap was observed, although the enhancement of E/n at the flame front was also discussed.

In addition to the fully coupled plasma, other breakdown modes that could *naturally* occur in the counterflow configuration, e.g. selective excitation of one of the reactant streams alone or a discharge that bridges the inter-electrode gap, were experimentally observed. Transition between modes depended on both the fluid configuration and the electrical parameters, although a detailed analysis of the different breakdown regions was hampered by the limitations of the equipment available.

The main limitation of the *floating* plasmas was found to be the low energy deposited in the gas, resulting in a trade-off between confinement and energy deposition. Going to significantly higher energy levels required full breakdown to allow a conduction current to flow between the electrodes.

As a direct consequence of the low energy deposition and the limited applied field accessi-

ble with the setup at hand, the flame-confined excitation did not have an impact on the main flame properties although it slightly affected the edge of the flame. This in contrast to the great perturbation introduced by the ns-spark, albeit it being uncontrolled. However, the envelope of the region of confinement could not be explored to its limits, so that the power into the gas can potentially be increased, while respecting the confinement, by increasing the applied voltage, the pulse repetition frequency, the voltage pulse duration or the conductivity of the gas. This would be an interesting extension of the proof of concept here presented in order to evaluate whether the confined strategy could be of use for a practical application, since it has several advantages such as its homogeneity, negligible heating or preserving the integrity of the electrodes.

Further studies of interest would include detailed measurements of the ionization produced by the high voltage pulses in the *floating* plasma cases since, at this point, experimental differentiation between the energy coupled to the chemi-ionization electrons and to the secondary electrons (produced through the RPND ionization) was not possible.

Chapter 6

Sub-breakdown kHz AC fields in counterflow nonpremixed flames

6.1 Introduction

In Chapters 3 and 5, different non-uniformities in the gaseous environment were exploited in order to couple the electrical energy delivered through high voltage RPND to specific regions. In these experiments, the electrical field was *locally* above the breakdown threshold. In Chapter 3, temperature and composition non-uniformities made the confinement of the discharge-created electrons (secondary electrons) to *hot* regions possible, and in Chapter 5 the coupling was facilitated by the localization of pre-existent electrons (primary electrons).

In this Chapter, a third coupling option for the counterflow nonpremixed flame platform is explored: transmission of the energy to the gas through the pre-existent ions (primary ions). In this case, the electric field needs to be slow enough so that the ions can respond, but fast enough so that the effect is localized. Following these guidelines, the response of the flame to AC voltage below the breakdown threshold and in the kHz range is studied.

Whereas, when using RPND plasmas, the possibilities of flame enhancement refer to a chemical impact since the energy is coupled to the electrons (although some hydrodynamic effects such as pressure waves generated by the fast energy deposition can arise for some plasma regimes), when coupling the energy to the ions, by using slow sub-breakdown fields, the impact on the flame is based on hydrodynamic effects, or *ionic winds*, that modify the

flow field in which the flame exists (see Section 1.5).

The counterflow nonpremixed flame is a very stable platform which is strongly influenced by the structure of the flow field. Because of this intrinsic stability and the low energy deposited by the RPND plasmas of Chapter 5, when localized to the high temperature region, these were unable to visibly modify the flame properties through chemical effects. In a recent paper, [47] proposed that high frequency (in the kHz range) electric fields were able to drive significant steady flows in flames. In this Chapter, the impact of such a strategy on a counterflow nonpremixed flame is evaluated, and it was seen that indeed it was possible to affect the flow field locally in the region of the flame, enough to change its position.

The structure of this Chapter is as follows. The experimental results of the impact of kHz frequency AC fields on a counterflow nonpremixed flame are presented in Sections 6.2 and 6.3. Next, Sections 6.4 through 6.6 present a model, based on induced flows, that offers an explanation to the experimental observations. Finally, Section 6.7 summarizes the main findings of the Chapter and recognizes some of the shortcomings of the model.

6.2 Experiments of flame dynamics under AC fields

In this Chapter, the impact of kHz frequency AC fields below the electrical breakdown threshold on a counterflow nonpremixed flame is explored. To that end, AC voltage of variable amplitude and frequency is applied to the bottom electrode of the setup described in Section 2.3 (the top electrode being grounded). Unless otherwise noted, the bottom jet corresponds to the oxidizer stream and the top jet to the fuel stream. The sign convention for the top and bottom nozzles is that of Figure 2-3(b), so that, in general the fuel is at $z \to -\infty$. The flame parameters used in the experiments of this Chapter are summarized in Table 6.1.

Table 6.1: Flame parameters used in the AC experiments.

a $[1/s]$	Dilutant	$X_{O_2,\infty}$	$X_{CH_4,-\infty}$	Z_{st}	ϕ	Power $[W]$
40	N_2 (oxidizer), Ar (fuel)	0.21	0.26	0.32	2.3	116

6.2.1 Frequency effect

Low frequency dynamics

The dynamics of the flame under different AC fields was video recorded using the setup described in Section 2.8.2. For each sequence of images taken under the influence of the AC field (generally 100 images), the baseline flame before and after was monitored to ensure that the flame position had not varied. Figure 6-1 shows a sequence of raw images of the flame response under an applied AC voltage of 2kV peak at 4Hz. For reference, the baseline flame is indicated by the white dashed line, whereas the instantaneous flame position is indicated by the red line. The images were taken during a cycle of oscillation of the applied voltage and correspond to equi-spaced snapshots during the 0.25s period.

From the images, it can be appreciated how, at low frequency, the flame oscillates between the electrodes with a certain amplitude with respect to an average position that does not correspond to the baseline flame, but is closer to the oxidizer stream. In addition, the end of the flame seems to follow a flapping-like behavior (curving of the flame at the ends), that is not evident from the photographs but was visible to the naked eye.

Figure 6-1: Flame dynamics during one cycle of oscillation for AC voltage of 2kV peak and 4Hz. White line corresponds to baseline (no electric field) and red line to instantaneous flame position. Bottom corresponds to oxidizer stream and powered electrode.

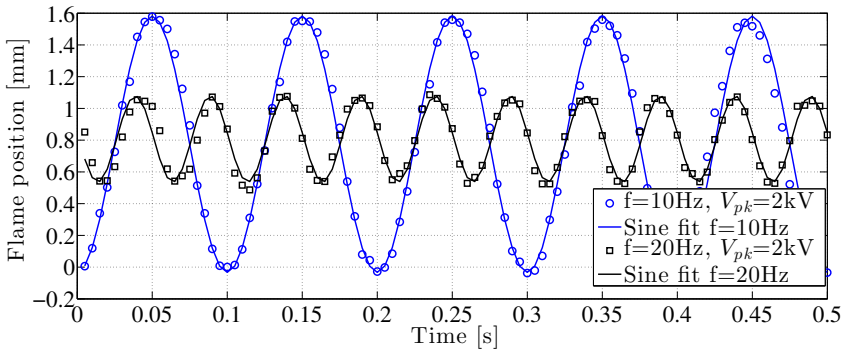

Figure 6-2: Time response of the flame for 2kV peak voltage, the response is sinusoidal and has the same frequency as the excitation. Measurement is relative to the baseline flame (z=0). Positive values indicate motion towards the oxidizer.

From the 2D images, the motion of the flat region of the flame was obtained by averaging the instantaneous position *along* the flame excluding the edges in which the curvature is finite. The time trace of the flame position, relative to the baseline flame, for two different frequencies is shown in Figure 6-2. Positive values indicate that the flame is closer to the oxidizer stream than the undisturbed case (baseline position is z=0mm).

From the time traces, two observations can be made. First, the flame follows a sinusoidal oscillation at the same frequency as the excitation voltage. Second, the mean flame position has shifted towards the oxidizer stream. Therefore, the flame motion can be fitted by:

$$z_{\text{fl}}(t) = \bar{z}_{\text{fl}} + A_{\text{fl}} \sin(2\pi f t + \phi),$$

where the frequency matches the excitation frequency, f, and the mean flame position, $\bar{z}_{\text{fl}}$, (positive indicates motion towards the oxidizer) and amplitude, A_{fl}, are fitted in the least squares sense to the experimental data. Figure 6-3 shows the dependence of A_{fl} and $\bar{z}_{\text{fl}}$ on f.

From Figure 6-3 it can be seen that the amplitude of the oscillation decays and vanishes for frequencies above 100Hz but the flame is displaced towards the oxidizer even for frequencies as high as 10kHz. The effect of the frequency on the flame displacement seems to be much less than on the oscillation amplitude. Moreover, the displacement is highly dependent on the applied voltage and a surprising observation is that it is higher for lower voltage values.

The low frequency sinusoidal motion and the amplitude decay with the frequency, for a

similar experimental platform, has also been reported by [36] (in Korean).

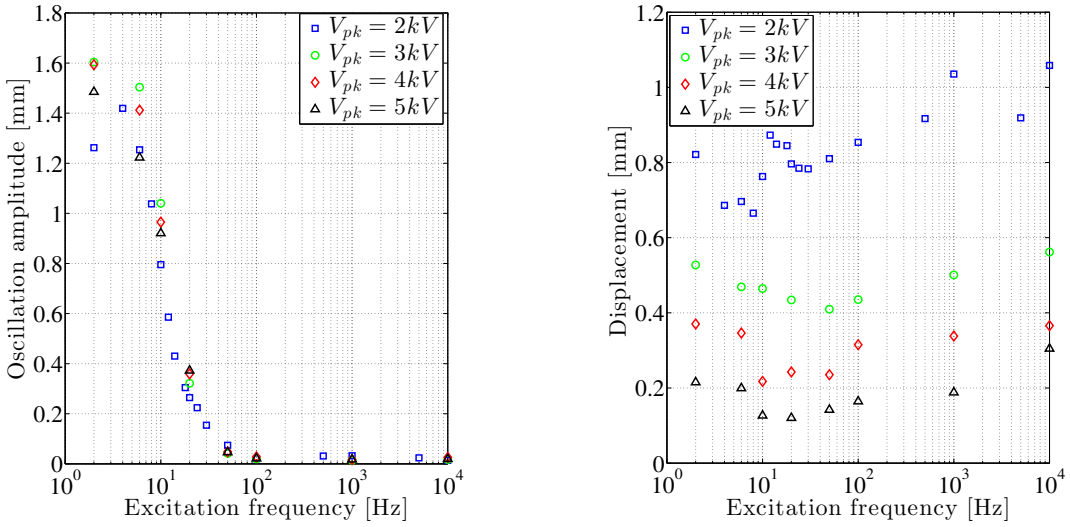

(a) Oscillation amplitude, A_{fl}.

(b) Mean displacement, $\bar{z}_{\text{fl}}$.

Figure 6-3: Amplitude of the oscillation and mean flame displacement (towards the oxidizer) for AC voltage ranging from 2Hz-10kHz.

Directionality of the flame oscillation: response to a voltage ramp

In order to discern the directionality of the instantaneous flame motion during the oscillation with respect to the applied voltage polarity, the response to a voltage ramp is shown in Figure 6-4. For positive values of the voltage, the flame moves to decreasing z_{fl} values (towards the grounded electrode, that is the cathode at that time), and vice versa, so that the flame's instantaneous motion is towards the cathode.

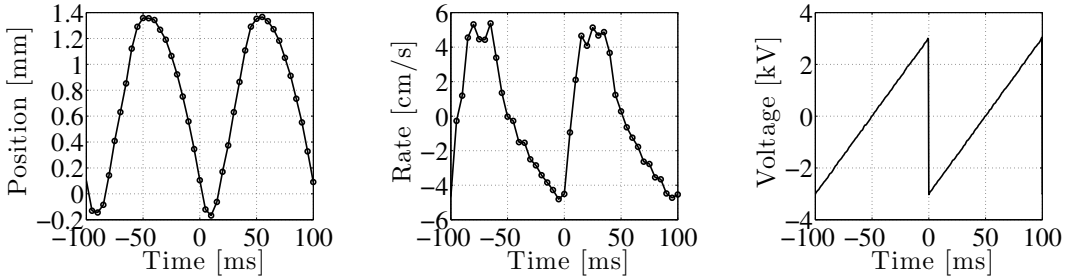

Figure 6-4: Response of the flame to a voltage ramp. The voltage is applied to the electrode placed at the oxidizer jet exit.

6.2.2 Voltage amplitude effect

High frequency response

As has been shown, at high frequencies, once the oscillation has been dampened out, there is a remanent flame displacement towards the oxidizer. The displacement presents a weak dependence on the frequency and is strongly dependent on the applied voltage level. Figure 6-5 shows the existence of a maximum displacement at around 1.5-2kV peak voltage, of around 1.2mm relative to the undisturbed position. In addition, at the higher voltages, higher frequencies lead to slightly larger displacements for fixed voltage.

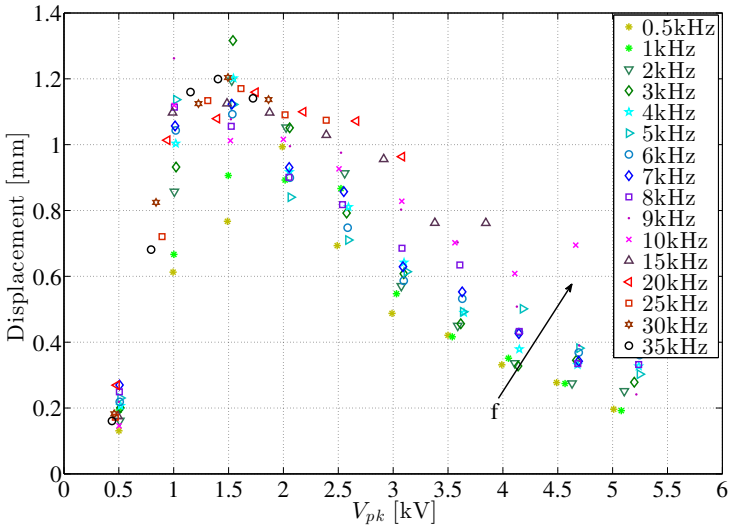

Figure 6-5: Displacement of the flame towards the oxidizer side when using kHz AC voltage.

Verification of the directionality of the flame displacement

In the experiments presented so far, the electrode that was powered was the one placed at the oxidizer jet exit (bottom one). In order to rule out a DC bias introduced by the power supply that might be flawing the results, the same displacement measurements were repeated by first reversing the polarity of the power supply (i.e., grounding the bottom electrode), and, second, keeping the bottom electrode powered but flipping the oxidizer and fuel streams. The results of the test, at a low (10Hz) and a high frequency (10kHz), are shown in Figure 6-6. It can be seen that the data coincide when reversing the polarity of the

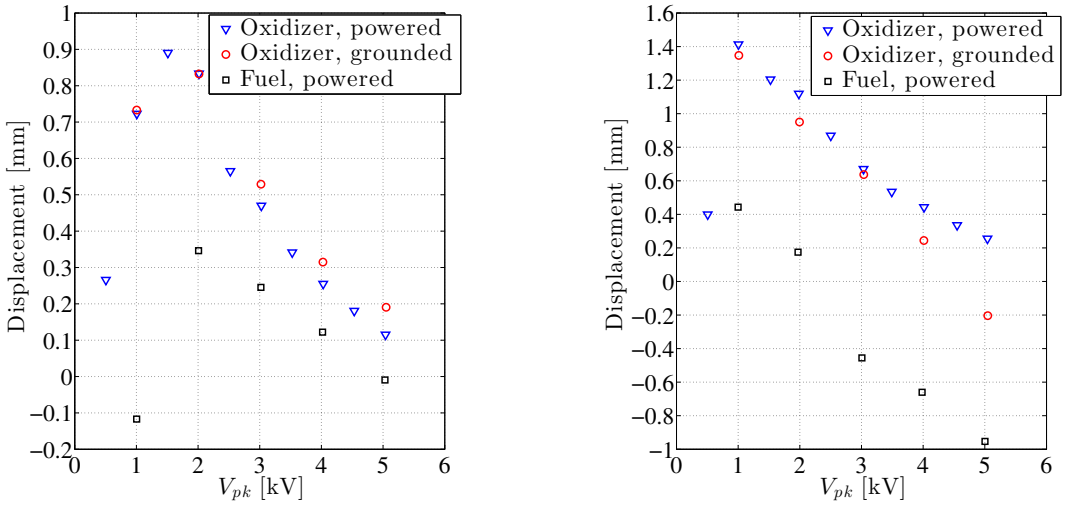

(a) f=10Hz.

(b) f=10kHz.

Figure 6-6: Directionality of the flame displacement. The legend corresponds to the conditions of the bottom jet/electrode. Positive values indicate displacement towards the oxidizer.

electrodes while keeping the oxidizer on the bottom jet. When the fuel and oxidizer's roles are flipped, the trends hold but the relative values are modified, as should be expected by the different densities of the streams amongst other things.

If instead of having the electrodes parallel to the flame, they are rotated to be orthogonal to it, no displacement towards the oxidizer is observed, indicating the essential role of the orientation of the electric field with respect to the flame and its flow field. This suggests that the energy coupling was through a dynamic effect, as chemical excitation of the mixture by the electric field would not depend on the orientation of the electrodes [78].

6.3 Electrical measurements of the flame

6.3.1 Impedance of the setup

In order to build a model that is able to elucidate the physical mechanisms that lead to the DC flame displacement under the influence of a high frequency AC field experimentally observed, a description of the flame as an electrically active component is needed. In this Section, the impedance of the setup, with the flame lit and unlit, was obtained by measuring

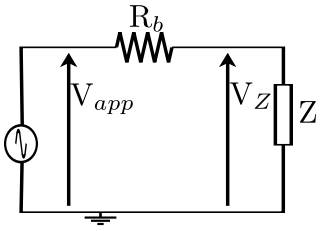

Figure 6-7: Schematic of the circuit for the measurement of the setup's impedance, Z.

the transfer function at the load, V_Z/V_{app}, of the circuit shown in Figure 6-7. In this circuit, a known ballast resistor, R_b=9.91MΩ, was connected in series with the experimental setup, of unknown impedance Z, and the high voltage AC power supply. The applied voltage, V_{app}, was monitored and the voltage at the load, V_Z, was measured using a LeCroy PPE 20kV probe with a 100MΩ system input resistance. Both waveforms were sinusoidal and had the same frequency but different amplitude and phase.

The transfer function is given by:

$$\frac{V_Z}{V_{app}} = \frac{Z}{Z + R_b}, \tag{6.1}$$

and its amplitude and phase as a function of the frequency, at a fixed peak applied voltage of 1kV, are shown in Figure 6-8. The frequency response was measured for a case in which the flame had not been lit and a case with the flame lit, everything else unchanged.

The complex impedance at the load, Z, can be obtained from equation 6.1, by re-arranging terms, and is plotted in Figure 6-9, comparing the flame and no flame cases. In this plot, the frequency is taken as a parameter and the impedance is plotted in the complex space.

From these figures, at low frequency, the circuit response is that of a resistive voltage divider. For the no flame case, the resistive voltage divider is composed of the ballast resistor, R_b=9.91MΩ, in series with the voltage probe resistance (∼100MΩ). When the flame is lit, the amplitude of the transfer function decreases, indicating that the resistance of the load has also decreased as there is a finite conductance (due to the presence of the flame-produced charged species) now connected in parallel with the voltage probe.

From Figure 6-9, the setup mainly behaves as a resistance R in parallel with a capacitance

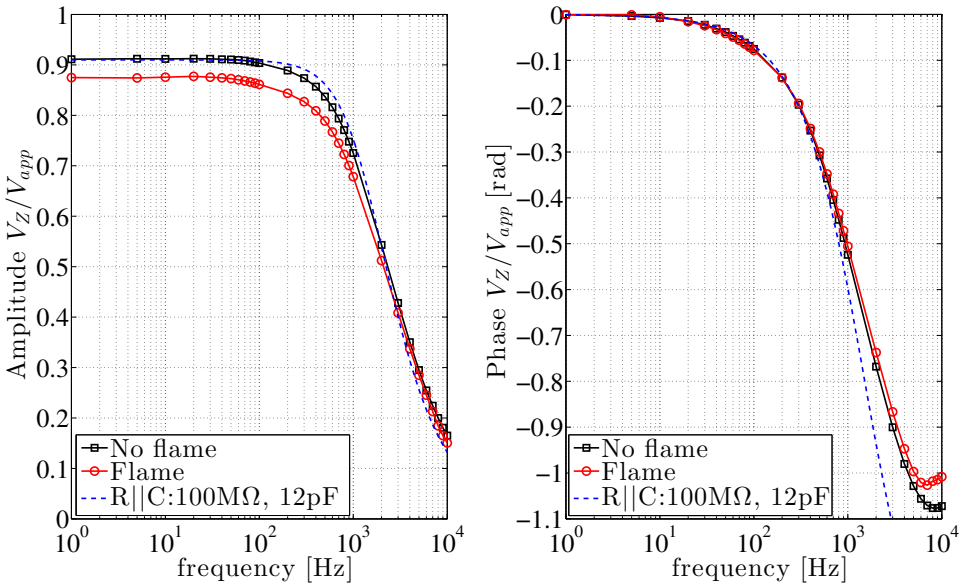

Figure 6-8: Frequency response of the circuit in Figure 6-7 without and with the flame lit, for 1kV peak applied voltage. For reference, the theoretical transfer function for a resistor in parallel with a capacitor is shown (blue dashed line).

C, for which, the parametric representation of the impedance in terms of the frequency, is a translated circle:

$$\left(\mathrm{Re}(Z) - \frac{R}{2}\right)^2 + \mathrm{Im}(Z)^2 = \left(\frac{R}{2}\right)^2,$$

where the resistance R is that of the probe connected in parallel with either the flame or an open circuit, and the capacitance is the total including the parallel electrodes, cables, voltage probe and oscilloscope, $C \sim 12pF$ (and does not influence the Nyquist representation).

At the highest frequencies tested, $f > 1kHz$, the amplitude of the transfer function for the flame and no flame cases can hardly be distinguished since the capacitive component of Z dominates and its value is only very slightly affected by the presence of the flame. In addition, there was a non-negligible noise level synchronized with the applied voltage that affected the relative phase of the signals, hampering the identification with a circuit model like in the low frequency case.

The dependence of the low frequency resistance of the system on the applied voltage was measured through the circuit response at a fixed frequency of 5Hz. The results are shown in

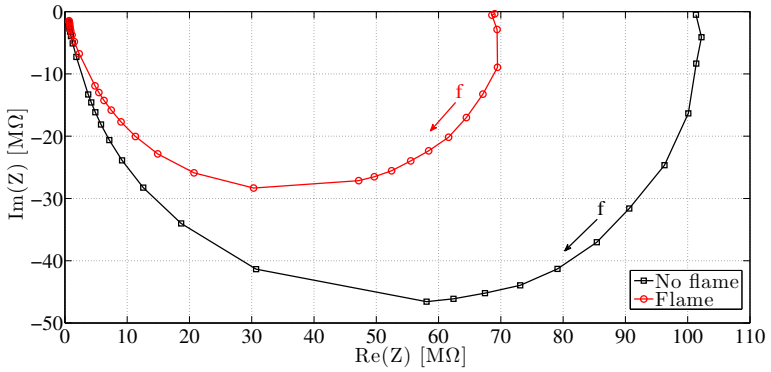

Figure 6-9: Nyquist plot comparing the complex electrical impedance of the experimental setup with the flame lit and unlit. Same case as Figure 6-8.

Figure 6-10(a).

At this low frequency, Z behaves like a pure resistance, which for no flame, corresponds to the value of the voltage probe alone R_{probe} ~100MΩ (black line in Figure 6-10(b)) and is independent of the applied voltage, as expected. When the flame is lit, its finite resistance is connected in parallel so that the total resistance, R_{total}, drops (red line).

From these estimates, the flame resistance R_{flame} was obtained (Figure 6-10(b)), and was seen to increase almost linearly with the applied voltage at a rate of $s = 5.55 \cdot 10^4 \Omega/V$. The linear relationship between resistance and voltage can be interpreted, by analogy to the DC response of flames[1], as operation in the *saturation* regime [102], with a constant current.

In the saturation regime, the rate of ion generation balances the rate of ion removal due to the electric field, so that an increase in voltage does not produce a further rise in ion current. From this definition of the saturation regime:

$$\dot{n}_i \mathcal{V} = v_d \mathcal{A} n_i, \tag{6.2}$$

where $\dot{n}_i$ is the rate of ion generation in the flame, $\mathcal{V}$ and $\mathcal{A}$ are the volume and area,

[1]For DC operation, the voltage-current characteristic plot presents three different regions [102]. For low voltage, within the *sub-saturation* regime, an increase in the voltage results in a quadratic increase in the ion current since more charge is being pulled out of the flame by the field. For intermediate voltages, the rate of ion generation is balanced by the ion removal due to the electric field and a plateau in the current is reached (*saturation*). Finally, for high enough voltages, the electric field is high enough for the onset of secondary ionization to occur, and so a further increase in the current is observed (*super-saturation*).

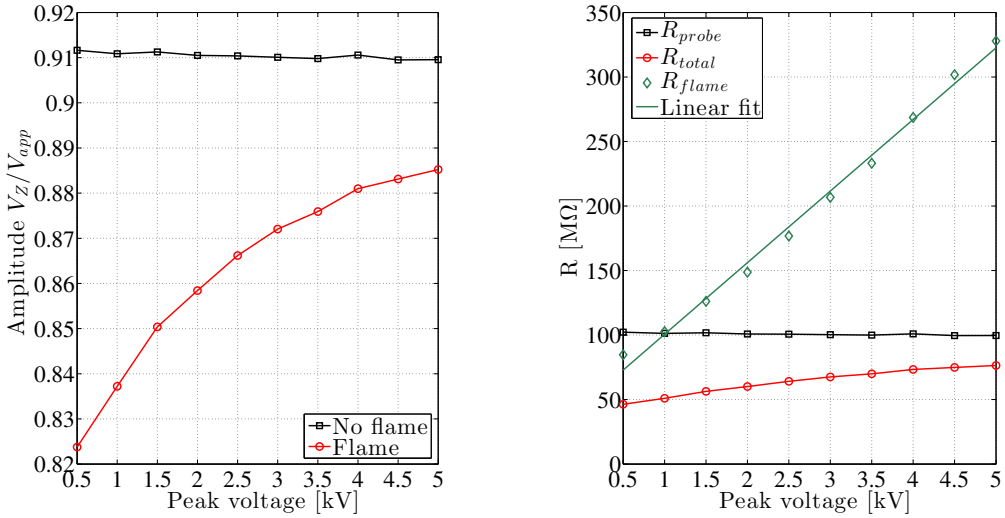

(a) Transfer function gain.

(b) Resistance values.

Figure 6-10: Transfer function, V_Z/V_{app}, and inferred resistance values, as a function of the applied voltage amplitude at 5Hz, without (black) and with flame (red).

respectively, of the region of ion production, n_i is the ion density and v_d the ion drift.

From equation 6.2, the ion density becomes:

$$n_i = \frac{\dot{n}_i \delta_i}{\mu_i E} \tag{6.3}$$

with δ_i the chemi-ionization region thickness, μ_i the ion mobility and E the electric field. From this estimate, the resistance of the flame can be obtained through the conductivity σ:

$$R_{flame} = \frac{\delta_i}{\mathcal{A}\sigma} = \frac{\delta_i}{\mathcal{A}e\mu_i n_i} = \frac{V}{\mathcal{A}e(\delta_i \dot{n}_i)}, \tag{6.4}$$

and the linear dependence on the voltage becomes explicit (note that this condition is equivalent to a constant current). Using the slope of the flame resistance versus voltage plot, s, and a flame radius of 1cm, the rate of ion production per unit flame area becomes $\delta_i \dot{n}_i = 1/(\mathcal{A}es) \approx 3.6 \cdot 10^{13} cm^{-2} s^{-1}$. This estimate is consistent with measurements reported in the literature, e.g. [101] measured the ion production rates per unit flame area for premixed methane/air at atmospheric pressure to be between $3{\cdot}10^{13}$-$6{\cdot}10^{14}$cm^{-2}s^{-1}, where the peak occurs for stoichiometric mixtures.

6.3.2 Capacitance of the electrode system

In Section 3.4 it was discussed that the measured capacitance of the setup is higher than that of the electrodes alone, since there are other capacitances connected in parallel (wires, voltage probe, etc). Using the analytical formulation of [134], the capacitance of the electrodes was estimated to be $C_e \approx 2.4pF$. This estimate was checked experimentally by measuring the response of a circuit like the one in Figure 6-7 to a step function. The value of the resistance R_b was in this case R_b=473$k\Omega$, and the time constant of the circuit was used to infer the capacitance.

To that end, two different loads Z were used. In the first case, the voltage probe alone was connected to the open ends of the circuit constituted by the ballast resistor and the power source. This measurement was used to estimate the total capacitance C' of the setup excluding the electrodes' contribution, i.e. that of the probe, the cables and the scope, giving τ'=1.9μs or C'=4pF. In the second case[2], the electrodes were connected in parallel to the voltage probe (no flame), giving τ=3μs or C=6.34pF. The capacitance of the electrode system was then obtained from the difference between these two measurements, $C_e \approx 2.34pF$, which is consistent with the theoretical estimation. Figure 6-11 shows the experimental determination of the electrode system capacitance.

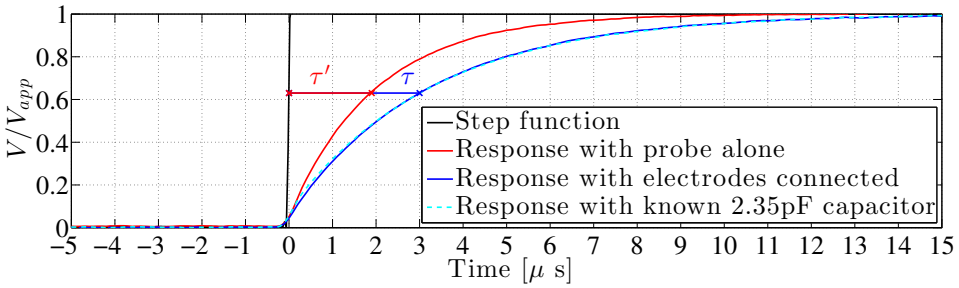

Figure 6-11: Experimental measurement of the capacitance of the electrode system. Substitution of the electrodes by a known capacitance of 2.35pF validates the measurement.

[2]This value does not match the total capacitance reported in Section 6.3.1 because a different voltage probe and cables were used.

6.4 Model of the flame displacement at high frequencies

It is a well known phenomenon that, DC and low frequency, sub-breakdown electric fields acting upon flames induce *ionic winds* [101, 102]. For an applied field sufficiently slow so that the ions have time to respond (unlike the RPND discussed up to this part), ions will acquire momentum while moving down the potential gradient, and that momentum will on average be lost in collisions with the neutral atoms and molecules. This results in a body force on the fluid, of equal magnitude to the one experienced by the ions, that modifies the flow field and, in turn, can vary the structure of the flame.

The flame motion in the low frequency experiments of Section 6.2.1 can be interpreted as a consequence of the flow field modification by the ionic wind. For the low frequency experiments, the application of a sinusoidal voltage resulted in a sinusoidal flame oscillation where, the instantaneous flame motion was in the direction of the applied electric field (e.g. towards the cathode, see experiment for the response to a voltage ramp in Section 6.2.1), superimposed to a mean flame displacement towards the oxidizer. The instantaneous flame motion towards the cathode defines the direction of the instantaneous induced force and implies that there are excess positive ions being accelerated by the field as compared to negative ions (since the force on the positive ions points towards the cathode). This point will be used when proposing a model for the response of the flame under an AC field, since only positive ions will be considered. Although there does not seem to be consensus in the literature in terms of the identity of the negative charge carriers (relative amounts of electrons and negative ions), and it is highly dependent on the conditions in any case, it is in general accepted that the concentration of negative ions is lower than that of positive ions [30, 83], consistent with the observations here presented.

At the higher frequencies, the nature of the flame response is not so clear. A chemical effect based on vibrational excitation by the electric field was ruled out by checking the dependence of the flame displacement on the electrodes' orientation, as proposed by [78] (Section 6.2.2). In addition, the similarity of the flame response for both the low frequency and high frequency experiments, points that the same phenomenon is probably responsible. Based on these observations, in what follows, a model based on induced ionic winds is

proposed to explain the nonpremixed counterflow flame DC displacement under kHz AC fields. A recent article by A. M. Drews et al. in 2012 [47], reporting experimental evidence of induced steady flows in a Bunsen-burner type methane flame when applying AC voltage up to 1kHz, supports the hypothesis here made.

The model is used to explain the experimental findings of Section 6.2.2, mainly:

1. The existence of a rectification effect that results in a DC displacement of the flame under the influence of a high frequency AC field.

2. The directionality of the flame displacement towards the oxidizer side.

3. The qualitative dependence at fixed frequency on the applied electric field and the existence of a maximum.

A model of the flame as an electrically active component of a circuit is then incorporated into the fluid problem as a closure to capture the remaining experimental findings, mainly:

4. The practical independence on the frequency except at the higher voltages.

5. The quantitative dependence of the displacement on the voltage and the existence of a maximum at around 1.5-2kV$_{pk}$.

The presentation of the model is organized as follows. Section 6.4.1 overviews the classical 1D theory of counterflow nonpremixed flames upon which the dynamic model is built. Next, Section 6.4.2 presents the structure of the fluid model here developed and its different parts are detailed in Sections 6.4.3 through 6.4.5. Section 6.4.6 evaluates the impact of some of the effects that the model has neglected. Finally, the electrical model of the flame is incorporated in Section 6.5 and the experimental data are fit to the model in Section 6.6.

6.4.1 Classical 1D theory of the counterflow nonpremixed flame

The classical model for the steady laminar nonpremixed flame is based on the conservation of a passive scalar, the mixture fraction Z, defined as[3]:

$$Z(\vec{x}) = \frac{sY_f(\vec{x}) - Y_{ox}(\vec{x}) + Y_{ox,\infty}}{sY_{f,-\infty} + Y_{ox,\infty}},$$

with $s = \frac{M_{ox}\nu_{ox}}{M_f\nu_f}$, and where the symbols have the same meaning as in Section 2.3.1. The mixture fraction represents the mass fraction of the fuel stream in the mixture, and similarly, $(1 - Z)$ represents the mass fraction of the oxidizer stream in the mixture (both the fuel and oxidizer streams may contain inert gases). Thus, $Z = 1$ indicates the fuel stream exit and $Z = 0$ indicates the oxidizer stream exit. At the flame front, fuel and oxidizer meet at stoichiometric conditions so that $Z = Z_{st}$. Therefore, between the oxidizer exit and the flame front, $Z \leq Z_{st}$ and, between the flame front and the fuel exit, $Z \geq Z_{st}$.

The introduction of the mixture fraction essentially decouples the analysis into two problems. The first one is the flame structure problem: determining the temperature and composition as a function of the mixture fraction, $T(Z)$, $Y_i(Z)$. The second, is the mixing problem: determining the spatial field of the mixture fraction, $Z(\vec{x})$.

For a detailed derivation of the equations, the reader is referred to any combustion textbook [63, 161, 210]; here the fundamentals required for the development of the flame displacement model are summarized.

Flame structure problem

The simplest representation of the temperature and composition as a function of the mixture fraction is the Burke-Schumann solution. The Burke-Schumann flame assumes infinitely fast chemistry, so that fuel and oxidizer cannot coexist, constant pressure, constant and equal diffusion coefficients and heat capacities for all species, and unity Lewis number. In this approximation, from the conservation equations, the temperature and composition become linear functions of the mixture fraction on either side of the reaction sheet.

[3]Note that this is the general form of the particularization in Section 2.3.1 (equation 2.3) to the stoichiometric location, where the mass fractions of fuel and oxygen go to zero, as they are consumed at the flame front.

Mixing problem

Using the same approximations, it can be shown that the mixture fraction is given as the solution to the convection-diffusion equation, without a chemical source term:

$$\nabla \cdot (\rho \vec{v} Z) = \nabla \cdot (\rho D \nabla Z), \tag{6.5}$$

with boundary conditions $Z = 1$, on the fuel-side, and $Z = 0$, on the oxidizer-side. The solution to this equation depends on the flow field $\vec{v}$.

In the case of an opposed jet burner, such as the one here considered, the velocity field is that of a stagnation point flow, given in cylindrical coordinates (r,z) by:

$$\begin{aligned} v_z &= -az, \\ v_r &= \frac{ar}{2}, \end{aligned} \tag{6.6}$$

where $z = 0$ is the stagnation plane and a is the strain rate, assumed constant (constant density assumption). The solution of equation 6.5 in this velocity field is:

$$Z(z) = \frac{1}{2}\left(1 - \mathrm{erf}\left(z\sqrt{\frac{a}{2D}}\right)\right), \tag{6.7}$$

and only depends on the coordinate orthogonal to the flame, z.

6.4.2 Incorporating the effect of a sub-breakdown AC electric field

Upon application of an AC electric field, the chemi-ionization ions and electrons present in the flame are accelerated. The momentum transfer from the electrons to the neutral gas atoms and molecules is very small due to the small electron mass, whereas the transfer of momentum from the ions results in a body force that modifies the velocity field of equation 6.6. Since the time scale of the oscillation of the ions (which matches the excitation period$\sim$0.1-1ms) is faster than the flame dynamics timescale (of the order of the inverse of the strain rate$\sim$25ms), the time-averaged velocity field, within a period of oscillation of the charged particles, can be used to solve for the new steady-state flame structure. A summary of the modeling approach

that introduces the effect of the AC field is given in Figure 6-12.

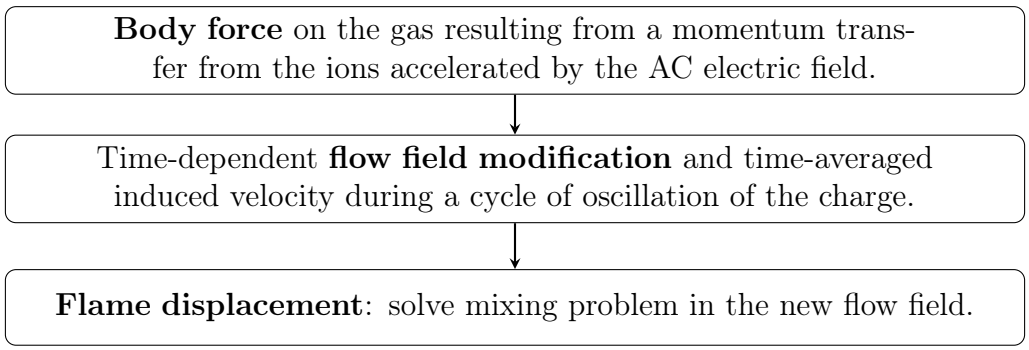

Figure 6-12: Structure of the flame displacement model.

6.4.3 Time-dependent body force

In Section 6.3.1 it was seen that, at least at the low excitation frequencies, the rate of charge extraction balanced the rate of charge production at the flame front. The production rate of the charge per unit area is given by:

$$\dot{\sigma} = e(\delta_i \dot{n}_i), \tag{6.8}$$

where σ now refers to the charge per unit area. In this part, a discrete charge extraction model is used in which the flame front acts as a source of disks of positive charge. Only positive charge is considered, following the discussion in Section 6.4, although the inclusion of negatively charged disks is explored in Section 6.4.6.

The simplest approach is to consider one of these disks, of charge σ_0, and see how the electric field affects it. The effect of having multiple disks and different extraction rates will be explored in Section 6.4.6 but was seen not to affect the qualitative results.

Starting from the 1D governing equations for charged species motion under the influence of an electric field described in Section 4.2.1, and neglecting both the diffusion and charge production terms, the equation of motion of the charged disk becomes:

$$\left(\frac{\partial}{\partial t} + \mu_+ E(t)\frac{\partial}{\partial z}\right)\sigma = 0, \tag{6.9}$$

with initial condition: $\sigma(z, t = 0) = \sigma_0 \delta(z)$.

For a cosinusoidal excitation, $E(t) = \hat{E} \cos(\omega t)$, the solution is:

$$\sigma(z,t) = \sigma_0 \delta\left(z - \frac{\mu_+ \hat{E}}{\omega} \sin(\omega t) \right),$$

which corresponds to an oscillation around the flame position between $[-\frac{\mu_+ \hat{E}}{\omega}, \frac{\mu_+ \hat{E}}{\omega}]$ at the same frequency as the excitation and with a $\pi/2$ phase difference. The excursion of the charged disk is inversely proportional to the excitation frequency so that, the higher the frequency, the lower the amplitude of the oscillation. E.g. for a voltage of 5kV over a 17mm gap, and an ion mobility of $2.7 cm^2/V/s$ (H_3O^+ in N_2 [215, 216]), the amplitude of the oscillation is ∼10cm at 100Hz and ∼1mm at 10kHz, so that, in the first case, the charge will be absorbed by the electrodes, whereas in the second case, the charge oscillation will be contained between the electrodes.

The force per unit area acting on the disk becomes:

$$\frac{F}{\mathcal{A}} = p_E = \sigma_0 \hat{E} \cos(\omega t), \tag{6.10}$$

so that the force acting on the neutral gas flow is a distributed force located at the oscillating disk position, $z = \frac{\mu_+ \hat{E}}{\omega} \sin(\omega t)$, along the direction of the electric field, and with magnitude given by equation 6.10.

Note that within the model's assumptions, both the oscillation of the charge and the force on the fluid have the same frequency as the excitation voltage.

6.4.4 Flow field modification

Flow induced by an *oscillating porous disk*

For a flow that is both incompressible and irrotational, the velocity field is obtained by solving Laplace's equation for the streamfunction with the relevant boundary conditions. Therefore, existing force fields will impact the pressure field alone, and not the velocity field.

If now the irrotational condition is relaxed, but the flow is still incompressible, and

inviscid, and considering only forces that derive from a potential function, the momentum conservation equation can be written (in its vorticity form) as:

$$\frac{D\vec{\omega}}{Dt} = \vec{\omega} \cdot \nabla \vec{v},$$

so that the velocity field is again fully defined by the boundary and initial conditions and cannot be modified by a force that derives from a potential function.

This would be the case for an oscillating infinite flat plate with the time dependent unidirectional force of equation 6.10. However, the finite size of the oscillating disk introduces a sharp discontinuity in the force that goes from having a value of p_E inside the disk to zero outside (no charge), breaking the ideal assumptions at the disk's rim (in the sense that the force is no longer irrotational, because it has concentrated vorticity at the edge). Therefore, the finite size of the disk of charge (i.e. of the flame) is essential to transmit an induced velocity to the flow.

Except for the discontinuity at the disk of charge, the flow is irrotational, $\vec{v} = \nabla\varphi$, and from the momentum equation, will follow:

$$\nabla \left(\frac{\partial \varphi}{\partial t} + \frac{1}{2}v^2 + \frac{p}{\rho} \right) = f = -\nabla \left(\frac{p_E}{\rho} \right), \tag{6.11}$$

where f is the force per unit mass acting on the fluid.

Equation 6.11 can be integrated across the disk to obtain the discontinuity condition at its surface, $\Delta\varphi$, as the pressure and the kinetic energy do not change across the disk:

$$\left. \frac{\partial \varphi}{\partial t} \right|_{\text{disk}}^{\text{disk}^+} = \frac{\partial \Delta\varphi}{\partial t} = -\frac{(0 - p_E)}{\rho} = \frac{p_E}{\rho}.$$

Integrating in time, and using the expression for the electrostatic pressure in equation 6.10, gives the discontinuity in the velocity potential across the disk:

$$\Delta\varphi = \frac{\sigma_0 \hat{E}}{\rho\omega} \sin(\omega t). \tag{6.12}$$

Since the fluid is incompressible, the velocity field at time t is that due to the instan-

taneous velocity potential jump $\Delta\varphi$ at that time. The fact that the velocity potential has a discontinuity means there is a fluid dipole layer, at the disk, of strength equal to that discontinuity.

This problem is mathematically the same as that of finding the electric potential of a disk of electric dipoles, terminated by the circle bounding the disk; or analogously, to finding the magnetic potential of a disk of magnetic dipoles, again terminated by the circle bounding the disk. From elementary electromagnetic theory, this is also equivalent to the magnetic potential caused by a circular loop of wire, coincident with the edge of the disk, carrying a current I [124].

The solution to this last magnetic problem can be found in [77], Table 6.2 summarizes the correspondences between the fluid problem and that of a current ring on that same circle.

Table 6.2: Magnetics-fluids problem analogy used to solve for the induced flow field.

Fluid problem	Magnetic problem
Velocity, $\vec{v}_i$	Magnetic field, $\vec{B}$
Vector potential, $\vec{B}^i$	Vector potential, $\vec{A}$
Velocity potential jump, $\Delta\varphi$	Current, $\mu_0 I$
Radius of the disk of charge, R	Radius of the loop of current, R

Following [77], the solution for the velocity vector potential, in spherical coordinates associated to the disk of charge (Figure 6-13), becomes:

$$B'_{\phi'}(r',\theta') = \frac{\Delta\varphi}{\pi}\frac{1}{\left(1+\left(\frac{r'}{R}\right)^2+2\frac{r'}{R}\sin\theta'\right)^{1/2}}\left(\frac{(2-k^2)K(k)-2E(k)}{k^2}\right), \tag{6.13}$$

where K and E are the complete elliptic integrals with argument k^2 given by:

$$k^2 = \frac{4\frac{r'}{R}\sin\theta'}{1+\left(\frac{r'}{R}\right)^2+2\frac{r'}{R}\sin\theta'},$$

and the velocity field is obtained from $\vec{v}_i = \vec{\nabla}\times\vec{B}^i$.

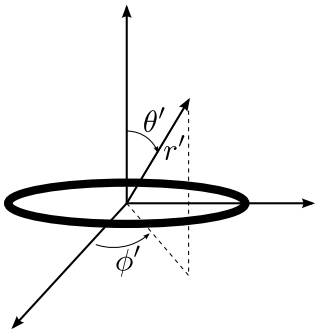

Figure 6-13: Spherical coordinates associated to the disk of charge / loop of current.

Superposition

The modified flow field can be obtained by the superposition of the stagnation point flow of equation 6.6 and the flow induced by the *oscillating porous disk* (equation 6.13).

Using for the reference length the flame radius, R, and for the reference time the inverse of the strain rate, a^{-1}, the non-dimensional stagnation point flow velocity vector becomes:

$$\begin{aligned} \bar{v}_r^s &= \frac{\bar{r}}{2}, \\ \bar{v}_z^s &= -\bar{z}, \end{aligned} \tag{6.14}$$

which can also be written in terms of the curl of a vector, $\vec{\bar{v}}^s = \vec{\bar{\nabla}} \times \vec{B}^s$, by defining $\vec{B}^s$ as:

$$\vec{B}^s(\bar{r}, \bar{z}) = -\frac{\bar{r}\bar{z}}{2}\vec{u}_\theta. \tag{6.15}$$

The induced velocity vector potential, given by equation 6.13, needs to be referred to the fixed reference system of the baseline stagnation point flow and expressed in terms of the same cylindrical coordinates (r,θ,z). After some algebra, the (non-dimensional) induced velocity vector potential becomes:

$$\vec{B}^i(\bar{r}, \bar{z}, \tau) = \frac{\chi \sin\tau}{\pi} \frac{1}{\left(1 + \bar{r}^2 + 2\bar{r} + (\bar{z} - \beta\sin\tau)^2\right)^{1/2}} \left(\frac{(2-k^2)K(k) - 2E(k)}{k^2}\right) \vec{u}_\theta, \tag{6.16}$$

and k^2 can be expressed in terms of the new coordinates as:

$$k^2 = \frac{4\bar{r}}{1+\bar{r}^2+2\bar{r}+(\bar{z}-\beta\sin\tau)^2}.$$

The parameters that appear in these expressions, β, χ and τ are respectively, the non-dimensional displacement of the disk of charge with respect to the undisturbed stagnation plane, the non-dimensional jump in the velocity potential and the oscillation phase of the disk. That is:

$$\beta = \frac{\mu_+ \hat{E}}{\omega R}, \quad \chi = \frac{|\Delta\varphi|_{max}}{aR^2}, \quad \tau = \omega t. \tag{6.17}$$

Finally, the analytical induced velocities are given by:

$$\bar{v}_r^i = -\frac{\partial B_\theta^i}{\partial \bar{z}} = \frac{\chi\sin\tau(\bar{z}-\beta\sin\tau)}{\pi\left(1+\bar{r}^2+2\bar{r}+(\bar{z}-\beta\sin\tau)^2\right)^{3/2}}\left(\frac{-2K(k)+E(k)\frac{2-k^2}{1-k^2}}{k^2}\right), \tag{6.18}$$

$$\bar{v}_z^i = \frac{1}{\bar{r}}\frac{\partial(\bar{r}B_\theta^i)}{\partial\bar{r}} = \chi\sin\tau\Bigg\{\frac{\bar{r}+1}{\pi\left(1+\bar{r}^2+2\bar{r}+(\bar{z}-\beta\sin\tau)^2\right)^{3/2}}\left(\frac{(2-k^2)K(k)-2E(k)}{k^2}\right)+\dots$$

$$\dots-\frac{2(1+(\bar{z}-\beta\sin\tau)^2-\bar{r}^2)}{\pi\left(1+\bar{r}^2+2\bar{r}+(\bar{z}-\beta\sin\tau)^2\right)^{5/2}}\left(\frac{K(k)-\frac{E(k)}{1-k^2}}{k^2}\right)\Bigg\}.$$

The total velocity can be obtained from $\vec{v} = \vec{v}^s + \vec{v}^i$ or, using the vector potentials, from:

$$\vec{v}(\bar{r},\bar{z},\tau) = \vec{\bar{\nabla}}\times\vec{B},$$
$$\text{with} \quad \vec{B}(\bar{r},\bar{z},\tau) = B_\theta\vec{u}_\theta = \vec{B}^s(\bar{r},\bar{z}) + \vec{B}^i(\bar{r},\bar{z},\tau).$$

This latter representation is very convenient since the streamfunction, that represents the instantaneous streamlines (iso-Ψ lines), is given by:

$$\Psi = -\bar{r}B_\theta,$$

where, by symmetry, $\Psi = 0$ corresponds to the stagnation point streamlines: $\bar{r} = 0$ and $B_\theta(\bar{r},\bar{z},\tau) = 0$.

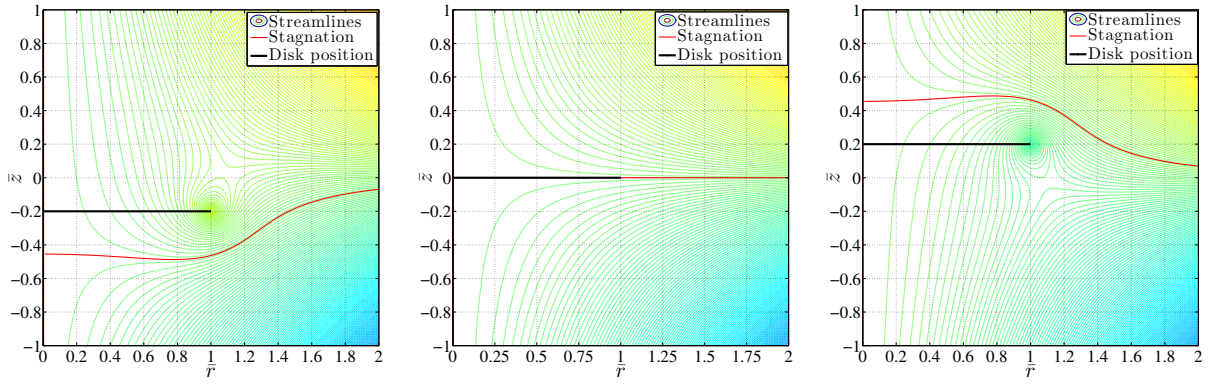

(a) $\tau = -\pi/2$. (b) $\tau = 0$. (c) $\tau = \pi/2$.

Figure 6-14: Instantaneous streamlines for β=0.2 and χ=1 at three positions during the oscillation cycle, τ=$-\pi/2$, 0 and $\pi/2$. The streamlines that go through the stagnation point are marked in red. The position of the oscillating porous disk is marked in black.

Figure 6-14 shows an example, with parameters β=0.2 and χ=1, of the instantaneous streamlines at three different times during the oscillation period of the charged disk.

The induced velocity field consists of concentrated eddies around the edge of the disk that are superimposed to the axi-symmetric stagnation point flow. $\tau = \pm\pi/2$ corresponds to the maximum excursion of the charged disk to a position $\pm\beta$ from the unperturbed stagnation plane at $\bar{z} = 0$. Streamlines for $\pm\tau$ are symmetric with respect to $\bar{z} = 0$.

The maximum displacement of the disk also corresponds with the maximum perturbation of the flow field as the induced contribution to the streamfunction is proportional to $\sin\tau$. In this case, the surface that goes through the stagnation point is deformed from the $\bar{z} = 0$ plane to a surface that has been displaced in the same direction as the disk for values corresponding to radii inside the disk, $\bar{r} < 1$, and that tends to the undisturbed plane position far from the disk, $\bar{r} >> 1$. Thus, the motion of the stagnation point surface has a flapping-like behavior, with curving at the edge of the disk.

For $\tau = 0$, the disk is at $\bar{z} = 0$ and there is no induced velocity (since the perturbation is proportional to $\sin\tau$), so that the streamlines correspond to the undisturbed stagnation point flow.

Fluid particle trajectories and time-averaged streamlines

Ignoring the reaction and diffusion terms, once the velocity vector field is known, the fluid particle trajectories can be integrated from:

$$\begin{aligned} \frac{d\bar{r}_p}{d\tau} &= \frac{a}{\omega}\bar{v}_r(\bar{r},\bar{z},\tau), \\ \frac{d\bar{z}_p}{d\tau} &= \frac{a}{\omega}\bar{v}_z(\bar{r},\bar{z},\tau), \end{aligned} \tag{6.19}$$

with initial conditions $(\bar{r}(\tau_0),\bar{z}(\tau_0)) = (\bar{r}_0,\bar{z}_0)$.

Due to the different time scales of the disk oscillation, under kHz excitation, and the unperturbed flow time scale, $\sim 25ms$, individual particles released at the opposed tubes' exit areas will essentially be affected by the *mean* perturbation. This is shown by comparing the calculated trajectories of the fluid particles (with time as a parameter) in Figure 6-15(a), for β=0.2, χ=1 and $a/\omega = 3\cdot 10^{-3}$, to the *time-averaged* streamlines in Figure 6-15(b).

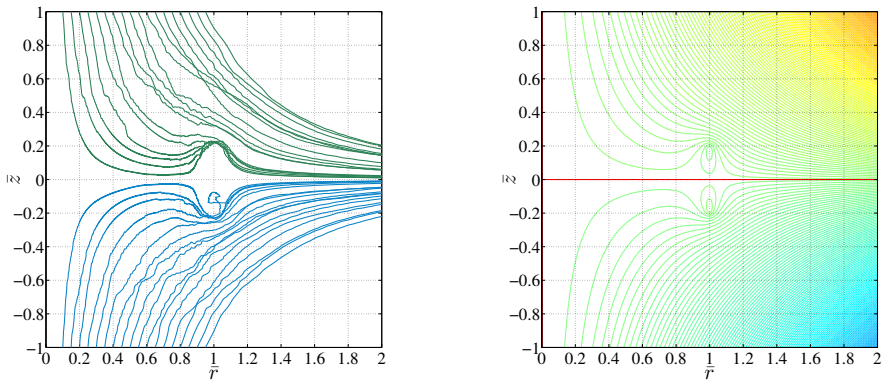

(a) Particle trajectories.

(b) Time-averaged streamlines.

Figure 6-15: Trajectories for fluid particles released at $\bar{z} = \pm 1$ and time-averaged streamlines (over a cycle of oscillation of the charge). The stagnation plane is marked in red. Parameters used: β=0.2, χ=1, $a/\omega = 3\cdot 10^{-3}$.

Therefore, individual fuel and oxidizer particles will approximately follow the time-averaged streamlines over a cycle of oscillation of the charge, which can be obtained from:

$$< \Psi >= \frac{1}{2\pi}\int_0^{2\pi} \Psi(\bar{r},\bar{z},\tau)d\tau. \tag{6.20}$$

Similarly, the *cycle-averaged* velocity components are given by:

$$< \bar{v}_z > = \frac{1}{2\pi} \int_0^{2\pi} \bar{v}_z(\bar{r}, \bar{z}, \tau) d\tau, \tag{6.21}$$
$$< \bar{v}_r > = \frac{1}{2\pi} \int_0^{2\pi} \bar{v}_r(\bar{r}, \bar{z}, \tau) d\tau.$$

This has a few immediate consequences, for the continuing discussion:

- Although the instantaneous stagnation plane has important excursions of the order of the charged disk displacement, the *cycle-averaged* stagnation plane remains at $\bar{z} = 0$ for a symmetric oscillation in which $\beta(\bar{z} < 0) = \beta(\bar{z} > 0)$ (equal mobilities in both streams).

- The flow field distortion is greatest at the border of the flame, $\bar{r} \approx 1$, where vortices and recirculation bubbles appear, even after integration over an oscillation cycle.

- The different time scales of the problem (flow versus electric excitation) allow to evaluate the *time-averaged* flow-field, in a cycle of oscillation of the charge, so that now the problem can be treated as steady-state.

- Close to the center of the flame the forced entrainment at the edge is not seen, so that a 1D similarity solution can be used to evaluate the impact on the flame position (discussion to follow).

1D similarity solution close to the flame center, approximations for small $\bar{r}$

Close to the flame center, $\bar{r} << 1$, the expressions for the instantaneous induced velocity components (equation 6.18) and vector potential (equation 6.16) become, to first order in $\bar{r}$:

$$B_\theta^i \approx \chi \sin\tau \frac{\bar{r}}{4\left(1 + (\bar{z} - \beta\sin\tau)^2\right)^{3/2}}, \tag{6.22}$$
$$\bar{v}_r^i \approx -\frac{\bar{r}}{2} \frac{\partial F_i}{\partial \bar{z}} \chi \sin\tau,$$
$$\bar{v}_z^i \approx F_i(\bar{z} - \beta\sin\tau)\chi\sin\tau,$$
$$\text{with:} \quad F_i(\bar{z} - \beta\sin\tau) = \frac{1}{2\left(1 + (\bar{z} - \beta\sin\tau)^2\right)^{3/2}}.$$

So that the form of the velocity vector for small $\bar{r}$ is the same as that of the stagnation point flow (1D solution from 2D axisymmetric field).

The (non-dimensional) strain rate is defined as:

$$\varepsilon = -\frac{\partial \bar{v}_z}{\partial \bar{z}} = 1 - \chi \sin\tau \frac{\partial F_i}{\partial \bar{z}} = 1 + \frac{3\chi \sin\tau}{2} \frac{\bar{z} - \beta \sin\tau}{\left(1 + (\bar{z} - \beta \sin\tau)^2\right)^{5/2}}, \tag{6.23}$$

where the unperturbed strain rate is $\varepsilon = 1$.

Close to the stagnation plane where the flame front sits, $\bar{z} \approx 0$, the strain rate becomes:

$$\varepsilon_s = 1 - \frac{3\chi\beta}{2} \frac{\sin^2\tau}{\left(1 + \beta^2 \sin^2\tau\right)^{5/2}}, \tag{6.24}$$

which means that it is locally reduced independently of the charged disk's position. The same is true for the time-averaged strain rate:

$$< \varepsilon_s >= 1 - \Delta\varepsilon_s = 1 - \frac{3\chi\beta}{2} \frac{1}{2\pi} \int_0^{2\pi} \frac{\sin^2\tau}{(1 + \beta^2 \sin^2\tau)^{5/2}} d\tau. \tag{6.25}$$

All in all, close to the center of the flame, the net effect of the oscillating charged disk is to locally reduce the strain rate (by $\Delta\varepsilon_s$), which will naturally affect the position of the flame.

At this point, before continuing the discussion, it is interesting to review the different phases and amplitudes of the variables involved, in order to provide a physical explanation of this *rectification* effect.

On the one hand, the position of the charged disk is retarded 90° with respect to the applied electric field, since the charged particle drift is proportional to the field and the position is given by its integral. On the other hand, the instantaneous induced velocities are also retarded 90° with respect to the electric field, since they go as the velocity potential jump. This means that when the disk is at a displaced position *upwards* of the undisturbed stagnation plane, the induced velocity is also *upwards*, and vice versa for the *downwards* direction. However, the magnitude of the induced velocity at a fixed point in space depends on the relative position with respect to the disk (equation 6.22), and is maximum precisely at the disk location. Therefore, even after integrating in a cycle of oscillation of the charge,

there will be a net *upwards* velocity, *upwards* of the stagnation plane, and a net *downwards* velocity, *downwards* of the stagnation plane. This is precisely what produces the local reduction of the total strain rate close to the stagnation plane position.

6.4.5 Flame displacement

For an opposed-jet-type flow field, the flame position will depend on the stagnation plane location (it will be close to it since that is where the mixing zone between the two jets lies), and, with respect to the latter, on the strain rate magnitude. Under the effect of a fast oscillating field, and close to the axis of the flame, the stagnation plane will remain in its undisturbed position and the strain rate will be slightly reduced, by $\Delta\varepsilon_s$ given in equation 6.25.

The location of the flame in such a flow field has a simple analytical solution that was reviewed in Section 6.4.1. Using the non-dimensionalization introduced in Section 6.4.4, from equation 6.7, the position of the perturbed flame $\bar{z}_{\rm fl}^{p}$ under the influence of a fast AC field, with respect to the stagnation plane, becomes:

$$\bar{z}_{\rm fl}^{p} = \sqrt{\frac{2\bar{D}}{<\varepsilon_s>}}\,\mathrm{erf}^{-1}\left(1-2Z_{st}\right), \tag{6.26}$$

where the non-dimensional diffusion coefficient is given by $\bar{D} = D/(aR^2)$. Since the actual position of the stagnation plane has not been measured, it is more convenient in terms of comparison with the experiments, to evaluate the displacement of the flame $\Delta z_{\rm fl}^{p}$ with respect to the undisturbed flame position $z_{\rm fl}^{u}$ (baseline without an applied field), which is known:

$$\frac{\Delta z_{\rm fl}^{p}}{z_{\rm fl}^{u}} = \frac{z_{\rm fl}^{p} - z_{\rm fl}^{u}}{z_{\rm fl}^{u}} = \frac{1}{\sqrt{<\varepsilon_s>}} - 1. \tag{6.27}$$

From equation 6.27, $\Delta z_{\rm fl}^{p} > 0$, since $(<\varepsilon_s>) < 1$, so that the flame is displaced towards the oxidizer side in agreement with the experimental results in Section 6.2.2.[4]

Moreover, by recalling the dependencies of β and χ on the plasma and electrical parame-

[4]The oxidizer boundary condition corresponds to $Z = 0$ which, from equation 6.7, happens when $\bar{z} \to \infty$. Therefore, positive displacement indicates motion towards the oxidizer side.

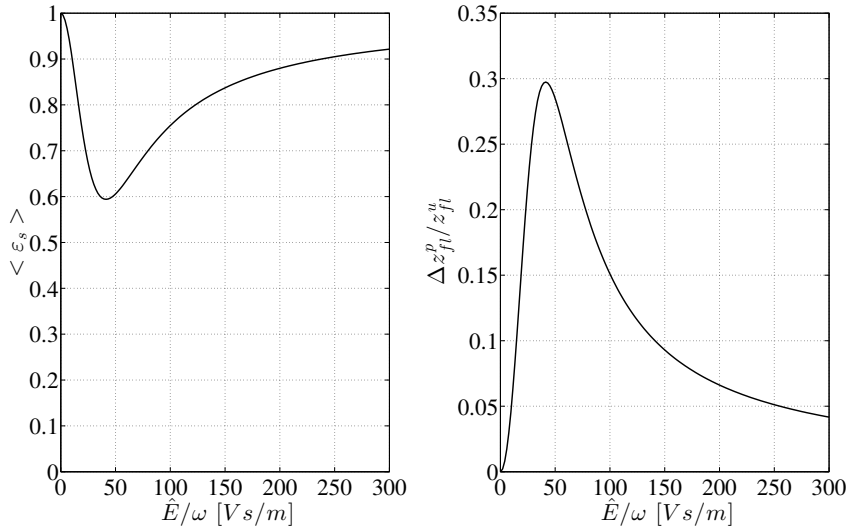

Figure 6-16: Strain rate reduction and flame displacement (towards the oxidizer) as a function of the electric field divided by the frequency. Parameters used are $\beta = 2.7{\cdot}10^{-2}\frac{\hat{E}}{\omega}$ and $\chi = 5.2{\cdot}10^{-2}\frac{\hat{E}}{\omega}$, both in S.I. units.

ters, it can be seen that they are both proportional to the local electric field, at the position of the charge, and inversely proportional to the excitation frequency, that is $\beta \propto \chi \propto \hat{E}/\omega$. The constant of proportionality for β is (μ_+/R) and for χ, $\sigma_0/(a\rho R^2)$. The variability of the modified strain rate and the flame displacement with $\hat{E}/\omega$ is shown in Figure 6-16 for $\beta = 2.7{\cdot}10^{-2}\frac{\hat{E}}{\omega}$ and $\chi = 5.2{\cdot}10^{-2}\frac{\hat{E}}{\omega}$, both in S.I. units.[5]

For now, the dependence has been written in terms of $\hat{E}/\omega$ since at this point the disk of charge has not been modeled as a circuit element and nothing has been said about the electric field *seen* by it. It is clear that $\hat{E}$ is proportional to the applied voltage amplitude so that the qualitative shape of the curve in Figure 6-16 is representative of the dependence on the applied voltage. However, $\hat{E}$ will most likely also depend on the frequency, as will be proposed in Section 6.5, so that the curve is not representative of the dependence on the frequency.

Therefore, Figure 6-16 already explains the surprising observation that the displacement has a maximum at a certain value of the applied voltage (for fixed frequency) so that, increasing the applied voltage, does not necessarily result in a larger flame displacement.

[5]These values correspond to using: μ_+=2.7cm^2/V/s, R=1cm, a=40s^{-1}, ρ=0.21kg/m^3, δ_i=0.6mm, n_i=4.6·10$^{17}m^{-3}$ and $\sigma_0 = e\delta_i n_i$.

Note that the existence of this maximum perturbation with $\hat{E}/\omega$ can be explained as the competing effect between the *strength* of the perturbation (χ) and its *localization* (β).

Another interesting finding is that the position of the maximum perturbation depends on (μ_+/R) alone, as can be seen when using equation 6.25 to evaluate:

$$\frac{\partial(\Delta\varepsilon_s)}{\partial(\hat{E}/\omega)} = 0 \quad \longrightarrow \quad \left.\frac{\hat{E}}{\omega}\right|_{\max(\Delta\varepsilon_s)} = f\left(\frac{\mu_+}{R}\right), \tag{6.28}$$

so that it only depends on the identity of the ions and the size of the flame, and not on the amount of charge that is oscillating.

In order to be able to perform a quantitative comparison with the experimental data, a model for $\hat{E} = \hat{E}(V_{pk}, \omega)$ is proposed in Section 6.5.

6.4.6 Other effects

A symmetric model with a single oscillating charged disk already predicts a reduction of the strain rate that results in a displacement of the flame towards the oxidizer side (equation 6.27) and the existence of a maximum, of this displacement, with the applied voltage. In this Section, three aspects that were ignored are briefly explored to check that they do not contradict the results from the simplified case. Those three effects are the existence of negatively charged ions, asymmetries in the charge oscillation, and the continuity of the charge extraction model including a finite ionization rate and the charge disappearance, through recombination and electrode absorption (for large oscillations).

Two disks of charge (positive and negative)

For two disks, one with positive charge and the other with negative charge, but otherwise identical, i.e. $\beta_+ = \beta_-$ and $\chi_+ = \chi_-$, that are *released* from the flame at the same time and do not interact with each other, their oscillations will be symmetrically synchronized. This means that their individual *time-integrated* effect over one cycle of oscillation will be equal (the instantaneous perturbation is out of phase by π but otherwise the same). Therefore, the time-integrated perturbation simply adds up, the maximum of $\Delta\varepsilon_s$ will occur for the same $\mu_+/R = \mu_-/R$ and the amplitude of the perturbation will be doubled ($\chi \to 2\chi$).

Asymmetries in the charge oscillation

Asymmetries in the charge oscillation will arise from:

- Different mobilities for the fuel and oxidizer sides $\mu_f \neq \mu_{ox}$. E.g., for the experiments in this Chapter, the fuel is highly diluted in argon and the oxidizer in nitrogen. The mobility of the expected most abundant ion, H_3O^+, in argon is $\mu_+ \approx 3.6 cm^2/V/s$, whereas in nitrogen it is $\mu_+ \approx 2.7 cm^2/V/s$ (value at 300K and 80Td) [215,216]. These values imply that $\beta_f/\beta_{ox} \approx 1.3$, so that the disk's excursion towards the fuel is around 30% longer than towards the oxidizer.

- Differences in the identity of the positive and negative ions ($\beta_+ \neq \beta_-$ and $\chi_+ \neq \chi_-$).

- If the negative ions are created through electron attachment, differences in attachment coefficients of the fuel and oxidizer sides will result in an asymmetry in the location of the negative ion birth.

The main effect that these asymmetries introduce in the model is the displacement of the stagnation plane to a new equilibrium position. For the most notorious difference of unmatching mobilities in the fuel and oxidizer sides, the effect is analyzed in what follows.

In Section 6.4.4, the position of the instantaneous stagnation surface was given by $B_\theta = 0$, where B_θ for small $\bar{r}$ was simplified to the summation of equations 6.15 and 6.22. Considering differences in the mobilities in the oxidizer ($0 \leq \tau < \pi$) and fuel ($\pi \leq \tau < 2\pi$) sides, and integrating over an oscillation cycle, the perturbed stagnation plane position, $\bar{z}_s^p(\chi, \beta_{ox}, \beta_f)$, is obtained from:

$$\frac{\bar{z}_s^p}{2} - \frac{1}{2\pi}\left(\int_0^\pi \frac{\chi \sin\tau}{4\left(1+(\bar{z}_s^p - \beta_{ox}\sin\tau)^2\right)^{3/2}}d\tau + \int_\pi^{2\pi} \frac{\chi \sin\tau}{4\left(1+(\bar{z}_s^p - \beta_f \sin\tau)^2\right)^{3/2}}d\tau\right) = 0, \tag{6.29}$$

where, for $\beta_{ox} = \beta_f$, $\bar{z}_s^p = 0$ consistently with the symmetric model of the previous sections.

Figure 6-17 shows the stagnation plane displacement when using β_{ox}= $2.7{\cdot}10^{-2}\frac{\hat{E}}{\omega}$ and χ=$5.2{\cdot}10^{-2}\frac{\hat{E}}{\omega}$ (S.I. units) as before and now $\beta_f = 1.3\beta_{ox}$. In this case, the displacement of the stagnation plane is also in the direction of the oxidizer (positive values), and the position

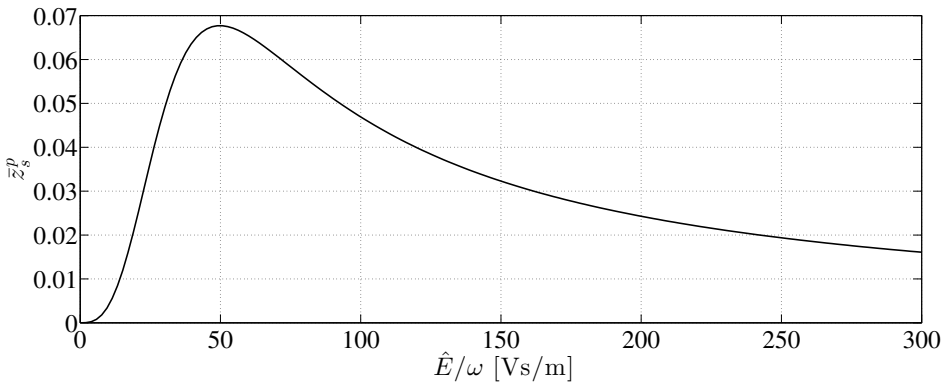

Figure 6-17: Stagnation plane displacement (towards the oxidizer) for an asymmetric oscillation of the charge as a function of the electric field divided by the frequency, where the mobility in the fuel stream is 30% higher than in the oxidizer stream. Parameters used are β_{ox}= $2.7{\cdot}10^{-2}\frac{\hat{E}}{\omega}$ and χ=$5.2{\cdot}10^{-2}\frac{\hat{E}}{\omega}$, both in S.I. units.

of the maximum displacement with $\hat{E}/\omega$ is close to the position of maximum strain rate modification.

In addition to the stagnation plane displacement, the local strain rate will still be reduced (by the expression in equation 6.25 but now separating the integral into two parts, [0,π) and [π,2π) with different β) and the two effects will add up to a larger displacement towards the oxidizer. Also, note the different scales used in Figures 6-16 and 6-17, where, in the first case, the flame displacement is non-dimensionalized by its unperturbed position, $\bar{z}_{\rm fl}^u$, and, in the second, by the flame radius. Using $\bar{D}$ = 0.1 (a=40s^{-1}, R=1cm, D=4cm^2/s) and Z_{st}=0.32, $\bar{z}_{\rm fl}^u$=0.15 ($z_{\rm fl}^u$ ≈1.5mm), so that the stagnation plane displacement and the displacement of the flame, relative to the new stagnation plane position, can become comparable.

All in all, the most important finding from this part is that the asymmetry is required to displace the stagnation plane (where the direction of the displacement depends on the relative values of β on either side) but not to displace the flame towards the oxidizer, and for the experimental parameters used, both contributions add up in the same direction and are of the same order of magnitude.

Finite ionization rate and charge removal

The model up to now has considered a single charged disk oscillating under the influence of the applied voltage. In reality, the charge production will be continuous and there will be

mechanisms of charge loss such as recombination or electrode absorption (for large amplitude oscillations). In this part, the ionization at the flame front is modeled discretely as a *source* of disks of charge per unit area σ_0 and *release* frequency f_i, so that the production rate is given by:

$$\dot{\sigma}_i = \sigma_0 f_i,$$

and all the disks are released from the same location, $\bar{z} \approx 0$.

The motion of the individual disks is still considered independent of the presence of other disks, but the disks are *removed* from the domain at a frequency f_r, so that the removal rate is given by:

$$\dot{\sigma}_r = -\sigma_0 f_r,$$

and they can be removed anywhere within the inter-electrode space.

Within this approximation, each individual disk will follow the equations of motion given in equation 6.9, but now, for each disk $i = 1, 2, 3, \ldots N$, the integrations will be performed from $\tau = \tau_i = \omega \frac{i-1}{f_i}$ instead of $\tau = 0$ (instant when the disk is released). The total number of disks released within a cycle of excitation, N, will be given by $N{=}f_i/f$ (where N is rounded to the largest integer that does not exceed f_i/f, and for $f_i/f < 1$, $N{=}1$).

The total perturbation will be equal to adding the individual contributions, e.g. for the strain rate modification: $\Delta\varepsilon_s = \sum_{i=1}^{N} (\Delta\varepsilon_s)_i$, and from equation 6.25, $(\Delta\varepsilon_s)_i$ becomes:

$$(\Delta\varepsilon_s)_i = \frac{3\chi\beta}{2} \frac{1}{2\pi} \int_{\tau_i}^{\tau_r} \frac{(\sin\tau - \sin\tau_i)^2}{\left(1 + \beta^2 (\sin\tau - \sin\tau_i)^2\right)^{5/2}} d\tau,$$

where the individual integration limits are between τ_i and $\tau_r = \tau_i + \omega/f_r$, with both τ_i and $\tau_r \in [0, 2\pi]$. Finally, the trajectories followed by the disks will be given by:

$$\bar{z}_i(\tau) = \beta (\sin\tau - \sin\tau_i), \qquad \tau \in [\tau_i, \tau_f].$$

Since the problem, after averaging over a cycle of excitation, is in steady state, it will

be assumed that all the charge that is created is removed, that is f_i=f_r. To estimate the frequency f_i, the charge per unit area will be approximated by σ_0=$e(\delta_i n_i)$, and the rate of disk extraction by f_i=$\dot{\sigma}_i/\sigma_0$=$(\delta_i \dot{n}_i)/(\delta_i n_i)$. So that, for $\delta_i \approx 0.6mm$, $n_i \approx 4.6 \cdot 10^{17} m^{-3}$ and $\delta_i \dot{n}_i \approx 3.6 \cdot 10^{17} m^{-2} s^{-1}$, the frequency is f_i ∼1kHz. Since the excitation frequency is in the 1-35kHz range, the approximation of a single oscillating disk is ok. For $f_i > f$, the situation is plotted in Figure 6-18, with parameters β= $2.7{\cdot}10^{-2}\frac{\hat{E}}{\omega}$ and χ=$5.2{\cdot}10^{-2}\frac{\hat{E}}{\omega}$ (S.I. units) and $f/f_i = 0.1$. In the latter case, the amplitude of the oscillation is limited since the charged disks *disappear* during their trajectories. This oscillation limitation has a similar effect to reducing β and the maximum perturbation moves to higher $\hat{E}/\omega$, but it is still encountered. For $f_i < f$, the disks perform full sinusoidal oscillations. Absorption by the electrodes would result in a similar effect but instead of truncating the trajectories at a fixed time after release, they need to be truncated at a fixed distance from $\bar{z}$=0.

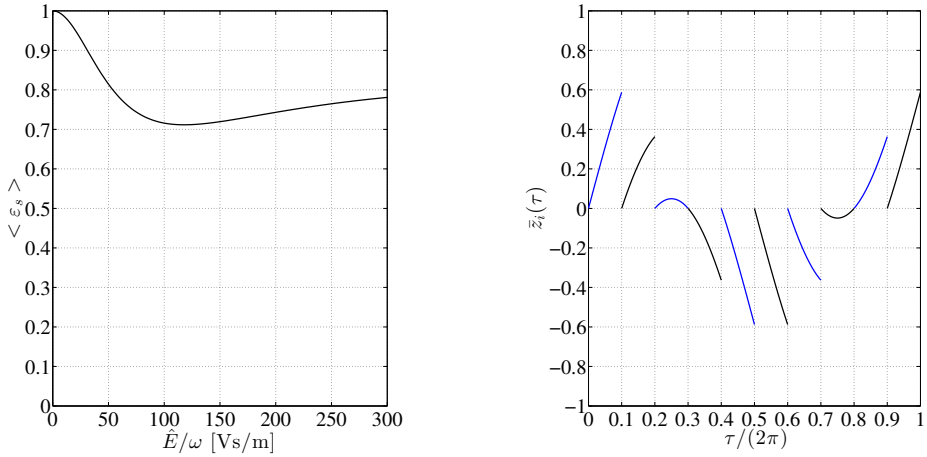

(a) Strain rate modification.

(b) Disk trajectories.

Figure 6-18: Impact of a finite disk-release rate and disk removal on the strain rate reduction and disk trajectories. Parameters used are β= $2.7{\cdot}10^{-2}\frac{\hat{E}}{\omega}$ and χ=$5.2{\cdot}10^{-2}\frac{\hat{E}}{\omega}$, both in S.I. units, and f/f_i=0.1 (excitation frequency over disk *release* frequency).

6.5 Electrical model of the flame

6.5.1 Charge in contact with the electrodes

The description of a flame as an electrically active component of a circuit has been studied, to name a couple of examples, in the context of electrothermal loudspeakers [172] and active closed-loop control of flames [18].

At low frequencies, when the charge from the flame has time to redistribute throughout the extent of the inter-electrode space, the circuit description is well-know and consists of a resistance (that of the ions and electrons) in parallel with the capacitance of the electrodes, as reported in [18, 172] for different types of flames and electrode orientations. In this case, the critical condition so that the model holds is that, indeed, the charge is in contact with the electrodes.

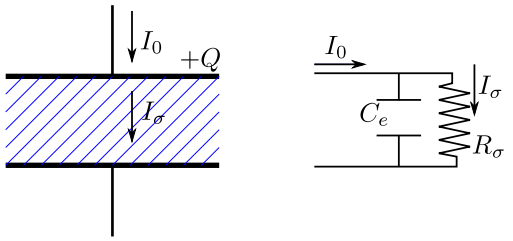

Figure 6-19: Equivalent electrical circuit when the charge is redistributed in all the inter-electrode space. Region shaded in blue indicates volume occupied by charge.

The schematic in Figure 6-19 (left image) illustrates the parallel plate electrodes with a volumetric charge occupying all the inter-electrode space from which the equivalent circuit is extracted. I_0 is the total current through the gap, I_σ is the conduction current flowing through the charge and Q is the charge accumulation at the electrodes. The rate of charge arriving at the electrodes will then be given by the net current across them, that is:

$$\frac{dQ}{dt} = I_0 - I_\sigma.$$

In addition, the conduction current is related to the resistance of the volumetric charge,

and the accumulated charge to the capacitance of the electrodes by:

$$I_\sigma = \frac{V}{R_\sigma}, \qquad Q = C_e V.$$

Combining these expressions, the total current is given by:

$$I_0 = C_e \frac{dV}{dt} + \frac{V}{R_\sigma},$$

which corresponds to the equivalent circuit of a capacitance in parallel with a resistance shown in Figure 6-19 (image on the right). This model is consistent with the electrical measurements in Section 6.3.1.

6.5.2 Floating charge

At sufficiently high frequencies, the situation changes since the charge is oscillating within the inter-electrode gap without being in contact with the electrodes as discussed in Section 6.4.3. The schematic of the parallel electrodes with a floating volumetric charge is shown in Figure 6-20 (left image), where, in addition to the symbols already introduced, q refers to a possible charge accumulation / separation at the limits of the charged region, symmetry has been assumed for simplicity, and H and δ refer to the half-length of the electrode gap and charged region respectively and V' and V'_σ to the potential half-drop across the full gap (applied voltage) and across the charged region respectively.

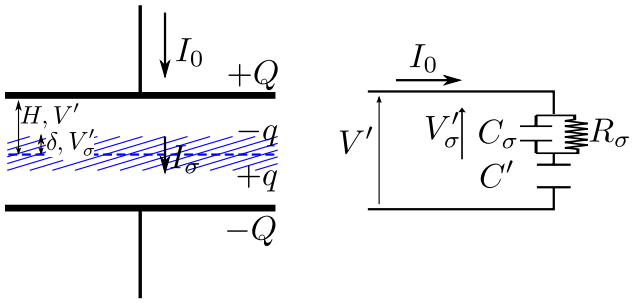

Figure 6-20: Equivalent electrical circuit for a *floating* charge not in contact with the electrodes. Region shaded in blue indicates volume occupied by charge.

From this schematic, and recalling that now there is no conduction current out of the

region occupied by the charge (blue shaded region in the Figure), the rate of charge arriving at the edge of the charged region and at the electrodes becomes respectively:

$$\frac{dq}{dt} = I_\sigma, \qquad \frac{dQ}{dt} = I_0.$$

The conduction current is still related to the resistance of the floating charge but now the potential drop across it is only a fraction of the full voltage:

$$I_\sigma = \frac{V'_\sigma}{R_\sigma},$$

and the surface charges, $Q/\mathcal{A}$ and $q/\mathcal{A}$, will be given by:

$$Q/\mathcal{A} = \varepsilon_0 E' = \varepsilon_0 \frac{V' - V'_\sigma}{H - \delta}, \qquad q/\mathcal{A} = \varepsilon_0 (E' - E'_\sigma) = \varepsilon_0 \left(\frac{V' - V'_\sigma}{H - \delta} - \frac{V'_\sigma}{\delta} \right).$$

Combining these expressions, and identifying the capacitances involved as $C_e = \mathcal{A}\varepsilon_0/H$ (capacitance of the parallel electrodes), $C_\sigma = \mathcal{A}\varepsilon_0/\delta$ (capacitance of the charged region) and $C' = \mathcal{A}\varepsilon_0/(H - \delta)$ (remainder), the total current is given by:

$$I_0 = C_\sigma \frac{dV'_\sigma}{dt} + \frac{V'_\sigma}{R_\sigma} = C' \frac{d(V' - V'_\sigma)}{dt},$$

which corresponds to the equivalent circuit of a capacitance C' in series with $R_\sigma || C_\sigma$ shown in Figure 6-20 (image on the right).

Note that this circuit model is also representative of the *floating* discharges observed in Section 3.3.1 (N_2-He-N_2 GBD) and 5.4.1 (selective RPND excitation of the flame).

The transition from the first model (charge in contact with the electrodes, Section 6.5.1) to the second model (floating charge, Section 6.5.2) is continuous, since as $\delta \to H$, $C_\sigma \to C_e$, $C' \to \infty$ (short circuit) and $V' \to V'_\sigma$. Also, the series connection of C_σ and C' corresponds to the total capacitance of the electrodes C_e.

A model like the one in Figure 6-20 was also used in [185] for a Meker-type premixed hydrogen/air flame (with additives) when applying a ∼100MHz electric field, without going into the derivation of the circuit.

For a thin region of charge ($\delta << H$), $C_\sigma >> C'$ and to first approximation C_σ will be ignored, so that the amplitude of the voltage *seen* by the charged disk, as a function of the applied voltage and the frequency, becomes:

$$\left|\frac{V'_\sigma}{V'}\right| = \frac{\omega/\omega_c}{\sqrt{1+(\omega/\omega_c)^2}}, \tag{6.30}$$

with ω_c the characteristic frequency given by $\omega_c = (R_\sigma C')^{-1}$.

Note that this second model is not incompatible with the measurements in Section 6.3.1, since at high frequency, the capacitance dominates and the system response includes the contribution of several capacitances in parallel (not that of the electrodes alone). Also, at frequencies above ∼1kHz there was a noise coupled to the signal that impeded a proper interpretation of the results (in particular the phase measurement).

For an estimate of the characteristic frequency, the capacitance C' will be close to the electrode capacitance C_e measured in Section 6.3.2, $C_e \approx 2.3pF$. For the resistive component, R_σ, only its value at low frequency (when the first circuit model applies) could be measured and was estimated to be in the range $R_\sigma \sim$ 75-325$M\Omega$. The resistance at high frequency (when the physics are best represented by the second model) could not be determined from the measurements but in any case, it should be lower since it is proportional to the length of the region of conduction. Thus, a very crude evaluation gives $f_c > 1kHz$.

6.6 Parameter fit of the model to the experiment

6.6.1 Fully symmetric model

The experimental flame displacement data from Figure 6-5 were fitted to the baseline oscillating charge model and the results are plotted in Figure 6-21. In this situation, the flame displacement towards the oxidizer side is exclusively due to a local reduction in the strain rate.

To that end, the flame displacement given by equation 6.27 (with the expression for the perturbed strain rate given by equation 6.25) was complemented by the circuit model for a *floating* charge (equation 6.30) in order to express the parameters β and χ (equation 6.17)

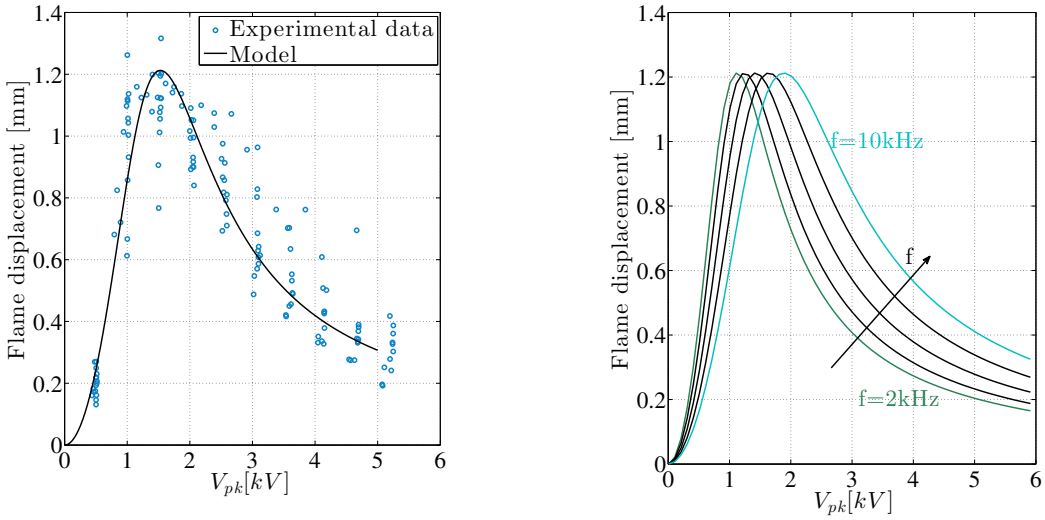

(a) Model fit for all frequencies.

(b) Frequency dependence (model).

Figure 6-21: Model fit to experimental data of Figure 6-5. Fully symmetric model. Strain rate reduction effect.

in terms of the applied voltage V_{app} and the excitation frequency f, that is:

$$\beta = \frac{\mu_+}{2\pi R\delta f_c}\frac{V_{\text{app}}}{\sqrt{1+(f/f_c)^2}},$$
$$\chi = \frac{\sigma_0}{aR^2\rho 2\pi\delta f_c}\frac{V_{\text{app}}}{\sqrt{1+(f/f_c)^2}}.$$

The coefficients $\beta_0 = \frac{\mu_+}{2\pi R\delta f_c}$ and $\chi_0 = \frac{\sigma_0}{aR^2\rho 2\pi\delta f_c}$ were obtained by ignoring the dependence on the frequency (Figure 6-21(a)) and fitting the data in a least-squares sense, and then the frequency effect was incorporated by selecting the characteristic frequency f_c.

The model was fitted by the parameter values:

$$\beta_0 = 3.4\cdot 10^{-3}V^{-1},$$
$$\chi_0 = 1.03\cdot 10^{-3}V^{-1},$$

and f_c=7kHz (the value of z_{fl}^u was taken as 1.5mm).

The parameters thus obtained are not unrealistic, e.g. using μ_+=$3.6cm^2/V/s$, R=$1cm$, $\delta \sim \delta_i \sim 0.5mm$, $n_i \sim 4\cdot 10^{17}m^{-3}$, ρ=$0.21kg/m^3$ and a=$40s^{-1}$, they become $\beta_0 \sim 1.6\cdot 10^{-3}V^{-1}$ and $\chi_0 \sim 1.7\cdot 10^{-3}V^{-1}$.

The trends with both the applied voltage and the frequency are captured by the model. However, the parameter fit results in an *agitation* parameter β_0 that is very high, which means that it is dubious whether the charge oscillations will be contained within the gap for the higher voltages (containment requires $\beta < \frac{L/2}{R}$, with L the inter-electrode distance).

6.6.2 Contribution of the asymmetry in the ion mobility

The parameter fit is now performed by including the effect of an asymmetry in the charge oscillation, in which the mobilities of the positive ions are different in the oxidizer and fuel sides by 30% (consistent with the compositions of the experimental jets), i.e. $\mu_{ox} = \mu_+$, $\mu_f = 1.3 \cdot \mu_+$, as discussed in Section 6.4.6. The results are plotted in Figure 6-22.

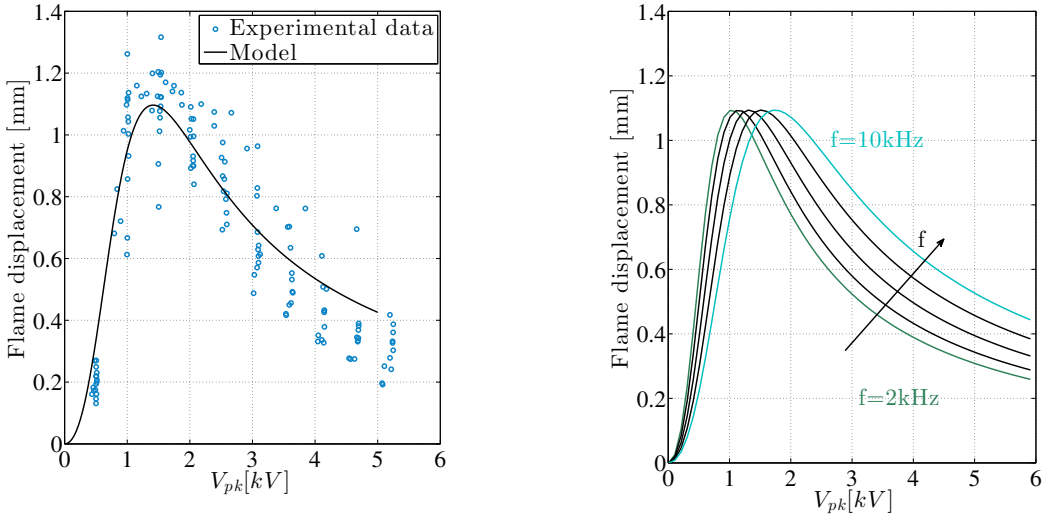

(a) Model fit for all frequencies.

(b) Frequency dependence (model).

Figure 6-22: Model fit to experimental data of Figure 6-5. Asymmetric model that includes a 30% difference in the ion mobilities in the fuel and oxidizer sides. Contribution of strain rate reduction and stagnation plane displacement.

In this case, the total flame displacement needs to incorporate the contribution of the stagnation plane displacement, due to the asymmetry in the oscillation of the charge, and, relative to the latter, the flame displacement due to the strain rate reduction. That is,

$$z_s^p + \Delta z_{fl}^p.$$

The stagnation plane displacement, z_s^p, is given by equation 6.29 (were the flame radius is taken as 1cm). The contribution of the reduction of the strain rate is incorporated as before, where now, the integral in the expression for the perturbed strain rate given by equation 6.25 needs to be separated into two parts, $[0, \pi)$ and $[\pi, 2\pi)$, with different β.

The parameter fit is done in the least-squares sense as before, for β_0 and χ_0, keeping the same critical frequency f_c=7kHz, and recalling that the asymmetry is introduced through:

$$\beta_{ox} = \beta_0 \frac{V_{\text{app}}}{\sqrt{1 + (f/f_c)^2}},$$
$$\beta_f = 1.3 \cdot \beta_0 \frac{V_{\text{app}}}{\sqrt{1 + (f/f_c)^2}}.$$

In this case, the model was fitted by the parameter values:

$$\beta_0 = 2.46 \cdot 10^{-3} V^{-1},$$
$$\chi_0 = 1.22 \cdot 10^{-3} V^{-1}.$$

Note the lower *agitation* parameter β_0, compared to the symmetric case.

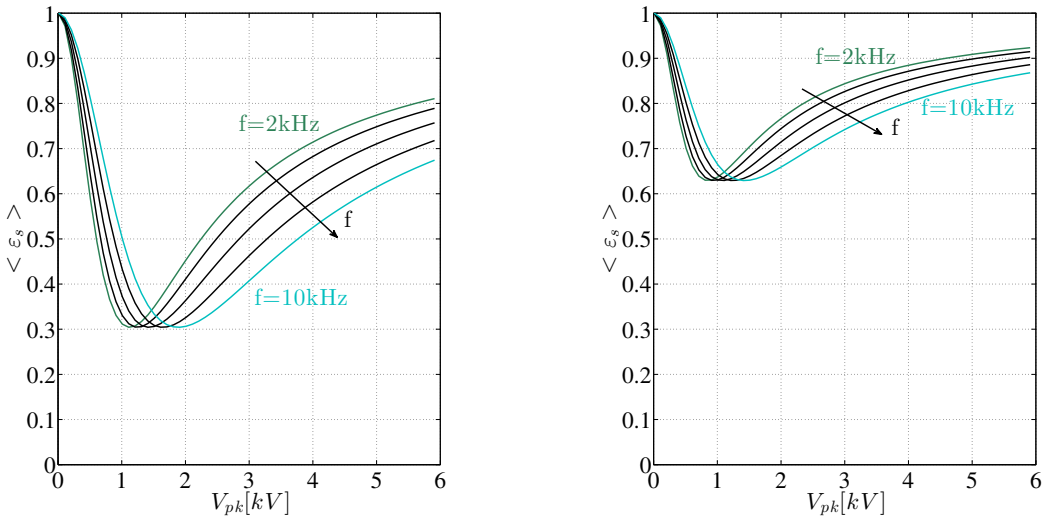

(a) Symmetric.

(b) Asymmetric.

Figure 6-23: Strain rate modification required to explain the experimental data when the flame displacement is solely due to a strain rate reduction (symmetric model, Section 6.6.1) and when the stagnation plane displacement is included (asymmetric model, Section 6.6.2).

In addition, the strain rate reduction required to explain the flame displacement is significantly reduced when including the asymmetric contribution of the stagnation plane displacement, see Figure 6-23. For the asymmetric case, the contribution of the stagnation plane displacement and the strain rate reduction become comparable, Figure 6-24(a).

Finally, as an academic exercise, it is interesting to evaluate what the flame displacement would be if the same β_0 is used but now the mobility in the fuel side is 30% *lower* than in the oxidizer side, that is $\beta_f = 0.7\beta_{ox}$, see Figure 6-24.

Both for $\beta_f = 1.3\beta_{ox}$ and $\beta_f = 0.7\beta_{ox}$, there is a strain rate reduction for all applied voltages and frequencies that results in a flame displacement towards the oxidizer side, relative to the stagnation plane. However, the direction of the displacement of the stagnation plane depends on the relative values of β on either side: i.e. for $\beta_f > \beta_{ox}$ the stagnation plane is displaced towards the oxidizer, Figure 6-24(a), and for $\beta_f < \beta_{ox}$ the stagnation plane is displaced towards the fuel, Figure 6-24(b). The total flame displacement depends on the relative contributions of both effects and is shown in Figure 6-24.

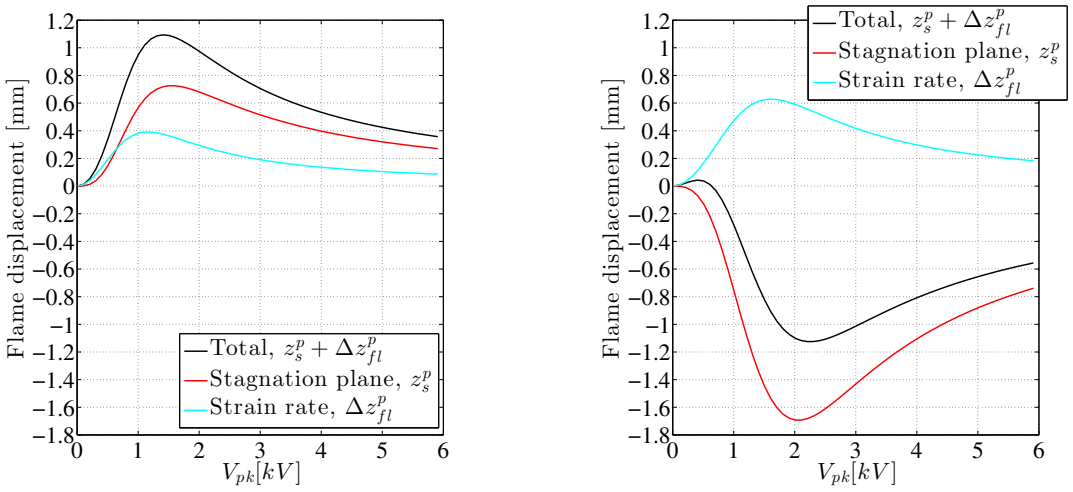

(a) $\beta_f = 1.3\beta_{ox}$.

(b) $\beta_f = 0.7\beta_{ox}$.

Figure 6-24: Contributions to flame displacement: stagnation plane displacement and strain rate reduction. Effect of relative values of β in the fuel and oxidizer sides. Positive values indicate displacement towards the oxidizer.

6.7 Summary of findings and implications

In this Chapter, experimental evidence of the displacement of a counterflow nonpremixed flame to a new steady position under the influence of high frequency AC fields is presented. The displacement of the flame was towards the oxidizer side, it had a maximum with the voltage amplitude and had little dependence on the excitation frequency.

An analytical model was proposed to explain the experimental results, in particular some of the surprising observations such as the maximization of the displacement at a given voltage (intuitively, a larger voltage would be thought to enhance the effect).

The dynamic model proposed was based on an oscillating charge of *finite* diameter that induced a velocity through localized eddies at the rim of the charged region. It was proposed that, the non-uniformity introduced by the finite extent of the flame was key in the conversion of the electrical energy to kinetic energy of the flow.

Within the model's assumptions, the *cycle-averaged* oscillation of the charge produced a *local* reduction of the strain rate, close to the region where the flame sits, which resulted in a displacement of the flame towards the oxidizer side, as in the experimental measurements. An unexpected observation from this model is that, contrary to many justifications in the literature, a fully *symmetric* model of the fluid properties (no differences between the fuel and oxidizer sides) was sufficient to justify the flame displacement towards the oxidizer side. However, the oxidizer / fuel asymmetries were required to produce a displacement of the stagnation plane. The total flame displacement would be given by the combination of the stagnation plane displacement and, relative to the latter, by the strain rate reduction. Due to the different time scales of the problem, both effects contribute to a rectification effect that results in a DC displacement of the flame under the influence of an AC field. An important extension of the work presented would be to visualize the flow field to discern whether the main contribution to the flame displacement was through the stagnation plane displacement or through the strain rate modification.

The counterflow nonpremixed flame is a very stable platform, from the model, a displacement of $\sim$1mm, requires a reduction in the local strain of a few 10%.

In order to justify the very weak dependence on the frequency, a circuit model of the

flame was proposed, that was different depending on whether or not the charge occupied the whole inter-electrode space. Although the model seems reasonable and both versions have been found in the literature, the model for the higher frequencies could not be verified experimentally. In addition, other effects such as the resistance dependence on the frequency and the voltage in this regime were not explored and could contribute to the independence on the frequency. An important extension of the model would be to analyze the dependence of σ_0, here considered constant, on voltage and frequency; which could prove to be a more accurate explanation than the high pass filter used, and might help overcome the large *agitation* (amplitude of the oscillation of the charged disk) obtained in the parameter fit.

All in all, the main contributions of this Chapter have been to present new evidence of the driving of steady flows in flames by AC fields as proposed by [47] and to propose a detailed, first-principles based explanation of the experimental observations with some unexpected findings.

In terms of the applicability of these findings, a local decrease in the strain rate can be used to increase the global extinction strain rate (e.g. velocity of injection of the reactants), since the local value is reduced. This can be of use to help control a vigorous flame, attenuate instabilities and so on. Moreover, by using high frequency AC fields, the agitation is concentrated close to the flame position and the localized effect avoids the waste of stirring the fluid far from it.

Chapter 7

Conclusion

7.1 Contributions of this thesis

In the first part of this dissertation (Chapters 3 through 5) the problem of the development of a fast modulated discharge in highly non-uniform gases has been explored. This fundamental problem is found in many technological applications (PAC, plasma development in mixing layers for aerodynamic actuation, plasma jets used as a source of reactive gas ...) as well as in naturally-occurring phenomena (sprites, TLE ...). Most of the work on streamer discharges in inhomogeneous gases has been performed either for the configuration of APPJ [24, 129] or for structures that resemble some phenomenom related to sprites [109, 140]. However, in the area of plasma assisted combustion, the structure of the gas discharge is also of paramount importance in terms of understanding where the species are being produced and how to tailor their appearance to the region where they are most effective.

In this thesis, a novel platform was developed to study the impact of strong inhomogeneities when using RPND, one of the main strategies used for plasma creation in the fields of PAC/PAI. The simplified model was named the Gas-confined Barrier Discharge, and used a nearly uniform electric field to highlight the dependencies on the gradients in composition and temperature. The main findings from these studies can be summarized as follows:

1. Two discharge regimes have been observed when applying RPND to a *layered* gas configuration: breakdown of the full discharge gap or selective breakdown of the layer

of most favorable ionization conditions. Transition between modes depends on the selection of the electrical and geometrical parameters.

2. It was argued that the insulating layers of gas behaved as pseudo-dielectrics (with important differences with respect to solid dielectrics that were explored), so that streamers would stagnate or even deflect at the interface of the different gases, and the ionization (and excitation) could be confined to the *hot* regions. The hypothesis was confirmed experimentally using differences in composition (helium versus nitrogen) and temperature, both for *filamentary-like* and *glow-like* breakdown.

3. The idea of having a *floating* plasma in specific regions of the flow field might be of interest for some applications since a purely non-thermal plasma is obtained and contact with the electrodes is avoided. However, the energy that can be coupled is inherently low, and an accurate estimation was not possible. In this work, proof-of-concept was provided, future work will need to explore ways of increasing the energy.

4. For the counterflow nonpremixed flame platform, selective excitation of the flame region was possible using RPND. Coupling of the plasma near the start of the reaction zone is interesting since it ensures that the short-lived species can participate in the combustion reactions. For the experiments performed, the impact of the RPND on the flame was limited to a slight curving at the edge of the flame (and not always). However, the envelope of the confinement could not be pushed (since the power supply available was used to its maximum capabilities) and it is yet to be determined if a fully confined plasma can have enough authority to modify the flame parameters.

5. More interestingly, it was shown how to couple the plasma to different regions of the flow field, offering an image of how the discharge would *naturally* develop in a complex combustion situation with flamelets and hot spots (if *unconstrained* by the electrodes).

Finally, the lack of authority encountered at atmospheric pressure on the counterflow nonpremixed flame when using RPND, for regimes outside of the ns-spark, shifted the efforts for the last part of this dissertation (Chapter 6) to the use of AC fields. The main contributions of this part can be summarized as follows:

6. A steady displacement of the flame towards the oxidizer side was experimentally observed when applying sub-breakdown high frequency (100Hz-10kHz) AC fields. The displacement had a maximum with the applied voltage amplitude and presented little dependency on the excitation frequency.

7. A detailed explanation of the experimental observations was proposed, based on a local reduction of the strain rate (when considering symmetric oxidizer and fuel sides) and a displacement of the stagnation plane (when considering oxidizer/fuel asymmetries). Both effects resulted in a displacement of the flame towards the oxidizer stream, in agreement with the experiments. In this problem, the finite size of the flame was key in the conversion of the electrical energy to kinetic energy of the flow.

7.2 Recommendations for future work

In view of the main findings of this research, a few areas of further investigation are recommended, mainly:

- *Further exploration of the GBD concept.* To the best of the author's knowledge, the idea of using insulating layers of gas to localize the plasma away from the electrodes, when using fast modulated discharges, is a novel one. In this work, an explanation of the physics of the dynamics of the plasma has been offered, and experimental confirmation based on the localization of the excitation of the plasma has been presented.

  The study can be extended at the fundamental level by providing more advanced diagnostics measurements to this configuration. On the one hand, the spatial and temporal structure of the emission and chemistry induced should be measured, as well as the spatially and temporally resolved nature of the ionized species present. Confinement could then be described in terms of which layers produce ionization and which do not.

  These studies would also determine whether the chemical activity of such a structure could be of any interest to other applications, that require the creation of a non-thermal plasma with no gas heating.

In addition, a detailed experimental exploration of the analytical regions of confinement predicted in this dissertation, including the existence of a minimum pressure for confinement etc, is recommended. In this work, the exploration of the map was hampered by experimental limitations.

- *Independent study of the impact of a pre-ionization layer in the GBD configuration.* In this dissertation, a sequential, simplified approach to the plasma-flame coupling problem was proposed in which first, the structure of RPND in a non-reactive gas environment was studied, followed by the fully reactive problem. For the non-reactive experiments, the impact of different temperatures and compositions was studied. However, an independent study of the impact of a pre-ionized layer (all other variables uniform) was not performed. This study would help answer questions such as the role of the pre-ionization electrons on the uniformity of the discharge and its localization.

  Simple methods to provide a source of pre-ionization include [222]: the double discharge method, in which a low-energy auxiliary discharge creates initial electrons that serve as an initial condition for the main discharge, and the ultraviolet pre-ionization method, in which the initial electron density is ensured by ultraviolet radiation [165, 233]. For the three-parallel jet experiment used in this dissertation, the pre-ionization could be limited to the center jet by injecting in that stream trace organic compounds or other seed gases with low ionization potential (such as alkali metals), while irradiating the volume with a UV lamp. For experiments in air an extensively cited organic compound used for these purposes is TMAE, tetrakis (dimethylamino) ethylene, [81] that has an ionization potential of 6.1eV, and avoids the high reactivity of the alkali metals. E.g. using TMAE and a UV laser-beam, [1] claim that it is possible to obtain a pre-ionization of $n_e > 5 \cdot 10^{11} cm^{-3}$, in air at atmospheric pressure, which is precisely the characteristic value of the chemi-ionization electron density in a flame.

- *Energy measurements and increasing the energy deposition.* From the results of this dissertation, the interest of a RPND plasma fully coupled to a counterflow nonpremixed flame is questionable since the properties of that flame could barely be modified. The lack of authority was partially justified by the limited energy that could be coupled. In

addition, accurate energy measurements could not be performed and it is recommended that better estimates are attempted.

More importantly, the experiments presented were limited by the power supply available, and it was argued that more intense plasmas could in theory be achieved. More specifically, experiments that push the envelope of existence of a fully confined RPND plasma to the flame region are recommended including: using longer voltage pulse duration, higher applied voltages, and higher pulse repetition frequencies.

- *Role of primary electrons versus secondary electrons in the flame-confined plasma.* The voltage amplitudes used in the RPND experiments on the counterflow nonpremixed flame platform were barely above the local Meek breakdown condition (higher voltages could not be explored). This leaves the question open as to whether the plasma emission observed was due to electron-impact excitation triggered by the primary electrons or if significant secondary (electric-field induced) ionization was being produced. Simple estimates seemed to indicate that the fraction of secondary electrons at that electric field level was lower than the chemi-ionization seed. Different experiments can be performed to explore this point.

  First, use of non-hydrocarbon fuels (e.g. CO or H_2), for which chemi-ionization based on reactions with CH should be negligible. In this case, the flame can simply be modeled as a high temperature region, without having to worry about the pre-ionization condition.

  Second, experiments using premixed flames instead of nonpremixed flames. By using a premixed flame, the experiments with RPND could be directly compared to the MW experiments by the Princeton Applied Physics Group [116, 198], in which the energy was directly coupled to the chemi-ionization electrons as could be seen by a local temperature increase in the reaction region alone. Note that, whereas for the nonpremixed flame case, the reaction zone and the high temperature zone are superimposed, for the premixed flame, the high temperature region extends to the products of combustion.

- *Theoretical determination of the requirements on the plasma source to have a specific*

impact on the counterflow nonpremixed flame platform. As seen in this dissertation, the counterflow nonpremixed flame is an extremely robust platform pretty much determined by the stagnation point flow field. In particular, when using the non-thermal RPND plasma only its edge could (barely) be affected, and the theoretical estimations when using AC fields to directly modify the flow field required a reduction in the local strain of a few 10% to displace the flame by only a fraction of a *mm*.

A theoretical study would help answer questions such as: *which* plasma-created species should be preferentially produced to have the greatest impact on the flame properties? *where* should they be produced to have the greatest effect? in *what amount* are these species needed? The outcome of this study would be the power coupling that is required from the plasma source as well as the optimum spatial structure of the energy deposition.

- *Flamelet libraries for PAC.* If non-thermal plasma technologies are to be incorporated into real combustors, *flamelet libraries* that incorporate both the *kinetics* and *dynamics* of the plasma under counterflow nonpremixed flame conditions will have to be provided. This dissertation has offered a first step to cover the latter aspect of the problem, and hopefully it inspires enough interest to tackle the *full coupled problem* of the kinetics and dynamics of plasma-flame interaction.

- *RPND applied to spray combustion.* Another source of inhomogeneity in a combustor environment, neglected in this dissertation, is the existence of different thermodynamic phases (gas, liquid, solid). In particular, in many realistic combustion situations, the injection of the fuel is made as a shower of drops in liquid phase. To the best of the author's knowledge, the dynamics of RPND under such a situation has not been studied but it would be of immense interest to the combustion community. Initial studies could consider RPND applied to single drop combustion, which would then be extended to a spray [35].

- *Impact of RPND on edge-flames.* Edge-flames are ubiquitous in extinction and ignition processes of turbulent flames, and so complement the 1D studies of flamelets. The

possibility of closing flame holes or extending burning areas by use of non-thermal strategies is a problem that remains unexplored.

- *Theoretical models of the effects of slow sub-breakdown electric fields on different types of flames and flow fields.* In this dissertation, some headway has been made in offering a theoretical explanation to experimental observations of the impact of sub-breakdown kHz AC fields on a counterflow nonpremixed flame. Although the match between theory and experiment is sound, a few points should be revised.

  First, measurements of the impedance of the flame at high frequencies when the *floating* charge electrical model of the flame applies are needed, since this regime could not be verified experimentally. The explanation that was here offered to the independency on the excitation frequency was based on the behavior of the *disk of charge* as a high pass filter. Other explanations based on the dependence of the value of the charge itself, σ_0, on this excitation frequency (and in addition on the applied voltage) were not explored, and they indeed could prove to be more important.

  Second, a basic model based on a disk of charge was proposed. This model could be enhanced by a better representation of the spatial distribution of the net charge.

  In general, the theory of AC sub-breakdown fields in flames that can be found in the literature is limited. Simplified analytical models help understand the physics involved and contribute to moving on to real applications.

Appendix A

Quantitative Schlieren calibration

The calibration method used to obtain the refractive index gradient field from the Schlieren photography is that proposed by Schardin et al. [73][1]. In the reference paper [73], the measurement was used to obtain a temperature field, in the present work the necessary modifications have been introduced to measure composition.

Schardin's method uses a simple positive lens as a calibration object to relate the refraction angle to the measured pixel intensity.

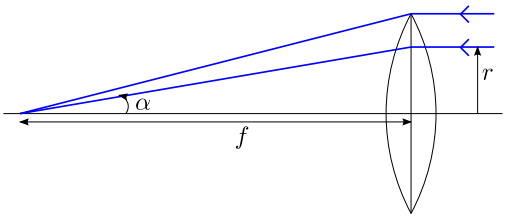

Figure A-1: Calibration object for quantitative Schlieren calibration.

From Figure A-1, using simple geometrical optics, it can be seen that the deflection angle of the parallel rays due to the presence of the positive lens, α, is directly related to the position where the ray meets the lens (its distance from the lens center, r) by:

$$\alpha \approx \tan\alpha = \frac{r}{f},$$

where f is the focal length of the calibration object.

[1]Suggested by Prof. H. Kleine and S. O'Byrne of the Univ. of New South Wales.

For the calibration procedure, this lens is placed in the test section of the Schlieren setup (refer to Figure 2-8). As explained in Section 2.6.1, the orientation of the knife-edge decides the gradients that are observed. For the image shown in Figure A-2, the knife-edge was horizontal and so the vertical deflections of the light are revealed. From this image, the calibration curve is obtained by assigning a pixel intensity to each vertical pixel location with respect to the center of the lens. In practice, to reduce noise, the mean intensity for each horizontal pixel-line within the lens is used. The background was subtracted in all images before post-processing them. To illustrate the procedure, Figure A-2 shows a calibration curve including the mean intensity for the whole pixel-line within the lens, the intensity of the center line and the background intensity. Note that, for the example shown, the usable region of the calibration curve is around 150 pixels.

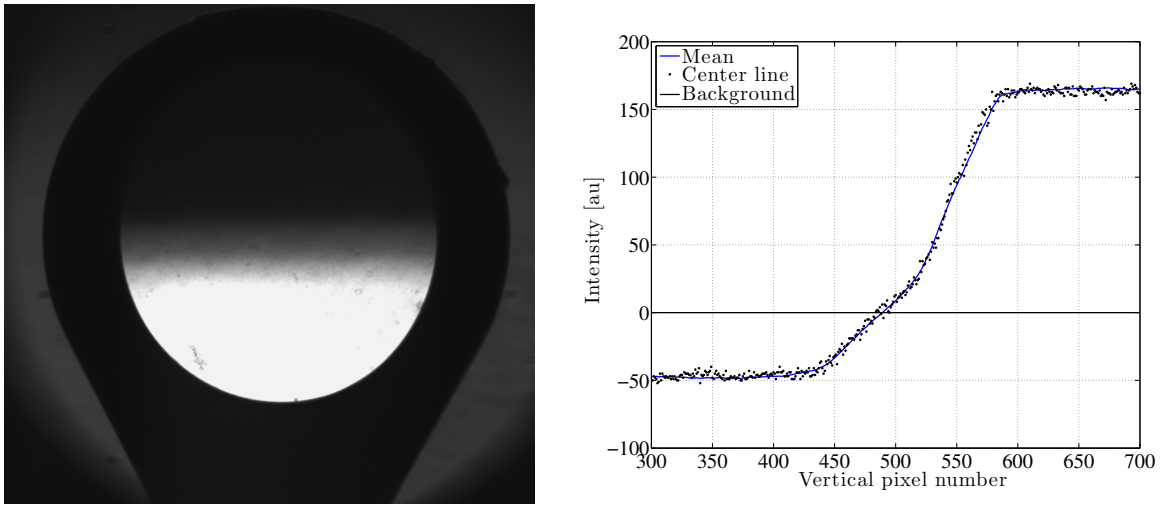

(a) Calibration lens.

(b) Calibration curve.

Figure A-2: Calibration procedure using a simple positive lens.

This curve is then used to translate the pixel intensities in the Schlieren images of the three parallel jets (the Schlieren object) to a refractive index gradient field. Each pixel in the image is assigned a radial distance, corresponding to the calibration lens, which can then be related to the gradient of the refractive index through:

$$\frac{\partial n}{\partial y} = \frac{n}{L_z}\left(\frac{r - r_0}{f}\right),$$

where, for the parallel jets experiment the depth of the object is $L_z = 35mm$, $n \approx 1$, two

calibration lenses were used with f=1m and 2m respectively, the pixel number is related to radial distance by the corresponding scale factor and both positive and negative distances are contemplated. In the example, the knife-edge was placed horizontal, revealing streamwise (y) gradients in n for vertical jets. An equivalent procedure applies to visualize the crosswise (x) gradients.

As explained in Section 2.6.1, the refractive-index gradient can now be related to composition gradients. For the helium-nitrogen mixture, the gradients in helium mole fraction are directly proportional to the gradients in refractive index by:

$$\frac{\partial X_{He}}{\partial y} = \frac{R_u T}{p(G_{He} M_{He} - G_{N_2} M_{N_2})} \frac{\partial n}{\partial y},$$

where the symbols are the same as used in Section 2.6.1 and the Gladstone-Dale constants for nitrogen and helium are taken as $G_{N_2} = 0.238 \cdot 10^{-3} m^3 kg^{-1}$ and $G_{He} = 0.196 \cdot 10^{-3} m^3 kg^{-1}$ respectively.

The helium mole fraction X_{He} can then be integrated along each line using appropriate boundary conditions. For the quantitative curves shown in Section 3.3.5, streamwise gradients were used since, although crosswise gradients were stronger and easier to visualize, in practice it was difficult to avoid saturation and be inside the calibration range. Additionally, the boundary conditions are not well defined for the crosswise case. For the streamwise case, integration can be done along the flow, assuming pure helium and nitrogen at the exit slot; or opposed to the flow, assuming a perfect mixture far upstream. Both approaches should be equivalent. Figure A-3 shows raw Schlieren images of the three parallel jets, N_2-He-N_2, changing the orientation of the knife edge (downstream is bottom).

Note: Since the Schlieren method is used to infer an unknown quantity, as a sanity check, the method was validated with the experiment proposed in [73], a laminar free-convection flat plate thermal boundary layer. The Schlieren method was used to measure the 1D temperature profile over a hot plate at 356K and contrasted with thermocouple measurements.[2]

[2]This experiment was done as part of a collaboration with visiting student J. Ruiz-Ruiz and the Schlieren curve was in perfect agreement with the thermocouple measurements.

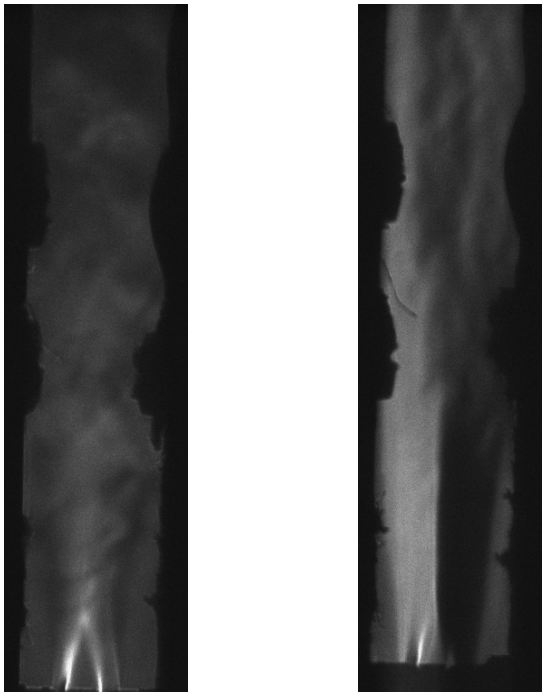

(a) Streamwise. (b) Crosswise.

Figure A-3: Schlieren visualization of refractive index gradients in the three plane parallel jets experiment.

Appendix B

Temperature determination from Rayleigh scattering imaging

In this Appendix, the calibration method used to obtain temperature fields using the laser Rayleigh scattering setup of Section 2.8.1 is described.

B.1 Radial temperature profile

In Section 5.4.6, radial temperature profiles of the counterflow nonpremixed flame in the peak temperature region, with and without plasma application, are presented. The calibration procedure to obtain them from the Rayleigh scattering measurements is that proposed by [13] and the implementation used for the present work is summarized in what follows.

As seen in Section 2.8.1, the Rayleigh-scattering intensity, I_R, imaged by the ICCD camera, is proportional to the gas density, N:

$$I_R(\vec{x}) = C I_L(\text{shot}) N(\vec{x}) \frac{\partial \sigma}{\partial \Omega}(\vec{x}),$$

where the geometric and optical transmission parameters have been grouped in the collection factor C, which will be constant for the experimental setup, and the spatial dependencies have been explicitly stated. In addition, the laser intensity fluctuates and in general cannot be assumed equal for two different images.

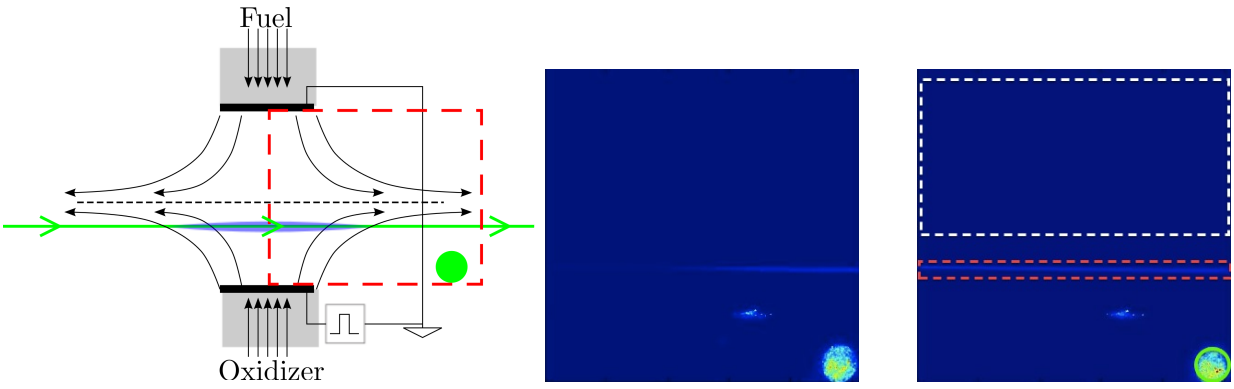

(a) Calibration method. (b) Raw image with flame. (c) Raw image without flame.

Figure B-1: Region imaged with the laser Rayleigh scattering strategy. In the schematic, the laser beam is indicated in green, and the region imaged by the camera is marked in red.

W. H. Beck et al. [13] proposed a calibration method that accounts for laser shot-to-shot fluctuations, $I_L(\text{shot})$, by directing part of the laser beam with an optic fiber bundle and placing the other end within the field of view of the camera. Figure B-1(a) shows a schematic of the method: the laser trajectory is shown in green, the focused fiber representing the laser intensity is the green disk in the right-hand bottom corner and the red-dashed cell represents the region imaged by the ICCD camera. Only half of the flame is imaged exploiting its symmetry. Two representative raw images taken with the flame (Figure B-1(b)) and without the flame, i.e. opposed isothermal jets (Figure B-1(c)), are also shown. It can be appreciated how, for the isothermal case, the scattered intensity is approximately constant whereas, in the presence of the flame, two distinct intensity levels can be appreciated: low intensity in the high temperature region and high intensity in the low temperature region.

Using this method and referring to Figure B-1(c), each image has information about the incident intensity (indicated in green), the background (indicated in white) and the Rayleigh scattering within the medium to be probed (indicated in red). For each image, the Rayleigh scattering intensity along the laser beam (1D profile) is obtained by subtracting the mean background to the peak intensity within the red region across the beam. This signal will be named $\bar{I}_R(r)$, the bar indicates that it has arbitrary units. A signal proportional to the incident laser intensity is obtained by integrating the intensity in the region within the optical fiber bundle (green circle). This signal will be named $\bar{I}_L$.

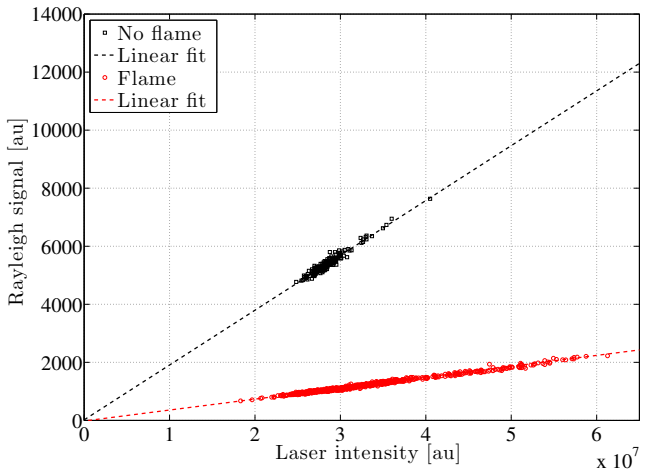

Figure B-2: Linearity of the Rayleigh signal with the incident laser intensity.

Figure B-2 shows the linearity of $\bar{I}_R$ (value showed is the mean in a small region of isothermal temperature within and outside the flame) with $\bar{I}_L$; each measurement corresponds to a single image and the variation in the laser intensity is that of shot-to-shot fluctuations.

The temperature is obtained by comparing the signals from an image with the flame present (subscript fl) and another with the same composition in the impinging jets but without having lit the flame (subscript iso). This last image represents a case of approximately uniform temperature, $T_{\text{iso}} = 293K$, and composition close to the flame case (the difference is due to the products of combustion, however the flames are highly diluted in nitrogen). Note that having approximately the same composition in the two images to be compared is important since the Rayleigh scattering cross section of different molecules can be very different (e.g. $\sigma_{CH_4}/\sigma_{N_2} \approx 2.1$). With this in mind, the temperature profile is obtained from:

$$T_{\text{fl}}(r) = \frac{\left(\bar{I}_R(r)/\bar{I}_L\right)_{\text{iso}}}{\left(\bar{I}_R(r)/\bar{I}_L\right)_{\text{fl}}} T_{\text{iso}}.$$

For the results presented in Section 5.4.6, for each profile, the mean of 200 images for both the flame and isothermal case has been used. The error (standard deviation) at each position, r, in the temperature measurement is evaluated from:

$$\frac{\sigma_T}{\mu_T} = \sqrt{\left(\frac{\sigma_{\text{iso}}}{\mu_{\text{iso}}}\right)^2 + \left(\frac{\sigma_{\text{fl}}}{\mu_{\text{fl}}}\right)^2},$$

with μ_i and σ_i being the mean and standard deviation of the flame temperature for $i = T$, and of the ratio of $\bar{I}_R/\bar{I}_L$ for the isothermal (i =iso) and flame (i =fl) cases respectively.

For these measurements, the camera gate width used was $0.5\mu s$ and was synchronized with the probe laser to capture the ∼10ns laser pulse. When there were pulsed nanosecond-duration discharges applied to the flame, these were triggered in a continuous mode and no synchronization of the camera was used, assuming the flame had reached a steady state.

B.2 2D temperature map

Prior to implementing the method described in Section B.1, 2D imaging of the experiment had been performed. These images include the axial temperature profile presented in Section 5.2.2, obtained by averaging the 2D measurements radially within the central region of the flame. The calibration in this case was made without directly measuring the laser intensity; and, for each measurement, three images were taken: background (with no Rayleigh scattering by setting the polarizer to 0°), isothermal jets (as explained in Section B.1) and flame to be probed.

When needed, a dust filter was applied to the images in order to remove the bias introduced by very intense pixels corresponding to the Rayleigh scattering of dust particles.

The Rayleigh scattering intensity was obtained for the isothermal case, $I_R(\vec{x})_{\text{iso}}$, and the flame case, $I_R(\vec{x})_{\text{fl}}$, by subtracting the background image. The 2D temperature field was then obtained from:

$$T_{\text{fl}}(\vec{x}) = \frac{I_R(\vec{x})_{\text{iso}}}{I_R(\vec{x})_{\text{fl}}} \frac{I_{L\text{fl}}}{I_{L\text{iso}}} T_{\text{iso}},$$

where the factor that accounts for laser intensity fluctuations can be evaluated if the temperature of one point of the image under study is known.

For these measurements, the camera gate width used was $0.5\mu s$ and was synchronized with the probe laser to capture the ∼10ns laser pulse. 20 images were used for the profile shown in Section 5.2.2.

Appendix C

Details of the discharge numerical model

In this Appendix, the numerical solution method of the discharge model of Chapter 4 is detailed. The method implemented is the one proposed by [71], which consists on a semi-implicit treatment of the particle densities, n_e and n_i, as well as the electric potential, V; and the charged particle fluxes are represented by the exponential scheme of D. L. Scharfetter and H. K. Gummel [176]. For details on the benefits of the method, the reader is referred to the article by G. J. M Hagelaar and G. M. W. Kroesen [71].

In the first part of this Appendix (Section C.1), the structure of the code developed for this work is presented, and the time and spatial discretization used are summarized. The second part of this Appendix (Sections C.2 and C.3), presents verification and validation of the numerical code.

C.1 Numerical method

The numerical code written to solve the system of three PDEs of Section 4.2.1 is largely based on the method proposed by [71], where the necessary modifications have been incorporated to account for the inhomogeneities in the gas and the particularities of the problem at hand. A flow chart that summarizes the numerical solution scheme used is shown in Figure C-1.

At each time-iteration step, the equations are solved in a sequential manner, starting from Poisson's equation, updating the relevant quantities, next solving the ion continuity equation and finally the electron continuity equation. A minimum ion and electron density

is forced at every time-step (e.g. to provide the seed of electrons necessary for cathode-directed streamer propagation), in the nodes where it is necessary, the density is restored to the minimum value as proposed by [149].

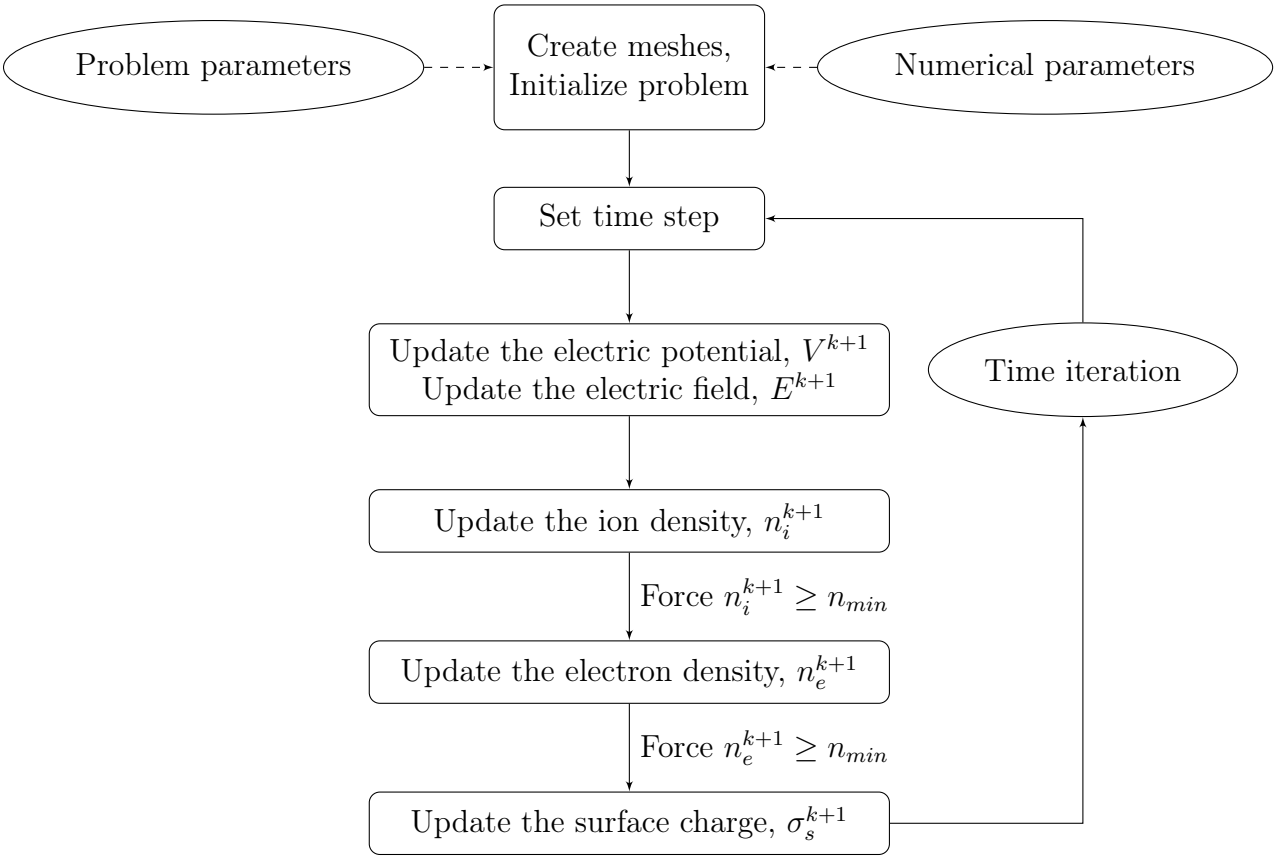

Figure C-1: Flow chart of the numerical solution scheme. The superscript $(k+1)$ refers to the current time step.

C.1.1 Discretization in time

The equations are discretized in time using the trapezoidal rule, and the order in which the equations are solved is exploited to make the solution method semi-implicit. This relaxes the constraints on the time-step without the complications of a fully implicit treatment (specially considering the nonlinearity of the transport and ionization parameters).

Poisson's equation, equation 4.2, is solved first, so that an estimate for the charged particle densities, $\hat{n}_p^{k+1}$ with $(p = i, e)$, needs to be anticipated, that is:

$$\nabla \cdot \left(\epsilon_r \varepsilon_0 \nabla V^{k+1}\right) = -e\left(\hat{n}_i^{k+1} - \hat{n}_e^{k+1}\right), \tag{C.1}$$
$$\text{with:} \quad \hat{n}_p^{k+1} = n_p^k - \nabla \cdot \hat{\vec{\Gamma}}_p\left(n_p^k, V^{k+1}, \mu_p^k, D_p^k\right)\Delta t,$$

where the explicit dependencies on the electric potential are evaluated at the current time step, V^{k+1}, but the transport coefficients are evaluated in the previous time step, μ_p^k, D_p^k. In the number density expression, the source terms are omitted since they cancel when $(\hat{n}_i - \hat{n}_e)$ is evaluated.

Next, the ion continuity equation is solved, followed by the electron continuity equation. The temporal discretization of equation 4.1 reads:

$$\frac{n_p^{k+1} - n_p^k}{\Delta t} + \nabla \cdot \vec{\Gamma}_p^{k+1}\left(n_p^{k+1}, V^{k+1}, \mu_p^{k+1}, D_p^{k+1}\right) = \quad S^k\left(n_p^k, E^{k+1}, \mu_p^{k+1}, D_p^{k+1}\right), \tag{C.2}$$

where, since the electric potential has already been updated, all the quantities related to it[1] are evaluated at the current time, $k+1$. For the particle densities, the semi-implicit scheme used is that the densities appearing in the source term are evaluated at the previous time, k, and those appearing in the particle flux are evaluated at the current time, $k+1$. The spatial discretization of the particle flux makes the flux divergence linear in the densities.

Although this semi-implicit treatment relaxes the constraints in the time-step, in practice, for the streamer simulations, the time step used was the smallest of $\frac{\varepsilon_0}{e n_p \mu_p}$ and a fixed constant.

C.1.2 Discretization in space

The gas gap was discretized using a rectangular grid of $N_{xg} \times N_y$ points, yielding rectangular cells of size $\Delta x_g = L_g\left(N_{xg} - 1\right)^{-1}$ and $\Delta y = \frac{L_y}{2}\left(N_y - 1\right)^{-1}$ (domain in which the fluid equations apply). The discretization for Poisson equation was the same within the gaseous region, and was extended within the dielectrics using rectangular cells of dimensions $\Delta x_d = L_d\left(N_{xd} - 1\right)^{-1}$ and $\Delta y = \frac{L_y}{2}\left(N_y - 1\right)^{-1}$, so that the full domain had $\left(N_{xg} + 2N_{xd} - 2\right) \times N_y$ nodes. In general, a finer mesh was used within the gas gap than in the solid dielectrics.

[1] This is slightly different than in [71], since they do not update the transport parameters at this stage.

Scharfetter-Gummel discretization of the particle fluxes

The drift-diffusion flux, given by equation 4.3, has been discretized using the exponential representation due to D. L. Scharfetter and H. K. Gummel [176], which is based on an analytic solution of the drift-diffusion equation in an individual cell. E.g. in two dimensions, the flux along x reads (refer to Figure C-2 for a diagram of the nodes):

$$(\Gamma_x)^{k+1}_{i+\frac{1}{2},j} = -\frac{1}{\Delta x_g} D^{k+1}_{i+\frac{1}{2},j} \left(n^{k+1}_{i+1,j} f_1(z_{i+\frac{1}{2},j}) - n^{k+1}_{i,j} f_2(z_{i+\frac{1}{2},j}) \right), \tag{C.3}$$

$$\text{with:} \quad f_1(z) = \frac{z}{e^z - 1},$$

$$f_2(z) = e^z \frac{z}{e^z - 1},$$

$$\text{and:} \quad z_{i+\frac{1}{2},j} = \text{sign}(q) \frac{\mu^{k+1}_{i+\frac{1}{2},j}}{D^{k+1}_{i+\frac{1}{2},j}} (E_{\text{x}})^{k+1}_{i+\frac{1}{2},j} \Delta x_g.$$

For $z >> 1$, $z << 1$ and $z = 0$, the corresponding limits have been used instead of the analytic expressions for f_1 and f_2 (to avoid numerical errors). The electric field is given by:

$$(E_{\text{x}})^{k+1}_{i+\frac{1}{2},j} = -\frac{V^{k+1}_{i+1,j} - V^{k+1}_{i,j}}{\Delta x_i}. \tag{C.4}$$

For the fluxes appearing in Poisson's equation, that contribute to the estimated update of the net space charge, a different representation based on a linearization in time is used as proposed by [71] (equation C.10).

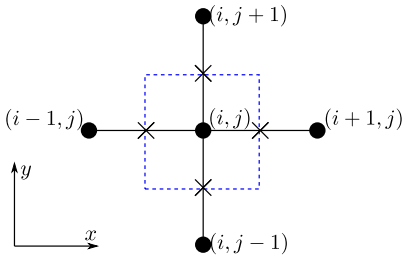

Figure C-2: Nodes for the numerical evaluation of the fluxes. The crosses indicate the mid-points. The blue cell indicates an individual element for the continuity equation balance.

Species continuity

The electron and ion continuity equations (equation 4.1) have been spatially discretized using a finite element approach, by writing the corresponding mass balance in the blue cell of Figure C-2. Re-arranging (the subscript p has been dropped):

$$n_{i,j}^{k+1} - n_{i,j}^{k} + \frac{\Delta t}{\Delta x_g}\left((\Gamma_x)_{i+\frac{1}{2},j}^{k+1} - (\Gamma_x)_{i-\frac{1}{2},j}^{k+1}\right) + \frac{\Delta t}{\Delta y}\left((\Gamma_y)_{i,j+\frac{1}{2}}^{k+1} - (\Gamma_y)_{i,j-\frac{1}{2}}^{k+1}\right) = S_{i,j}^{k}\Delta t. \quad \text{(C.5)}$$

Equation C.5 can be recast as: $\mathbf{A}_{\mathrm{p}}\underline{\mathrm{n}}_p^{k+1} = \underline{\mathrm{b}}_{\mathrm{p}}$, with $\underline{\mathrm{n}}_p^{k+1}$ being the vector of particle densities at the updated time, $k+1$, and each entry refers to a different node.

For the *interior* nodes, the discretization of the fluxes, $(\Gamma_x)_{i+\frac{1}{2},j}^{k+1}\ldots$, to be used is the one given by equation C.3.

For the boundaries, the mass balance needs to be rewritten for only half of the cell of Figure C-2. E.g. for a cell at the $i = 1$ boundary, equation C.5 is substituted by:

$$\frac{\left(n_{i,j}^{k+1} - n_{i,j}^{k}\right)}{2} + \frac{\Delta t}{\Delta x_g}\left((\Gamma_x)_{i+\frac{1}{2},j}^{k+1} - \Gamma_{b.c.}\right) + \frac{\Delta t}{2\Delta y}\left((\Gamma_y)_{i,j+\frac{1}{2}}^{k+1} - (\Gamma_y)_{i,j-\frac{1}{2}}^{k+1}\right) = \frac{S_{i,j}^{k}}{2}\Delta t, \quad \text{(C.6)}$$

where the flux at $(\Gamma_x)_{i-\frac{1}{2},j}^{k+1}$ has been substituted by the corresponding boundary condition $\Gamma_{b.c.}$. Equivalent expressions can be written for the boundaries at $i = N_{xg}$, $j = 1$ and $j = N_y$. Note that, for ease of notation, when discussing the continuity equations, the counters i and j start at the boundaries of the gas gap.

The discretization of the boundary fluxes, $\Gamma_{b.c.}$, from equations 4.4, 4.5 and 4.6, can be explicitly written in terms of their dependence on $n_{i,j}^{k+1}$ as:

$$\Gamma_{b.c.} = \Gamma^{n} n_{i,j}^{k+1} + \Gamma^{c}. \quad \text{(C.7)}$$

For $j = N_y$ and $j = 1$ (symmetry condition and limit of the discharge cell), the condition of equation 4.6 yields $\Gamma^n = \Gamma^c = 0$. For the boundaries corresponding to the dielectric surfaces, $i = 1$ and $i = N_{xg}$, from equations 4.4 and 4.5, they become:

$$\Gamma^n = \pm a\mu_{b.c.}^{k+1}\text{sign}(q)(E_x)_{b.c.}^{k+1} \pm \frac{1}{4}v_{th}, \tag{C.8}$$
$$\Gamma_e^c = -\gamma_s\left(\vec{\Gamma}_i \cdot \vec{n}\right)_{b.c.}^{k+1},$$

where a is the same switching function as in Section 4.2.4. The plus / minus signs refers to the interfaces of dielectrics $d2$ and $d1$ respectively (Figure 4-1); Γ_e^c only applies for the electrons and is zero for the ions.

For the corners, the same procedure applies but, in this case, the conservation balance concerns one fourth of the cell of Figure C-2. In addition, two boundary fluxes (one along x and one along y) need to be substituted.

Electric potential

Laplace's operator was discretized using central differences and the fluxes were discretized in the same way as in the transport equations:

$$\frac{V_{i-1,j}^{k+1} - 2V_{i,j}^{k+1} + V_{i+1,j}^{k+1}}{\Delta x_i^2} + \frac{V_{i,j-1}^{k+1} - 2V_{i,j}^{k+1} + V_{i,j+1}^{k+1}}{\Delta y^2} = -\frac{e}{\epsilon_r\varepsilon_0}\Bigg\{n_{i(i,j)}^k - n_{e(i,j)}^k + \dots \tag{C.9}$$
$$\dots - \Delta t\left(\frac{(\hat{\Gamma}_{ix})_{i+\frac{1}{2},j} - (\hat{\Gamma}_{ix})_{i-\frac{1}{2},j}}{\Delta x_g} + \frac{(\hat{\Gamma}_{iy})_{i,j+\frac{1}{2}} - (\hat{\Gamma}_{iy})_{i,j-\frac{1}{2}}}{\Delta y}\right) + \dots$$
$$\dots + \Delta t\left(\frac{(\hat{\Gamma}_{ex})_{i+\frac{1}{2},j} - (\hat{\Gamma}_{ex})_{i-\frac{1}{2},j}}{\Delta x_g} + \frac{(\hat{\Gamma}_{ey})_{i,j+\frac{1}{2}} - (\hat{\Gamma}_{ey})_{i,j-\frac{1}{2}}}{\Delta y}\right)\Bigg\}.$$

Equation C.9 can be recast as: $\mathbf{A}_{\text{V}}\underline{\text{V}}^{k+1} = \underline{\text{b}}_{\text{V}}$, with $\underline{\text{V}}^{k+1}$ being the vector of electric potentials at the updated time, $k+1$, and each entry refers to a different node. The discretization used allows to solve for a linear equation for $\underline{\text{V}}^{k+1}$ at each time step.

For the nodes inside the dielectrics the right hand side of equation C.9 is zero and so the corresponding terms in $\mathbf{A}_{\text{V}}$ and $\underline{\text{b}}_{\text{V}}$ are greatly simplified.

For the nodes inside the gas gap, the discretization of the *approximate* fluxes $\hat{\Gamma}$, is the one proposed by G. J. M Hagelaar and G. M. W. Kroesen [71], in which the exponential

Scharfetter-Gummel fluxes are linearized in t^k, that is:

$$(\hat{\Gamma}_x)_{i+\frac{1}{2},j} = \left\{ \text{sign}(q)\mu_{i+\frac{1}{2},j} \left(g_1(z_{i+\frac{1}{2},j}) n_{i+1,j} - g_2(z_{i+\frac{1}{2},j}) n_{i,j} \right) \right\}^k \left(-\frac{V^{k+1}_{i+1,j} - V^{k+1}_{i,j}}{\Delta x_g} \right) + \ldots \tag{C.10}$$

$$\ldots - \left\{ D_{i+\frac{1}{2},j} h(z_{i+\frac{1}{2},j}) \frac{n_{i+1,j} - n_{i,j}}{\Delta x_g} \right\}^k,$$

with:

$$\begin{aligned} g_1(z) &= \frac{df_1}{dz} = \frac{(1-z)e^z - 1}{(e^z - 1)^2}, \\ g_2(z) &= \frac{df_2}{dz} = e^z \frac{e^z - 1 - z}{(e^z - 1)^2}, \\ \text{and:} \qquad h(z) &= f_1(z) - g_1(z) z = e^z \frac{z^2}{(e^z - 1)^2}. \end{aligned} \tag{C.11}$$

For $z >> 1$, $z << 1$ and $z = 0$, the corresponding limits have been used instead of the analytic expressions for g_1, g_2 and h (to avoid numerical errors).

At the powered anode boundary ($i = 1$), the conditions that need to be incorporated into equation C.9 are: $V^{k+1}_{i-1,j} = V_{\text{app}}(t^{k+1})$, for nodes within the extent of the electrode, and $V^{k+1}_{i-1,j} = V^{k+1}_{i,j}$, for nodes outside, imposing that no electric flux comes out of the domain. At the grounded cathode boundary ($i = N_{xg} + 2N_{xd} - 2$), the equivalent conditions are: $V^{k+1}_{i+1,j} = 0$, within the extent of the electrode, and $V^{k+1}_{i+1,j} = V^{k+1}_{i,j}$, outside.

At the symmetry boundary ($j = N_y$), the condition $E_y = 0$ needs to be incorporated into equation C.9, that is $V^{k+1}_{i,j+1} = V^{k+1}_{i,j}$. This is the same condition that is imposed to the outer edge of the discharge cell ($j = 1$), in which null electric flux along y is assumed $V^{k+1}_{i,j-1} = V^{k+1}_{i,j}$. These conditions also affect the fluxes $(\hat{\Gamma}_y)_{i,j\pm\frac{1}{2}}$ respectively.

For the corners, the corresponding pair of conditions needs to be imposed.

At the interface between the gas and the dielectrics, Poisson's equation is substituted by Gauss's law (equation 4.7), and the discretization at the limit of dielectric $d1$ becomes:

$$\epsilon_d \frac{V^{k+1}_{i,j} - V^{k+1}_{i-1,j}}{\Delta x_d} - \frac{V^{k+1}_{i+1,j} - V^{k+1}_{i,j}}{\Delta x_g} = \frac{\hat{\sigma}^{k+1}_{i,j}}{\varepsilon_0}, \tag{C.12}$$

where, consistently with the semi-implicit scheme for the interior points, the updated surface charge at the next step is approximated by ($(\hat{\Gamma}_x)_{i+\frac{1}{2},j}$ is given by equation C.10):

$$\hat{\sigma}_{i,j}^{k+1} = \sigma_{i,j}^{k} - \Delta t \left(e \frac{(\hat{\Gamma}_{ix})_{i+\frac{1}{2},j} - (\hat{\Gamma}_{ex})_{i+\frac{1}{2},j}}{\Delta x_g} \right). \tag{C.13}$$

An equivalent expression can be written for the interface at $d2$.

In all cases, the numerical solution of $\mathbf{A}\underline{\mathrm{x}} = \underline{\mathrm{b}}$ (in each time iteration, three systems of this type are solved for, one for the electric potential, one for the ion density and one for the electron density), was obtained using the backslash operator of MATLAB.

C.2 Numerical verification (1D)

In this Section, the choice of numerical parameters and background density level for the 1D simulation presented in Section 4.3 is justified. The test case presented is that of Section 4.3.1.

C.2.1 Time-step selection

Figure C-3 shows the electron number density profile during pulse application (at 25ns and 50ns after pulse onset) for different maximum time steps of 10^{-1}, 10^{-2} and 10^{-3}ns. There is no significant influence on the results, so that a value of $\Delta t_{max} = 0.1ns$ is adequate.

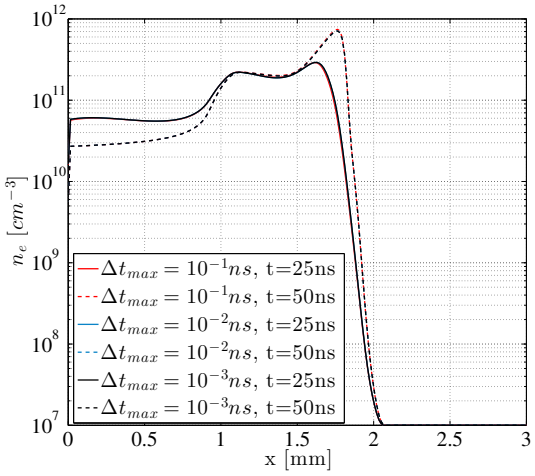

Figure C-3: Time-step effect on the electron density. Parameters: N_{xg}=200, n_{min}=10^7 cm^{-3}.

C.2.2 Mesh size convergence

Figure C-4 shows the electron number density profile during pulse application (at 50ns after pulse onset) for different number of numerical nodes of $N_{xg} = 1000$, 500, 200, 100 and 70. For $N_{xg} \geq 200$ there is no significant influence on the calculation results, independently of the background density chosen, indicating convergence. For $N_{xg} < 200$, the results suffer from numerical diffusion, which produces artificial seeds of electrons locally in front of the streamer head and makes the streamer propagate further. This effect is obvious when employing a low background density (e.g. $10^2 cm^{-3}$). For a converged grid, the streamer propagates further the higher the background density but, in any case, the streamer will not penetrate the cathode-side nitrogen layer. For the results in Section 4.3, $N_{xg} = 1000$ was chosen.

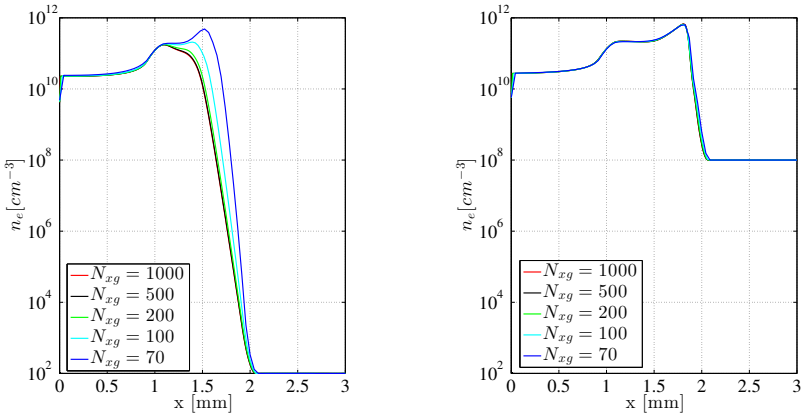

(a) $n_{min} = 10^2 cm^{-3}$. (b) $n_{min} = 10^8 cm^{-3}$.

Figure C-4: Mesh-size effect. Snapshot of streamer at 50ns after pulse onset. Δt_{max}=0.1ns.

C.2.3 Impact of the background density level

A minimum background density of $10^8 cm^{-3}$ was assumed in the results presented in Section 4.3. Different values of this background density were tested, Figure C-5 (ranging from 10^4-$10^8 cm^{-3}$)[2]. Quantitatively, the background density affects how far the streamer travels within the helium layer, and its speed of propagation, but in any case the ionization front does not penetrate the cathode-side nitrogen layer. The conclusions derived in Section 4.3.2 hold for a wide range of pre-ionization densities.

[2]Suggested by T. Unfer (IMFT) during the Aerospace Thematic Workshop, Aussois, France, 2013.

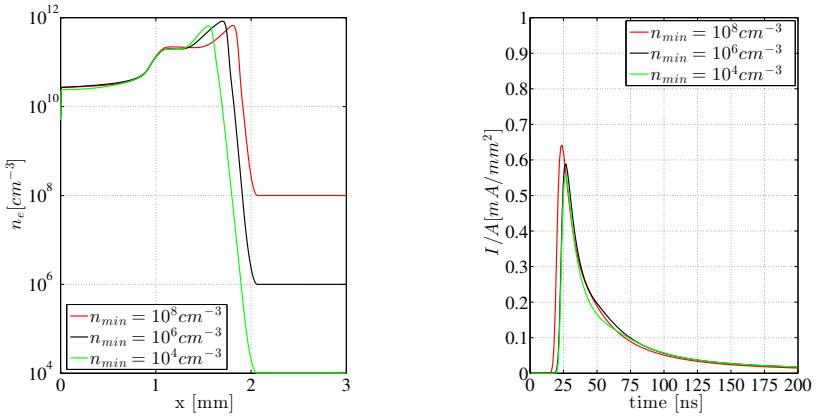

(a) n_e and n_i at 50ns.

(b) Current (conduction).

Figure C-5: Effect of the background density level. Parameters: N_{xg}=1000 and Δt_{max}=0.1ns.

C.3 Physical validation (2D)

The 2D numerical model developed was able to reproduce various discharge physics phenomena reported in the literature, namely: homogeneous and patterned glows in DBD discharges; as well as volumetric streamer development.

C.3.1 Homogeneous and patterned glow (Townsend breakdown)

At low *pd* values (pressure times distance), the breakdown in a DBD usually takes place through the Townsend mechanism, so that a glow or Townsend discharge is favored.

The main characteristic of a glow discharge is that the accumulated positive space charge is large enough to trap the electrons creating a plasma. In the DBD, the expansion of the plasma is limited by dielectric charging (local reduction of the electric field).

Depending on the conditions, the glow can be uniform (*diffuse*) or present many long-lived discharge columns that are regularly distributed in space (*patterned*). The patterned glow has been observed and modeled by many researchers [14, 16, 55, 62, 132, 141, 169] and is characterized by self-organized patterns generated in phase (one current pulse per half-cycle).

The test case selected to validate the numerical model for Townsend-type breakdown is that reported in the paper by X. Duan et al. [49], since they present consistent experimental and numerical results both for uniform and patterned glows. The geometry is essentially

that of Figure 4-1, with $L_d = L_g = 1mm$, $L_y = 4cm$, $L_e = 2cm$, uniform pressure of 25Torr, ambient temperature, and uniform neon composition. The applied voltage is a square wave of ±165V and variable frequency. Under these conditions, X. Duan et al. report a critical frequency below which the discharge is uniform and above which the discharge is patterned.

The code of Section C.1 was used to reproduce their results. At 50kHz the homogeneous glow was obtained and at 120kHz the patterned glow was captured, as in [49]. For both simulations, the initial condition was a uniform density of $10^{12}m^{-3}$. The results presented are for a half cycle of the voltage oscillation, after the periodic response has been reached.

Homogeneous glow

Figures C-6 and C-7 show the evolution of the uniform glow during a current pulse.

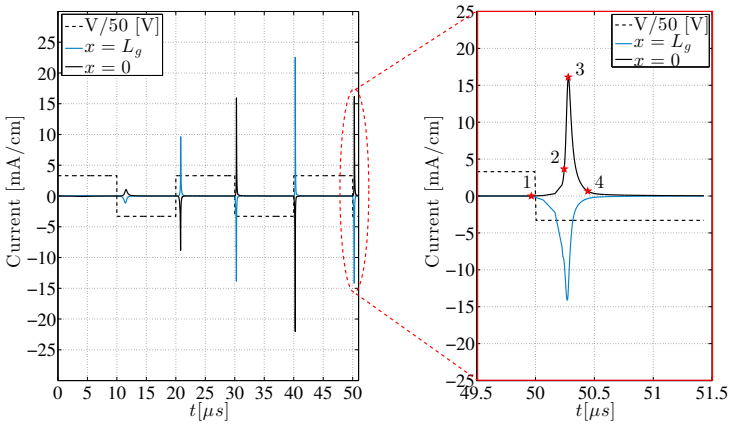

Figure C-6: Flux of charge to walls for uniform glow. Compare to results in [49].

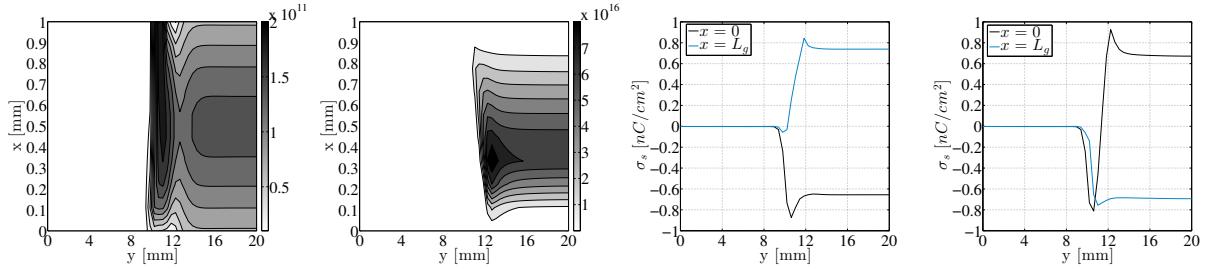

(a) n_e at 1 $[m^{-3}]$. (b) n_e at 4 $[m^{-3}]$. (c) σ_s at 1 $[nC/cm^2]$. (d) σ_s at 4 $[nC/cm^2]$.

Figure C-7: Evolution of the electron density and the surface charge on the dielectrics during a current pulse. Snapshots correspond to moments marked in Figure C-6. During this half cycle (2-3-4), anode is on top (grounded) and cathode on bottom. Compare to [49].

The evolution of the electron density and the charging of the electrodes are in agreement with the results presented in [49]: compare to Figures 7 and 11 of this reference.

Patterned glow

By increasing the frequency to 120kHz, all other conditions unchanged, the patterned glow is obtained. [49] explains this transition by the change in initial conditions every time the voltage is reversed since, at the higher frequencies, the volume charge has no time to homogeneously diffuse. Figures C-8 and C-9 show the evolution of the patterned glow during a current pulse (once a periodic response has been reached).

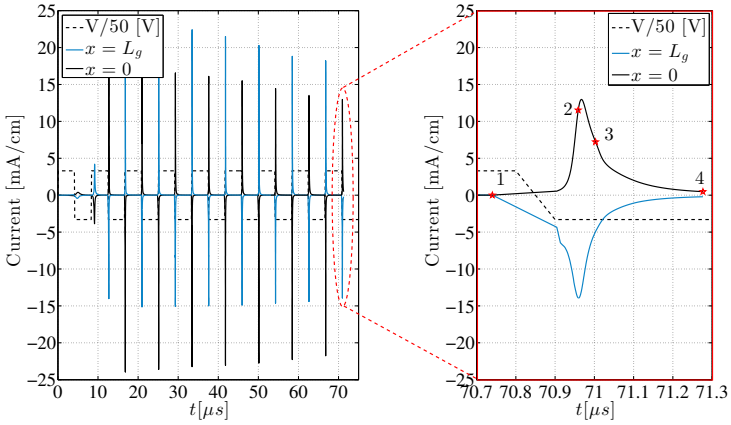

Figure C-8: Flux of charge to walls for patterned glow. Notice the unique current pulse per half-cycle. Compare to results in [49].

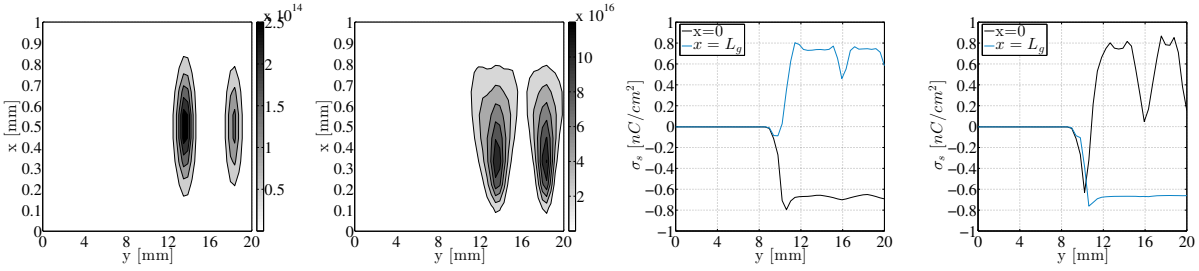

(a) n_e at 1 $[m^{-3}]$. (b) n_e at 4 $[m^{-3}]$. (c) σ_s at 1 $[nC/cm^2]$. (d) σ_s at 4 $[nC/cm^2]$.

Figure C-9: Evolution of the electron density and the surface charge on the dielectrics during a current pulse. Snapshots correspond to moments marked in Figure C-8. During this half cycle (2-3-4), anode is on top (grounded) and cathode on bottom. Compare to [49].

The evolution of the electron density and the charging of the electrodes are in agreement with the results presented in [49]: compare to Figures 8 and 10 of this reference.

C.3.2 Volume streamer development (streamer breakdown)

Finally, the discharge dynamics code also captures the main features of the streamer breakdown mode. Mainly a thin structure with a steep ionization front and amplification of the electric field at the streamer head.

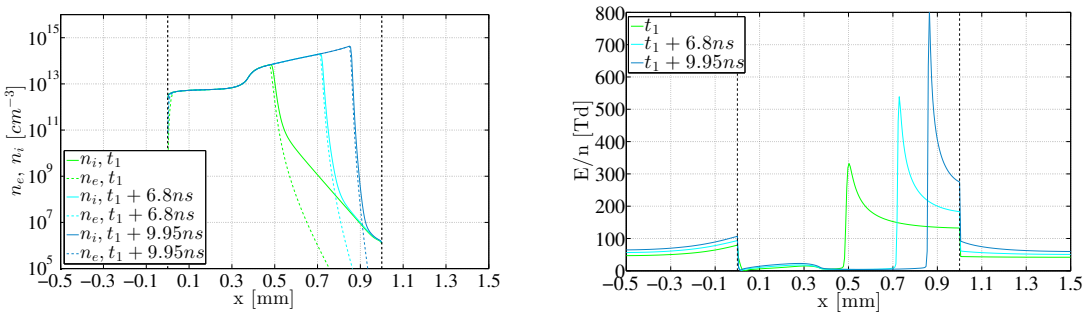

(a) n_e, n_i (streamer axis).

(b) E_x/n (streamer axis).

Figure C-10: Evolution of the space charge and the axial electric field at the axis of symmetry of a cathode-directed streamer. Anode is at $x = -0.5mm$ and cathode at $x = 1.5mm$.

The example in Figure C-10 shows the evolution of a cathode-directed volumetric streamer in the same DBD configuration of Figure 4-1, where the gas is argon at atmospheric pressure (uniform background), the discharge gap is 1mm and the applied voltage is 3.5kV. The initial conditions were a gaussian spot of plasma on the cathode-side dielectric so that the initial evolution is similar to the one in Section 4.3.2. The main features observed, as well as the structure of the ionization front and the electric field, are consistent with the well-known streamer characteristics and, in particular, with the propagation of a streamer in a short gap with dielectric barrier at the cathode (e.g. compare with Figures 4 through 6 in [152], and to Figure 4 in [232]). In this example, the velocity of the streamer is $\sim 4 \cdot 10^6 cms^{-1}$, consistent with measurements of *short* streamers in argon [2].

Appendix D

2D numerical results of the GBD

The results presented in Section 4.3, for the nitrogen-helium-nitrogen GBD, were for a 1D case, since the mesh could not be refined sufficiently to ensure a converged solution in the 2D case.

In this Appendix, a preliminary 2D simulation is presented. The parameters used are the same as in Section 4.3.1, where the length of the electrodes and the discharge cell (y-direction) were taken as L_y=L_e=15mm. For the 2D simulation a lower background density was used to avoid triggering a uniform discharge, $n_{min} = 10^6 m^{-3}$.

The grid used had 70×70 elements, on the gas region, and 90×70 elements, when including the dielectrics. These grids are very coarse and the results presented suffer from numerical diffusion, which produces artificial seeds of electrons locally in front of the streamer head [52].

Figure D-1 shows a snapshot of the electron and ion densities, and the electric field components, during pulse application. The same comments as in Section 4.3.2 apply. The additional insight gained by the 2D simulation is that, after the volumetric streamer reaches the helium/nitrogen interface, two lateral streamers can start propagating along the mixing layer. This solution is similar to the behavior in a standard DBD configuration once the streamer reaches the dielectric barrier [152] or to plasma bullets in APPJ [17]. The lateral streamers contribute to a residual current, after the main current spike, due to the conductive channel created and the continuous production of electrons, Figure D-2.

Finally, after the voltage pulse is turned off, the same comments as in Section 4.3.3 apply, as shown in Figure D-3.

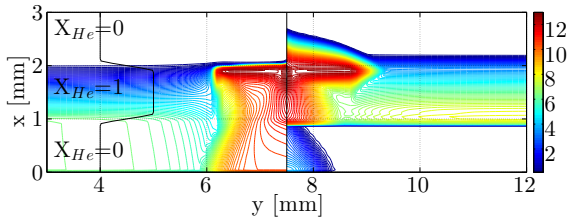

(a) Electron (left) and ion number density (right). Scale is in $log_{10}(n[cm^{-3}])$.

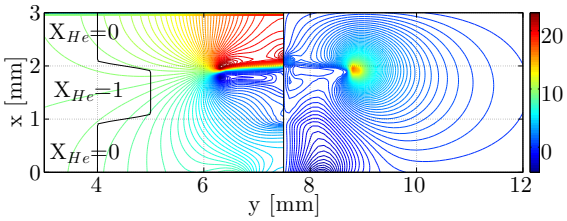

(b) Electric field in x (left) and y (right). Scale is in [kV/cm].

Figure D-1: Snapshot of lateral streamer propagating along mixing layer (150ns after pulse onset). Anode is on bottom, cathode on top. The helium mole fraction is plotted for reference.

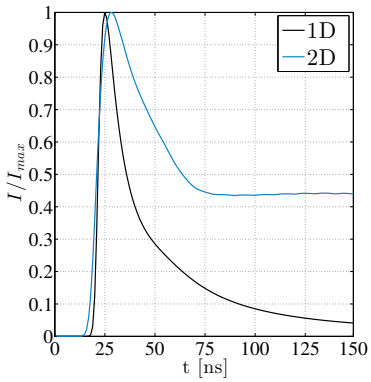

Figure D-2: Comparison of 1D and 2D conduction currents.

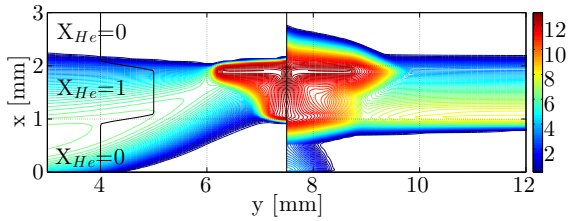

(a) Electron (left) and ion number density (right). Scale is in $log_{10}(n[cm^{-3}])$.

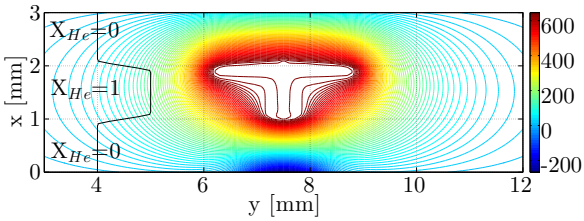

(b) Electric potential [V].

Figure D-3: Snapshot of the electron and ion densities and the electric potential during the afterglow phase (100ns after the pulse is switched off). The potential configuration is such that the electrons drift to the center layer. The helium fraction is plotted for reference.

Appendix E

Supporting evidence of RPND coupling to a flame

In this Appendix, digital camera photographs of the coupling of the RPND plasmas to the flame are shown. In Section 5.4.1, ns-resolved photography of a methane/air counterflow nonpremixed flame was presented as evidence of the plasma coupling to the flame front. The same confinement of the emission was observed when the fuel was diluted in nitrogen, argon or helium; examples for no dilution and dilution in nitrogen are shown in Figures E-1 and E-2, the experimental parameters used are summarized in Table E.1.

Table E.1: Estimated flame parameters, and RPND conditions, for the images shown.

Case	a $[1/s]$	Dilutant	$X_{O_2,\infty}$	$X_{CH_4,-\infty}$	Z_{st}	ϕ	Power $[W]$	T_{max} $[K]$	Voltage $[kV]$	f $[kHz]$
1	25	N_2	0.21	1	0.055	12.8	65	2050	15.5	25
2	40	N_2	0.21	0.19	0.33	1.92	116	1625	15.5	27

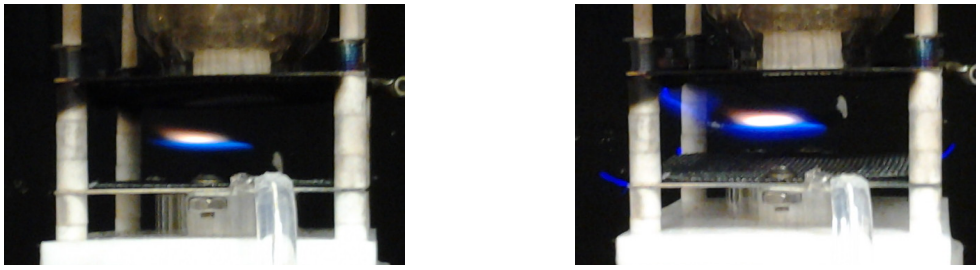

(a) Baseline. (b) RPND applied.

Figure E-1: Direct photographs of RPND coupling to flame (case 1, no fuel dilution).

(a) Baseline. (b) RPND applied.

Figure E-2: Direct photographs of RPND coupling to flame (case 2, diluted fuel).

Bibliography

[1] K. Akhtar, J. E. Scharer, S. M. Tysk, and C. M. Denning. Characterization of laser produced tetrakis (dimethylamino) ethylene plasma in a high-pressure background gas. *IEEE Transactions on Plasma Science*, 32(2):813–822, 2004.

[2] N. L. Aleksandrov, E. M. Bazelyan, and G. A. Novitskii. The effect of small O_2 addition on the properties of a long positive streamer in Ar. *Journal of Physics D: Applied Physics*, 34(9):1374–1378, 2001.

[3] N. L. Aleksandrov, S. V. Kindysheva, I. N. Kosarev, S. M. Starikovskaia, and A. Y. Starikovskii. Mechanism of ignition by non-equilibrium plasma. *Proceedings of the Combustion Institute*, 32(1):205–212, 2009.

[4] N. L. Aleksandrov, S. V. Kindysheva, M. M. Nudnova, and A. Y. Starikovskiy. Mechanism of ultra-fast heating in a non-equilibrium weakly ionized air discharge plasma in high electric fields. *Journal of Physics D: Applied Physics*, 43(25):255201, 2010.

[5] C. Alvarez-Herrera, D. Moreno-Hernandez, and B Barrientos-Garcia. Temperature measurement of an axisymmetric flame by using a Schlieren system. *Journal of Optics A: Pure and Applied Optics*, 10(10):104014, 2008.

[6] N. B. Anikin, S. M. Starikovskaia, and A. Y. Starikovskii. Study of the oxidation of alkanes in their mixtures with oxygen and air under the action of a pulsed volume nanosecond discharge. *Plasma Physics Reports*, 30(12):1028–1042, 2004.

[7] A. Ata, J. S. Cowart, A. Vranos, and B. M. Cetegen. Effects of direct current electric field on the blowoff characteristics of bluff-body stabilized conical premixed flames. *Combustion Science and Technology*, 177:1291–1304, 2005.

[8] N. Y. Babaeva and M. J. Kushner. Effect of inhomogeneities on streamer propagation: I. Intersection with isolated bubbles and particles. *Plasma Sources Science and Technology*, 18(3):035009, 2009.

[9] N. Y. Babaeva and M. J. Kushner. Effect of inhomogeneities on streamer propagation: II. Streamer dynamics in high pressure humid air with bubbles. *Plasma Sources Science and Technology*, 18(3):035010, 2009.

[10] N. Y. Babaeva and M. J. Kushner. Structure of positive streamers inside gaseous bubbles immersed in liquids. *Journal of Physics D: Applied Physics*, 42(13):132003, 2009.

[11] V. Ya. Basevich and S. M. Kogarko. Promotion of combustion. *Fizika Goreniya i Vzryva*, 5(1):99–105, 1969.

[12] E. M. Bazelyan and Y. P. Raizer. *Spark Discharge*. CRC Press LLC, 1998.

[13] W. H. Beck, E. S. Stockman, S. H. Zaidi, and R. B. Miles. Rayleigh scattering measurements for obtaining spatially-resolved absolute gas densities in large scale facilities. *AIAA Aerospace Sciences Meeting and Exhibit*, 44th, Reno, Nevada:AIAA 2006–835, 2006.

[14] B. Bernecker, T. Callegari, and J. P. Boeuf. Evidence of a new form of self-organization in DBD plasmas: the quincunx structure. *Journal of Physics D: Applied Physics*, 44(26):262002, 2011.

[15] J. P. Boeuf. A two-dimensional model of dc glow discharges. *Journal of Applied Physics*, 63(5):1342–1349, 1988.

[16] J. P. Boeuf, B. Bernecker, Th. Callegari, S. Blanco, and R. Fournier. Generation, annihilation, dynamics and self-organized patterns of filaments in dielectric barrier discharge plasmas. *Applied Physics Letters*, 100(24):244108, 2012.

[17] J. P. Boeuf, L. L. Yang, and L.C. Pitchford. Dynamics of a guided streamer (plasma bullet) in a helium jet in air at atmospheric pressure. *Journal of Physics D: Applied Physics*, 46(1):015201, 2013.

[18] F. Borgatelli and D. Dunn-Rankin. Behavior of a small diffusion flame as an electrically active component of a high-voltage circuit. *Combustion and Flame*, 159(1):210–220, 2012.

[19] A. Bourig, D. Thevenin, J.P. Martin, G. Janiga, and K. Zahringer. Numerical modeling of H_2-O_2 flames involving electronically-excited species $O_2(a^1\Delta_g)$,$(O^1\mathrm{D})$ and $\mathrm{OH}(^2\Sigma^+)$. *Proceedings of the Combustion Institute*, 32:3171–3179, 2009.

[20] S. A. Bozhenkov, S. M. Starikovskaia, and A. Y. Starikovskii. Nanosecond gas discharge ignition of H_2- and CH_4- containing mixtures. *Combustion and Flame*, 133(1-2):133–146, 2003.

[21] R. Brandenburg, Z. Navratil, J. Jansky, P. Stahel, D. Trunec, and H. E. Wagner. The transition between different modes of barrier discharges at atmospheric pressure. *Journal of Physics D: Applied Physics*, 42(8):085208, 2009.

[22] I. Brauer, C. Punset, H. G. Purwins, and J. P. Boeuf. Simulations of self-organized filaments in a dielectric barrier glow discharge plasma. *Journal of Applied Physics*, 85(11):7569–7572, 1999.

[23] D. Breden, K. Miki, and L. L. Raja. Computational study of cold atmospheric nanosecond pulsed helium plasma jet in air. *Applied Physics Letters*, 99(11):111501, 2011.

[24] D. Breden, K. Miki, and L. L. Raja. Modeling of an atmospheric pressure plasma jet in a helium-air diffusion zone. *50th AIAA Aerospace Sciences Meeting*, AIAA 2012-0794, Nashville Tennessee, 2012.

[25] D. Breden, K. Miki, and L. L. Raja. Self-consistent two-dimensional modeling of cold atmospheric-pressure plasma jets/bullets. *Plasma Sources Science and Technology*, 21(3):034011, 2012.

[26] D. Breden, L. L. Raja, C. A. Idicheria, P. M. Najt, and S. Mahadevan. A numerical study of high-pressure non-equilibrium streamers for combustion ignition application. *Journal of Applied Physics*, 114(8):083302, 2013.

[27] P. Bruggeman and C. Leys. Non-thermal plasmas in and in contact with liquids. *Journal of Physics D: Applied Physics*, 42(5):053001, 2009.

[28] J. Buckmaster. Edge-flames. *Journal of Engineering Mathematics*, 31:269–284, 1997.

[29] W. Rodi C. J. Chen. *Vertical turbulent buoyant jets: a review of experimental data.* Oxford, New York: Pergamon Press, 1980.

[30] H. F. Calcote. Ion production and recombination in flames. *Symposium (International) on Combustion*, 8(1):184–199, 1961.

[31] S. Célestin. *Study of the dynamics of streamers in air at atmospheric pressure.* PhD thesis, École Centrale Paris, 2008.

[32] Z. S. Chang, G. J. Zhang, X. J. Shao, and Z. H. Zhang. Diagnosis of gas temperature, electron temperature, and electron density in helium atmospheric pressure plasma jet. *Physics of Plasmas*, 19(7):073513, 2012.

[33] P. J. Chantry and R. E. Wootton. A critique of methods for calculating the dielectric strength of gas mixtures. *Journal of Applied Physics*, 52(4):2731–2739, 1981.

[34] A. Chirokov, A. Gutsol, A. Fridman, K. D. Sieber, J. M. Grace, and K. S. Robinson. Analysis of two-dimensional microdischarge distribution in dielectric-barrier discharges. *Plasma Sources Science and Technology*, 13(4):623–635, 2004.

[35] H. H. Chiu and T. M. Liu. Group combustion of liquid droplets. *Combustion Science and Technology*, 17(3):127–142, 1977.

[36] B. C. Choi, H. K. Kim, and S. H. Chung. Effect of AC electric fields on counterflow diffusion flame of methane. *Transactions of the Korean Society of Mechanical Engineers B*, 36(8):849–855, 2012.

[37] Y. H. Chung, D. G. Park, J. Park, O. B. Kwon, J. H. Yun, and S. I. Keel. Role of the outer-edge flame on flame extinction in nitrogen-diluted non-premixed counterflow flames with finite burner diameters. *Fuel*, 105:540–550, 2013.

[38] T. A. Cool and P. J. H. Tjossem. Direct observations of chemi-ionization in hydrocarbon flames enhanced by laser excited CH^* ($A^2\ \Delta$) and CH^* ($B^2\ \Sigma^-$). *Chemical Physics Letters*, 111(1-2):82–88, 1984.

[39] S. K. Dayal and T. P. Pandya. Optical study of counterflow diffusion flames in transverse electric fields. *Combustion and Flame*, 19(1):113–116, 1972.

[40] S. K. Dayal and T. P. Pandya. Structure of counterflow diffusion flame in transverse electric fields. *Combustion and Flame*, 35:277–287, 1979.

[41] S. K. Dhali and P. F. Williams. Two-dimensional studies of streamers in gases. *Journal of Applied Physics*, 62(12):4696–4707, 1987.

[42] G. Dixon-Lewis, M. D. Smooke, J. Warnatz, and et al. CHEMKIN Release 4.0. Reaction Design, Inc.: San Diego, California, 2004.

[43] H. Do, M. A. Cappelli, and M. G. Mungal. Plasma assisted cavity flame ignition in supersonic flows. *Combustion and Flame*, 157(9):1783–1794, 2010.

[44] A. Dogariu, M. N. Shneider, and R. B. Miles. Versatile radar measurement of the electron loss rate in air. *Applied Physics Letters*, 103(22):224102, 2013.

[45] J. W. Dold. Ends of laminar flamelets: their structure, behaviour and implications. *Nonlinear PDE's in Condensed Matter and Reactive Flows.* H. Berescki and Y. Pomeau (eds). Kluwer Academic Publishers, 2002.

[46] C. Douat, M. Fleury, M. Laroussi, and V. Puech. Interactions between two counterpropagating plasma bullets. *IEEE Transactions on Plasma Science*, 39(11):2298–2299, 2011.

[47] A. M. Drews, L. Cademartiri, M. L. Chemama, M. P. Brenner, G. M. Whitesides, and K. J. M. Bishop. AC electric fields drive steady flows in flames. *Physical Review E*, 86:036314, 2012.

[48] J. Du and R. L. Axelbaum. The effects of flame structure on extinction of CH_4-O_2-N_2 diffusion flames. *Symposium (International) on Combustion*, 26(1137-1142), 1996.

[49] X. Duan, F. He, and J. Ouyang. Uniformity of a dielectric barrier glow discharge: experiments and two-dimensional modeling. *Plasma Sources Science and Technology*, 21(1):015008, 2012.

[50] U. Ebert, C. Montijn, T. M. P. Briels, W. Hundsdorfer, B. Meulenbroek, A. Rocco, and E. M. van Veldhuizen. The multiscale nature of streamers. *Plasma Sources Science and Technology*, 15(2):S118–S129, 2006.

[51] U. Ebert, W. v. Saarlos, and C. Caroli. Propagation and structure of planar streamer fronts. *Physical Review E*, 55(2):1530–1549, 1997.

[52] O. Eichwald, H. Bensaad, O. Ducasse, and M. Yousfi. Effects of numerical and physical anisotropic diffusion on branching phenomena of negative-streamer dynamics. *Journal of Physics D: Applied Physics*, 45(38):385203, 2012.

[53] H. W. Ellis, R. Y. Pai, E. W. McDaniel, E. A. Mason, and L. A. Viehland. Transport properties of gaseous ions over a wide energy range. *Atomic Data and Nuclear Data Tables*, 17:177–210, 1976.

[54] G. P. Smith et al. GRI-MECH 3.0. http://www.me.berkeley.edu/gri_mech/.

[55] Y. Feng, C. S. Ren, Q. Y. Nie, and D. Z. Wang. Study of the self-organized pattern in an atmospheric pressure dielectric barrier discharge plasma jet. *IEEE Transactions on Plasma Science*, 38(5):1061–1065, 2010.

[56] L. Figura and A. Gomez. Laminar counterflow steady diffusion flames under high pressure ($p \leq 3$MPa) conditions. *Combustion and Flame*, 159:142–150, 2012.

[57] C. G. Fotache, T. G. Kreutz, D. L. Zhu, and C. K. Law. An experimental study of ignition in nonpremixed counterflowing hydrogen versus heated air. *Combustion Science and Technology*, 109:373–393, 1995.

[58] A. Fridman. *Plasma Chemistry*. Cambridge University Press, New York, 2008.

[59] A. Fridman and L. A. Kennedy. *Plasma Physics and Engineering*. Taylor and Francis, New York, 2004.

[60] C. E. Frouzakis, A. G. Tomboulides, J. Lee, and K. Boulouchos. From diffusion to premixed flames in an H_2/air opposed-jet burner: the role of edge flames. *Combustion and Flame*, 130:171–184, 2002.

[61] G. E. Georghiou, A. P. Papadakis, R. Morrow, and A. C. Metaxas. Numerical modelling of atmospheric pressure gas discharges leading to plasma production. *Journal of Physics D: Applied Physics*, 38(20):R303–R328, 2005.

[62] N. Gherardi, G. Gouda, E. Gat, A. Ricard, and F. Massines. Transition from glow silent discharge to micro-discharges in nitrogen gas. *Plasma Sources Science and Technology*, 9(3):340–346, 2000.

[63] A. Ghoniem. 2.28 Fundamentals and applications of combustion. *Massachusetts Institute of Technology: Lecture notes* 2009, 2011.

[64] R. J. Goldstein and T. H. Kuehn. *Fluid Mechanics Measurements*, chapter 7: Optical systems for flow measurement: shadowgraph, schlieren and interferometric techniques. Taylor and Francis, 1996.

[65] Y. B. Golubovskii, V. A. Maiorov, J. Behnke, and J. F. Behnke. Modelling of the homogeneous barrier discharge in helium at atmospheric pressure. *Journal of Physics D: Applied Physics*, 36(1):39–49, 2003.

[66] D. Goodwin, N. Malaya, H. Moffat, and R. Speth. CANTERA: An object-oriented software toolkit for chemical kinetics, thermodynamics, and transport processes. Version 2.0.2, available at https://code.google.com/p/cantera/, 2011.

[67] C. Guerra-Garcia and M. Martinez-Sanchez. Gas-confined barrier discharges: a simplified model for plasma dynamics in flame environments. *Journal of Physics D: Applied Physics*, 46(34):345204, 2013.

[68] J. Guikema, N. Miller, J. Niehof, M. Klein, and M. Walhout. Spontaneous pattern formation in an effectively one-dimensional dielectric-barrier discharge system. *Physical Review Letters*, 85(18):3817–3820, 2000.

[69] G.J.M Hagelaar. *Modeling of Microdischarges for display technology.* PhD thesis, Technical University of Eindhoven, 2000.

[70] G.J.M Hagelaar, F. J. de Hoog, and G.M.W. Kroesen. Boundary conditions in fluid models of gas discharges. *Physical Review E*, 62(1):1452–1454, 2000.

[71] G.J.M Hagelaar and G.M.W. Kroesen. Speeding up fluid models for gas discharges by implicit treatment of the electron energy source term. *Journal of Computational Physics*, 159(1):1–12, 2000.

[72] G.J.M Hagelaar and L.C. Pitchford. Solving the Boltzmann equation to obtain electron transport coefficients and rate coefficients for fluid models. *Plasma Sources Science and Technology*, 14(4):722–733, 2005.

[73] M. J. Hargather and G. S. Settles. A comparison of three quantitative schlieren techniques. *Optics and Lasers in Engineering*, 50(1):8–17, 2012.

[74] A. A. Ionin, I. V. Kochetov, A. P. Napartovich, and N. N. Yuryshev. Topical review: Physics and engineering of singlet delta oxygen production in low-temperature plasma. *Journal of Physics D: Applied Physics*, 40:R25–R61, 2007.

[75] Y. Itikawa. ITIKAWA database. www.lxcat.net, retrieved on August 12, 2013.

[76] Y. Itikawa and N. Mason. Cross sections of electron collisions with water molecules. *Journal of Physical and Chemical Reference Data*, 34(1):1–22, 2005.

[77] J. D. Jackson. *Classical Electrodynamics.* John Wiley and Sons, second edition, 1975.

[78] H. C. Jaggers and A. von Engel. The effect of electric fields on the burning velocity of various flames. *Combustion and Flame*, 16(3):275–285, 1971.

[79] F. L. Jones, P. M. Becker, and R. J. Heinsohn. A mathematical model of the opposed-jet diffusion flame: effect of an electric field on concentration and temperature profiles. *Combustion and Flame*, 19(3):351–362, 1972.

[80] Y. Ju, S. O. Macheret, M. N. Shneider, and R. B. Miles. Numerical study of the effect of microwave discharge on the premixed methane-air flame. *AIAA/ASME/SAE/ASEE Joint Propulsion Conference and Exhibit*, 40th:2004–3707, 2004.

[81] K. L. Kelly, J. E. Scharer, E. S. Paller, and G. Ding. Laser ionization and radio frequency sustainment of high-pressure seeded plasmas. *Journal of Applied Physics*, 92(2):698–709, 2002.

[82] J. Kestin, S. T. Ro, and W. A. Wakeham. Viscosity of the binary gaseous mixture helium-nitrogen. *Journal of Chemical Physics*, 56(8):4036–4042, 1972.

[83] M. K. Kim, S. H. Chung, and H. H. Kim. Effect of electric fields on the stabilization of premixed laminar bunsen flames at low AC frequency: bi-ionic wind effect. *Combustion and Flame*, 159(3):1151–1159, 2012.

[84] W. Kim, H. Do, M. G. Mungal, and M. A. Cappelli. Flame stabilization enhancement and NO_x production using ultra short repetitively pulsed plasma discharges. *44th AIAA Aerospace Sciences Meeting and Exhibit, Reno, Nevada*, pages AIAA 2006–560, 2006.

[85] W. Kim, H. Do, M. G. Mungal, and M. A. Cappelli. Investigation of NO production and flame structure in plasma enhanced premixed combustion. *Proceedings of the Combustion Institute*, 31(2):3319–3326, 2007.

[86] W. Kim, H. Do, M. G. Mungal, and M. A. Cappelli. A study of plasma-stabilized diffusion flames at elevated ambient temperatures. *IEEE Transactions on Plasma Science*, 36(6):2898–2904, 2008.

[87] W. Kim, M. G. Mungal, and M. A. Cappelli. Flame stabilization using a plasma discharge in a lifted jet flame. *43rd AIAA Aerospace Sciences Meeting and Exhibit*, Reno, Nevada, AIAA 2005-931, 2005.

[88] W. Kim, M. G. Mungal, and M. A. Cappelli. Formation and role of cool flames in plasma-assisted premixed combustion. *Applied Physics Letters*, 92(5):051503, 2008.

[89] W. Kim, M. G. Mungal, and M. A. Cappelli. The role of in situ reforming in plasma enhanced ultra lean premixed methane/air flames. *Combustion and Flame*, 157(2):374–383, 2010.

[90] U. Kogelschatz. Filamentary, patterned and diffuse barrier discharges. *IEEE Transactions on Plasma Science*, 30(4):1400–1408, 2002.

[91] U. Kogelschatz. Dielectric-barrier discharges: their history, discharge physics, and industrial applications. *Plasma Chemistry and Plasma Processing*, 23(1):R: 1–46, 2003.

[92] M. Kono, F. B. Carleton, A. R. Jones, and F. J. Weinberg. The effect of nonsteady electric fields on sooting flames. *Combustion and Flame*, 78(3-4):357–364, 1989.

[93] M. Kono, K. Iinuma, and S. Kumagai. The effect of DC to 10MHz electric field on flame luminosity and carbon formation. *Symposium (International) on Combustion*, 18(1):1167–1174, 1981.

[94] Y. D. Korolev and G. A. Mesyats. *Physics of Pulsed Breakdown in Gases*. Yekaterinburg, Ural Division of the Russian Academy of Sciences. ISBN 5-7691-0779-0, 1998.

[95] I. N. Kosarev, N. L. Aleksandrov, S. V. Kindysheva, S. M. Starikovskaia, and A. Starikovskii. Kinetics of ignition of saturated hydrocarbons by nonequilibrium plasma: CH_4- containing mixtures. *Combustion and Flame*, 154(3):569–586, 2008.

[96] I. N. Kosarev, N. L. Aleksandrov, S. V. Kindysheva, S. M. Starikovskaia, and A. Y. Starikovskii. Kinetics of ignition of saturated hydrocarbons by nonequilibrium plasma: C_2H_6- to C_5H_{12}- containing mixtures. *Combustion and Flame*, 156(1):221–233, 2009.

[97] I. N. Kosarev, V. I. Khorunzhenko, E. I. Mintoussov, P. N. Sagulenko, N. A. Popov, and S. M. Starikovskaia. A nanosecond surface dielectric barrier discharge at elevated pressures: time-resolved electric field and efficiency of initiation of combustion. *Plasma Sources Science and Technology*, 21(4):045012, 2012.

[98] C. H. Kruger, C. O. Laux, L. Yu, D. M. Packan, and L. Pierrot. Nonequilibrium discharges in air and nitrogen plasmas at atmospheric pressure. *Pure and Applied Chemistry*, 74(3):337–347, 2002.

[99] M. Laroussi and T. Akan. Arc-free atmospheric pressure cold plasma jets: a review. *Plasma Processes and Polymers*, 4(9):777–788, 2007.

[100] J. Lawton, P. J. Mayo, and F. J. Weinberg. Electrical control of gas flows in combustion processes. *Proceedings of the Royal Society of London. Series A*, 303(1474):275–298, 1968.

[101] J. Lawton and F. J. Weinberg. Maximum ion currents from flames and the maximum practical effects of applied electric fields. *Proceedings of the Royal Society of London. Series A*, 277(1371):468–497, 1964.

[102] J. Lawton and F. J. Weinberg. *Electrical aspects of combustion*. Oxford University Press, 1969.

[103] J. Lee, C. E. Frouzakis, and K. Boulouchos. Two-dimensional direct numerical simulation of opposed-jet hydrogen-air flames: transition from diffusion to an edge flame. *Proceedings of the Combustion Institute*, 28(1):801–806, 2000.

[104] S. R. Lee, Y. Na, and J. S. Kim. Application of the flame hole dynamics to a diffusion flame in channel flow. *KSME International Journal*, 17(11):1775–1783, 2003.

[105] J. I. Levatter and S. Lin. Necessary conditions for the homogeneous formation of pulsed avalanche discharges at high gas pressures. *Journal of Applied Physics*, 51(1):210–222, 1980.

[106] T. C. Lieuwen. *Unsteady combustor physics*, chapter 9. Cambridge University Press, 2012.

[107] A. Liñan. The asymptotic structure of counterflow diffusion flames for large activation energies. *Acta Astronautica*, 1:1007–39, 1974.

[108] S. Liu and M. Neiger. Excitation of dielectric barrier discharges by unipolar submicrosecond square pulses. *Journal of Physics D: Applied Physics*, 34(11):1632–1638, 2001.

[109] A. Luque and U. Ebert. Sprites in varying air density: charge conservation, glowing negative trails and changing velocity. *Geophysical Research Letters*, 37:L06806, 2010.

[110] A. Luque and U. Ebert. Density models for streamer discharges: beyond cylindrical symmetry and homogeneous media. *Journal of Computational Physics*, 231(3):904–918, 2012.

[111] C. S. MacLatchy. Langmuir probe measurements of ion density in atmospheric-pressure air-propane flame. *Combustion and Flame*, 36:171–178, 1979.

[112] C. S. MacLatchy, R. M. Clements, and P. R. Smy. An experimental investigation of the effect of microwave radiation on a propane-air flame. *Combustion and Flame*, 45:161–169, 1982.

[113] D. Maric, M. Radmilovic-Radenovic, and Z. L. Petrovic. On parametrization and mixture laws for electron ionization coefficients. *European Physical Journal D*, 35:313–321, 2005.

[114] A. Martinez-Gonzalez, J. A. Guerrero-Viramontes, and D. Moreno-Hernandez. Temperature and velocity measurement fields of fluids using a Schlieren system. *Applied Optics*, 51(16):3519–3525, 2012.

[115] E. W. McDaniel and E. A. Mason. *The Mobility and Diffusion of Ions in Gases*. New York: Wiley, 1973.

[116] J. B. Michael. *Localized Microwave Pulsed Plasmas for Ignition and Flame Front Enhancement*. PhD thesis, Princeton University, 2012.

[117] R. B. Miles. Personal communication, 2013.

[118] R. B. Miles, W. R. Lempert, and J. N. Forkey. Laser Rayleigh scattering. *Measurement Science and Technology*, 12(5):R33–R51, 2001.

[119] R. B. Miles, D. F. Opaits, M. N. Shneider, S. H. Zaidi, and S. O. Macheret. Nonthermal atmospheric pressure plasmas for aeronautic applications. *European Physical Journal - Applied Physics*, 47(2):22802, 2009.

[120] E. I. Mintoussov, S. V. Pancheshnyi, and A. Y. Starikovskii. Propane-air flame control by non-equilibrium low-temperature pulsed nanosecond barrier discharge. *42nd AIAA Aerospace Sciences Meeting and Exhibit, Reno, Nevada*, AIAA 2004-1013, 2004.

[121] J. P. Moeck, D. A. Lacoste, C. O. Laux, and C. O. Paschereit. Control of combustion dynamics in a swirl-stabilized combustor with nanosecond repetitively pulsed discharges. *51st AIAA Meeting, Grapevine, Texas*, pages AIAA 2013–0565, 2013.

[122] W. L. Morgan, J. P. Boeuf, and L. C. Pitchford. The Siglo Data base, CPAT and Kinema software. http://www.siglo-kinema.com.

[123] W. L. Morgan and Kinema Research. MORGAN database. www.lxcat.net, retrieved on August 27, 2013.

[124] P. M. Morse and H. Feshbach. *Methods of Theoretical Physics. Part II.* McGraw-Hill Book Company, Inc., 1953.

[125] G. V. Naidis. Modelling of streamer propagation in atmospheric-pressure helium plasma jets. *Journal of Physics D: Applied Physics*, 43(40):402001, 2010.

[126] G. V. Naidis. Modelling of plasma bullet propagation along a helium jet in ambient air. *Journal of Physics D: Applied Physics*, 44(21):215203, 2011.

[127] G. V. Naidis. Structure of streamers propagating in non-uniform gases. *30th International Conference on Phenomena in Ionized Gases*, Belfast, Northern Ireland, UK, 2011.

[128] G. V. Naidis. Modeling of helium plasma jets emerged into ambient air: influence of applied voltage, jet radius, and helium flow velocity on plasma jet characteristics. *Journal of Applied Physics*, 112(10):103304, 2012.

[129] G. V. Naidis. Simulation of a single streamer traveling along two counterpropagating helium jets in ambient air. *IEEE Transactions on Plasma Science*, 40(11):2866–2869, 2012.

[130] G. V. Naidis. Simulation of interaction between two counter-propagating streamers. *Plasma Sources Science and Technology*, 21(3):034003, 2012.

[131] V. Nayagam, R. Balasubramaniam, and P. D. Ronney. Diffusion flame-holes. *Combustion Theory and Modelling*, 3:727–742, 1999.

[132] Q. Y. Nie, C. S. Ren, D. Z. Wang, S. Z. Li, J. L. Zhang, and M. G. Kong. Self-organized pattern formation of an atmospheric pressure plasma jet in a dielectric barrier discharge configuration. *Applied Physics Letters*, 90(22):221504, 2007.

[133] H. Nishiyama and M. Nakamura. Capacitance of a strip capacitor. *IEEE Transactions on components, hybrids, and Manufacturing Technology*, 13(2):417–423, 1990.

[134] H. Nishiyama and M. Nakamura. Form and capacitance of parallel-plate capacitors. *IEEE Transactions on components, packaging, and Manufacturing Technology*, 17(3):477–484, 1994.

[135] M. Nudnova and A. Starikovskii. Streamer head structure: role of ionization and photoionization. *Journal of Physics D: Applied Physics*, 41(23):234003, 2008.

[136] T. Ombrello. *Plasma-Assisted Combustion: Systematic Decoupling of the Kinetic Enhancement Mechanisms of Ignition, Flame Propagation, and Flame Stabilization by Long-Lifetime Species*. PhD thesis, Princeton University, 2009.

[137] T. Ombrello, Y. Ju, and A. Fridman. Kinetic ignition enhancement of diffusion flames by nonequilibrium magnetic gliding arc plasma. *AIAA Journal*, 46(10):2424–2433, 2008.

[138] T. Ombrello, S. H. Won, Y. Ju, and S. Williams. Flame propagation enhancement by plasma excitation of oxygen. Part I: effects of O_3. *Combustion and Flame*, 157(10):1906–1915, 2010.

[139] T. Ombrello, S. H. Won, Y. Ju, and S. Williams. Flame propagation enhancement by plasma excitation of oxygen. Part II: effects of $O_2(a^1\Delta_g)$. *Combustion and Flame*, 157(10):1916–1928, 2010.

[140] D. F. Opaits, M. N. Shneider, P. J. Howard, R. B. Miles, and G. M. Milikh. Study of streamers in gradient density air: table top modeling of red sprites. *Geophysical Research Letters*, 37:L14801, 2010.

[141] J. T. Ouyang, X. X. Duan, S. W. Xu, and F. He. The key factor for uniform and patterned glow dielectric barrier discharge. *Chinese Physics Letters*, 29(2):025201, 2012.

[142] D. Packan. *Repetitive Nanosecond glow discharge in atmospheric pressure air*. Report TSD-152, 2003.

[143] D. Pai. *Nanosecond Repetitively Pulsed Plasmas in Preheated Air at Atmospheric Pressure*. PhD thesis, École Centrale Paris, 2008.

[144] D. Pai, D. A. Lacoste, and C. O. Laux. Images of nanosecond repetitively pulsed plasmas in preheated air at atmospheric pressure. *IEEE Transactions on Plasma Science*, 36(4):974–975, 2008.

[145] D. Pai, D. A. Lacoste, and C. O. Laux. Transitions between corona, glow, and spark regimes of nanosecond repetitively pulsed discharges in air at atmospheric pressure. *Journal of Applied Physics*, 107(9):093303, 2010.

[146] D. Pai, G. D. Stancu, D. A. Lacoste, and C. O. Laux. Nanosecond repetitively pulsed discharges in air at atmospheric pressure - the glow regime. *Plasma Sources Science and Technology*, 18(4):045030, 2009.

[147] A. J. Palmer. A physical model on the initiation of atmospheric-pressure glow discharges. *Applied Physics Letters*, 25(3):138–140, 1974.

[148] S. Pancheshnyi, M. Nudnova, and A. Starikovskii. Development of a cathode-directed streamer discharge in air at different pressures: Experiment and comparison with direct numerical simulation. *Physical Review E*, 71:016407, 2005.

[149] S. Pancheshnyi, P. Segur, J. Capeillere, and A. Bourdon. Numerical simulation of filamentary discharges with parallel adaptive mesh refinement. *Journal of Computational Physics*, 227(13):6574–6590, 2008.

[150] S. V. Pancheshnyi, D. A. Lacoste, A. Bourdon, and C. O. Laux. Ignition of propane-air mixtures by a repetitively pulsed nanosecond discharge. *IEEE Transactions on Plasma Science*, 34(6):2478–2487, 2006.

[151] S. V. Pancheshnyi, S. M. Starikovskaia, and A. Y. Starikovskii. Role of photoionization processes in propagation of cathode-directed streamer. *Journal of Physics D: Applied Physics*, 34(1):105–115, 2001.

[152] L. Papageorghiou, E. Panousis, J. F. Loiseau, N. Spyrou, and B. Held. Two-dimensional modelling of a nitrogen dielectric barrier discharge (DBD) at atmospheric pressure: filament dynamics with the dielectric barrier on the cathode. *Journal of Physics D: Applied Physics*, 42(10):105201, 2009.

[153] J. S. Park, D. J. Hwang, J. Park, J. S. Kim, S. Kim, S. I. Keel, T. K. Kim, and D. S. Noh. Edge flame instability in low-strain-rate counterflow diffusion flames. *Combustion and Flame*, 146(4):612–619, 2006.

[154] R.W.B Pease and A. G. Gaydon. *The identification of molecular spectra.* London Chapman and Hall. John Wiley and Sons, New York, 4th edition, 1976.

[155] T. Pedersen and R. C. Brown. Simulation of electric field effects in premixed methane flames. *Combustion and Flame*, 94(4):433–448, 1993.

[156] B. M. Penetrante and et al. Pulsed corona and dielectric-barrier discharge processing of NO in N_2. *Applied Physics Letters*, 68(26):3719–3721, 1996.

[157] G. Pilla. *Etude Expérimentale de la Stabilisation de Flammes Propane-Air de Prémélange par Décharges Nanosecondes Impulsionnelles Répétitives.* PhD thesis, École Centrale Paris, 2008.

[158] G. Pilla, D. Galley, D. A. Lacoste, F. Lacas, D. Veynante, and C. O. Laux. Stabilization of a turbulent premixed flame using a nanosecond repetitively pulsed discharge. *IEEE Transactions on Plasma Science*, 34(6):2471–2477, 2006.

[159] E. R. Place and F. J. Weinberg. Electrical control of flame carbon. *Proceedings of the Royal Society of London. Series A*, 289(1417):192–205, 1966.

[160] J. Poggie, I. Adamovich, N. Bisek, and M. Nishihara. Numerical simulation of nanosecond-pulse electrical discharges. *Plasma Sources Science and Technology*, 22(1):015001, 2013.

[161] T. Poinsot and D. Veynante. *Theoretical and numerical combustion.* Edwards, Inc., 2001.

[162] N. A. Popov. The effect of nonequilibrium excitation on the ignition of hydrogen-oxygen mixtures. *High Temperature*, 45(2):261–279, 2007.

[163] C. Punset, J. P. Boeuf, and L. C. Pitchford. Two dimenstional simulation of an alternating current matrix plasma display cell: cross-talk and other geometric effects. *Journal of Applied Physics*, 83(4):1884–1897, 1998.

[164] C. Punset, S. Cany, and J. P. Boeuf. Addressing and sustaining in alternating current coplanar plasma display panels. *Journal of Applied Physics*, 86(1):124–133, 1999.

[165] B. Qi, C. Ren, D. Wang, S. Z. Li, K. Wang, and Y. Zhang. Uniform glowlike plasma source assisted by preionization of spark in ambient air at atmospheric pressure. *Applied Physics Letters*, 89(13):131503, 2006.

[166] Y. Raitzer. *Gas Discharge Physics*. Springer-Verlag, 1991.

[167] G. G. Raju. *Gaseous electronics. Theory and practice*. Taylor and Francis Group, 2006.

[168] A. Rakitin, A. Nikipelov, and A. Starikovskiy. Ignition of hydrocarbon-air mixtures with non-equilibrium plasma at elevated pressures. *51st AIAA Meeting, Grapevine, Texas*, pages AIAA 2013–1054, 2013.

[169] J. Ran, H. Luo, and X. Wang. A dielectric barrier discharge in neon at atmospheric pressure. *Journal of Physics D: Applied Physics*, 44(33):335203, 2011.

[170] L. A. Rosocha, D. M. Coates, D. Platts, and S. Stange. Plasma-enhanced combustion of propane using a silent discharge. *Physics of Plasmas*, 11(5):2950–2956, 2004.

[171] L. A. Rosocha, Y. Kim, G. K. Anderson, S. Abbate, and R. Sanchez-Gonzalez. Non-thermal plasma-assisted combustion research at Los Alamos. *Pulsed Power Conference, 16th IEEE International*, 2007.

[172] G. A. Russell. Electrical impedance measurements of an electrothermal loudspeaker. *Journal of the Acoustical Society of America*, 47(6 (part 1)):1482–1484, 1970.

[173] Y. Sakiyama and D. B. Graves. Corona-glow transition in the atmospheric pressure RF-excited plasma needle. *Journal of Physics D: Applied Physics*, 39(16):3644–52, 2006.

[174] S. Samukawa and et al. Review article: the 2012 plasma roadmap. *Journal of Physics D: Applied Physics*, 45(25):253001 (37pp), 2012.

[175] V. S. Santoro, A. Liñan, and A. Gomez. Propagation of edge flames in counter-flow mixing layers: experiments and theory. *Proceedings of the Combustion Institute*, 28(2):2039–2046, 2000.

[176] D. L. Scharfetter and H. K. Gummel. Large-signal analysis of a silicon Read diode oscillator. *IEEE Transactions on Electron Devices*, 16(1):64–77, 1969.

[177] A. Schutze, J. Y. Jeong, S. E. Babayan, J. Park, G. S. Selwyn, and R. F. Hicks. The atmospheric-pressure plasma jet: a review and comparison to other plasma sources. *IEEE Transactions on Plasma Science*, 26(6):1685–1694, 1998.

[178] R. Seiser, K. Seshadri, E. Piskernik, and A. Liñan. Ignition in the viscous layer between counterflowing streams: asymptotic theory with comparison to experiments. *Combustion and Flame*, 122(3):339–349, 2000.

[179] E. S. Semenov and A. S. Sokolik. Thermal and chemical ionization in flames. *Fizika Goreniya i Vzryva*, 6(1):37–48, 1970.

[180] K. Seshadri, T. Lu, O. Herbinet, S. Humer, U. Niemann, W. J. Pitz, and C. K. Law. Experimental and kinetic modeling study of extinction and ignition of methyl decanoate in laminar nonpremixed flows. LLNL-PROC-400370. *32^{nd} International Symposium on Combustion, Montreal, Canada*, 2008.

[181] K. Seshadri and F. A. Williams. Laminar flow between parallel plates with injection of a reactant at high Reynolds number. *International Journal of Heat and Mass Transfer*, 21(2):251–253, 1978.

[182] G. S. Settles. *Schlieren and shadowgraph techniques: visualizing phenomena in transparent media*. Springer-Verlag, Berlin Heidelberg NY, 2001.

[183] K. Shinohara, N. Takada, and K. Sasaki. Enhancement of burning velocity in premixed burner flame by irradiating microwave power. *Journal of Physics D: Applied Physics*, 42(18):182008, 2009.

[184] R. S. Sigmond, T. Sigmond, L. Rolfseng, A. F. Bohman, F. T. Stormo, and L. Hvidsten. The aiming of the bolt: how a flashover finds the weak spot. *IEEE Transactions on Plasma Science*, 32(5):1812–1818, 2004.

[185] H. Smith and T. M. Sugden. Studies on the ionization produced by metallic salts in flames. III Ionic equilibria in hydrogen / air flames containing alkali metal salts. *Proceedings of the Royal Society of London. Series A*, 211(1104):31–58, 1952.

[186] S. Stange, Y. Kim, V. Ferreri, L.A.Rosocha, and D. M. Coates. Flame images indicating combustion enhancement by Dielectric Barrier Discharges. *IEEE Transactions on Plasma Science*, 33(2), 2005.

[187] A. M. Starik, V. E. Kozlov, and N. S. Titova. On mechanisms of a flame velocity increase upon activation of O_2 molecules in electrical discharge. *Journal of Physics D: Applied Physics*, 41(12):125206, 2008.

[188] A. M. Starik and N. S. Titova. Kinetics of ion formation in the volumetric reaction of methane with air. *Combustion, Explosion and Shock waves*, 38(3):253–268, 2002.

[189] S. M. Starikovskaia. Topical review: Plasma assisted ignition and combustion. *Journal of Physics D: Applied Physics*, 39(16):R265–R299, 2006.

[190] S. M. Starikovskaia, N. B. Anikin, S. V. Pancheshnyi, D. V. Zatsepin, and A. Starikovskii. Pulsed breakdown at high overvoltage: development, propagation and energy branching. *Plasma Sources Science and Technology*, 10(2):344–355, 2001.

[191] S. M. Starikovskaia, A. Starikovskii, and D. V. Zatsepin. The development of a spatially uniform fast ionization wave in a large discharge volume. *Journal of Physics D: Applied Physics*, 31(9):1118–1125, 1998.

[192] A. Y. Starikovskii, N. B. Anikin, I. N. Kosarev, E. I. Mintusov, M. M. Nudnova, A. E. Rakitin, D. V. Roupassov, S. M. Starikovskaia, and V. P. Zhukov. Nanosecond-pulsed discharges for plasma-assisted combustion and aerodynamics. *Journal of Propulsion and Power*, 24(6):1182–1197, 2008.

[193] A. Starikovskiy. Personal communication, 2013.

[194] A. Starikovskiy and N. Aleksandrov. *Plasma-Assisted Ignition and Combustion, Aeronautics and Astronautics*, Max Mulder (Ed.). ISBN: 978-953-307-473-3, InTech, DOI: 10.5772/17727, 2011.

[195] A. Starikovskiy and N. Aleksandrov. Review: Plasma-assisted ignition and combustion. *Progress in Energy and Combustion Science*, 39(1):61–110, 2013.

[196] A. Starikovskiy, A. Nikipelov, and A. Rakitin. Streamer breakdown development in undercritical electric field. *IEEE Transactions on Plasma Science*, 39(11):2606–2607, 2011.

[197] E. M. Stockman. *Microwave enhanced combustion of laminar hydrocarbon flame fronts*. PhD thesis, Princeton University, 2009.

[198] E. S. Stockman, S. H. Zaidi, R. B. Miles, C. D. Carter, and M. D. Ryan. Measurements of combustion properties in a microwave enhanced flame. *Combustion and Flame*, 156(7):1453–1461, 2009.

[199] L. Stollenwerk, S. Amiranashvili, J. P. Boeuf, and H. G. Purwins. Measurements and 3D simulation of self-organized filaments in a Barrier Discharge. *Physical Review Letters*, 96:255001, 2006.

[200] D. J. Sullivan, S. H. Zaidi, S. O. Macheret, Y. Ju, and R. B. Miles. Microwave techniques for the combustion enhancement of laminar flames. *40th AIAA/ASME/SAE/ASEE Joint Propulsion Conference*, pages AIAA–2004–3713, 2004.

[201] W. Sun. *Non-equilibrium plasma-assisted combustion*. PhD thesis, Princeton University, 2013.

[202] W. Sun, M. Uddi, T. Ombrello, S. H. Won, C. Carter, and Y. Ju. Effects of non-equilibrium plasma discharge on counterflow diffusion flame extinction. *Proceedings of the Combustion Institute*, 33(2):3211–3218, 2011.

[203] W. Sun, M. Uddi, S. H. Won, T. Ombrello, C. Carter, and Y. Ju. Kinetic effects of non-equilibrium plasma-assisted methane oxidation on diffusion flame extinction limits. *Combustion and Flame*, 159(1):221–229, 2012.

[204] W. Sun, S. H. Won, T. Ombrello, C. Carter, and Y. Ju. Direct ignition and S-curve transition by in situ nano-second pulsed discharge in methane/oxygen/helium counterflow flame. *Proceedings of the Combustion Institute*, 34(1):847–855, 2013.

[205] S. Tao, L. Kaihua, Z. Cheng, Y. Ping, Z. Shichang, and P. Ruzheng. Experimental study of repetitive unipolar nanosecond-pulse dielectric barrier discharge in air at atmospheric pressure. *Journal of Physics D: Applied Physics*, 41(21):215203, 2008.

[206] M. D. Teixeira. *Étude numérique de l'interaction d'une flamme de diffusion méthane-air avec une décharge à barrière diélectrique.* PhD thesis, Univ. Pierre et Marie Curie, ONERA, 2009.

[207] A. A. Tropina, M. Uddi, and Y. Ju. On the effect of nonequilibrium plasma on the minimum ignition energy. Part I: discharge model. *IEEE Transactions on Plasma Science*, 39(1):615–623, 2011.

[208] A. A. Tropina, M. Uddi, and Y. Ju. On the effect of nonequilibrium plasma on the minimum ignition energy. Part II. *IEEE Transactions on Plasma Science*, 39(12):3283–3287, 2011.

[209] H. Tsuji. Counterflow diffusion flames. *Progress in Energy and Combustion Science*, 8:93–119, 1982.

[210] S. R. Turns. *An introduction to combustion, concepts and applications.* McGraw-Hill Higher Education, 2 edition, 2000.

[211] UCSD. Chemical-kinetic mechanism for combustion applications. San Diego Mechanism web page, Mechanical and Aerospace Engineering (Combustion Research), University of California at San Diego (http://combustion.ucsd.edu).

[212] M. Uddi, N. Jiang, E. I. Mintusov, I. V. Adamovich, and W. R. Lempert. Atomic oxygen measurements in air and air/fuel nanosecond pulse discharges by two photon laser induced fluorescence. *Proceedings of the Combustion Institute*, 32:929–936, 2009.

[213] L. M. Vasilyak, S. V. Kostyuchenko, N. N. Kudryavtsev, and I. V. Filyugin. Fast ionization waves under electrical breakdown conditions. *Physics-Uspekhi*, 37(3):247–269, 1994.

[214] A. B. Vatazhin, V. A. Likhter, V. A. Sepp, and V. I. Shulgin. Effect of an electric field on the nitrogen oxide emission and structure of a laminar propane diffusion flame. *Fluid Dynamics*, 30(1):166–174, 1995.

[215] L. A. Viehland and C. C. Kirkpatrick. Relating ion/ neutral reaction rate coefficients and cross-sections by accessing a database for ion transport properties. *International Journal of Mass Spectrometry and Ion Processes*, 149-150:555–571, 1995.

[216] L. A. Viehland and C. C. Kirkpatrick. VIEHLAND database, www.lxcat.net, retrieved on April 1, 2014.

[217] A. Vincent-Randonnier. *Combustion Enhancement and Stabilization: Principles of Plasma Assistance and Diagnostics Tools. Handbook of Combustion.*, volume 5: 125-160. Wiley-VCH Verlag, 2010.

[218] A. Vincent-Randonnier, S. Larigaldie, P. Magre, and V. Sabel'nikov. Experimental study of a methane diffusion flame under dielectric barrier discharge assistance. *IEEE Transactions on Plasma Science*, 35(2):223–232, 2007.

[219] A. Vincent-Randonnier, S. Larigaldie, P. Magre, and V. Sabel'nikov. Plasma assisted combustion: effect of a coaxial DBD on a methane diffusion flame. *Plasma Sources Science and Technology*, 16(1):149–160, 2007.

[220] A. Vincent-Randonnier and D. Teixeira. Plasma assisted methane diffusion flame: experiments and numerical simulation. *International Journal of Plasma Environmental Science and Technology*, 2(2):119–127, 2008.

[221] A. Vincent-Randonnier and D. Teixeira. Interaction of plasma discharges with a flame: experimental and numerical study. *AIP Conference Proceedings*, 1282:82–86, 2010.

[222] N. T. Vuong and Z. Puzewicz. Stabilized TEA CO_2 laser with double photopreionization and low-ionization-potential additives. *Soviet Journal of Quantum Electronics*, 12(1):94–95, 1982.

[223] L. Wang, E. R. Hawkes, and J. H. Chen. Flame edge statistics in turbulent combustion. *Proceedings of the Combustion Institute*, 33(1):1439–1446, 2011.

[224] J. Warnatz, U. Maas, and R.W. Dibble. *Combustion: Physical and chemical fundamentals, modeling and simulation, experiments, pollutant formation*. Springer, 4th edition, 2006.

[225] F. J. Weinberg, K. Hom, A. K. Oppenheim, and K. Teichman. Ignition by plasma jet. *Nature*, 272(23):341–343, 1978.

[226] F. A. Williams. Progress in knowledge of flamelet structure and extinction. *Progress in Energy and Combustion Science*, 26(4-6):657–682, 2000.

[227] D. L. Wisman, S. D. Marcum, and B. N. Ganguly. Chemi-ion-current-induced dissociative recombination in premixed hydrocarbon/air flames. *Journal of Propulsion and Power*, 24(5):1079–1084, 2008.

[228] S. H. Won, M. S. Cha, C. S. Park, and S. H. Chung. Effect of electric fields on reattachment and propagation speed of tribrachial flames in laminar coflow jets. *Proceedings of the Combustion Institute*, 31(1):963–970, 2007.

[229] S. H. Won, S. K. Ryu, M. K. Kim, M. S. Cha, and S. H. Chung. Effect of electric fields on the propagation speed of tribrachial flames in coflow jets. *Combustion and Flame*, 152(4):496–506, 2008.

[230] D. A. Xu, D. A. Lacoste, D. L. Rusterholtz, P. Q. Elias, G. D. Stancu, and C. O. Laux. Experimental study of the hydrodynamic expansion following a nanosecond repetitively pulsed discharge in air. *Applied Physics Letters*, 99(12):121502, 2011.

[231] X. Yu, J. Peng, P. Yang, R. Sun, Y. Yi, Y. Zhao, D. Chen, and J. Yu. Enhancement of a laminar premixed methane/oxygen/nitrogen flame speed using femtosecond-laser-induced plasma. *Applied Physics Letters*, 97(1):011503, 2010.

[232] Y. V. Yurgelenas and H. E. Wagner. A computational model of a barrier discharge in air at atmospheric pressure: the role of residual surface charges in microdischarge formation. *Journal of Physics D: Applied Physics*, 39(18):4031–4043, 2006.

[233] Y. Zhang, B. Gu, W. Wang, D. Wang, and X. Peng. Experimental investigation on large-area dielectric barrier discharge in atmospheric nitrogen and air assisted by the ultraviolet lamp. *Spectrochimica Acta, Part A: Molecular and Biomolecular Spectroscopy*, 72(3):460–464, 2009.

[234] Y. Zhang, Y. Wu, H. Yang, H. Zhang, and M. Zhu. Effect of high-frequency alternating electric fields on the behavior and nitric oxide emission of laminar non-premixed flames. *Fuel*, 109:350–355, 2013.

[235] W. C. Zhu, Q. Li, X. M. Zhu, and Y. K. Pu. Characteristics of atmospheric pressure plasma jets emerging into ambient air and helium. *Journal of Physics D: Applied Physics*, 42(20):202002, 2009.